NASA-CR-196305

Technical Progress Report

Guaranteed Time Observations Support for Faint Object Spectrograph (FOS) on HST

NAG5-1630

November 1, 1993 -- April 30, 1994

Richard Harms, P.I.

University Of California, San Diego
9500 Gilman Drive, La Jolla CA 92093-0111

I. Overall Progress

A. Results Obtained During the Reporting Period

1. GTO Observations

The goals of the GTO effort are for investigations defined in previous years by the IDT to be carried out as HST observations and for the results to be communicated to the scientific community and to the public.
The following is a listing of FOS GTO observations performed from just after the First Servicing Mission, which defined the end of Cycle 3, until the end of the the reporting period. This period consisted almost entirely of Orbital Verification II and Science Verification II, so there were very few FOS GTO observations.

FOS GTO Tracking

FOS "PI": Angel, Bohlin, bUrbidge, Davidsen, Ford, Harms, Margon

Date	Prop	Cycl	Old#	PI	Title	Target	
11/15/93	4847	3	1029	A	Spectropol QSOs, Blazars & AGN Cy>3	B	MRK486
11/18/93	3196	1	1046	F	Im & UV Spectr Loc Grp Pl Neb (26), Cy1	W	K648/M15, LMC PNs
11/22/93	4861	3	1053	M	Binaries in Glob Clus M15 Im (37) Aug Cy 3	W	M15 Im
11/29/93	4856	3	1027	U	UV Spectra of QSOs with z>3.1 Cy 3		UM670
2/11/94	5267	3	5267	H	ERO - Velocity Dispersions in M87		M87, NGC4486
4/17/94	5098	4	1026	U	UV Spectra of Low-z QSOs (1), Cy 4 Im	U	3C286
5/5/94	5634	4	5267	H	ERO - Velocity Dispersions in M87	R	M87, NGC4486

The following observations were tentatively scheduled, but have not been noted in OSS reports

2/26-27/94	5122	3	1034	F	M87's Jet Nucleus & Hot Corona (12) Cy 3	U	M87

Bianchi, L., Ford, H. C., & Bohlin, R., 1994, "HST Imaging of the Planetary Nebula K648 in M15", [to be submitted to *ApJ].*

Blair, W. P., "Far-UV Observations of Supernova Remnants", 1993, in *Proceedings of IAU Colloquium 145 "Supernovae and Supernovae Remnants"*, ed. R. McCray and Z. Wang (Cambridge: Cambridge University Press), [in press].

Bianchi, L., et al., "Ultraviolet and Optical Spectroscopy of a B Supergiant Star in M31", *Astron. Astrophys.*, 1994, [in press].

Burks, G. S., Bartko, F., Shull, J. M., Stocke, J. T., Sachs, E. R., Burbidge, E. M., Cohen, R. D., Junkkarinen, V. T., Harms, R. J., Massa, D., "A Study of UV Absorption Lines through the Complete Galactic Halo by the Analysis of HST-FOS Spectra of Active Galactic Nuclei. I", [to appear in Ap. J. Dec. 20, 1994].

Diplas, A., Tripp, T. M., Beaver, E. A., "Observations of High Velocity Gas with HST/FOS and IUE," 1993, *Presented at the ST ScI Halos Workshop*, Baltimore, MD (submitted).

Diplas, A., Beaver, E. A., Blanco, P. R., "Application of the Pixon Based Restoration to HST Spectra and Comparison to the Richardson-Lucy and Jansson Algorithms--Restoration of Absorption Lines", presented at the *HST Image Restoration Workshop*, Baltimore, Maryland, 1993 [submitted].

Ferrarese, L., Ford, H. C., 1993, "Surface Brightness Parameters from Deconvolved PC Images of Elliptical Galaxies", in *"The Restoration of HST Images and Spectra II"*, eds R. Hanish and R. White, STSCI Publications [in press].

Ferrarese, L., Ford, H. C., Jaffe, W., van den Bosch, F., & O'Connell, R. W., 1993, "The Nuclear Disk of NGC 4261: HST Images and WHT Spectra", in the *Proceedings of the IAU Symposium 159 "Active Galactic Nuclei Across the Electromagentic Spectrum"*, eds T. J.-L. Courvoisier and A. Blecha [in press].

Ford, H. C., Harms, R. J., Tsvetanov, Z. I., Hartig, G. F., Dressel, L. L., Kriss, G. A., Davidsen, A. F., Bohlin, R. C., and Margon B., "Narrow Band HST Images of M87: Evidence for a Disk of Ionized Gas Around a Massive Black Hole", 1994 [to be submitted to *Ap. J.*].

Hamann, F., Junkkarinen, V., Cohen, R., Barlow, T., Beaver, E., Burbidge, E. M., and Lyons, R., "Time Variable Associated Absorption Article in the QSO UM675", 1994 [in preparation].

Hamann, F., Simon, M., Carr, J. S., and Prato, L., "[Fe II] 1.53 and 1.64 μm Emission from Pre-Main Sequence Stars", 1994 [submitted to *Ap.J*].

Harms, R. J., Ford, H. C., Tsvetanov, Z. I., Hartig, G. F., Dressel, L. L., Kriss, G. A., Bohlin, R., Davidsen, A. F., Margon, B., and Kochhar, A. K., "HST FOS Spectroscopy of M87: Evidence for a Disk of Ionized Gas Around a Massive Black Hole", 1994 [submitted to *Ap. J. Letters*].

Junkkarinen, V., Lyons, R., Beaver, E., Burbidge, E. M., Cohen, R., Barlow, T., and Hamann, F., "UV Spectroscopy of the QSO UM675 with the Hubble Space Telescope Faint Object Spectrograph", 1994 [in preparation].

Kriss, G. A. 1994, "Fitting Models to UV and Optical Spectral Data: Using SPECFIT in IRAF", *Astr. Soc. of the Pacific Conf. Series*, [in press].

Kriss, G. A., Evans, I. N., Ford H. C., Tsvetanov, Z., Davidsen, A. F., & Kinney, A. L., 1993 "Collimated Radiation in NGC 4151: HST Images and HUT Spectra", in *The Nature of Compact Objects in AGN*, eds. A. Robinson and R. J. Terlevich, (Cambridge University Press: Cambridge) [in press].

Kriss, G. A., Ford, H. C., Evans, I. N., Tsvetanov, Z., Uomoto, A., & Caganoff, S. 1993, "HST Imaging of Jets and Collimated Radiation in AGN", in *Astrophysical Jets*, (STScI: Baltimore) [in press].

Lyons, R. W., Beaver, E. A., Burbidge, E. M., Cohen, R. D., and Junkkarinen, V. T., "Low Resolution Observations of the UV Spectrum of the QSO 1442+101 (OQ 172) with the Faint Object Spectrograph", 1993 (in preparation).

Smith, P. S., Schmidt, G. D., Allen, R. G., and Angel, J. R. P. , "The Polarization and UV Spectrum of the Obscured Quasar Markarian 231" [in preparation].

Smith, P. S., Schmidt, G. D., Allen, R. G., and Angel, J. R. P. "Optical and UV Spectropolarimetry of I Zw 1 and Markarian 486", [in preparation].

Tsvetanov, Z., Evans, I. N., Kriss, G. A., & Ford, H. C., 1993, "HST Observations of NGC 4151: Implications for the Unified Model of AGN", in the *Proceedings of IAU Symp. 159 AGN Across the Electromagnetic Spectrum*, eds. T. J.-L. Courvoisier and A. Blecha [in press].

Tsvetanov, Z., Kriss, G. A., Dressel, L., Evans, I. N. & Ford, H. C., 1993, "Subarcsecond Optical Structure of the Nucleus of Mrk 3", [in preparation].

3. Presentations

Informing the scientific community also takes the form of presentations, workshops and meetings. FOS GTO team members attended and presented at the January 1994 AAS meeting in Washington D.C. FOS team members also took an active part in workshops at the STScI on Instrument Calibrations and Image Reconstruction in November 1993.

Informing the public is also a part of our mission. FOS GTO team members gave public information lectures at all team locations. One Co-Investigator provided a briefing of NAS and NASA-HQ personnel, while another served as a panel member of the "Space Astronomy Update" forum and press conference every 1.5 months during this period.

B. Scientific Significance of the Results

Perhaps the most exciting team project, the search for possible black holes in the nuclei of both normal and active nucleus galaxies, has had to be delayed to the post-servicing era, when we hope COSTAR will provide the subarcsecond angular resolution necessary for this program.

FOS spectropolarimetric observations of the nuclear region of the peculiar Seyfert galaxy Mrk 231 reveal that the continuum polarization peaks at 18% in the near UV and then declines rapidly toward shorter wavelengths. The polarization and flux spectra both suggest that the complex wavelength dependence of the polarization in the UV can be explained by a population of hot, young stars that dilutes the highly reddened and polarized light of the underlying AGN.

The papers on the absorption line analysis for our galactic halo address the spatial distribution of high and intermediate level ions in the halo and illustrate the patchy and heteregeous nature of the halo. Using QSOs as probes provides a complete path through the halo and offers the best means for understanding the spatial distribution of these ions and the sources providing the energetics for the ionization. We hope to have enough data to determine the scale heights of some high level ions such as NV and CIV. We are also trying to determine the spatial characteristics of intermediate level ions such as A1II and A1III. All of these factors bear on understanding the energetics and eventually the dynamics of the halo, its composition, spatial extent and mass. These are prerequisites to gaining insight into its origin and evolution in a more general context.

The papers on the scattering characteristics of the HST/FOS have provided us with data that shows that the HST mirror surfaces are quite smooth, even at the UV wavelengths. We are hoping that the post-costar data will tell us about the mid-spatial frequency ripple in the HST mirrors. These characteristics are important because they provide information on the limiting capability of HST to detect faint objects near bright sources. They also allow us to estimate the amount of unwanted (scattered light) that shows up in FOS observations and to correct for it.

WF-PC and FOC images of the halo PN K648 have been fully analyzed, and a paper is being submitted. Particular effort was required in fine-tuning the deconvolution process of the images, which is quite delicate in the case of a faint extended nebulosity surrounding a much brighter star. From the PC, FOC data , and complementary other data, we derived nebular quantities; and by analyzing IUE archive data, the atmostpheric and global parameters of the nucleus are interpreted with current evolutionary models. The object, previously unresolved from ground based data, is fully resolved with HST; and the morphology can be studied. A bipolar bright structure of 2.5 arcsec diameter is surrounded by a fainter spherical emission that is extended to about 5 arcssec diameter.

Assuming cylindrical symmetry, the observed intensity was deprojected to derive the bi-dimensional intensity (and electron density) distribution within the object, that can be compared with PN-shell-formation scenarios. Deriving accurate star and nebular parameters for this object is very important for two reasons: it is one of the few (nine to date) planetary nebulae known in the galactic halo, and one of the two that belong to a globular cluster. Therefore, K648 is particularly relevant and rare from an evolutionary point of view. In addition, we provide further evidence in our paper that the object actually belongs to the cluster M15. Its distance known to a superior accuracy than usually possible for planetary nebulae, since the distance to the cluster is known. Thus, quantities like dimensions and luminosity can be scaled to absolute units and compared with evolutionary scenarios. The measured diameter determines the mass of the ionized gas, M(gas)=0.07+/-0.02 solar masses.

Position Repeatability of Spectra Obtained with the FOS

R.W. Lyons[1], E.A Beaver[1], R.D. Cohen[1] and V.T. Junkkarinen[1]

Abstract

This paper deals with data taken before the on-board GIM correction was applied, and concerns observations taken in the atypical manner of many independent exposures. In this case, a GIM factor of 1.8 diodes Gauss^{-1} should be applied to Red side observations.

I. Introduction

FOS science proposals do not usually include requests for wavelength calibration exposures corresponding to the science exposures. Instead a standard wavelength calibration exposure is used to provide the correspondence between detector readout position (pixel number) and wavelength. The applicability of the standard calibration depends on the consistency with which the FOS hardware can place, and hold, spectra on the detector's diode array, exposure after exposure.

If we accept that wavelength errors are negligible for the standard calibration, then any difference we might find between the observed and expected wavelength of a given feature in a spectrum depends only on the hardware repeatability. Known factors affecting this repeatability are:

1) geomagnetically induced image motion or GIM (cf. Baity et al. 1993) This problem, identified early in Orbital Verification, was traced to poor quality magnetic shielding. Algorithms for its removal have been incorporated into the PODPS reduction software (see Keyes, this volume).

2) target centering error (1 to 2 quarter steps – Caganoff et al. 1992)

3) aperture wheel non–repeatability (small – Harms and Dressel 1992)

4) filter-grating wheel non-repeatability (Hartig 1989).

Other factors, such as temperature effects, may be important but have not been addressed.

A number of sky spectra were obtained with several low dispersion configurations as part of Science Verification. The output from several of the configurations contain well defined zero order spectra and atmospheric emission lines whose positions can be reliably compared from exposure to exposure. Since discrete targets are not

1. University of California, San Diego, CASS, La Jolla, CA 92093-0111

involved, the results are independent of target centering. The sky spectra form a consistent data set that can be used to study problems due to hardware repeatability.

II. Observations

Between February 1991 and March 1992, exposures of seventy sky fields were made using the G160L grating and the FOS Blue Digicon. During the same period exposures of 68 sky fields were obtained with the Red Digicon using the G160L and G650L gratings as well as the prism. The FOS target aperture, a 4.3 arcsec square, was used for all exposures. Fields which inadvertently contained point sources were identified using the zero order spectra present in the G160L and G650L exposures. These exposures and the prism sky spectra, which normally contain no discrete emission features, are not included in the following discussion.

III. Discussion

In practice, any observation run may be broken into several exposures to satisfy scheduling requirements. Each exposure, presented to the user in separate files, is usually broken up into several sub-exposures or readouts.

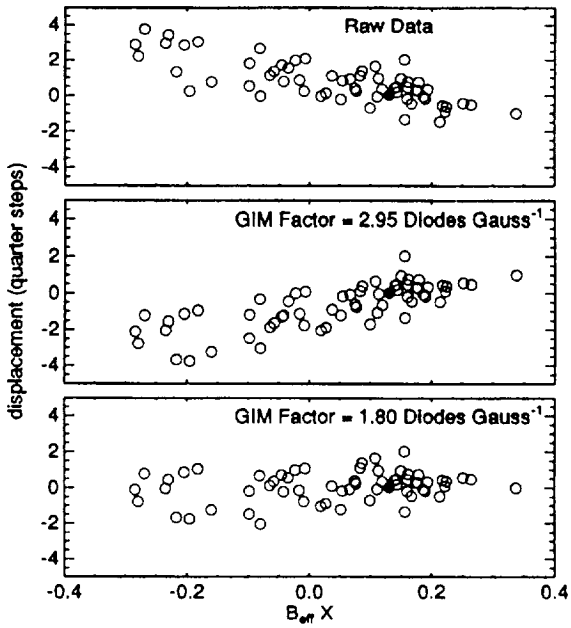

Fig. 1: Displacements for zero order of G160L Red detector data

As a first approximation to the variation due to non-repeatability, the raw data, corrected for bad channels but not for any geomagnetically induced motion, were used for each configuration. The zero order spectra were correlated with a standard chosen from the appropriate data set. For each configuration, only the first readout from each run was used since the hardware remained fixed for subsequent readouts. Figure 1 shows the position variation, in quarter steps relative to the chosen standard (filled circle), plotted against the component of the Earth's magnetic field

oriented along the detector array, $B_{eff}X$, for the G160L data taken with the Red detector. The correlation between displacement and magnetic field is apparent. A similar correlation occurs with the G650L data although the scatter is a bit larger due, perhaps, to the lower signal in the zero order spectra. The G160L data taken with the Blue detector show little correlation.

The dependence on the magnetic field, and hence the overall scatter, should be reduced by using data corrected for the geomagnetic image motion. The data were reduced in the standard manner but a dummy unit-value inverse sensitivity curve was used to avoid the loss of the zero order spectra. The standard reduction uses GIM factors of 2.95 diodes Gauss^{-1} for the Red detector and 0.7 diodes Gauss^{-1} for the Blue detector. Unexpectedly, the new results were worse for the Blue detector and different but not improved for the Red detector (see Figure 1).

Table I: Result of Zero Order Sky Spectrum Correlation

	σ (qs*)	Peak-to-Peak (qs*)	Linear Fit Slope (qs* Gauss^{-1})
G160L Blue – 64 Spectra			
Raw Data	0.47	2.1	0.67
GIM = 0.7 diodes Gauss^{-1}	0.72	3.5	3.28
GIM = 0.4 diodes Gauss^{-1}	0.47	2.1	0.90
G160L Red – 62 Spectra			
Raw Data	1.19	5.3	-5.81
GIM = 2.95 diodes Gauss^{-1}	1.22	5.8	6.01
GIM = 1.80 diodes Gauss^{-1}	0.83	4.1	1.33
G650L Red – 62 Spectra			
Raw Data	1.69	8.1	-6.23
GIM = 2.95 diodes Gauss^{-1}	1.64	7.2	5.50
GIM = 1.80 diodes Gauss^{-1}	1.40	5.9	1.02

* qs stands for quarter steps ~12.5μ (4 quarter steps diode^{-1})

Since these tests were run prior to implementation of the on-board GIM correction, each exposure was preceded by a degauss operation. The data set for each configuration was formed using only the first sub-exposure from each observation. These sub-exposures are completely independent and each was preceded immediately by a degauss operation. Previous work (Hartig et al 1991), confirmed by laboratory tests (Beaver and Foster 1992), indicated smaller GIM factors were required to register data immediately preceded by a degauss. For the Red side, the smaller factor is around 1.8 diodes Gauss^{-1} compared to 2.95 diodes Gauss^{-1} within an exposure. Similar tests have not been run on the Blue side but the Blue side is expected to be better by a factor of 4 or so, implying a reduced GIM factor around 0.4. The results on the Red side improved when the smaller GIM factor was used as can be seen in Figure 1.

The peak to peak scatter and internal scatter about the mean for the various configurations and conditions are presented in Table I. We believe that most of this scatter is due to filter-grating wheel non-repeatability. Keep in mind that these numbers refer to the position repeatability between independent exposures. Consecutive exposures made in a single run with the same instrument configuration are not independent since the filter–grating wheel is not moved.

IV. Conclusions

The GIM corrections were originally implemented to register sub-exposures within exposures, which they do. However, the manner of implementation has not corrected the lack of registration between exposures. Two GIM factors are required. The best factors determined in this analysis are smaller than those found previously or expected indicating the need for additional work. This is particularly true for the Blue detector since the factors are small and the best result was obtained with no GIM correction. Small position errors in the flat fields and the wavelength and intensity calibrations may be present due to the use of the wrong GIM factors.

For random observations the maximum differences in the zero points of the wavelength scales due to hardware non-repeatability are 2, 4, and 6 quarter steps for the G160L Blue, Red and G650L Red configurations respectively. (Note that the standard calibration observations are also subject to position non-repeatabilities.) The standard deviations are 0.5, 0.8 and 1.4 quarter steps respectively. The values for the G650L are less certain due to the poorer quality of the zero order spectra.

The G160L configuration on the Blue side corresponds to the same hardware configuration as the G270H on the Red side so we might expect that the uncertainties, with proper corrections, would be comparable. The uncertainties in the G130H can be assessed on the Blue side using the geocoronal Lyα line. Other acceptable features, such as strong interstellar lines, might be useable with some of the other configurations, especially the high dispersion ones.

For more information see Lyons et al. 1993.

Acknowledgment

This work was supported by NASA – NAS5-29293 and NAG5-1630.

References

Baity, W.A., Beaver, E.A., Cohen, R.D., Junkkarinen, V.T., Lyons, R.W, Fitch, J.E., Hartig, G.F., Lindler, D.J. 1993, "Performance of the FOS detectors in a variable external magnetic field," in Space Astronomical Telescopes and Instruments II, ed. P.Bely and J.Breckinridge (Bellingham, WA: SPIE) 1945, in press.

Beaver, E.A., Foster, P. 1992 "Lab Test Results of the FOS Detector Performance in a Variable External Magnetic Field," FOS Instrument Science Report CAL/FOS-082.

Caganoff, S., Tsvetanov, Z., Armus, L. 1992, "FOS Onboard Target Acquisition Tests," FOS Instrument Science Report CAL/FOS-081.

Harms, R., Dressel, L. 1992, "Aperture Calibrations During Science Verification of the FOS," FOS Instrument Science Report CAL/FOS-072, (report being rewritten – results quoted are from the FOS Science Verification Report Summary).

Hartig, G. 1989, ""FOS Filter–Grating Wheel Repeatability: Dependence on Motor Selection," FOS Instrument Science Report CAL/FOS-060.

Hartig, G., Lindler, D., Beaver, E., Junkkarinen, V., Lyons, R. 1991, "FOS Red-Side Sensitivity to the Geomagnetic Field," FOS Instrument Science Report (unnumbered).

Lyons, R.W., Beaver, E.A., Cohen, R.D., Junkkarinen, V.T. 1993, "Position Repeatability of Spectra Obtained with the FOS," FOS Instrument Science Report CAL/FOS-111.

Preliminary Comparison of the *HST* and White Dwarf Absolute Flux Scales[1]

Ralph Bohlin[2]

Summary

As part of an ongoing effort to develop a set of standard stars with accurate absolute spectrophotometry from 1050 to 10000Å, the FOS flux spectrum for G191B2B (WD0501+527) is divided by a model spectrum for the case of a pure hydrogen atmosphere to derive the difference between the current *HST* flux scale and the flux scale defined by the physics of model atmosphere calculations. Figure 1 and the Appendix specify the conversion function.

Discussion

G191B2B is one of four standard stars that are used to establish and routinely monitor FOS sensitivity. Figure 1 shows the ratio of the observed fluxes to the model for a) the FOS blue side, b) the FOS red side, and c) the composite reference spectrum of the *IUE*+Oke that resides in the STScI Calibration Data Base System (CDBS). These FOS spectra are from the high dispersion modes, which have a resolving power of ~1200. See Bohlin and Lindler (1992) for details of the pedigree of the CDBS reference spectra. The pure hydrogen model is for 60,000 K, log g = 7.5 and is normalized to m=11.79 mag at 5490Å, where m=0 corresponds to 3.61E-9 in F-lambda units (Finley, personal communication). The dots in the top three panels of Figure 1 a-c are the actual ratios of the observations/model in 10Å bins, while the heavy solid lines are spline fits to the ratios using 40 spline nodes. The bottom panel d) compares the adopted fit for the FOS blue side (heavy solid line) with the FOS red (dots) and the CDBS (dashed line).

The FOS spectra have been flux calibrated according to the prescription of Lindler and Bohlin (in prep), which will supersede the current pipeline procedure that is documented in Neill, Bohlin, and Hartig (1992). The main improvements in the new calibration procedure account for the changing sensitivity of FOS with time and for the OTA focus changes due to desorption (Lindler and Bohlin 1993). The agreement in Figure 1d to ~2 percent typically between the FOS blue and red side high dispersion fluxes in their overlap region longward of 1600Å is indicative of the internal consistency of the new flux calibration procedure. If the 4 coadded FOS blue side observations happened to be all low by a 2-3 sigma statistical scatter in the repeatability of FOS spectrophotometry, the systematic difference of ~4 percent between the FOS blue correction and the CDBS (i.e. *IUE*) correction in the 2000-

---

1. Originally published as Instrument Science Report on Standard Calibration Sources, 002
2. Space Telescope Science Institute, Baltimore, MD 21218

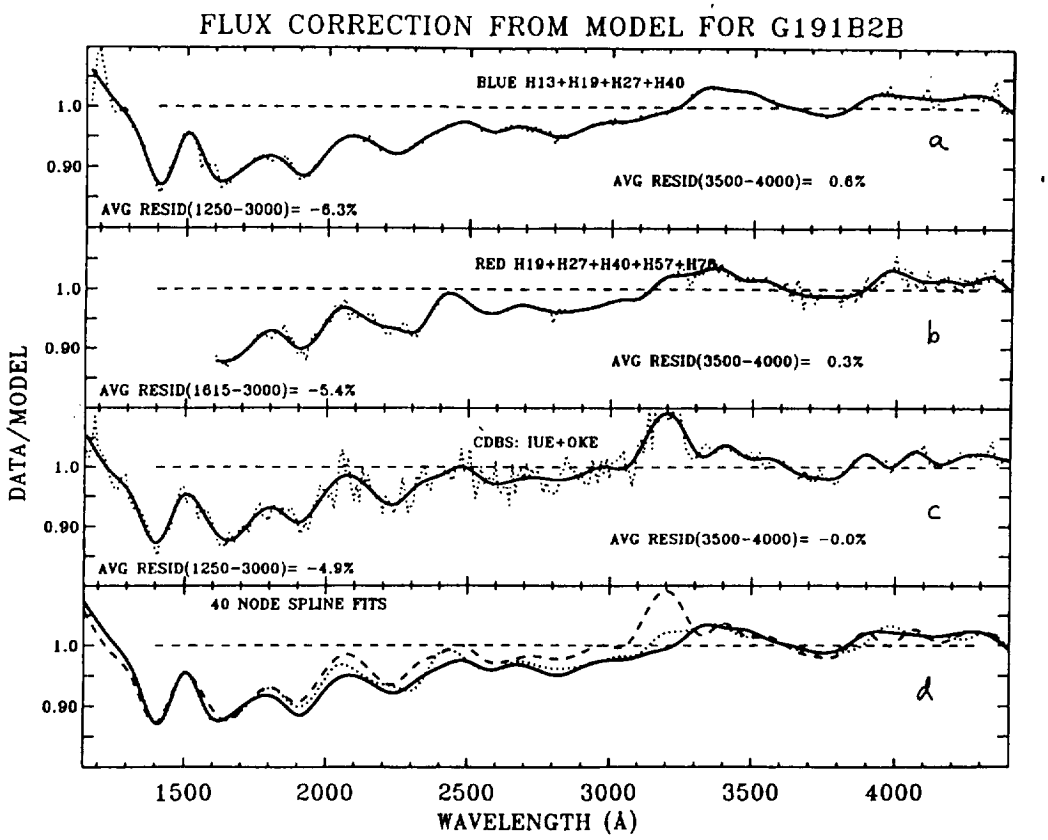

Figure 1: Montage shows the ratio of the observed fluxes to the model for a) the FOS blue side, b) the FOS red side, c) a composite *IUE* and Oke spectrum, and d) a comparison of the adopted fits.

3000Å region could be explained. Alternatively, our *IUE* reference spectrum of G191B2B (Bohlin et al. 1990) might be high by up to ~4 percent, since that flux level is defined by the sum of only 6 *IUE* long wavelength (LW) spectra. More study is need to resolve this small inconsistency.

The +10 percent bump in the CDBS correction at 3200Å is caused by a mismatch between the *IUE* and the Oke (1990) spectra. Since this region of the reference spectrum is ignored in the fitting process used to derive FOS calibrations, the residuals of the FOS fluxes with respect to the model are much less. However, the deviation of the FOS from the model at 3200-3500Å is probably due to the uncertainties of the Oke reference data. Longward of 3500Å, the residuals illustrate the current uncertainty level of ~3 percent in the data/model.

The preliminary conversion from the current *HST* flux scale to the WD flux scale is accomplished by dividing the current FOS fluxes by the function represented by the heavy solid line in the bottom panel of Figure 1. The Appendix is an IDL conversion procedure, which contains the table of the 40 spline nodes that define this conversion function.

Future Work

Without the complications of an intervening atmosphere, more accurate relative spectrophotometry should be possible with FOS than has been previously achieved over the wavelength range 1150-8500Å. Therefore, the goal of the analysis of the calibration data is to understand all uncertainties above the 1 percent level. Eventually, the adjustment of the *IUE-HST* absolute flux scale should probably be converted to the white dwarf flux standard. However, more FOS observations of white dwarfs with the purest hydrogen atmospheres are needed to derive the white dwarf based FOS calibration to greater precision. Additional work on the inclusion of metals in the model atmosphere calculations for G191B2B is needed, since Sion et al. (1992) have shown that absorption in metal lines is important at the ~2 percent level in some wavelength regions.

References

Bohlin, R. C., Harris, A. W., Holm, A., and Gry, C. 1990, Ap. J. Suppl., 73, 413.
Bohlin, R. C., & Lindler, D. J. 1992, Instrument Science Report CAL/SCS-001.
Lindler, D. J., & Bohlin, R. C. 1993, FOS Instrument Science Report CAL/FOS-102.
Neill, J. D., Bohlin, R. C., & Hartig, G. 1992, FOS Instrument Science Report CAL/FOS-077.
Oke, J. B. 1990, Astron. J., 99, 1621.
Sion, E., Bohlin, R., Tweedy, R., and Vauclair, G. 1992, Ap. J. Lett., 391, L29.

Appendix

```
FUNCTION FLXCOR,WAVE,FLX
;+
;
; PURPOSE:
;CORRECT UV FLUXES TO THE WD SCALE IN THE 1150-4400A RANGE. THESE
;PRELIMINARY CORRECTIONS ARE BASED ON FOS HI-DISP BLUE OBS AND
;FINLEY
;MODEL FOR G191B2B ONLY.  rcb
;
;calling sequence:
;CORRECTED_FLUX=FLXCOR(WAVE,FLX)
;
; input: WAVE-WAVELENGTH ARRAY OF FLUX VECTOR TO BE CORRECTED
; FLX-CORRESPONDING FLUX VECTOR TO BE CORRECTED
; output-THE FLX SPECTRUM CONVERTED TO THE WD STANDARD
; SPECTROPHOTOMETRY SCALE.
;
; HISTORY:
;93DEC8-RCB
;93DEC14-UPDATE SPLINE NODES
;-
; TABLE OF x spline nodes for g191b2b blue fos hi-disp
WFIT=[
$
1168.0,1250.8,1333.6,1416.5,1499.3,1582.1,1664.9,1747.7,1830.6,1913.4,$
1996.2,2079.0,2161.8,2244.7,2327.5,2410.3,2493.1,2575.9,2658.8,2741.6,$
2824.4,2907.2,2990.1,3072.9,3155.7,3238.5,3321.3,3404.2,3487.0,3569.8,$
3652.6,3735.4,3818.3,3901.1,3983.9,4066.7,4149.5,4232.4,4315.2,4398.0]

; TABLE OF y spline nodes for g191b2b blue fos hi-disp
CFIT=[
$
1.0616,1.0074,0.9473,0.8713,0.9547,0.8905,0.8843,0.9117,0.9121,0.8852,$
0.9250,0.9507,0.9369,0.9219,0.9443,0.9653,0.9745,0.9596,0.9675,0.9607,$
0.9507,0.9654,0.9754,0.9782,0.9893,1.0024,1.0322,1.0299,1.0255,1.0081,$
0.9979,0.9882,0.9954,1.0198,1.0222,1.0186,1.0157,1.0215,1.0200,1.     ]

GOOD=WHERE((WAVE GE 1150) AND (WAVE LE 4400))
CORRFLUX=FLX
CORRFLUX(GOOD)=FLX/CSPLINE(WFIT,CFIT,WAVE(GOOD))

RETURN,CORRFLUX
END
```

```
FUNCTION CSPLINE,XX,YY,TT
;+
;
;*NAME:CSPLINE
;
;*PURPOSE:
; function to evaluate a cubic spline at specified data points
;
;*CALLING SEQUENCE:
;result=cspline(x,y,t)
;
;*PARAMETERS:
; INPUTS:
;      x - vector of spline node positions
;      y - vector of node values
;      t - x-positions to evaluate the spline at
;
; OUTPUT:
;the values for positions t are returned as the function value
;
;METHOD:
;NUMERICAL RECIPES - natural cubic spline is used.
;
;HISTORY:
;version 1  D. Lindler May, 1989
;       Mar 16 1991      JKF/ACC     - forced doubleword to avoid
;                                      integer overflow errors.
;version 2  D. Lindler  Dec, 1991- moved to IDL V2.
;version 3 JKF/ACC      28-jan-1992 - handle not found case of WHERE
;-
;-------------------------------------------------------------------;
 x= double(xx)
 y= double(yy)
 t= double(tt)

 n=n_elements(x)
 y2=dblarr(n)      ;vector of 2nd derivatives at nodes in xtab
 u=dblarr(n)
;
; decomposition loop of tridiagonal algorithm
;
 for i=1,n-2 do begin
            sig=(x(i)-x(i-1))/(x(i+1)-x(i-1))
            p=sig*y2(i-1)+2.
            y2(i)=(sig-1.0)/p
            u(i)=(6.0*((y(i+1)-y(i))/(x(i+1)-x(i))-(y(i)-y(i-1))/$
                  (x(i)-x(i-1)))/(x(i+1)-x(i-1))-sig*u(i-1))/p
 end
; ,
; backsubstitution
;
 for i=n-2,0,-1 do y2(i)=y2(i)*y2(i+1)+u(i)
;
; find locations of t in xtab using bisection
```

```
;
 m=n_elements(t)
 klo=lonarr(m)
 khi=replicate(n-1,m)
 bisect:
      not_done=((khi-klo) gt 1)
      if max(not_done) gt 0 then begin
           k=(khi+klo)/2
           higher=x(k) gt t
           sub=where(not_done and higher, sub_found)
           if sub_found gt 0 then khi(sub)=k(sub)
           sub=where(not_done and (not higher), sub_found)
           if sub_found gt 0 then klo(sub)=k(sub)
           goto,bisect
      endif
;
; x(klo) and x(khi) now bracket t
;
 xhi=x(khi)
 xlo=x(klo)
 h=xhi-xlo
 a=(xhi-t)/h
 b=(t-xlo)/h
return,a*y(klo)+b*y(khi)+((a^3-a)*y2(klo)+(b^3-b)*y2(khi))*(h^2)/6.0
 end
```

UV Emission Lines in FOS Sky Spectra

R.W. Lyons[1], W.A. Baity[1], R.D. Cohen[1], V.T. Junkkarinen[1]

I. Motivation

Although sky light is recorded during exposures with the FOS, concurrent sky measurements are not made. Sky continuum background light during the *HST* nighttime arises mainly from zodiacal light and diffuse galactic light and can be corrected with reasonable confidence. The sky background can be quite variable for daytime exposures and has been detected in the UV down to ~1500Å on a number of occasions. The sky background increases in significance as one moves to longer wavelengths, becoming most significant at visible wavelengths. As well as a continuum contribution, there are a number of emission lines, mostly from hydrogen, oxygen and nitrogen species. Most of the lines show up at visible wavelengths and their presence, albeit rather erratic, appears to be limited to daytime observations. A few, however, occur in the UV and may have some impact on the interpretation of UV spectra, and it is to these UV lines that this contribution is devoted.

This work is based on three Science Verification tests, SV2965, SV2966 and SV2967, made to determine the nature and significance of the sky contribution in FOS spectra. Various aspects of these tests have been discussed previously in Lyons et al. (1992, 1993a and 1993b).

II. Observations

Exposures of seventy sky fields were made using the G160L grating and the Blue Digicon of the FOS between early 1991 and early 1992. During the same time period, exposures of 68 other sky fields were obtained with the Red Digicon using the G160L and G650L gratings as well as the prism. The FOS target aperture, a 4.3″ square, was used for all exposures. Any field which inadvertently contained a bright discrete source could be identified by examining the line spread function of the zero order spectrum obtained as part of the G160L and G650L exposures. Data from these fields are not included in the results presented here.

III. Discussion

Geocoronal Lyα and O I have been discussed previously (cf. Lyons et al. 1993a). As shown in Figure 1, the line strengths, expressed in counts sec^{-1} $pixel^{-1}$, depend mainly on the angle between the Sun and the Earth as seen from the spacecraft (the Sun-Earth angle or SEA). Lyα is always present while O I is only seen during the

1. University of California, San Diego, CASS, La Jolla, CA 92093-0111

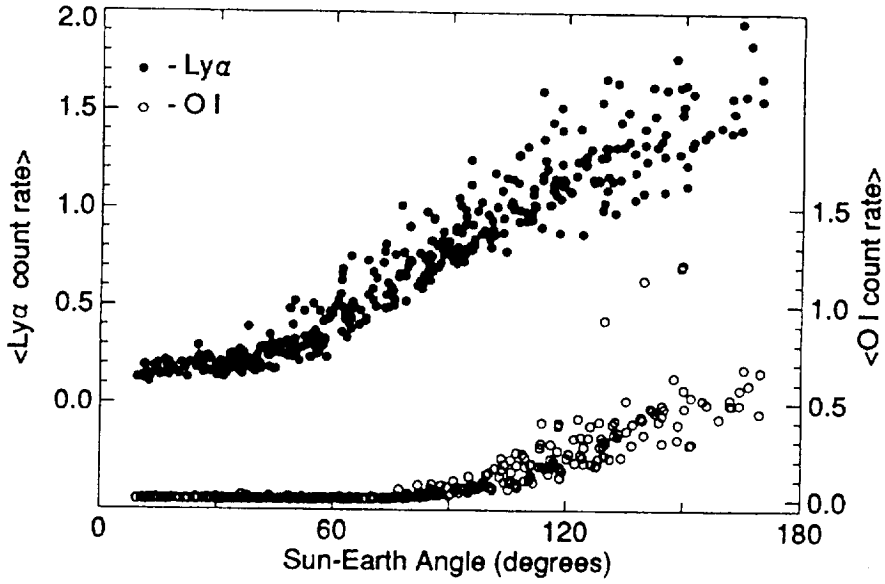

Figure 1: G160L Blue - Emission Line Strengths

daytime (SEA > 66°). On one run during a period of intense solar activity, unusually high O I rates were detected (Lyons et al. 1993a). Some of the scatter at any particular Sun-Earth angle results from a secondary dependence on the Earth-target angle or ETA, the angle between the center of the Earth and the target as seen from the spacecraft. Both of these lines were expected and their behavior is fairly predictable.

The behavior of other UV lines, one at ~2137Å , one at 2470Å previously identified as [O II] (Kinney 1993), and one at ~2802Å is much more erratic. Based on the position of the telescope when these emission lines appear, it seems that they, like the

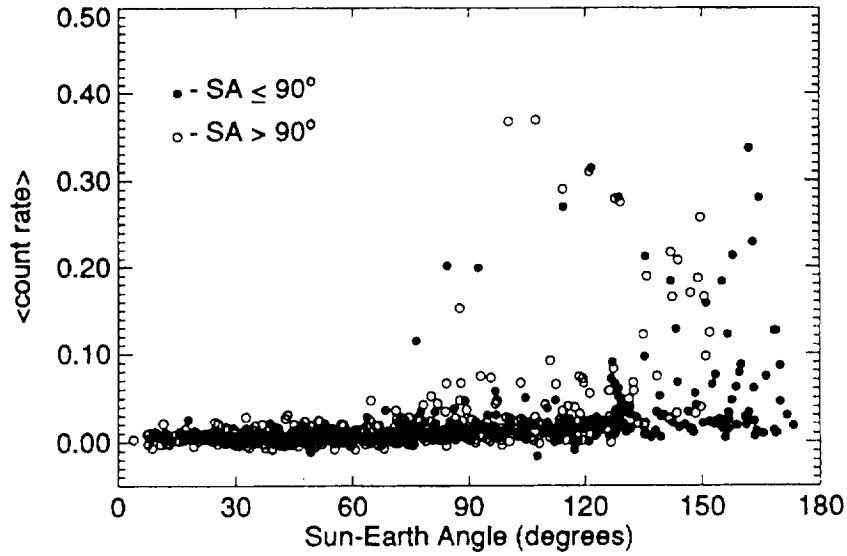

Figure 2: Relationship of [O II] count rate and SEA for prism spectra.

emission lines seen in the visible, occur exclusively during daytime exposures. However, they are absent on most of the daytime spectra taken. Since the large aperture was used for these exposures, the lines are very broad and their presence at low levels cannot be ruled out.

The line at 2137Å was evident on at least one prism spectrum in which the [O II] λ2470 line is also present. The sensitivity of the prism configuration this far into the UV is very poor. It is clearly seen on several of the G160L spectra taken with the Red detector.

Of these three UV lines, [O II] λ2470 is detected most often. When the count rate above the local continuum short of the line is plotted against SEA (Figure 2), it is apparent that the rate is elevated significantly above zero only during the *HST* daytime. Other than that there is no correlation with this angle. There is also no correlation with the Sun angle, SA (angle between the Sun and target as seen from the telescope), which is approximately constant for any observation run. A plot of the count rate against the Earth-target angle (Figure 3) does show a correlation, in the sense that higher rates are recorded for angles nearly tangential to the orbit, although it is apparent that at least one other factor is involved.

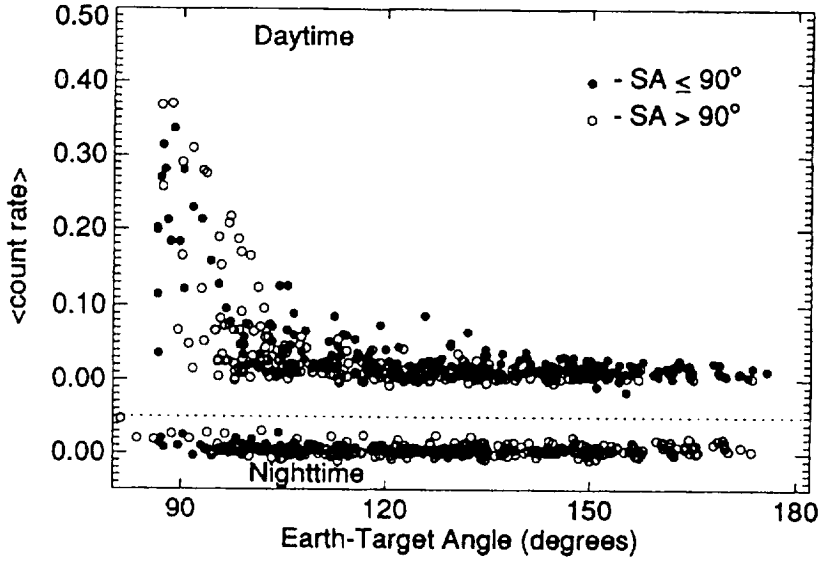

Figure 3: Relationship of [O II] count rate and ETA for prism spectra.

The available data on the third line, 2802Å, is sparse but a plot of the count rate against the Earth-target angle (Figure 4) suggests a correlation similar to that for the [O II] line. We suggest that this line is Mg II.

IV. Example

As a caution to other observers, we offer the following real life example. Figure 5a shows the total counts obtained plotted against wavelength for two consecutive exposures of a QSO taken with the Red Digicon and the G270H grating through the target acquisition aperture. The exposures were made entirely during the *HST*

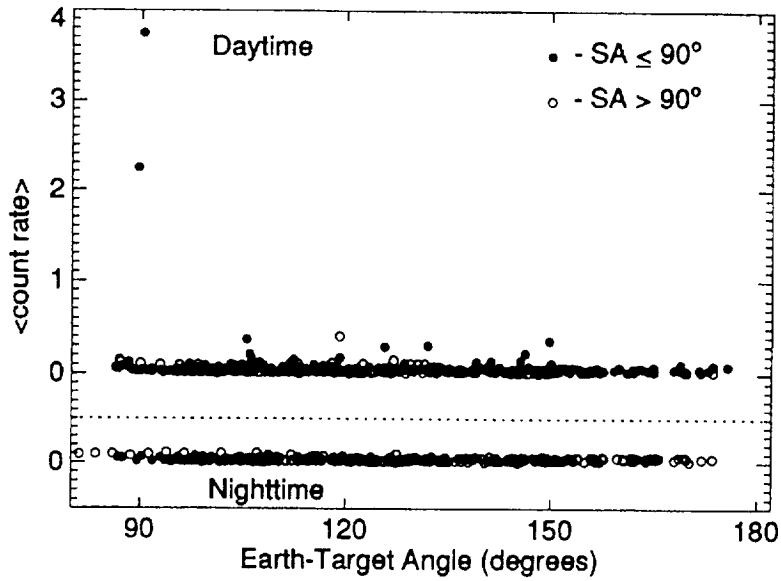

Figure 4: Relationship between 2802 A line and ETA from prism spectra.

daytime but on different orbits. Notice that the strengths of the emission features at 2470Å and 2802Å are consistent between the two exposures. Each exposure consisted of 12 sub-exposures. Two sub-exposures separated by about 7 minutes are shown in Figure 5b. The variation in the emission lines is clear. If this variation had been due to noisy channels, the number of pixels affected would have been different. The exposure time per pixel is indicated in the figure.

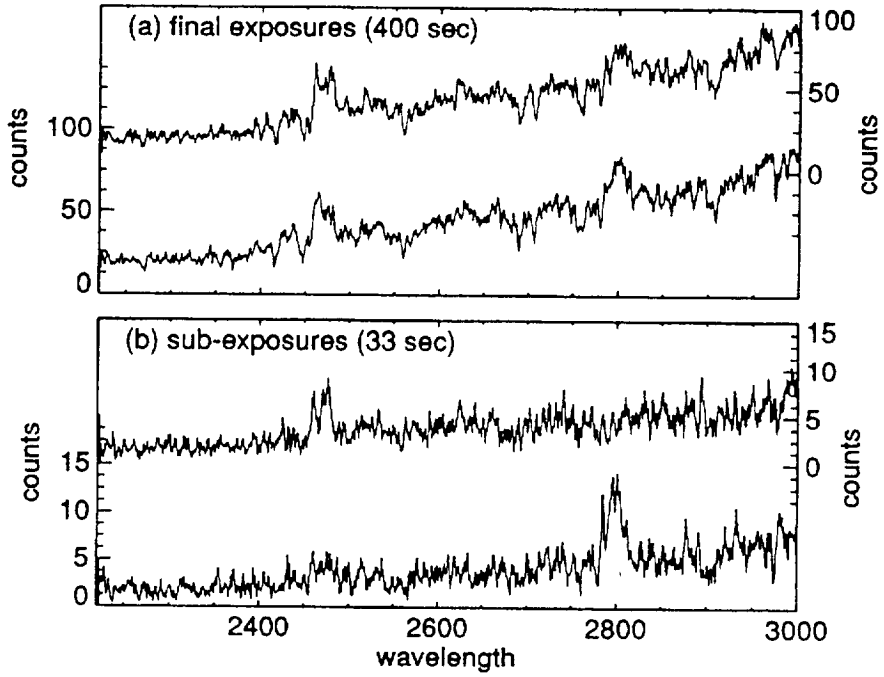

Figure 5: Sky lines in QSO exposures (G270H Red detector)

To the best of our knowledge at the moment, problems of this nature are restricted to the daytime portion of an observation. Further study is required to confirm whether this is correct. We note that the observations shown occurred at Earth-target angles above 114°, angles above those expected to produce any major problem based on the prism sky data.

Acknowledgments

This work was supported by NASA — NAS5-29293 and NAG5-1630.

References

Kinney, A. 1993, "Faint Object Spectrograph Instrument Handbook Version 4.0," Space Telescope Science Institute.

Lyons, R.W, Baity, W.A., Beaver, E.A., Cohen, R.D., Junkkarinen, V.T., Linsky, J.B. 1992, "Faint Object Spectrograph On-Orbit Sky Background Measurements," FOS Instrument Science Report CAL/FOS-083 (preliminary).

Lyons, R.W, Baity, W.A., Beaver, E.A., Cohen, R.D., Junkkarinen, V.T., Linsky, J.B., Bohlin, R.C. 1993a, "On-orbit sky background measurements with the FOS," in SPIE Proc. "Space Astronomical Telescopes and Instruments II," ed. P. Bely and J. Breckinridge (Bellingham, WA: SPIE), 1945 (in press).

Lyons, R.W., Baity, W.A., Beaver, E.A., Cohen, R.D., Junkkarinen, V.T., Bohlin, R.C.1993b, "Sky Background for the *HST*'s Faint Object Spectrograph," BAAS, 25, 1246.

Pre-COSTAR FOS Aperture Transmissions for Point Sources and Surface Brightness of Diffuse Sources[1]

R. C. Bohlin[2]

Abstract

The FOS absolute sensitivities are determined by observations of standard stars in the 4.3 arcsec acquisition aperture. For estimates of absolute fluxes of point sources that are observed in smaller apertures, the apparent, measured transmission of the smaller aperture relative to the 4.3 arcsec aperture is required. Proposal 4211 was designed to extend our knowledge of these aperture corrections and to verify the stability of the throughput relative to earlier measurements by proposal 3106 in 1991. Despite a lack of a theoretical explanation, the data demonstrate that the aperture corrections depend on the detector and grating and, therefore, differ from the true transmission of the aperture, which is a function of only the aperture size and the PSF at the relevant wavelength.

The formula for computing the specific intensity of sources of diffuse surface brightness depends on the absolute fractional transmission of the 4.3 aperture for a point source but NOT on the aperture correction for a smaller observation aperture.

I. Observations

In order to compute the relative aperture throughput, the count rate spectrum in the smaller apertures is divided by the countrate spectrum of the same star in the A1(4.3 arcsec) aperture. All of the mean measured aperture corrections in Table 1 are derived from countrates that are corrected to the optimal (zero) OTA focus position according to step 1 of the prescription of Lindler & Bohlin (1993), which is an improvement on the focus correction used to compute the corresponding throughput ratios that appeared in Table 4 of Neil, Bohlin & Hartig (1992); hereafter NBH. The OTA focus was +10 microns on 1991.43 for the Prop 3106 blue side data, –4 microns on 1991.96 for the Prop 3106 red side data, and –3.5 microns for the Prop 4211 measurements on 1992.77. The maximum focus corrections are on 1991.43 for the blue side, where the B2(0.3 arcsec) correction is .92 for the short wavelength gratings H13 and L15 but is less than 5 percent for the other gratings. For the larger apertures, the correction from +10 to 0 microns is less than 3 percent, so that errors in the correction procedure cannot cause anomalies larger than 1-2 percent. The data are recorded at three ybase positions perpendicular to the dispersion and verify the photometric precision, despite the ybase positioning errors discovered by Koratkar

1. Originally published as FOS Instrument Science Report CAL/FOS-106.
2. Space Telescope Science Institute, Baltimore, MD 21218

and Taylor (1993). The values in Table 1 represent the average ratio of the mean spectrum in the designated aperture divided by the mean spectrum in the A1 (4.3 arcsec) aperture, as discussed in more detail by NBH.

Table 1: Mean Aperture Throughput Ratios

Grat	Blue	Red	Blue	Red	Blue	Red	Blue	Red
	B3 (1 arcsec)		B1 (0.5 arcsec)		B2 (0.3 arcsec)		C2-SLIT	
H13	0.59	—	0.40	—	0.26	—	0.39	—
H13[a]	0.58	—	—	—	—	—	—	—
H19	0.60	0.60	0.42	0.44	0.26	0.31[b]	0.39	0.41
H19[c]	0.57	0.60	0.41	0.40[d]	0.29	0.21[d]	0.40	0.42
H19[a]	0.58							
H27	0.57	0.59	0.42	0.44	0.26	0.32	0.39	0.42
H27[a]	0.57							
H40	0.57	0.61	0.42	0.44	0.27	0.32	0.38	0.42
H57	—	0.59	—	0.44	—	0.31	—	0.41
H78	—	0.58	—	0.43	—	0.28	—	0.39
L15	0.65	0.67	0.46	0.50	0.31	0.30[b]	0.42	0.45
L15[c]	0.64[b]	0.66	0.46	0.44[d]	0.32	0.25[d]	0.44	0.45
L65	—	0.67	—	0.51	—	0.35	—	0.45
PRI[c]	0.53	0.54	0.37	0.36[d]	0.26	0.20[d]	0.37	0.39

a. prop 3235
b. Ystep repeatability worse than 3 percent. Excess jitter or ybase error.
c. prop 4211. Otherwise prop 3106.
d. Bad target acquisition. Use as lower limits.

The target acquisition for these data consists of a four stage peakup, where the final stage is in the B2(0.3 arcsec) aperture on 0.05 arcsec centers in order to limit the pointing uncertainty to 0.025 arcsec in each axis. There is an additional pointing tweak in the slit on 0.05 arcsec centers in the X axis only. During the side switch from blue to red in prop 4211, only the final stage of the peakup was done in the B2(0.3 arcsec) aperture. Unfortunately, the extent of this raster pattern was insufficient to account for the uncertainty in the offset between the sides and resulted in a pointing error of about 0.12 arcsec (Bohlin 1993). This 0.12 arcsec error means that the red side measurements in 4211 for the 0.5 arcsec and the 0.3 arcsec apertures are spuriously low. The subsequent red slit tweak up corrected the pointing error for the red side slit observations.

II. Comparison with models

Table 2 summarizes the expected aperture transmission of the four commonly used apertures relative to the A1(4.3 arcsec) aperture at optimal OTA focus, as derived from the Table 2 of Lindler & Bohlin (1993), who used the TIM software of Burrows & Hasan (1993) to estimate the aberrated PSF at the FOS entrance apertures. The weak wavelength dependence is caused by the change in the modeled PSF with wavelength and is <2 percent for the B3(1 arcsec) and slit over the most relevant wavelength range of 1400 to 5000Å on the blue side. The B2(0.3 arcsec) increases by 4 percent, while a drop of 10 percent is predicted for B1(0.5 arcsec) over the same range. Differences of a few percent between Table 2 and the relative transmissions of Evans (1993) are indicative of the fidelity of the TIM model PSFs. In order to compare the data with the theory, Table 3 contains the ratios of the measurements of Table 1 to the predictions of Table 2. The lower limits are omitted in Table 3.

Table 2: Relative Aperture Transmission From TIM Theory at OTA Nominal Focus

Grat	WL	Blue	Red	Blue	Red	Blue	Red	Blue	Red
		B3 (1arcsec)		B1 (0.5 arcsec)		B2 (0.3 arcsec)		C2-SLIT	
.H13	1400	.618	—	.483	—	.314	—	.427	—
H19	2000	.614	.612	.473	.475	.315	.317	.425	.414
H27	3000	.610	.610	.462	.462	.316	.320	.423	.415
H40	4000	.610	.609	.450	.450	.322	.323	.422	.415
H57	5000	.609	.607	.438	.437	.327	.326	.422	.416
H78	8000	—	.614	—	.437	—	.303	—	.407
L15	2000	.614	.612	.473	.475	.315	.317	.425	.414
L65	5000	.609	.607	.438	.437	.327	.326	.422	.416
PRI	3000	.610	.610	.462	.462	.316	.320	.423	.415

III. Discussion and Recommendations

The aperture corrections are difficult to measure to a 1 percent accuracy because of GIMP (Fitch et al. 1993; and see this volume), pointing errors, OTA breathing, jitter, and ybase errors. Even though many of the deviations from unity in Table 3 cannot be explained by these difficulties, the statistical significance of the deviations of the data from the predictions seems undeniable. In particular, consider the differences between the red and blue sides for the high dispersion H gratings. For the 14 cases where the same grating is measured on both sides, all of the red side values exceed the blue measurements, except for one case of equal throughput. This difference is not predicted by the theory; and the predicted 10 percent drop with wavelength for B1 is not observed, i.e. the measurements of Table 1 are nearer to being constant than the ratios to the theory in Table 3. The TIM output images have a strong resemblance to actual PSFs but are known to suffer some serious imperfections, especially for some non-prime *HST* camera modes such as PC8. The uncertainties in

the model PSFs at the FOS entrance apertures are not quantified and cannot be the basis for the recommended final aperture corrections.

The following is a case-by-case discussion for each aperture-grating combination. These recommended aperture corrections are summarized in Table 4.

Table 3: Measured Throughput Relative to Theoretical Value

Grat	Blue	Red	Blue	Red	Blue	Red	Blue	Red
	B3 (1 arcsec)		B1 (0.5 arcsec)		B2 (0.3 arcsec)		C2-SLIT	
H13	0.95	—	0.83	—	0.83	—	0.91	—
H19	0.98	0.98	0.89	0.93	0.83	0.98	0.92	0.99
H19[a]	0.93	0.98	0.87	—	0.92	—	0.94	1.01
H27	0.93	0.97	0.91	0.95	0.82	1.00	0.92	1.01
H40	0.93	1.00	0.93	0.98	0.84	0.99	0.90	1.01
H57	—	0.97	—	1.01	—	0.95	—	0.99
H78	—	0.94	—	0.98	—	0.92	—	0.96
L15	1.06	1.09	0.97	1.05	0.98	0.95	0.99	1.09
L15[a]	1.04	1.08	0.97	—	1.02	—	1.04	1.09
L65	—	1.10	—	1.17	—	1.07	—	1.08
PRI[a]	0.87	0.89	0.80	—	0.82	—	0.87	0.94

a. prop=4211. Otherwise prop=3106

Table 4: Recommended Aperture Corrections and Uncertainties at Nominal OTA Focus

GRAT MODE	Blue	Red	Unc[a]	Blue	Red	Unc	Blue	Red	Unc	Blue	Red	Unc
	B3 (1 arcsec)			B1 (0.5 arcsec)			B2 (0.3 arcsec)			C2-SLIT		
HIGH	0.58	0.60	.02	0.41	0.44	.02	0.27	0.31	.03	0.39	0.41	.02
LOW	0.65	0.67	.06	0.46	0.50	.04	0.31	0.35	.03	0.43	0.45	.03
PRISM	0.53	0.54	.06	0.37	0.39	.04	0.26	0.30	.03	0.37	0.39	.03

a. The uncertainties (Unc) do not include the possible contributions of pointing errors, OTA "breathing," jitter, or ybase errors in an arbitrary science observation.

High Dispersion

The small scatter in each of the 8 columns of data for the H gratings in Table 1 suggests that an average of each column might reduce the uncertainties further. An exception is H78, which is slightly low in all four cases

B3 (1 arcsec)

The blue side average is 0.58 with a maximum deviation of 0.02 or 3 percent, while the red side mean is 0.60 with 0.02 uncertainty. The excluded measurement for H78 is within the 3 percent uncertainty.

B1 (0.5 arcsec)

The blue side average is 0.41 with a maximum deviation of 0.01 or 2 percent, while the red side mean is 0.44 with no scatter among the 4 valid entries. A reasonable error estimate might be 3 percent. The excluded measurement for H78 is within the uncertainty.

B2 (0.3 arcsec)

The blue side average is 0.27 with a maximum deviation of 0.02 or 7 percent, while the red side mean is 0.31 with 0.01 scatter among the 4 valid entries. The excluded measurement for H78 is 10 percent lower than the average; and 10 percent might be a good choice for an uncertainty, since this small aperture is most susceptible to pointing problems and jitter. For precise absolute flux measurements of point sources, a larger aperture should be used.

C2 (0.25x2 slit)

The blue side average is 0.39 with a maximum deviation of 0.01 or 3 percent, while adopting a red side mean of 0.41 with a nominal 5 percent or 0.02 uncertainty encompasses the H78 measurement.

Low Dispersion

Because of the extreme differences that approach 20 percent between the prism and the L15 measurements, one case of the blue B3(1 arcsec) aperture is investigated in detail. Pointing errors and jitter problems are minimal for this aperture. Only the L15 spectrum in B3 for prop 4211 shows a spread in the three different Y-base countrates as large as 3 percent. Y-base errors can only cause a loss of signal, so the aperture correction of 0.64 could be a lower limit but is too large already in comparison with the prism value of 0.53 for the same aperture. The other known effect on aperture transmission is OTA "breathing", i.e. short term OTA focus changes, which are observed to deviate from the nominal by 5 microns during an orbit. However, the A1 reference spectra for the prism and L15 were taken only 4 min

apart, while the B3 spectra were also separated by a 4 min time interval. A shift in OTA focus of at least 30 microns in 4 min would be required to cause the observed difference in transmission! Therefore, differences in aperture corrections among dispersing elements must be accepted along with the differences between the blue and red sides.

B3 (1 arcsec)

For L15 on the blue side, 0.65 is recommended because of the possible Y-base error for the other measurement of 0.64, while the red side mean for L15 and L65 is 0.67 with 0.01 scatter. There are only single measurements for the prism. These values differ by around 10 percent from the high dispersion values, so 10 percent seems like a safe uncertainty estimate.

B1 (0.5 arcsec)

For L15 on the blue side, 0.46 is the value for both entries in Table 1, while 0.50 is suggested for the red side L15 and L65. There is no valid measurement for the red side prism, so the blue side is scaled up by the typical difference from the blue to the red side. Again, 10 percent seems like a safe uncertainty estimate.

B2 (0.3 arcsec)

For L15 on the blue side, 0.31 is the smaller of the two entries in Table 1, while 0.35 is the one valid entry for L65. There is no valid measurement for the red side prism, so the blue side is scaled up by the 0.04 difference between red and blue for the gratings. Again, 10 percent seems like a safe uncertainty estimate.

C2 (0.25x2 arcsec slit)

The blue side L15 average is 0.43 with a deviation of 0.01 or 3 percent, while all three L values on the red side are 0.45. Symmetry with respect to high and low dispersion for the B1(0.5 arcsec) aperture suggests that the prism corrections for the slit might be 0.02 lower than the quoted values from the single measurements, so 0.03 should be a safe error estimate.

IV. Wavelength Dependence Within the Range of a Single Disperser

According to the theoretical predictions, the variation in the aperture correction within the wavelength range covered by a grating is always less than the ~4 percent for the B1 (0.5 arcsec) aperture on the blue L15. For the broad coverage of the prisms, the predicted variation with wavelength approaches 10 percent. NBH (1992) fit straight lines or quadratics to the aperture corrections as a function of wavelength. Table 5 summarizes the slope of the curve in terms of the ratio of the longest wavelength fit point to the first fit point for the quadratic fits. The aperture

corrections do not agree with the predicted transmissions, for example the measured slope for the case of B1(0.5 arcsec)-blue-L15 is 1.03-1.06 in Table 5, while the TIM prediction is ~0.96. Therefore, the question of wavelength dependence must be answered by the data. One of the main purposes of prop 4211 was to check the repeatability of these slopes that were first measured in prop 3106 by NBH. The slopes did repeat for the test cases of H19 and L15 to an accuracy of 6 percent. Unfortunately, a couple of the more important cases in the B3 aperture for H13 (0.91) and H27 (0.92) on the blue side show more than a 6 percent deviation from unity and confirm the necessity of aperture correction that vary with wavelength.

Table 5: Slopes of Aperture Ratios Across Each Spectrum

Grat	Blue	Red	Blue	Red	Blue	Red	Blue	Red
	B3 (1 arcsec)		B1 (0.5 arcsec)		B2 (0.3 arcsec)		C2-SLIT	
H13	0.91	0.00	0.89	0.00	1.00	0.00	0.96	0.00
H13[a]	0.90							
H19	0.98	0.99	1.05	1.06	1.05	1.06	1.06	1.04
H19[b]	0.96	1.02	1.00	1.04	1.04	1.13[c]	1.01	1.01
H19[a]	0.97							
H27	0.92	0.95	0.97	0.97	0.97	0.95	0.98	0.97
H27[a]	0.93							
H40	0.94	0.97	0.94	0.94	0.96	0.97	0.96	0.97
H57	0.00	1.01	0.00	1.02	0.00	0.93	0.00	0.95
H78	0.00	0.96	0.00	1.01	0.00	0.88	0.00	0.94
L15	0.96	0.89	1.06	0.95	1.17	0.94	1.07	0.97
L15[b]	0.96	0.94	1.03	0.98	1.11	0.95[c]	1.08	0.91
L65	0.00	0.98	0.00	1.00	0.00	0.95	0.00	0.95
PRI[b]	0.98	1.19	1.02	1.05	1.06	1.04	1.04	1.12

a. prop 3235.
b. prop 4211. Otherwise prop 3106.
c. Bad target acquisition. Do not use for final average polynomial fits.

A search of the archive revealed one more prop 3235, which again verifies the repeatability of both the aperture correction and the slope for the important cases of B3(1 arcsec) on the blue side for H13, H19, and H27. In comparison with the adopted value of 0.58 in Table 4, the 3235 data for the aperture corrections are 0.58, 0.58, and 0.57, respectively. All three slopes are within 1 percent of the values in Table 5! Therefore, the existence of the slopes found by NBH is verified. The aperture corrections are derived from the least square fit of quadratic polynomials as a function of wavelength. For some FOS dispersers that have a rapid drop in sensitivity, separate secondary quadratic fits are required and improve on the single

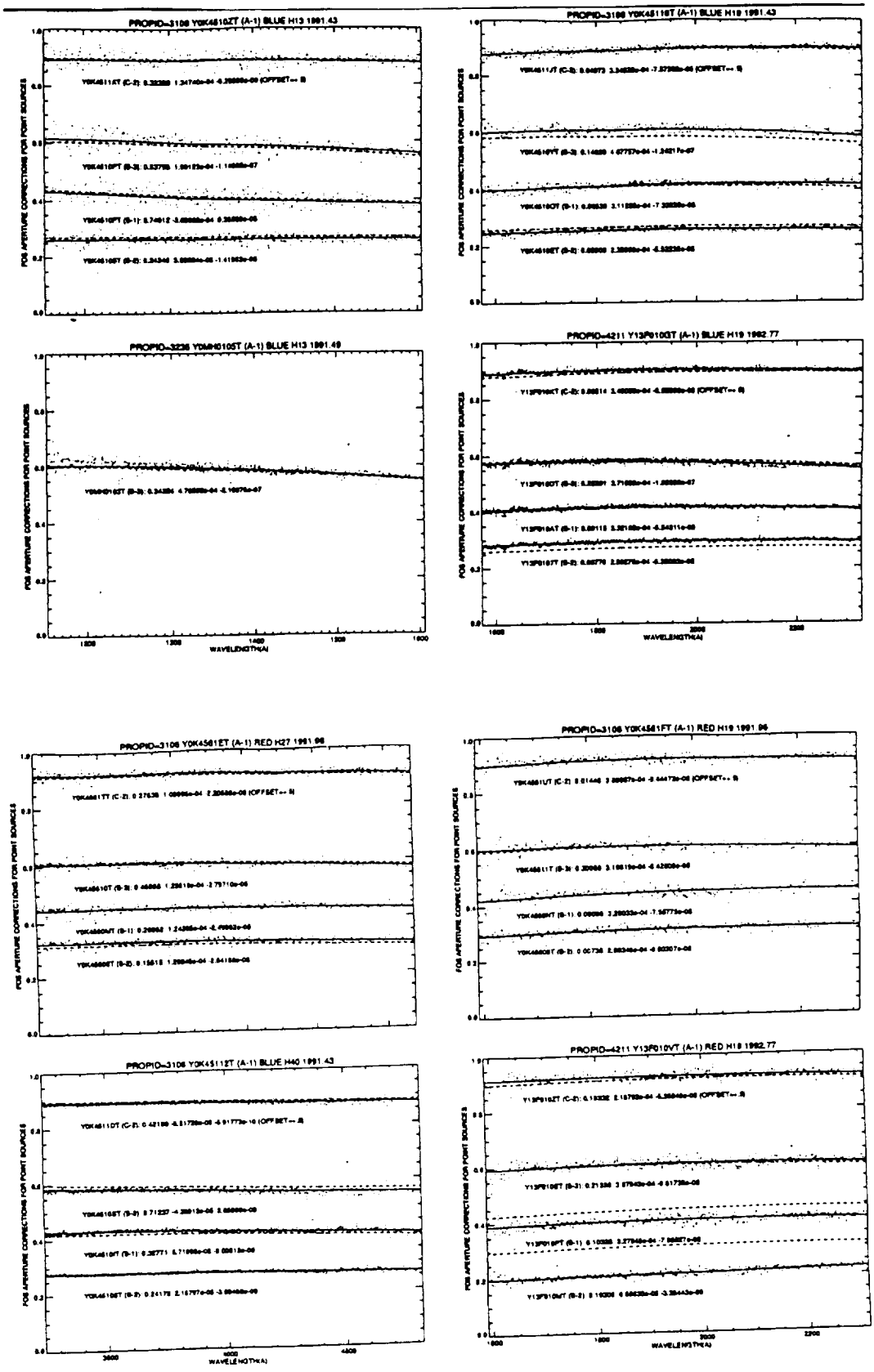
PROPID=3106 Y0K4511ZT (A-1) BLUE H13 1991.43
PROPID=3106 Y0K4511BT (A-1) BLUE H19 1991.43
PROPID=3236 Y0MH0105T (A-1) BLUE H13 1991.49
PROPID=4211 Y13P0103T (A-1) BLUE H19 1992.77
PROPID=3106 Y0K4561ET (A-1) RED H27 1991.96
PROPID=3106 Y0K4561FT (A-1) RED H19 1991.96
PROPID=3106 Y0K4511ST (A-1) BLUE H40 1991.43
PROPID=4211 Y13P010VT (A-1) RED H19 1992.77
FOS APERTURE CORRECTIONS FOR POINT SOURCES
WAVELENGTH(A)

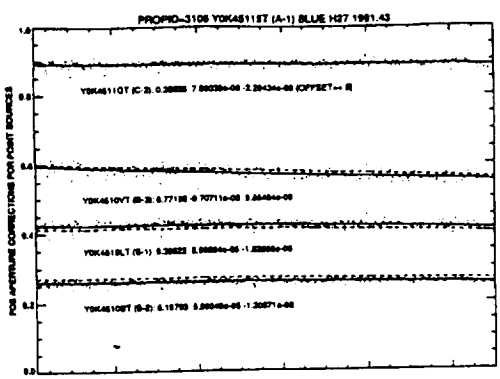
PROPID=3106 Y0K4511ST (A-1) BLUE H27 1991.43
FOS APERTURE CORRECTIONS FOR POINT SOURCES

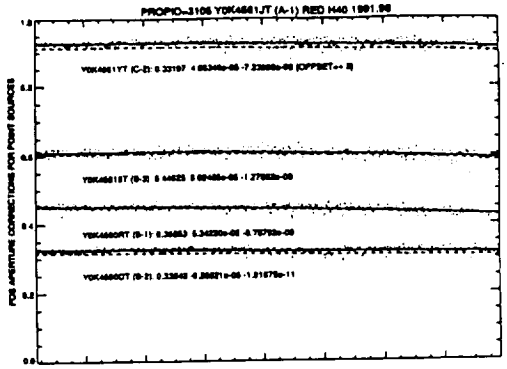
PROPID=3106 Y0K4561JT (A-1) RED H40 1991.96
FOS APERTURE CORRECTIONS FOR POINT SOURCES

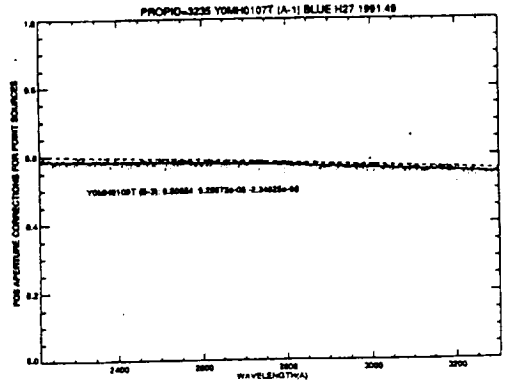
PROPID=3235 Y0M401077 (A-1) BLUE H27 1991.49
FOS APERTURE CORRECTIONS FOR POINT SOURCES
WAVELENGTH(A)

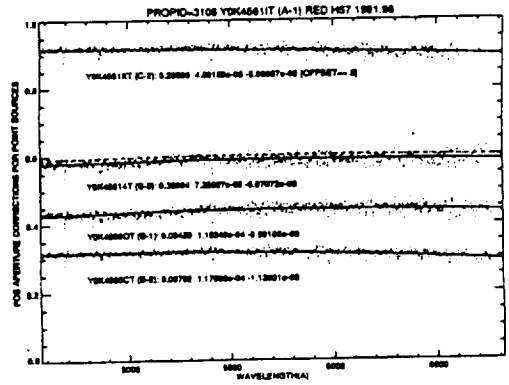
PROPID=3106 Y0K4561IT (A-1) RED H57 1991.96
FOS APERTURE CORRECTIONS FOR POINT SOURCES
WAVELENGTH(A)

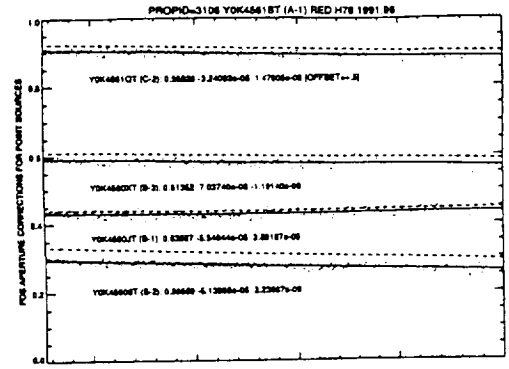
PROPID=3106 Y0K4561ST (A-1) RED H78 1991.96
FOS APERTURE CORRECTIONS FOR POINT SOURCES

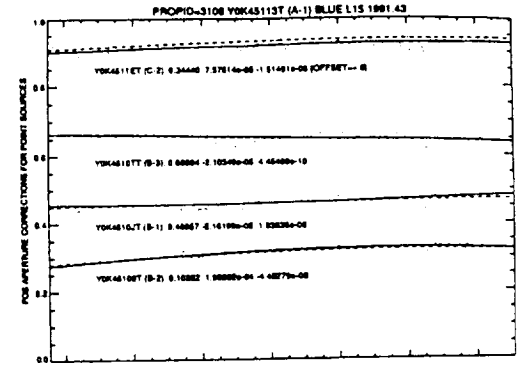
PROPID=3106 Y0K4511ST (A-1) BLUE L15 1991.43
FOS APERTURE CORRECTIONS FOR POINT SOURCES

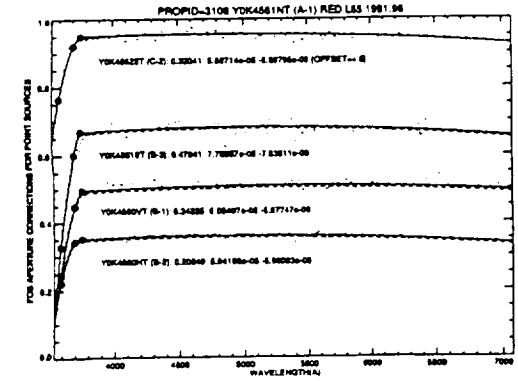
PROPID=3106 Y0K4561NT (A-1) RED L65 1991.96
FOS APERTURE CORRECTIONS FOR POINT SOURCES
WAVELENGTH(A)

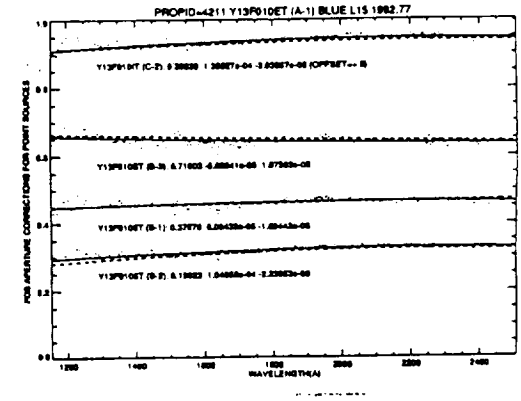
PROPID=4211 Y13F910ET (A-1) BLUE L15 1992.77
FOS APERTURE CORRECTIONS FOR POINT SOURCES
WAVELENGTH(A)

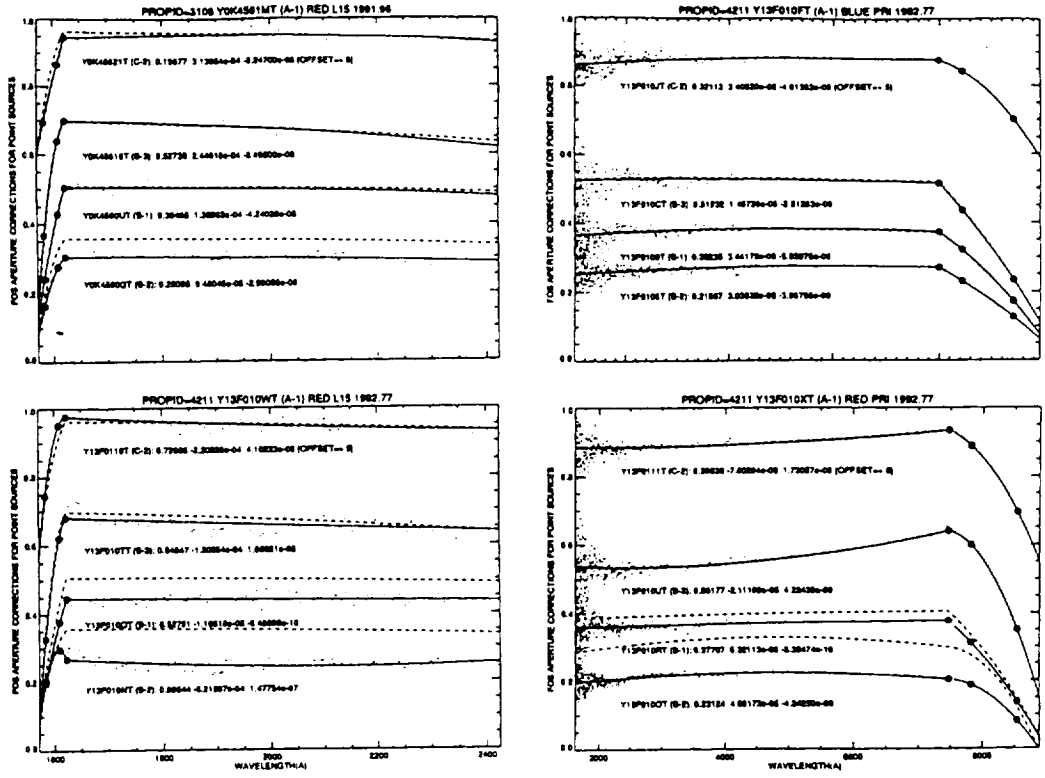

Figure 1

fit reported by NBH. These cases that show a discontinuity in the aperture corrections are caused by the broad aberrated PSF in the 4.3 arcsec aperture that results in a slower drop with wavelength in the A1(4.3 arcsec) aperture than for the smaller apertures. The fits are all shown as the solid line in Figure 1; and the second fit is defined by the three large filled circles. One of the three filled circles always lies at the endpoint of first fit in order to force continuity between the two quadratics. The other two filled circles are the binned averages of the remaining data points. The dashed lines are the adopted average fit, as described in the next paragraph.

The final adopted aperture corrections are the averages of the coefficients from the quadratic fits for the individual measurement sets, where the individual fits are first normalized to the average corrections of Table 4 over the wavelength range of the primary fit. The individual coefficients of the primary fits are written on the plots in Figure 1, while Table 6 contains the applicable wavelength range and number of data sets used to define each set of three average coefficients. The two of the three most discrepant observations in the small B2(0.3 arcsec) aperture from prop 4211 are excluded from the averaging process for the bad target acquisition on the red side. The H19 and L15 are excluded, while the prism must be used, since 4211 contained the only data available for the prism aperture corrections.

Table 6: Summary of average FOS Aperture Coefficients[a]

Detec	FGWA	APER	C0	C1	C2	WMIN	WMAX	NAV
BLUE	H13	B-1	7.40123e-01	-3.69668e-04	9.36560e-08	1151.00	1609.00	1
BLUE	H13	B-2	2.43460e-01	3.89984e-05	-1.41963e-08	1151.00	1609.00	1
BLUE	H13	B-3	4.40583e-01	3.33357e-04	-1.66872e-07	1151.00	1610.00	2
BLUE	H13	C-2	3.23279e-01	1.34740e-04	-6.20508e-08	1151.00	1610.00	1
BLUE	H19	B-1	8.82408e-02	3.21723e-04	-7.93770e-08	1567.00	2335.00	2
BLUE	H19	B-2	1.83798e-02	2.45943e-04	-5.92163e-08	1567.00	2335.00	2
BLUE	H19	B-3	2.30025e-01	3.88200e-04	-1.05693e-07	1567.00	2335.00	3
BLUE	H19	C-2	4.79387e-02	3.37304e-04	-8.19981e-08	1567.00	2335.00	2
BLUE	H27	B-1	3.05223e-01	8.90864e-05	-1.82856e-08	2213.00	3308.00	1
BLUE	H27	B-2	1.97932e-01	5.99049e-05	-1.20871e-08	2214.00	3308.00	1
BLUE	H27	B-3	6.38760e-01	-2.25195e-06	-6.79883e-09	2213.00	3308.00	2
BLUE	H27	C-2	3.88393e-01	7.00039e-06	-2.29434e-09	2213.00	3308.00	1
BLUE	H40	B-1	3.27705e-01	5.71995e-05	-9.00812e-09	3229.00	4830.00	1
BLUE	H40	B-2	2.41780e-01	2.16797e-05	-3.59468e-09	3229.00	4830.00	1
BLUE	H40	B-3	7.12372e-01	-4.36912e-05	2.65989e-09	3229.00	4830.00	1
BLUE	H40	C-2	4.21993e-01	-5.51728e-06	-5.91773e-10	3229.00	4830.00	1
BLUE	L15	B-1	4.32666e-01	1.45117e-05	2.19650e-10	1151.00	2523.00	2
BLUE	L15	B-2	1.49524e-01	1.51922e-04	-3.35666e-08	1151.00	2523.00	2
BLUE	L15	B-3	7.01490e-01	-3.88495e-05	5.60088e-09	1151.00	2523.00	2
BLUE	L15	C-2	3.16397e-01	1.05644e-04	-2.27679e-08	1151.00	2523.00	2
BLUE	PRI	B-1	3.22353e-01	3.44178e-05	-5.03978e-09	1498.00	4995.00	1
BLUE	PRI	B-1	-1.21560e+00	8.38476e-04	-1.04393e-07	4993.00	5961.00	1
BLUE	PRI	B-2	2.15567e-01	3.03832e-05	-3.96765e-09	1498.00	4995.00	1
BLUE	PRI	B-2	-4.04202e-01	4.26773e-04	-5.85007e-08	4993.00	5961.00	1
BLUE	PRI	B-3	5.12325e-01	1.49739e-05	-2.81263e-09	1498.00	4995.00	1
BLUE	PRI	B-3	-3.05272e-02	5.52881e-04	-8.87815e-08	4993.00	5961.00	1
BLUE	PRI	C-2	3.21130e-01	3.40020e-05	-4.61383e-09	1498.00	4995.00	1
BLUE	PRI	C-2	-4.03502e+00	1.87340e-03	-1.98278e-07	4993.00	5961.00	1
AMBER	H19	B-1	9.71168e-02	3.27939e-04	-7.71301e-08	1588.00	2316.00	2
AMBER	H19	B-2	7.38173e-03	2.89346e-04	-6.80307e-08	1588.00	2317.00	1

Table 6: Summary of average FOS Aperture Coefficients[a]

Detec	FGWA	APER	C0	C1	C2	WMIN	WMAX	NAV
AMBER	H19	B-3	2.57219e-01	3.53731e-04	-9.02272e-08	1588.00	2316.00	2
AMBER	H19	C-2	1.03904e-01	3.02940e-04	-7.40159e-08	1588.00	2316.00	2
AMBER	H27	B-1	2.89623e-01	1.24265e-04	-2.49962e-08	2217.00	3284.00	1
AMBER	H27	B-2	1.55147e-01	1.29845e-04	-2.64168e-08	2217.00	3283.00	1
AMBER	H27	B-3	4.68684e-01	1.25618e-04	-2.79710e-08	2217.00	3284.00	1
AMBER	H27	C-2	2.76376e-01	1.09996e-04	-2.20588e-08	2217.00	3284.00	1
AMBER	H40	B-1	3.68828e-01	5.34220e-05	-8.78792e-09	3226.00	4791.00	1
AMBER	H40	B-2	3.35431e-01	-6.26521e-06	-1.91675e-11	3226.00	4791.00	1
AMBER	H40	B-3	4.46254e-01	9.02458e-05	-1.27862e-08	3229.00	4790.00	1
AMBER	H40	C-2	3.31970e-01	4.88348e-05	-7.23698e-09	3226.00	4788.00	1
AMBER	H57	B-1	9.42854e-02	1.18346e-04	-9.99186e-09	4559.00	6829.00	1
AMBER	H57	B-2	7.82160e-03	1.17688e-04	-1.12031e-08	4559.00	6829.00	1
AMBER	H57	B-3	3.86043e-01	7.25897e-05	-6.07072e-09	4561.00	6831.00	1
AMBER	H57	C-2	2.98603e-01	4.89152e-05	-5.08857e-09	4561.00	6829.00	1
AMBER	H78	B-1	6.35974e-01	-5.54944e-05	3.89157e-09	6260.00	8501.00	1
AMBER	H78	B-2	5.66594e-01	-5.13968e-05	2.23867e-09	6263.00	8501.00	1
AMBER	H78	B-3	6.13518e-01	7.03740e-06	-1.19140e-09	6260.00	8501.00	1
AMBER	H78	C-2	5.68258e-01	-3.24092e-05	1.47605e-09	6263.00	8501.00	1
AMBER	L15	B-1	4.61080e-01	6.36551e-05	-2.16757e-08	1619.00	2444.00	2
AMBER	L15	B-1	-1.16501e+02	1.38912e-01	-4.11667e-05	1568.00	1622.00	2
AMBER	L15	B-2	2.80945e-01	9.48045e-05	-2.96085e-08	1619.00	2441.00	1
AMBER	L15	B-2	-1.86656e+02	2.29110e-01	-7.01678e-05	1568.00	1622.00	1
AMBER	L15	B-3	6.86425e-01	6.20320e-05	-3.42390e-08	1619.00	2444.00	2
AMBER	L15	B-3	-4.64569e+02	5.71654e-01	-1.75590e-04	1568.00	1622.00	2
AMBER	L15	C-2	4.41812e-01	4.65140e-05	-2.07239e-08	1619.00	2444.00	2
AMBER	L15	C-2	-2.42038e+02	2.96294e-01	-9.04966e-05	1568.00	1622.00	2
AMBER	L65	B-1	3.42255e-01	6.08407e-05	-5.67747e-09	3752.00	7077.00	1
AMBER	L65	B-1	-8.79137e+01	4.65463e-02	-6.12597e-06	3538.00	3755.00	1
AMBER	L65	B-2	2.08488e-01	5.94196e-05	-5.96003e-09	3752.00	7077.00	1
AMBER	L65	B-2	-8.24104e+01	4.42530e-02	-5.91574e-06	3538.00	3755.00	1
AMBER	L65	B-3	4.79409e-01	7.78557e-05	-7.63811e-09	3752.00	7077.00	1
AMBER	L65	B-3	-1.15509e+02	6.10988e-02	-8.03209e-06	3538.00	3755.00	1

Table 6: Summary of average FOS Aperture Coefficients[a]

Detec	FGWA	APER	C0	C1	C2	WMIN	WMAX	NAV
AMBER	L65	C-2	3.20407e–01	5.68714e–05	–5.89795e–09	3752.00	7077.00	1
AMBER	L65	C-2	–8.30983e+01	4.43141e–02	–5.87591e–06	3538.00	3755.00	1
AMBER	PRI	B-1	3.77070e–01	6.32113e–06	–3.38474e–10	1618.00	7480.00	1
AMBER	PRI	B-1	–1.52755e+00	6.96870e–04	–5.86245e–08	7478.00	8890.00	1
AMBER	PRI	B-2	2.31237e–01	4.06172e–05	–4.24250e–09	1618.00	7480.00	1
AMBER	PRI	B-2	–7.26827e+00	2.04362e–03	–1.37986e–07	7478.00	8890.00	1
AMBER	PRI	B-3	5.61766e–01	–2.11169e–05	4.22438e–09	1618.00	7480.00	1
AMBER	PRI	B-3	–1.13509e+01	3.24538e–03	–2.19561e–07	7478.00	8890.00	1
AMBER	PRI	C-2	3.96385e–01	–7.60294e–06	1.73057e–09	1618.00	7480.00	1
AMBER	PRI	C-2	–6.45283e+00	1.92644e–03	–1.34419e–07	7478.00	8890.00	1

a. $A(ap) = C0 + C1 \times W + C2 \times W^2$, where W is the wavelength in Angstroms.

In order for a GO to understand the errors in the pipeline fluxes that are based on the NBH aperture corrections, the following list describes the major changes in order of decreasing numerical effect.

a) Over the small wavelength ranges for the four cases of detector-disperser modes with the secondary fits, the rapid drop in the aperture correction increases the calibrated fluxes by a factor of up to ~5.

b) NBH did not have measurements for the prisms and used the average for the high dispersion gratings. For example, the value for the B3(1.0 arcsec) aperture should be 0.53 instead of the 0.59 used by NBH for the blue side prism.

c) The biggest difference for the B3(1.0 arcsec) aperture between NBH and the Table 4 averages is for the high dispersion blue side average of 0.58 and the NBH value of 0.61 for blue H19.

d) A few of the smaller aperture transmission estimates are now ~10 percent larger than the NBH estimates; and the red side B2 aperture correction for L15 is 0.35 in Table 4, while the spuriously low NBH value of 0.29 was caused by large jitter that carried the star out of the 0.3 arcsec aperture for a significant fraction of the integration time.

V. Diffuse Sources

The above discussion of the relative aperture corrections of small apertures with respect to the 4.3 arcsec aperture for point sources is NOT relevant to absolute surface brightness estimates for diffuse sources. In terms of the inverse sensitivity,

$S(4.3)$, of a point source at zero focus in the FOS 4.3 arcsec aperture, the flux of a point source with response, C, in counts/sec is

$$F = C \times S(4.3)/A(ap),$$

where A(ap) is the aperture correction defined by Table 6 for the aperture used to make the observation, where C is corrected to zero focus, and where A(4.3)=1 by definition. The inverse sensitivity S(ap)=S(4.3)/A(ap) is the calibration that actually resides in PODPS and that is distributed on request. The specific surface intensity, I, of a diffuse source that overfills an aperture with effective solid angle of omega(ap) is

$$I = C \times S(4.3) \times T(4.3)/omega(ap),$$

where the best estimates of the effective solid angle subtended by an aperture is still in Lindler, Bohlin, & Hartig (1985), where C is independent of focus and NOT corrected, and where $T(4.3)$ is the absolute transmission at zero focus of the 4.3 arcsec acquisition aperture that is used for the primary calibration observations of the standard stars. $T(4.3)$ cannot be measured directly but is estimated to be ~0.73 by Lindler & Bohlin (1993) and 0.70-0.72 by Evans (1993).

VI. Future Calibration Changes

Since there is little time left before the *HST* servicing mission, the new aperture corrections will not be immediately implemented in the PODPS pipeline reduction system. Instead, these new aperture corrections will be implemented along with the full scheme to handle the FOS changes in sensitivity with time that is in preparation by Lindler & Bohlin. Following the deployment of COSTAR, any reprocessing of old pre-COSTAR archival data will have the best estimates for FOS calibration parameters.

In the future, even after installation of the COSTAR optics, every absolute calibration observation should include aperture correction measurements for a couple of gratings in order to better characterize the repeatability of the relative throughput for any aperture that is normally used to make precise flux measurements of point sources. The blue side gratings H13 and H27 that have the biggest slopes in the prop 3106 data would be good choices for repeats in the B3 aperture. Since the aperture corrections are a function of grating and detector, all combinations must be done at least once following COSTAR deployment. Hopefully, these new aperture corrections will be more consistent with our expectations.

Ed Smith read a draft of this paper and provided several comments that improved the clarity and content.

References

Bohlin, R. C. 1993, FOS Instrument Science Report CAL/FOS-097.
Burrows, C., & Hasan, H. 1993, Telescope Image Modelling User Manual, Version 7c, Release 25 and updates through Release 28.
Evans, I. N. 1993, FOS Instrument Science Report CAL/FOS-105.
Fitch, J. E., Hartig, G. F., Beaver, E. A., and Hier, R. G. 1993, FOS Instrument Science Report CAL/FOS-098.
Koratkar, A., and Taylor, C. J. 1993, FOS Instrument Science Report CAL/FOS-096.
Lindler, D. J., & Bohlin, R. C. 1993, FOS Instrument Science Report CAL/FOS-102.
Lindler, D., Bohlin, R., & Hartig, G. 1985, FOS Instrument Science Report CAL/FOS-019.
Neill, J. D., Bohlin, R. C., & Hartig, G. 1992, FOS Instrument Science Report CAL/FOS-077 (NBH).

Science in crowded fields with Hubble Space Telescope Faint Object Spectrograph plus COSTAR

Richard Harms
Applied Research Corporation
8201 Corporate Drive, Suite 1120
Landover, MD 20785

Holland Ford
Johns Hopkins University
Department of Physics and Astronomy
Homewood Campus
Baltimore, MD 21218

George Hartig
Space Telescope Science Institute
Homewood Campus
Baltimore, MD 21218

Frank Bartko
Bartko Science and Technology
4363 South Quebec, Apt. 4314
Denver, CO 80237

ABSTRACT

We describe plans for several science programs in crowded fields using the Faint Object Spectrograph (FOS) which rely critically on the enhanced angular resolution provided by the COSTAR corrective optics. Based on ground-based calibration of the COSTAR and on-orbit performance of the FOS, the anticipated performance of the COSTAR+FOS should allow many important scientific studies to be completed which have had to be postponed due to the spherical aberration in the HST primary mirror. Particularly impacted by spherical aberration, and thus able to benefit most dramatically from the installation of COSTAR, are spectroscopic observations with FOS in crowded fields. Many of the most important science goals for the FOS instrument involve observations of crowded fields, for which the restored high-angular resolution of HST is essential – not only to isolate features of small angular extent, but also to eliminate optical contamination from the surrounding luminous regions. Spectroscopy of the nuclei of galaxies to obtain rotation curves and velocity dispersions which might reveal the presence of central black holes benefits dramatically from the enhanced angular resolution of HST as restored by COSTAR. We present models based on our current understanding of the dynamics of galaxy nuclei to illustrate the dramatic improvement in sensitivity in searching for black holes made possible by restoring HST's image quality. Two other categories of scientific investigations in crowded fields which will benefit greatly from restoring HST's image quality are spectroscopy of the luminous material (presumably distant galaxies) surrounding quasistellar objects, and spectroscopy of individual stars in globular clusters. The promise of finally being able to carry out these exciting scientific programs with the FOS on the restored HST explains why our team of scientists, along with many other astronomers, look forward to using the restored HST to carry out the scientific investigations for which it was originally intended.

1 INTRODUCTION

The Hubble Space Telescope (HST) first servicing mission was successful not only in recovering the originally intended high-angular-resolution imaging capabilities of the HST's two cameras, but also succeeded in provid-

0-8194-1493-X/94/$6.00

ing the two spectrographs with a similar improvement in angular resolution. While the second-generation wide field/planetary camera (WFPC-2) could incorporate corrective optics to compensate for the HST's spherical aberration, the first-generation Faint Object Camera (FOC) and the two spectrographs, the Faint Object Spectrograph (FOS) and the Goddard High Resolution Spectrograph (GHRS), were provided with corrected images from the newly-installed Corrective Optics Space Telescope Axial Replacement (COSTAR) instrument. Other papers presented at this conference describe the optical performance of the COSTAR instrument[1] and how it was aligned to provide images to the first-generation spectrographs[2] and the Faint Object Camera.[3] We discuss some of the initial results of the optical performance of the FOS + COSTAR imaging performance in a separate paper[4] at this conference.

For spatially unresolved sources, such as stars and most quasars, the improved performance with COSTAR is a substantial gain in instrument efficiency for all spectroscopic observations. At the time this paper is being written (late February 1994), photometric calibration of the post-COSTAR FOS have not yet been completed, but initial measurements indicate that most spectroscopic observations of pointlike targets with FOS will benefit from increased system efficiency by factors from 2 to 4. These improved efficiencies, consistent with prelaunch predictions, result from the increased amount of light entering the FOS entrance apertures (factors of 3 to 7, depending on aperture size and, to a lesser degree, on wavelength) with the aberration-compensated images, along with the losses (approximately 30% throughout most of the wavelength range) due to the two extra reflections in the COSTAR's reimaging optics.

At first, it might seem that spectroscopy of extended objects could actually suffer from the introduction of COSTAR; not only does the throughput from a source with approximately uniform surface brightness not benefit from a gain in fraction of light entering the FOS entrance aperture, but throughput decreases both from the two extra mirror reflections within the COSTAR and because a smaller region of the target is subtended by the FOS entrance aperture after COSTAR reimages the original f/24 HST beam at f/28. Thus, for a uniform surface brightness target, the sensitivity actually is multiplied by a factor of approximately $(0.7)*(24/28)^2 \approx 0.5$, leaving us worse off by a factor of 2. Of course, this result applies only for spatially and spectrally uniform surface brightness distributions; such targets, of course, would not be good candidates for HST observations.

Fortunately, an enormous variety of extremely interesting astronomical objects do exhibit variability on the sub-arcsecond angular scales which can now be well sampled with the HST instruments. The improvement in performance for FOS spectroscopy of several classes of spatially resolved targets (for example, nuclei of galaxies, the extended envelopes of quasars, or dense stellar systems such as globular clusters) is even greater than that for unresolved sources, often by truly huge factors. Prior to the servicing mission, this manifested itself as a negative statement – the loss in observing efficiency for a large class of candidate targets was so great that the observations were postponed as being essentially impractical. The reason for this is straightforward. FOS spectroscopy of a specific feature of interest, typically of subarcsecond angular extent, suffered a loss in throughput about equal to that for unresolved sources as discussed above. However, far more deleterious to the observation is the mixing of light from the neighboring regions, which usually would have resulted in a substantial increase in noise. To illustrate the impact upon several classes of FOS crowded-field spectroscopic programs, in the next section we compare the performance of the FOS before and after COSTAR for two somewhat idealized situations relevant to many planned spectroscopic observations in crowded fields.

2 SPECTROSCOPY IN CROWDED FIELDS

As the model calculations below demonstrate, correction of the aberrated HST images with COSTAR produces enormous improvements in the ability to obtain spectra of targets in crowded fields.

2.1 Multiple Closely-Spaced Targets of Comparable Brightness

As a first case, let us consider a simplified, but realistic, model to illustrate the size of the effect for several classes of FOS crowded-field spectroscopy observing programs. Suppose we wish to resolve several neighboring regions on the sky separated by a few tenths of an arcsecond from one another. The regions may be roughly comparable in brightness, but possess variations in spectral properties of astronomical interest. Such a model is valid for the study of the dynamics of the nuclei of galaxies, where changes in radial velocities or velocity dispersions on a subarcsecond scale are crucial to investigating the presence or absence of massive black holes in the cores of galaxies. The model also applies for a program which attempts to recover a nova by spectroscopy of closely separated stars in a globular cluster.

When the HST is pointed at one of the targets of interest, only a portion of the light will actually enter the FOS aperture. The fraction of light from the original HST image of the target entering the FOS, which we will denote by ε, will depend on many factors: the size of the FOS aperture, the wavelength of the light, and whether the image is that of the original aberrated HST or the COSTAR-corrected image. (Note that ε includes the reflection losses in COSTAR as well as the effect of the point spread function's overfilling the entrance aperture.) In addition to the signal from the desired target, each of the nearby surrounding targets will also contribute (unwanted) light into the FOS aperture. For our simplified model, let us assume that from each of the nearby sources a portion, $\eta * \varepsilon$, of the light enters the FOS aperture. Thus, η is the ratio of the off-target to on-target efficiency for coupling light into the aperture. The ratio η will depend on the same factors as does ε; in addition, η will of course depend on the angular separation of the off-axis light source from the target. For our idealized model, we will consider a set of approximately equally bright target areas (which may be either separate entities such as stars or portions of an extended object such as a galaxy nucleus) spaced nearly equidistantally from one another, so that a single value of η can be used for all off-axis light sources.

If we wish to preserve the full spectroscopic resolving power of the FOS, and if the regions to be studied are separated by a few tenths of an arcsecond, the FOS entrance aperture of choice will usually be the 0.30 arcsecond (pre-COSTAR) diameter circular aperture, which subtends about 0.26 arcseconds diameter post-COSTAR. Typical values for ε and η in the visible portion of the spectrum with targets separated by a few tenths of an arcsecond will then be: $\varepsilon \approx 0.15$ and $\eta \approx 0.3$ for the pre-COSTAR situation, while $\varepsilon \approx 0.5$ and $\eta \ll 1$ post-COSTAR.

Suppose that the i'th target of the M closely-spaced sources, if all the light from its HST image entered the FOS entrance aperture, would produce x_i counts for a given FOS pixel. Then, the corresponding counts in our model will be given by: $\mathbf{Ax} = \mathbf{C} + \mathbf{N}$, where $\mathbf{x}$ is the vector of M ideal-HST counts x_i, $\mathbf{C}$ is the vector of M actual counts C_i observed when looking at each i'th source, $\mathbf{N}$ is the vector of M noise terms N_i associated with the counts C_i, and $\mathbf{A}$ is the M by M matrix with elements A_{ij} describing the amount of light contributed from the j'th source to the counts received when observing the i'th target. Under our simplifying assumptions, $A_{ij} = \varepsilon\delta_{ij} + \varepsilon\eta(1 - \delta_{ij}) = \varepsilon[\delta_{ij} + \eta(1 - \delta_{ij})]$. We have a system of M linear equations:

$$\begin{pmatrix} \varepsilon & \varepsilon\eta & \cdots & \cdots & \varepsilon\eta \\ \varepsilon\eta & \varepsilon & \cdots & \cdots & \varepsilon\eta \\ \vdots & \cdots & \ddots & \cdots & \vdots \\ \vdots & \cdots & \cdots & \ddots & \vdots \\ \varepsilon\eta & \varepsilon\eta & \cdots & \cdots & \varepsilon \end{pmatrix} \begin{pmatrix} x_1 \\ x_2 \\ \vdots \\ \vdots \\ x_M \end{pmatrix} = \begin{pmatrix} C_1 \\ C_2 \\ \vdots \\ \vdots \\ C_M \end{pmatrix} + \begin{pmatrix} N_1 \\ N_2 \\ \vdots \\ \vdots \\ N_M \end{pmatrix}.$$

For most FOS observations, the dominant noise term is simply photon counting statistics. For reasonably large C_i, we have N_i given by a random Gaussian distribution with a mean of 0 and standard deviation of $\sqrt{C_i}$. The signal-to-noise ratio (SNR) to which we can determine the spectra for each of the targets x_i will depend not only on the number of detected counts but also on the condition of the matrix $\mathbf{A}$: $\mathrm{SNR}(x_i) \sim \sqrt{\varepsilon x_i}/\mathrm{cond}(\mathbf{A})$. For our simplified M by M matrix $\mathbf{A}$, $\mathrm{cond}(\mathbf{A}) = \frac{1+(2M-3)\eta}{1-\eta}$, where $0 < \eta < 1$. Note that when little off-intended-target

light is mixed into the aperture, we have $\eta \rightarrow 0$ and $\mathrm{cond}(\mathbf{A}) \rightarrow 1$. By contrast, when off-target mixing is severe, we have $\eta \rightarrow 1$ and $\mathrm{cond}(\mathbf{A}) \rightarrow \infty$. This latter limit reflects the extreme difficulty in disentangling information from sources with separations not large compared to the width of the point spread function.

Let us compare performance pre- and post-COSTAR for obtaining spectra of M = 7 targets within a few tenths of an arcsecond from one another. With the aberrated pre-COSTAR images, typical values are $\varepsilon \approx 0.15$ and $\eta \approx 0.3$, which gives $\mathrm{cond}(\mathbf{A}) = \frac{1+(11)(0.3)}{1-0.3} \approx 6$. Then $\mathrm{SNR}(x_i) \approx \frac{\sqrt{0.15x_i}}{6} \approx 0.06\sqrt{x_i}$. With the post-COSTAR images, $\varepsilon \approx 0.5$ and $\eta \ll 1$ (so that $\eta \approx 0$ is an adequate approximation; off-target contamination is very small in many cases of interest), which produces the desirable result that $\mathrm{cond}(\mathbf{A}) \approx 1$ and $\mathrm{SNR}(x_i) \approx \sqrt{0.5x_i} \approx 0.7\sqrt{x_i}$. In this simplified but realistic case, the SNR achieved for a given length of observations is approximately 11 times greater with the post-COSTAR images as for the aberrated pre-COSTAR images. Obtaining a scientific result always requires some minimum SNR; in our modeled case, an observing program prior to COSTAR installation would have required slightly over 100 times longer total on-target integration time than is now necessary with the corrected images. It is easy to understand why planned FOS observations of subarcsecond variations of velocities and velocity dispersions in the nuclei of galaxies and spectroscopy of stars in dense fields had to be postponed until after the servicing mission. Many of our most interesting observing programs will require several hours to a few tens of hours exposure time, making them difficult but feasible. The pre-COSTAR necessary exposure durations, hundreds to thousands of hours in length, were regretfully but easily judged to be totally impractical.

2.2 Faint Target Near a Much Brighter Object

A second class of FOS crowded-field science involves obtaining spectra of faint targets in the vicinity of a much brighter source of light. Spectroscopy of the extended luminosity surrounding many quasars, which may arise from host galaxies in which quasars are embedded, is a scientifically interesting example of this second case. Because quasars are intrinsically exceedingly luminous, the contrast ratio between the quasar and its surrounding luminosity (galaxy?) usually is large, over 100, even in observationally favorable cases.

The analysis of this second case is similar to the preceding section, but simpler, since the model reduces to a pair of linear equations $\mathbf{Ax} = \mathbf{C} + \mathbf{N}$, with dimension M=2. Let i=1 represent the bright source and i=2 represent the faint nearby target for which we wish to obtain the spectrum. A straightforward calculation produces the resulting SNR for determining the spectrum of the faint target:

$$SNR(x_2) = [\sqrt{\varepsilon x_2}] \left[\frac{1-\eta^2}{\sqrt{1+\left(\frac{2\eta x_1}{x_2}\right)+\eta^2}} \right] \xrightarrow{x_1 \gg \frac{x_2}{\eta}} [\sqrt{\varepsilon x_2}] \left[\frac{1-\eta^2}{\sqrt{\left(\frac{2\eta x_1}{x_2}\right)}} \right].$$

Let us compare pre- and post-COSTAR performance for the case where the target is 5 magnitudes, a factor of 100, fainter than the nearby bright source. As before, typical values for ε and η in the visible portion of the spectrum with targets separated by a few tenths of an arcsecond will then be: $\varepsilon \approx 0.15$ and $\eta \approx 0.3$ for the pre-COSTAR situation, while $\varepsilon \approx 0.5$ and $\eta \ll 1$ post-COSTAR. Because the off-target source is far brighter than the target itself, we cannot approximate $\eta \ll 1$ by $\eta \approx 0$ as we could for less luminous nearby sources. The actual value of η for post-COSTAR observations will depend very strongly on the separation of the two sources. Preliminary measurements indicate that $\eta \approx 0.01$ is achieved for separations of about 0.36 arcseconds with the post-COSTAR PSF and the (now) 0.26 arcsecond diameter circular entrance aperture. With the aberrated images, pre-COSTAR $SNR(x_2) \approx [\sqrt{0.15x_2}] \left[\frac{1-0.02}{\sqrt{\left(\frac{2*0.3*100x_2}{x_2}\right)}} \right] \approx 0.05\sqrt{x_2}$. For the unaberrated images, we have post-COSTAR $SNR(x_2) \approx [\sqrt{0.5x_2}] \left[\frac{1}{\sqrt{1+\left(\frac{2*0.01*100x_2}{x_2}\right)}} \right] \approx 0.4\sqrt{x_2}$. For this (actually rather favorable) case, the

post-COSTAR SNR is about 8 times better than the pre-COSTAR SNR, which translates into an improvement by a factor of 64 in observing time required to carry out such a program.

3 DYNAMICS OF GALACTIC NUCLEI

3.1 Physical Processes in Centers of Galaxies

Spectroscopic study of the centers of galaxies to attempt to understand the wide variety of physical processes occurring within them has long been a major scientific goal for the FOS. Typically, such research programs involve an initial reconnaissance with either or both of the HST cameras in selected wavelength bands to identify interesting subarcsecond-scale structures which can be analyzed with follow-up spectroscopy. During the initial checkout of HST scientific performance in 1991, members of the FOS science team investigated the capability of the aberrated HST for carrying out investigations in galactic nuclei. (This was part of a substantial set of evaluation programs carried out by HST scientists.) Imaging of the inner region of the barred spiral Seyfert galaxy NGC 1068 indicated[5] some of the potential and limitations for imaging with an aberrated HST. Narrowband images clearly resolved subarcsecond structures not previously seen from ground-based telescopes, and image deconvolution techniques were successfully used to identify several enhanced-brightness condensations of ionized gas within a roughly conical region presumably photoionized from energy sources within the nucleus. Spectroscopic studies of a few of these features illustrated[6] the difficulties produced by mixing of the light from sources separated by a few tenths of arcseconds. The emission lines from these regions were complex in shape and clearly contained contributions from several regions of differing velocities and velocity dispersions. Disentangling the spectra from the nearby regions was impractical with the aberrated HST PSF, but should be possible (and is planned) with the COSTAR-corrected PSF.

3.2 Search for Massive Black Holes in Centers of Galaxies

Arguably the most exciting program for which the FOS instrument was designed is the attempt to determine whether massive black holes exist within the nuclei of any, some, or most galaxies. Spectrographic searches for black holes attempt to detect the velocity changes in surrounding objects (such as stars) produced by the gravitational field of the black hole. The process is likely to be one of elimination; having seen gravity-induced motions, one must convincingly demonstrate that less exotic forms of gravitating matter do not produce the gravitational fields before concluding the gravity source must be a black hole. Because nuclei of galaxies often have large concentrations of matter within small volumes of space, and because many energetic phenomena such as optical and radio jets are seen to emanate from some galactic nuclei, many astronomers suspect that some, if not most, galactic nuclei contain black holes.

The specific method of detecting mass, whether black holes or less exotic material such as stars, by its gravitational effects within galaxies depends on galaxy type. In spiral galaxies, rotation about a preferred axis can be detected (so long as the galaxy is not face on) as a systematic variation in radial velocity across the galaxy. Elliptical galaxies generally exhibit little rotation about a preferred axis, so that the influence of gravity on their stars must be detected as variation of velocity dispersion across the galaxy. At a practical observational level, measurement of velocity dispersions generally is more difficult than detection of comparably large velocity shifts, requiring higher SNR spectra and somewhat better spectral resolution. Nonetheless, because several of the strongest suspects to harbor massive black holes are elliptical galaxies, measurement of velocity dispersions within (elliptical) galaxies is planned to be a major FOS crowded-field spectroscopy activity.

Angular resolution is important for two reasons in the search for black holes. First, the gravitational field of

the black hole itself affects surrounding matter with proportionality: $a \sim \frac{M_{BH}}{R^2} \sim \frac{V^2}{R}$, so that $M_{BH} \sim V^2 R$, where a is acceleration (due to gravity of the black hole), M_{BH} is the mass of the black hole, R is the distance from the black hole of the luminous material we measure, and V is a typical velocity of the material at R produced by the gravitational field. The constants of proportionality depend moderately upon ellipticities of the orbits of the material around the black hole. However, the simple scaling argument above illustrates that, for a given spectroscopic capability to detect variations in velocity or in velocity dispersions, the sensitivity for detecting a black hole, ignoring other sources of gravity, scales linearly with angular resolution (which projects linearly to R). Second, and more important, as we look further toward the center of a galaxy, the gravitational effect from stars diminishes rapidly, as $M_S(R)$, the amount of stellar matter interior to R, diminishes as $M_S(R) \sim R^{-3}$ for uniform density. Even for the normal case in which stellar densities rise nearing the galactic nucleus, the rapid decrease in $M_S(R)$ as R decreases aids greatly in allowing the gravitational influence of the black hole to dominate that of the stars. Thus, improved angular resolution aids the detection of black holes both by enhancing the gravitational influence of the black hole and by reducing the competing influence from other matter (mainly stars) in the galaxy.

One countervailing observational effect relevant for observations of elliptical galaxies needs to be mentioned. As the velocity dispersion increases, the spectral features of the stars we are observing become wider and shallower. Particularly with low SNR spectra, typically all we can obtain due to the low surface brightness of galaxies, shallow absorption lines can be difficult to detect with high confidence. For velocity dispersion, it is not always true that more is better. Thus, the optimum radius for detecting a given black hole may not always be the minimum radius we can spatially resolve, but rather that radius for which $\sigma \approx 400$ to 600 km/sec for the FOS spectral resolving power. This is still likely to favor subarcsecond angular scales, however; otherwise the massive black holes would probably already have been detected from ground-based spectroscopic measurements. (Of course, we have no way of knowing in advance the mass of the black hole we are seeking, so we must cover the angular range from approximately 0.1 arcsecond, about the best HST can do, to around 2 arcseconds, about the ground-based telescope limit. The discussion above simply alerts us to the possibility that, given a fortuitous black hole mass, we might most convincingly detect the black hole by its effect on stars at some location other than the one closest to the black hole.)

3.3 Testing if M87 Contains a Massive Black Hole

Velocity dispersion measurements made in 1978 identified the giant elliptical galaxy M87 as a strongcandidate to contain a massive black hole,[7] which also provided a plausible mechanism to power its X-ray and radio emission and its famous optical jet. The spectroscopic evidence, based on close-in measurements which push the angular resolution limits of ground-based telescopes, has never been fully conclusive,[8] however. With the COSTAR-restored angular resolution of HST, a greatly improved investigation of the possible presence of a massive black hole in M87 becomes an exciting and feasible scientific program. In this section, we model the velocity dispersion effects of an M87 black hole, and briefly describe the initial evaluation of the FOS feasibility tests of M87 observations.

In the best tradition of theory, we will develop a simple "spherical-cow"-level model, to derive approximately the dependence of surface brightness and velocity dispersion in M87 upon mass of a central black hole. Specifically, we make the simplifying assumptions of:
1) spherical symmetry (including negligible net rotation),
2) constant stellar mass and luminosity function over volumes of interest,
3) central point mass (the black hole) plus smooth mass distribution of stars, and
4) Maxwellian velocity distribution in local Virial equilibrium.

The assumption of spherical symmetry is probably reasonably good, since M87 is an E0 galaxy; however, velocity anisotropies or even rotating structures near the center of M87 cannot be ruled out. Slight variations in stellar mass (and luminosity) functions should not greatly affect the results below. Our assumption that any black

hole is located at the center of M87's stellar distribution is plausible and consistent with the velocity dispersion and surface brightness data previously available. The assumption that the stars are locally Virialized and in local thermal equilibrium is almost certainly not correct; corrections for unknown velocity anisotropies and the distribution of ellipticities of stellar orbits near the nucleus will probably produce the largest uncertainty for the mass or upper limit of the mass of a black hole in M87. Of course, if future FOS data were to indicate some deviation from spherical symmetry, such as an off-center black hole or a central subarcsecond rotating disk, such a discovery would be a welcome disproof of this simple model.

With the assumptions above, each star serves as a test mass probing the gravitational potential with $\Phi(R) + 2K(R) = 0$, where the gravitational potential per unit mass $\Phi(R) = -\frac{G*M(R)}{R}$ and the kinetic energy per unit mass $K(R) = \frac{\langle V^2_{star}(R)\rangle}{2}$ are locally in Virial equilibrium. G is the gravitational constant, $\langle V^2_{star}(R)\rangle$ the average squared velocity of stars located at R, and $M(R)$ the mass interior to radius R. Let M_{BH} be the mass of the central black hole and $\rho(R)$ be the stellar mass density at R. Then $M(R) = M_{BH} + 4\pi \int_0^R r^2\rho(r)dr$. The observed radial velocity dispersion $\sigma(R)$ is related to the mean square velocity by the relation $\sigma(R) = \sqrt{\frac{\langle V^2_{star}(R)\rangle}{3}}$. If we measure mass in solar units ($M_\odot = 1.99 * 10^{33}$ grams), distance in parsecs (1 parsec = 3.086*10^{18} cm), and velocity dispersions in km/sec, then the relationships above imply

$$\sigma(R) = 3.786 * 10^{-2}\sqrt{\frac{M_{BH} + 4\pi \int_0^R r^2\rho(r)dr}{R}}.$$

Our assumption of constant stellar mass and luminosity functions implies that the emission we will detect in our spectra from each volume element is given simply by a constant stellar emission template for a specific stellar distribution function with intensity directly proportional to the local mass density $\rho(R)$ and spectrally broadened (convolved) with a Gaussian of width $\sigma(R)$.

The probability for finding a given star with velocity $\mathbf{V}$ in a Maxwellian distribution is given by:

$$P(\mathbf{V}) = \frac{e^{-\frac{V^2}{2\sigma^2}}}{2\pi\sigma^3\sqrt{2\pi}}.$$

In the formula above, the dependence on R is understood for $\mathbf{V} = \mathbf{V}(R)$ and $\sigma = \sigma(R)$, while $V^2 = \|\mathbf{V}\|^2$. We can integrate this equation to obtain the probability distribution for radial velocity, V_Z, by integrating over V_X and V_Y:

$$P(V_Z) = \int_{-\infty}^{\infty} dV_X \int_{-\infty}^{\infty} dV_Y \left(\frac{e^{-\frac{(V_X^2+V_Y^2+V_Z^2)}{2\sigma^2}}}{2\pi\sigma^3\sqrt{2\pi}}\right) = \frac{e^{-\frac{V_Z^2}{2\sigma^2}}}{\sigma\sqrt{2\pi}}.$$

Note that $\int_{-\infty}^{\infty} dV_Z\,[P(V_Z)] = 1$, $\langle V_Z\rangle = \int_{-\infty}^{\infty} dV_Z\,[V_Z P(V_Z)] = 0$, and $\langle V_Z^2\rangle = \int_{-\infty}^{\infty} dV_Z\,[V_Z^2 P(V_Z)] = \sigma^2$.

The contribution from a volume element at location R to the observed spectrum is that of the intrinsic spectrum of the stellar mix in the observed galaxy, with total intensity at R proportional to $\rho(R)$ [we have assumed constant mass-to-light ratio in the region of interest), convolved with the distribution function $P(V_Z(R))$. The predicted spectrum we observe is obtained by computationally intensive but straightforward integration of the emission from the volume elements lying within the 3-dimensional volume of the galaxy lying within the field of view of the FOS entrance aperture. (The effect of the PSF in the image entering the FOS aperture must be taken into account also, although for the sharp post-COSTAR images, this effect is usually not very significant.) Models of surface brightness variations with R are computed simply by integrating the emission intensity at R (proportional to $\rho(R)$) over the same 3-D volume of the galaxy in the FOV of the FOS aperture.

Although our analysis emphasizes the role of velocity dispersion for detection of a black hole in M87, the variation of surface brightness with position in the galaxy provides a complementary means to detect such a

central mass. The predicted surface brightness profile is, of course, model dependent, but a massive central black hole is can generally be predicted to enhance surface brightness as $R \rightarrow 0$. Ground-based surface brightness observations of M87 deviated within the central 10 arcseconds from an isothermal model and were interpreted[9] as evidence for a central black hole of mass $M_{BH} = (2.6 \pm 0.5) * 10^9 M_\odot$. Images of M87 taken in the V and I bands using the (pre-COSTAR) HST Planetary Camera[10] show that the stellar surface brightness within $R < 3$ arcseconds ($\leftrightarrow R < 230$ parsecs assuming a distance of 16 Mpc for M87) varies approximately as $\mu(R) \sim R^{-0.26}$, steepening for $R > 10$ arcseconds $\leftrightarrow R > 770$ pc to a relation $\mu(R) \sim R^{-1.3}$, with maximum change of slope around $R = 7$ arcseconds $\leftrightarrow R = 540$ pc. The authors[10] conclude that the surface brightness profile of M87 is consistent with a central black hole of mass $M_{BH} \geq 10^9 M_\odot$, but that velocity dispersion measurements within the central 0.5 arcsecond region are required to establish this conclusively.

We have incorporated our assumptions into models with various masses of central black holes to explore the sensitivity of velocity dispersion measurements within the inner 2 arcseconds of M87 for detecting a central black hole. In order to match the surface brightness profiles at both large and small radii, we chose the easily integrable form for stellar density $\rho(R)$ to be:

$$\rho(R) = \frac{(\rho_0)(R + 1260)}{(R^{1.25})(R + 540)^2}.$$

The mass interior to R, $M(R)$, is then given simply by:

$$M(R) = M_{BH} + \frac{16\pi\rho_0 R^{1.75}}{R + 540}.$$

Note that $\rho(R) \sim R^{-1.25}$ as $R \rightarrow 0$ and that $\rho(R) \sim R^{-2.25}$ as $R \rightarrow \infty$. We then expect that the surface brightness $\mu(R)$ will scale as $R\ \rho(R)$, closely matching the observed radial power-law dependence for both small and large R. The density is then scaled by adjusting ρ_0 to give velocity dispersions at radii larger than 2 arcseconds in agreement with previous observations.

Figure 1 shows the density profile used in our model calculations. Figure 2 plots the surface brightness versus radius; that the surface brightness possesses the proper radial dependence at small and large r is illustrated in Figure 3. The results presented in Figures 1 - 3 are, by our assumptions, independent of the existence of any central black hole. Figure 4 depicts the interior mass distributions for central black holes with $M_{BH} = 0, 10^8$, and $10^9 M_\odot$. The mass $M(R)$ interior to R, of course, depends strongly on the mass of the central black hole at small radii. The local velocity dispersions versus radius for these three cases are shown in Figure 5, and the LOS-column-averaged velocity dispersions, corresponding approximately to what we can measure in our observations, are plotted in Figure 6. It is clear that the observable column-averaged velocity dispersion becomes sensitive to black hole masses of order $10^9 M_\odot$ only within approximately the central 1 arcsecond (77 parsecs) in our model. Modifying the model assumptions, say, replacing Virial equilibrium at each radius with isothermality, allowing preferentially high or low ellipticity orbits, or introducing departures from sphericity, would be expected to modify the conclusions by factors only of order unity. (However, more realistic assumptions in the limit $R \rightarrow 0$, where Virialization must break down, would almost certainly avoid the decrease in velocity dispersion at very small R computed using our model assumptions.) In any case, it seems probable that HST observations of velocity dispersions in M87 can detect a central black hole in M87 with mass of 10^8 to $10^9 M_\odot$, but will not be able to detect a substantially smaller central black hole.

On 11 February 1994, the FOS early release observation (ERO) program, designed to test the post-COSTAR scientific utility of the FOS, was carried out to obtain spectra at three locations in M87. These spectra were taken using the 0.26 arcsecond diameter entrance aperture and the G570H grating, which provides spectral resolution about 5 Å over the range 460 nm $< \lambda <$ 680 nm approximately. Nominal locations for the observations were at radii of 0.00, 0.25, and 2.00 arcseconds from the nucleus of M87. The off-nuclear spectra achieved the expected (low; the ERO program integration time amounted to only about 10% of what we estimate will be necessary for the GTO program on M87) signal-to-noise ratio. The observation nominally centered on the nucleus clearly was off-center by an unknown amount we estimate to be approximately 0.10 arcseconds. The nucleus was clearly seen in the target acquisition peak-up images, which should have resulted in a better-centered spectrum of the

nucleus with an order of magnitude more counts than were obtained. The cause of the mispointing is under investigation,[11] as is a repeat of (at least a portion of) the FOS ERO.

Even without the targeting anomaly, the low SNR data we obtained were not expected to be adequate for reliably assessing the existence of a massive black hole in M87. The data do indicate the feasibility of the planned GTO program, however. The (perhaps rather limited) conclusions which can be drawn from the ERO data will be published in a future paper.

4 ACKNOWLEDGMENTS

One of the most valuable gifts one can receive is often a second chance. We thank all the many individuals within NASA, at the STScI, and at several aerospace companies and universities, who made the HST servicing mission the success which provides all astronomers a second chance to carry out the scientific investigations long planned for this observatory. Especially, we thank the STS-61 astronauts who carried out the HST servicing mission in such spectacularly successful fashion, beyond even our most optimistic hopes.

Finally, we thank the US taxpayers for funding the FOS team's scientific investigations, including the studies described in this paper, under NASA Grant NAS5-1630.

THE ASTROPHYSICAL JOURNAL, 427:L47–L50, 1994 May 20

ULTRAVIOLET INTERSTELLAR POLARIZATION OBSERVED WITH THE *HUBBLE SPACE TELESCOPE*[1]

W. B. SOMERVILLE,[2,3] R. G. ALLEN,[4] D. J. CARNOCHAN,[2] LIDA HE,[5] D. MCNALLY,[2] P. G. MARTIN,[6,7] D. H. MORGAN,[8] K. NANDY,[8] J. R. WALSH,[9] D. C. B. WHITTET,[5] R. WILSON,[2] AND M. J. WOLFF[10]

Received 1993 December 20; accepted 1994 March 2

ABSTRACT

We have used the Faint Object Spectrograph of the *Hubble Space Telescope* to observe interstellar linear polarization from 1300 to 3300 Å in two stars with well-studied interstellar polarization at visible wavelengths. The wavelength dependence of linear polarization declines smoothly with decreasing wavelength and is devoid of structure associated with the prominent 2175 Å absorption bump in the interstellar extinction curve. The data for one star (HD 161056) are consistent with an extrapolation based on the Serkowski formula of a fit to the ground-based polarization; the other star (HD 7252) shows excess (super-Serkowski) polarization relative to this extrapolation. Out of a total of 10 stars now studied by means of spectropolarimetry in the satellite ultraviolet, including eight observed with the Wisconsin Ultraviolet Photopolarimeter, five (those of longest λ_{max}) show Serkowski behavior, and four others show super-Serkowski behavior; only one (HD 197770) shows evidence for polarization associated with the 2175 Å bump. These results place important constraints on the nature of the bump feature.

Subject headings: dust, extinction — stars: individual (HD 7252, HD 161056) — techniques: polarimetric — ultraviolet: ISM

1. INTRODUCTION

The physical nature and chemical composition of interstellar dust grains are as yet poorly understood. From various types of observation it has become clear that they consist mainly of a mixture of silicates and some form of solid carbon, perhaps graphite, with the addition of ice mantles in molecular clouds, but a unique model for interstellar extinction has yet to emerge (see Whittet 1992 for a review). The extinction curve is dominated by the dramatic and ubiquitous "bump" centered at 2175 Å. The bump is often attributed to graphite, but there are significant problems with this identification: indeed, the identity of the particles responsible for the bump is amongst the most significant unsolved problems in astronomical spectroscopy (Draine 1989; Draine & Malhotra 1993; Mathis 1994).

Spectropolarimetric observations in the satellite ultraviolet (UV) have the potential to provide unique insight into both the optical properties of grains which contribute to extinction at these wavelengths and their ability to align in the ambient magnetic field (Somerville 1991). The overall shape of the continuum polarization is closely related to the grain size distribution. The wavelength dependence of polarization across a dust-related absorption feature is a general diagnostic of the shape, size distribution, refractive index and alignment properties of the carrier. A spectral signature in the polarization is expected for significant alignment of aspherical carrier grains, and this has been observed, for example, in the infrared at wavelengths corresponding to the principal vibrational resonance in silicates near 10 μm (e.g., Whittet 1992), indicating that silicate particles are alignable and may contribute to the general continuum polarization. Whether or not this property is shared by the carrier of the bump is a key question with important implications for grain models: Draine (1988) pointed out that aspherical graphite grains, if appreciably aligned, would produce distinctive linear polarization in the UV and that the predicted polarization is an important constraint on graphite as a component of grain models. Spectropolarimetric results available to date are intriguing. An early experiment (Gehrels 1974) suggested a lack of significant excess above the continuum predicted by an extrapolation of the visible polarization curve to ultraviolet wavelengths. In the recent past, data from the Wisconsin Ultraviolet Photopolarimeter Experiment (WUPPE) have become available, which suggest the presence of a 2175 Å interstellar polarization excess in one star out of eight observed (Taylor et al. 1991; Clayton et al. 1992; Schulte-Ladbeck et al. 1992). Here, we present the first observations of UV interstellar polarization to be made with the *Hubble Space Telescope* (*HST*). These observations represent an advance in quality over those previously available.

2. OBSERVATIONS AND RESULTS

Observations of three program stars were made in Cycle 1 of the *HST* Guest Observer program in September, 1992. Results for two of them are presented here (see Table 1). Observation of the third target, HD 98695, suffered from a spacecraft pointing error (it was recently reobserved in one grating segment). Early-type stars were selected on the basis of previous observations of UV extinction and visible polarization to give varia-

[1] Based on observations with the NASA/ESA *Hubble Space Telescope*, obtained at the Space Telescope Science Institute, which is operated by the Association of Universities for Research in Astronomy, Inc., under NASA contract NAS 5-26555.

[2] Department of Physics and Astronomy, University College London, Gower Street, London WC1E 6BT, UK.

[3] I: wbs@star.ucl.ac.uk; D: 19752::WBS.

[4] Steward Observatory, University of Arizona, Tucson, AZ 85721.

[5] Department of Physics, Rensselaer Polytechnic Institute, Troy, NY 12180.

[6] Canadian Institute for Theoretical Astrophysics, University of Toronto, Toronto, Ontario, Canada M5S 1A7.

[7] Theoretical Astrophysics 130-33, Caltech, Pasadena, CA 91125.

[8] Royal Observatory Edinburgh, Blackford Hill, Edinburgh EH9 3HJ, UK.

[9] ST-ECF, European Southern Observatory, Karl-Schwarzschild Strasse 2, D-85748, Garching bei München, Germany.

[10] Space Astronomy Laboratory, University of Wisconsin at Madison, 1150 University Avenue, Madison, WI 53706.

TABLE 1

PROGRAM STARS

HD	Spectral Type	E_{B-V}	l, b	d (pc)	p_{max}	λ_{max} (μm)	2175 Å	FUV	Grating	Exposure (minutes)
7252	B1 V	0.34	125.7, −1.9	824	3.49% ± 0.02%	0.52 ± 0.01	Strong	Strong	G130H	83.4
									G190H	36.3
									G270H	12.3
161056	B1.5 V	0.63	18.7, +11.6	295	4.03% ± 0.01%	0.59 ± 0.01	Normal	Normal	G130H	124.6
									G190H	64.6
									G270H	16.9

tion in bump amplitude, far-UV extinction amplitude, and the wavelength (λ_{max}) of maximum polarization. Table 1 lists spectral types and reddening (E_{B-V}) for the program stars (from Carnochan 1986), together with Galactic coordinates and distances (derived assuming $A_V = 3.1E_{B-V}$ and the absolute magnitude calibration from Gottlieb 1978). Polarization parameters (see below) and comments on the UV extinction curve are also given. The latter indicate the strengths of the 2175 Å feature and the far-UV extinction rise, relative to the mean extinction curve, using data from the S2/68 telescope on the *TD-1* satellite (Carnochan 1986).

The *HST* Faint Object Spectrograph (FOS) was used in spectropolarimetric mode (see Allen et al. 1993 for a description), using the blue digicon and wave plate B. Data were acquired at eight position angles of the wave plate. Gratings and total exposure times are listed in Table 1. The spectral range 1300–3300 Å was covered in three overlapping segments at a nominal spectral resolution of 2–4 Å. The segment ranges were 1279–1603 Å (G130H grating), 1575–2324 Å (G190H grating) and 2224–3295 Å (G270H grating). Exposure times were chosen to give the same nominal accuracy in the percentage polarization p in each grating segment, using S2/68 fluxes. All observations were made through the 4.3 arcsec square aperture. The data were processed independently using standard STSDAS pipeline procedures at ST-ECF and dedicated software available at the university of Arizona (Allen & Smith 1992). All of the FOS linear polarization measurements have been adjusted to allow for the bias that occurs when the expected error is more than a small fraction of the measurement itself (Wardle & Kronberg 1974). The data were binned to give 10 points per grating segment, as plotted in Figure 1; only error bars in excess of 0.04% polarization (1 σ) are shown. Note that both the signal-to-noise ratio and the spectral resolution, especially at the shortest wavelengths, are superior to those achieved with WUPPE. The FOS also reaches down to shorter wavelengths, 1279 Å compared with 1400 Å for WUPPE.

New ground-based linear polarimetry covering the spectral range 3500–7400 Å was obtained for the two program stars with the 0.9 m telescope and spectropolarimeter of the Pine Bluff Observatory, Madison, Wisconsin (PBO) (see Nordsieck et al. 1992; Nook 1990). Additional ground-based visible and near-infrared data are available from the literature (HD 7252, Coyne & Gehrels 1967; HD 161056, Coyne & Gehrels 1966; Coyne & Wickramasinghe 1969; Wilking et al. 1980; Nagata 1990). Ground-based and UV polarization data were combined to plot polarization curves (Fig. 1) extending in wavenumber from 0.4 to 8.0 μm^{-1}. Standard empirical curves represented by the Serkowski law $p(\lambda)/p_{max} = \exp[-K \ln^2(\lambda_{max}/\lambda)]$ (Serkowski, Mathewson, & Ford 1975)

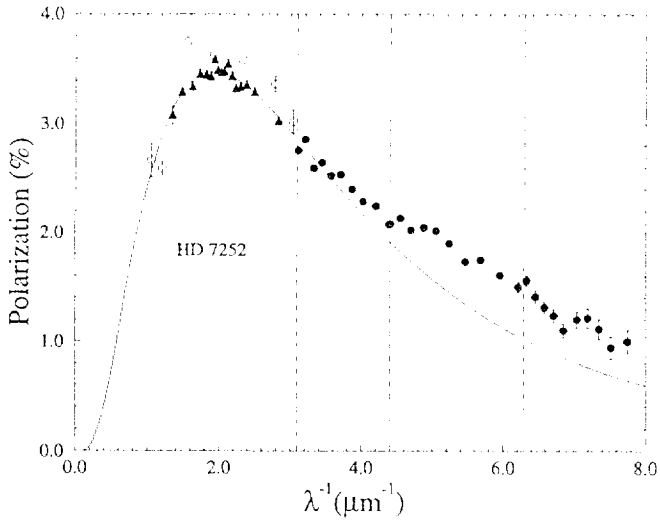

FIG. 1a

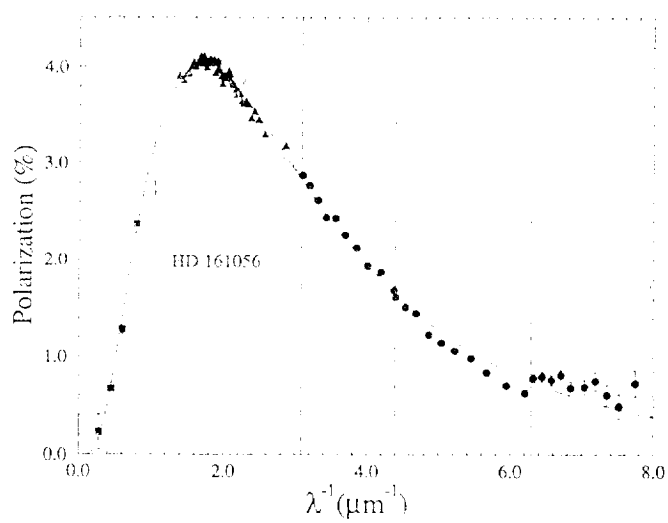

FIG. 1b

FIG. 1.—Interstellar polarization curves for the program stars: (*a*) HD 7252; (*b*) HD 161056. *HST* data are represented by filled circles, and the vertical dashed lines indicate the approximate division by grating segment (see § 2). Ground-based data are represented by filled triangles (previously unpublished observations from the PBO), open circles (from Coyne & Gehrels 1966, 1967; Coyne & Wickramasinghe 1969), and filled squares (near-infrared data from Wilking et al. 1980; Nagata 1990). The curves are least-squares fits to selected ground-based data (see text) using the Serkowski formula with $K = 1.66\lambda_{max}$(Whittet et al. 1992). Values of p_{max} and λ_{max} derived from the fits are given in Table 1.

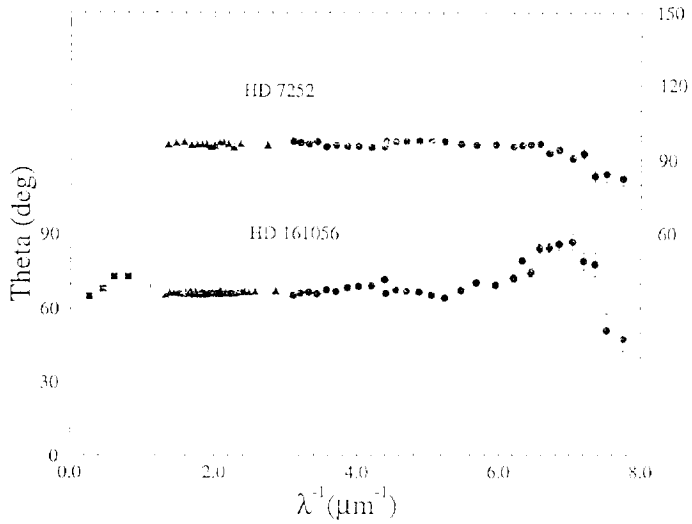

FIG. 2.—The wavelength dependence of the position angle θ of polarization for the two program stars. The right and left vertical scales refer to HD 7252 and HD 161056, respectively. Symbols have the same meaning as in Fig. 1.

with $K = 1.66\lambda_{max}$ (Whittet et al. 1992) were fitted to the ground-based data. In the case of HD 7252, the data of Coyne & Gehrels (1967; *open circles* in Fig. 1*a*) are excluded from the fit because of scatter and systematic inconsistency with the more recent ground-based data. Similarly, in the case of HD 161056, the data of Coyne & Gehrels (1966) and Coyne & Wickramasinghe (1969) (*open circles* in Fig. 1*b*) are excluded from the fit, but the near-infrared data (*filled squares*) are included, along with the PBO data (*filled triangles*). Values of p_{max} and λ_{max} derived from the fits are listed in Table 1; in both cases, these are in reasonable agreement with previous values quoted in the literature (Serkowski et al. 1975; Wilking et al. 1980).

The position angle (θ) of polarization was examined for systematic variability with wavelength, comparing UV and ground-based data. Results are presented in Figure 2. In the visible, the individual values of θ are consistent with the mean value to an accuracy of better than $\pm 2°$ in each line of sight. The dispersion is somewhat higher in the UV, particularly at the shortest wavelengths, where the degree of polarization is low, but there is no evidence for significant systematic dependence of θ on wavelength toward either of the program stars, except possibly below 1350 Å.

3. QUALITY OF THE DATA

In this section we discuss possible systematic effects in FOS polarimetry which are not included in the errors indicated in the figures. Examination of the wavelength regions which overlap between two gratings provides an internal check. The degree of linear polarization shows satisfactory agreement (within 1 σ error bars), except for the G190H to G130H transition in HD 161056, where the polarization jumps from $0.63\% \pm 0.04\%$ at 1611 Å to $0.78\% \pm 0.04\%$ at 1585 Å, opposite to the trend of a decrease in polarization with wavenumber. Systematic behavior can be seen in θ as well. These discontinuities probably result from the effects of geomagnetic distortion. The diode array in the FOS digicon is overfilled by the stellar image because of the spherical aberration in the telescope primary mirror. The spillover losses vary slightly with the orientation of the spacecraft to Earth's magnetic field; this introduces spurious polarization that varies as a function of wavelength. Since the amount of polarization depends on the accuracy of the grating mechanism, the effects are slightly different whenever the grating is moved.

The level of instrumental polarization for the FOS has been discussed by Allen et al. (1993), on the basis of observations of the unpolarized standard star BD $+28°4211$ at two roll angles separated by 45 degrees. Their results indicate that the FOS instrumental polarization is less than 0.1% over the entire wavelength range of our observations. However, because the detector counts are lowest in the G130H range, it contained only two wavelength bins: G130H is a region of particular concern because the polarization for the program stars is smallest there, and the detected counts are low on account of the falling sensitivity of the detector to short wavelengths, so we have made an independent analysis using the two sets of observations of BD $+28°4211$ in the G130H grating. We confirm the result of Allen et al. (1993) but caution that any polarizations below 0.2% must be considered highly uncertain; therefore, any interpretation of the data judged only from the formal statistical errors that depends on the errors being less than 0.1% is unwise.

A case in point is the G130H data for HD 161056, where the measured linear polarization is only slightly above 0.5% and is therefore most susceptible to both types of systematic error. The change in θ seen below 1350 Å seems well established because it appears in all five sets of data (because of its length, the exposure had to be divided between five orbits of the spacecraft). However, if there are systematic errors of the order of 0.2% in polarization, then the accompanying errors in θ could be at least 10°, lowering our confidence in the reality of this change. While the linear polarization of HD 7252 declines smoothly over all three gratings, a slight decrease in θ is seen below 1350 Å. This change in θ is also only marginally significant.

Finally, there is some structure seen in the linear polarization of HD 7252, in association with its super-Serkowski behavior. This structure, which is within the data for a single grating, appears to be real.

4. DISCUSSION

The empirical fits to ground-based data are shown in Figure 1 with extrapolation to shorter wavelengths. There is, of course, no a priori reason to suppose that this extrapolation will provide a good fit to the observed polarization (Martin 1989). From their analysis of WUPPE data, Wolff, Clayton, & Meade (1993) recognized three types of behavior: (1) stars with UV data well-matched by the extrapolated fit (Serkowski behavior); (2) stars exhibiting excess continuum polarization with respect to the extrapolated fit (super-Serkowski behavior); and (3) one star with excess polarization apparently associated with the 2175 Å bump. Examination of Figure 1 suggests that one of the two stars observed with the *HST* (HD 161056) exhibits Serkowski behavior, and the other (HD 7252) exhibits super-Serkowski behavior. It might be significant that the latter star also has the stronger far-UV extinction. However, we note that the "Serkowski excess" extends across the UV spectrum from $\lambda^{-1} \sim 3.8\ \mu m^{-1}$ to the far-UV (Fig. 1*a*), whereas the far-UV extinction rise sets in only at $\lambda^{-1} > 6.0\ \mu m^{-1}$. Perhaps of greater significance is the fact that HD 7252 has the lower λ_{max} value. This is in qualitative agreement with WUPPE results: Wolff et al. find Serkowski behavior for four stars with $\lambda_{max} \geq 0.55\ \mu m$ and super-Serkowski behavior for

three stars with $\lambda_{max} \leq 0.51$ μm. We note that members of the latter class should have relatively large "Serkowski" polarization in the UV by virtue of both smaller λ_{max} and the wider polarization curve (systematically decreased K with λ_{max}); the "excess" is perhaps simply another manifestation of this behavior, and the failure of the Serkowski curve to describe it adequately is certainly no particular surprise.

An important conclusion is that neither of our program stars exhibits a polarization signature that can be attributed to the 2175 Å (4.6 μm^{-1}) extinction bump. Of a total of 10 stars now studied in the UV with WUPPE or *HST*, only one, HD 197770, shows any evidence for polarization structure associated with the bump. On the basis of its λ_{max} value, 0.51 μm, HD 197770 might be expected to show super-Serkowski behavior. One may thus argue that the anomaly could be characterized not as a polarization excess at 4.6 μm^{-1} but instead as unusually low polarization at $\lambda^{-1} > 5$ μm^{-1} (see Fig. 5 of Wolff et al. 1993). Further observations of this star are needed to settle this issue.

Limits on the amplitude of polarization structure, Δp, are of quantitative interest. For example, from our data for HD 161056 (Fig. 1*b*), we estimate that $\Delta p/p < 0.06$ near 4.6 μm^{-1}, whereas for the extinction bump in this line of sight $\Delta\tau/\tau \approx 0.6$ using extinction parameters from Carnochan (1986). In other combinations $p/\tau \simeq 0.004$ and $\Delta p/\Delta\tau < 0.0004$. The latter can be compared to Draine's (1988) models of the potential bump polarization which give $\Delta p/\Delta\tau \sim 0.3$–0.8 for perfect alignment of small prolate or oblate graphite particles with axial ratio 1.5. Our observations therefore place tight constraints on some combination of the degrees of asphericity and alignment of these particles. Wolff et al. (1993) found that the excess polarization in the region of the 2175 Å bump for HD 197770 can be fitted well by small aligned graphite disks. We estimate that $\Delta p/\Delta\tau \sim 0.004$ for that line of sight, an order of magnitude larger than the upper limit for HD 161056 (the limit for HD 7252 is 0.001), but still much less than the maximum possible.

Observations of UV interstellar polarization are providing impetus for theoretical work designed to test existing models for the wavelength dependence of extinction, and the degree of grain alignment as a function of grain size. Wolff et al. (1993) have investigated the applicability of existing grain models to WUPPE data. They conclude that both Serkowski and super-Serkowski behavior can be understood in terms of the model of Mathis (1986) by varying the adjustable parameters of the size distribution. This model is based on the bare graphite/silicate extinction model (Mathis, Rumpl, & Nordsieck 1977), with the additional assumption that only the silicate component becomes aligned. A crucial feature of this model is a prediction that the degree of alignment should decrease systematically toward smaller particles, and hence that the polarization should decline to shorter ultraviolet wavelengths, where the polarization is most sensitive to small particles. This prediction is in good agreement with observations from both WUPPE and *HST*.

If interstellar polarization is produced primarily by silicate grains, as in the Mathis (1986) model, then structure in the polarization curve is expected to occur in the far-UV. This arises because of the onset of electronic absorption in the adopted silicate: in olivine, for example, it takes the form of a downturn in the predicted polarization beyond ~ 6 μm^{-1} (see, e.g., the MRN curve in Fig. 3 of Wolff et al. 1993). Kim & Martin (1994) discuss this effect and find that the downturn continues to larger wavenumbers, making it difficult to fit stars with super-Serkowski behavior. However, olivine might not be very representative of interstellar silicates, and other forms may have optical constants that lead to acceptable fits. We conclude that our data may be used to constrain the optical constants of interstellar silicates.

Independent of a specific model, Kim & Martin (1994) have shown how systematic changes in the underlying size distribution of the aligned grains can produce the varying behavior with λ_{max}. Compared to the size distributions of grains that give extinction, the aligned grain size distributions are very much lacking in small particles; in particular, there is no evidence so far that the grains that cause the far-UV extinction rise make an appreciable contribution to the polarization. Such investigations benefit from extension of the polarization data as far as possible to short wavelengths, as we are attempting to do with *HST*.

Support for this work was provided by NASA through grant number GO-2245.01-87A from the Space Telescope Science Institute. We wish to acknowledge the generous data support provided by the University of Wisconsin's PBO research team and technical staff. W. B. S. acknowledges travel funding from the UK Science and Engineering Research Council.

REFERENCES

Allen, R. G., & Smith, P. S. 1992, FOS IDT Report CAL/FOS-078
Allen, R. G., Smith, P. S., Angel, J. R. P., Miller, B. W., Anderson, S. F., & Margon, B. 1993, ApJ, 403, 610
Carnochan, D. J. 1986, MNRAS, 219, 903
Clayton, G. C., et al. 1992, ApJ, 385, L53
Coyne, G. V., & Gehrels, T. 1966, AJ, 71, 355
———. 1967, AJ, 72, 887
Coyne, G. V., & Wickramasinghe, N. C. 1969, AJ, 74, 1179
Draine, B. T. 1988, ApJ, 333, 848
———. 1989, in IAU Symp. 135, Interstellar Dust, ed. L. J. Allamandola & A. G. G. M. Tielens (Kluwer: Dordrecht), 313
Draine, B. T., & Malhotra, S. 1993, ApJ, 414, 632
Gehrels, T. 1974, AJ, 79, 590
Gottlieb, D. M. 1978, ApJS, 38, 287
Kim, S.-H., & Martin, P. G. 1994, ApJ, in press
Martin, P. G. 1989, in IAU Symp. 135, Interstellar Dust, ed. L. J. Allamandola & A. G. G. M. Tielens (Kluwer: Dordrecht), 55
Mathis, J. S. 1986, ApJ, 308, 281
———. 1994, ApJ, 422, 176
Mathis, J. S., Rumpl, W., & Nordsieck, K. H. 1977, ApJ, 217, 425
Nagata, T. 1990, ApJ, 348, L13
Nook, M. A. 1990, Ph.D. thesis, Univ. of Wisconsin, Madison
Nordsieck, K. H., Babler, B., Bjorkman, K. S., Meade, M. R., Schulte-Ladbeck, R. E., & Taylor, M. J. 1992, in Nonisotropic and Variable Outflows from Stars, ed. L. Drissen, C. Leitherer, & A. Nota (ASP Conf. Ser., 22), 114
Schulte-Ladbeck, R. E., et al. 1992, ApJ, 391, L37
Serkowski, K., Mathewson, D. S., & Ford, V. L. 1975, ApJ, 196, 261
Somerville, W. B. 1991, Vistas Astron., 34, 51
Taylor, M., et al. 1991, ApJ, 382, L85
Wardle, J. F. C., & Kronberg, P. P. 1974, ApJ, 194, 249
Whittet, D. C. B. 1992, Dust in the Galactic Environment (Bristol: Inst. of Physics)
Whittet, D. C. B., Martin, P. G., Hough, J. H., Rouse, M. F., Bailey, J. A., & Axon, D. J. 1992, ApJ, 386, 562
Wilking, B. A., Lebofsky, M. J., Martin, P. G., Rieke, G. H., & Kemp, J. C. 1980, ApJ, 235, 905
Wolff, M. J., Clayton, G. C., & Meade, M. R. 1993, ApJ, 403, 722

THE ASTROPHYSICAL JOURNAL, 427:L21–L24, 1994 May 20

HUBBLE SPACE TELESCOPE FINE GUIDANCE SENSOR INTERFEROMETRIC OBSERVATIONS OF THE CORE OF 30 DORADUS

M. G. LATTANZI,[1,2,3] J. L. HERSHEY,[4] R. BURG,[5,1] L. G. TAFF,[1] S. T. HOLFELTZ,[1] B. BUCCIARELLI,[1,3] I. N. EVANS,[1] R. GILMOZZI,[1,2] J. PRINGLE,[6] AND N. R. WALBORN[1]

Received 1994 January 14; accepted 1994 March 2

ABSTRACT

We present the results of the first high angular resolution observations taken with a Fine Guidance Sensor (FGS) aboard the *Hubble Space Telescope* (*HST*) of a star cluster embedded in very bright background. The strong and complex background around the R136 cluster in the 30 Dor nebula does not prevent the FGS from achieving performance close to its angular resolution limit of approximately 0".015 per axis with reliable photometry. These FGS observations establish that the central object in R136a is a triple star with the third component $\Delta V = 1.1$ mag fainter than the primary star a1 $\sim 0''.08$ away. We estimate from the grid of models of Maeder (1990) that the present mass of a1 is between 30 and 80 solar masses, with the main-sequence progenitor between 60 and 120 solar masses.

Subject headings: Magellanic Clouds — stars: early-type — stars: luminosity function, mass function — stars: Wolf-Rayet — techniques: interferometric

1. INTRODUCTION

The establishment of an upper mass limit for individual stars remains an open question of great importance in astronomy. Its resolution will influence the studies of the evolution of stars, H II regions, and galaxies. Observations of the giant H II region 30 Doradus have provided some of the best candidates for the most massive stars. In this *Letter*, we report on high angular resolution observations of the bright core of the massive star cluster R136 within 30 Doradus, R136a, which had for many years been unresolved and whose structure and photometry are still not fully explored.

The measurements were performed using the TRANSfer Mode of the Fine Guidance Sensor 3 (FGS3) as part of the FGS Cycle 3 Calibration program. We have detected 10 sources within 1", with a resolution of approximately 0".015 per axis. Accurate astrometry (to $\sim 0''.010$ or better in separation and $\sim 1°$ in position angle) and new V-band photometry (to 0.1 mag, internal error) are provided for most of these components. The mass of the brightest component of R136a, based solely on the FGS photometry of the resolved stars, is estimated.

2. TECHNIQUE AND MEASUREMENTS

Bradley et al. (1991) and Taff (1990, 1991) provide a detailed description of the FGS optical system, operating modes, and calibration principles. The FGS measurements consist of 10 identical position angle, consecutive scans, each 2".1 long with a step size of 0".0006, through R136a. The Transfer Function (TF) refers to the fringe visibility pattern produced by the Koester's prism-based interferometers inside the FGS when the $5'' \times 5''$ instantaneous field-of-view (FOV) is scanned across an object. A polarizing beam-splitter before the prisms provides sensitivity in two orthogonal directions, referred to as the X and Y directions in detector space. The fringe is detected by two pairs of photomultipliers (PMTs), one pair per axis. We can regard the $X(Y)$ scan as driving a slit of the size of the resolution limit in $X(Y)$ and 5" wide in the $Y(X)$ direction along the scan path. The TFs of the reference single star used as a template in this study are shown in Figure 1. Another object appearing anywhere in the rectangular slit has the same projected $X(Y)$ coordinate, within the resolution limit, as that of the primary target. The resulting fringe will have an amplitude that is the sum of the two individual fringe amplitudes.

The actual geometry of the scans is shown in Figure 2. The star field is that of the high-resolution FOC F/288 image discussed by Weigelt et al. (1991, page L22). The orientation of the detector axes as projected onto the plane of the sky is also shown. "Actual Scan" defines the path of the center of the FGS FOV as it moved across the star field, while "Center of Scan" identifies the location to which the center of the FOV was commanded at the end of the acquisition procedure. A pointing bias of about 0".5 (subsequently removed from the acquisition procedure) is evident. However, given the large FOV, this bias did not prevent the observation from being successful, although in consequence the X, but not the Y, scan fell short of reaching stars a3 and a6. The scan direction makes a 45° angle to the X and Y axes (about 1".5 each in length).

The PMT integration time was 0.025 s. To increase the signal-to-noise ratio (S/N) 10 consecutive scans were taken and added together for a total exposure time of 10.3 minutes. Each individual scan has a S/N of about 3. Co-adding the scans together increases the S/N to ~ 11, consistent with the expected improvement of $\sqrt{10}$.

The spherical aberration of the primary combined with known FGS misalignments causes a reduction of the visibility function and adds spurious structures to the TF. Optimal sensitivity for detection in a complex region is obtained by using the PUPIL position in the filter wheel. This introduces a field stop into the beam that eliminates most of the aberration to the wave front by reducing by $\frac{1}{3}$ the effective mirror diam-

[1] Space Telescope Science Institute, 3700 San Martin Drive, Baltimore, MD 21218.
[2] Affiliated with the Space Sciences Department, ESA.
[3] On leave from Osservatorio di Torino.
[4] Astronomy Programs, Computer Sciences Corporation at Space Telescope Science Institute.
[5] Department of Physics and Astronomy, the Johns Hopkins University.
[6] Institute of Astronomy, Madingley Road, Cambridge, CB3 0HA, England.

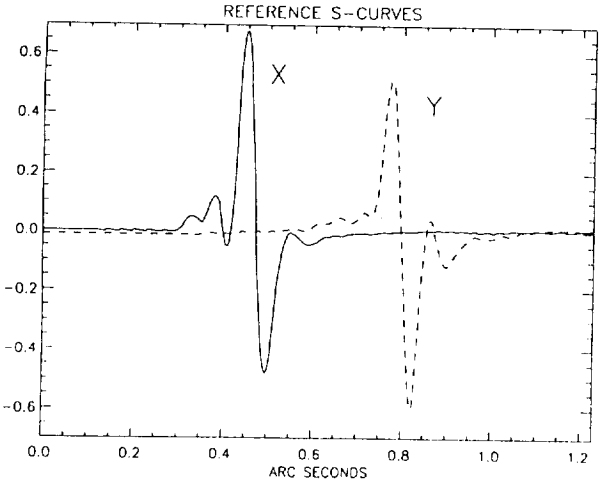

FIG. 1.—Normalized Transfer Functions (TFs) of the reference single star Upgren 69 taken through the PUPIL filter. The thick curve labeled X refers to the *X*-axis TF; the dashed curve represents the *Y*-axis TF. Note that the relative peak-to-peak amplitude is ~1.1 for both TFs.

eter. Although angular resolution is formally reduced by $\frac{1}{3}$, we observed R136a with the PUPIL.

An accurate photometric calibration of the PUPIL filter has not been carried out by the observatory. A careful comparison of the throughput of the FGS with the PUPIL and with the F583W (clear) filter shows that the bandpasses are quite similar (Abramowicz-Reed 1994), with the blue cutoff at ~4600 Å defined by the FGS relay optics and the red cutoff at ~7000 Å defined by the S20 cathode. We have, therefore, adopted for use with the PUPIL the effective wavelength of 5830 Å, bandpass of 2340 Å, and the carefully calibrated transformation to Johnson-*V* for the F583W filter determined by Bucciarelli et al. (1994). This calibration shows that, for hot stars, the color correction would amount to less than 0.05 mag.

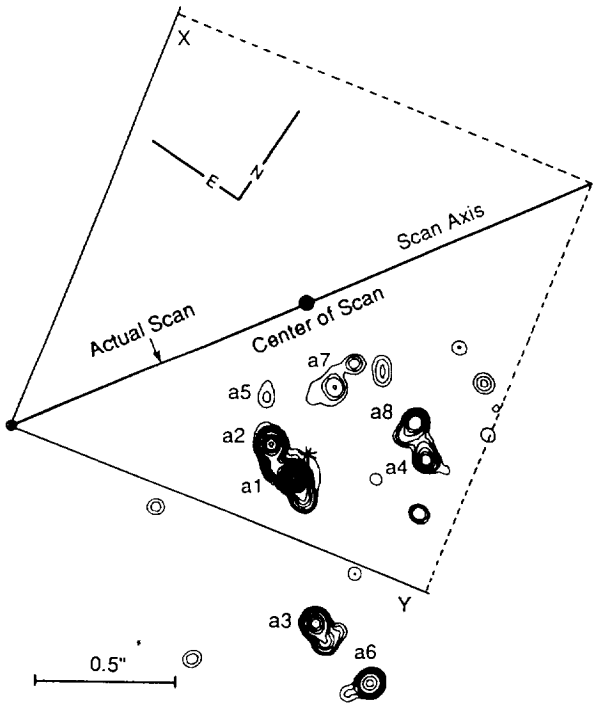

FIG. 2.—Overlay of the geometry of the FGS scan with the F/288 FOC image of Weigelt et al. (1991). The figure shows the innermost 1".7 × 1".7 of the 30 Dor core. The location of the new component a1B is denoted by an asterisk(*).

Although the algorithms described in Hershey (1992), Lattanzi et al. (1992), and Bernacca et al. (1993) for measuring double stars must be modified to deal with the complexity of R136a, the basic technique remains unaltered. Simply, the measurement of separations and magnitude differences of multiple component objects is performed, as for double stars, by measuring the departures of the corresponding TFs from the template TFs of a reference single star. The *X* and *Y* template TFs shown in Figure 1 were taken with the PUPIL on our reference single star Upgren 69 in NGC 188 (see Bernacca et al. 1993 and references therein) and are closest, both in time and in detector space, to the observations of R136a. The procedure described in Lattanzi et al. (1992) has been generalized as follows. A set of equal brightness and equally spaced single-star TFs are "placed" on a scan. The location of the first component is shifted stepwise while the others are kept fixed and a synthetic TF model is calculated at every step. The least-squares minimum in the residual curve TF(model)–TF (observed) yields the best location for the current star. With the star fixed at this location, a new minimum is searched for by varying the intensity of this star relative to the others. Relative intensity and position fully characterize the contribution of this component to the model scan. After going through all the components initially placed on a scan, the procedure is iterated to make sure that a global minimum is found. Final inspection of the residuals reveals if more components are necessary at particular locations along the scans, in which case, the program is restarted from the beginning. Twenty-four stars were used in this investigation. Figures 3*a* and 3*b* show the results for the *X* and *Y* scans, respectively. The thick curves represent the observed TFs, and the dashed lines superimposed are the residual curves. The locations and relative amplitudes, proportional to the relative brightnesses, of the "spikes" appearing on the abscissas represent the solutions of our adjustments. The dashed curves shown in the bottom part of Figures 3*a* and 3*b* represent the result of applying Hershey's (1992) deconvolution technique to the *observed* TFs. There is quite good agreement between this independent method and the other solutions. As expected, Hershey's deconvolved TFs generally overlay the locations and the relative amplitudes of the set of point source positions deduced from the synthetic TF method. At this stage, local variations must be attributed to the limitations of the present implementation of the synthetic TF method, as the deconvolved TFs contain all the information of the co-added scans.

3. RESULTS AND THE MASS OF R136a1 REVISITED

The unambiguous identification of components a1 and a2 from our solution is simple, since they are the closest, most luminous pair of objects in the field. The finite resolving power of the instrument, and the crowded field, make the firm identifications of the remaining sources on the sky impossible (see § 2). Even two independent directions will not solve the problem, although for a given resolution limit there is a minimum non-redundant set that will. Alternatively, we can use images of comparable resolution to help establish the identifications. Thanks to the extensive observational campaign in this field with the FOC and the PC during the last three years, we now have images that can be used for this purpose. The identifications shown in Figures 3*a* and 3*b* combine the results of pro-

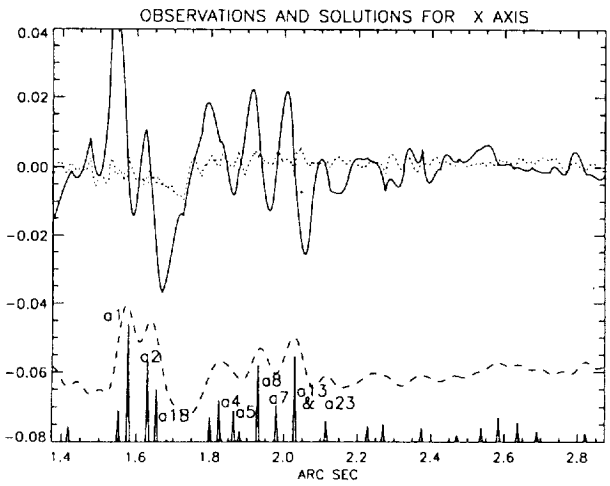

FIG. 3a

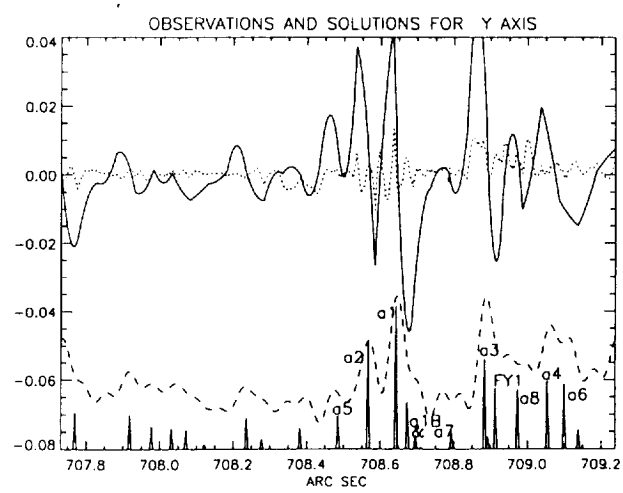

FIG. 3b

FIG. 3.—The results of interpreting the 30 Dor signal on the X (a) and Y (b) axes. Thick curves are the normalized observed TFs, dotted lines are the residual curves, and dashed curves are the profiles generated from the deconvolution of the TFs. The low peak-to-peak amplitude of these TFs, compared to those of Fig. 1, is due to the very high background which depresses the fringe visibility of the stellar sources. The position and relative amplitude of the spikes on the abscissa represent the individual stellar components from our adjustments. The amplitude of the spikes is proportional to the relative brightness of the components. Only the sharpest features are identified (see text).

jecting the FOC f/288 image discussed in Weigelt et al. (1991) and the F368M PC image of Campbell et al. (1992, plate 115) onto the FGS X and Y axes. For this *Letter*, we have limited the identifications to the "classical" eight objects of Weigelt & Baier (1985) and to new components which appear as close companions of some of them. This is justified since our simulations show that, in excess of the 99.7% confidence level, no spike with a relative amplitude above 0.015 can be spurious.

Table 1 lists separations (ρ), position angles (PAs) (J2000 equinox), and magnitude differences (ΔV Johnson per axis and average) with respect to star a1, according to the identifications given in Figures 3*a* and 3*b*. The ρ's and the PAs have been derived from the projected separations reported in detector space in Table 1 (detector space is a double, north-south and east-west, reflection of the FGS axes shown in Fig. 2). For components a3 and a6 we have only the Y scan, as mentioned earlier in § 2. The location on the sky of component a1B is marked with an asterisk (*) in Figure 2. This new component of the a1-a2 system is about 1.1 mag fainter than a1 and 0".08 away from it. On the Y scan, a7 is partially aligned with the a1-a2 system (as seen on the FOC and PC images). According to the X scan magnitudes, a7 is 0.4 mag fainter than a1B. This explains the less satisfactory quality of the fit near the spikes identified as "a1B and a7" on the Y scan (Fig. 3*b*) when compared to the residuals near the X-scan spike of a1B, but the magnitude difference is still consistent between the two axes. A third component is also in Campbell et al. (1992; see their star number 9 in Table 2) but not in Weigelt et al. (1991) or in the most recent ground-based speckle work at $\lambda \sim 7000$ Å by Pehlemann, Hoffman, & Weigelt (1992). Component a9 given in Campbell et al. (1992) has an F555W magnitude comparable to that of stars a1 and a2, while we see a somewhat fainter star, and the PA in Campbell et al. (1992) is significantly different from that of component a1B reported here. The smallest projected separation resolved here is ~0".025 between a1B and a2, which is consistent with the 0".015 resolution limit established through Monte Carlo simulations (Lattanzi et al. 1992).

TABLE 1

THE STELLAR CONTENT OF R136a

	SEPARATIONS				MAGNITUDES		
IDENTIFICATION	Δx	Δy	ρ	PA	ΔV_x	ΔV_y	$\langle \Delta V \rangle$
1	...	...	...	...	...	...	...
2	0".05	−0".08	0".09	66°	0.4	0.3	0.4
1B	0.08	0.03	0.08	349	0.9	1.2	1.1
3	...	0.24	...	...	...	0.5	0.5
FY1	...	0.27	...	...	...	0.9	0.9
4	0.25	0.41	0.48	312	1.1	0.8	1.0
5	0.29	−0.16	0.33	40	1.4	1.6	1.5
6	...	0.46	...	...	...	0.9	0.9
7	0.40	0.03	0.40	7	1.3	1.2	1.3
8	0.35	0.33	0.48	328	0.5	1.0	0.8

Campbell et al. (1992) list a10 and a11 as close companions of a3 and a6, respectively. FY1 is our candidate for a10, although the FGS photometry is ~0.7 mag brighter. The projection of the field is particularly crowded in that portion of the Y scan, and in the absence of an X scan (which would yield a much clearer signal in this case) we expect a larger error in our photometry. Therefore, FY1 is most likely Campbell et al's object a10. As for a11, we see a component in our Y-axis solution at about 709".138 (Fig. 3*b*), about 0".040 away from a6, consistent with the total separation given in Campbell et al. (1992) (~0".070). However, a11 is 0.5 mag brighter than a6 according to the PC photometry, and our candidate for a11 is 1.3 mag fainter than a6, which is fainter than the mag limit of interest here. Components a4 and a8 are clearly resolved with a separation of 0".13. Star a8 has the largest discrepancy between ΔV_X and ΔV_Y with ΔV_Y probably with a larger error as the X-scan solution shows better agreement between the synthetic method and the deconvolved TF. Finally, the sharp spike at 2".029 seen on the X-axis is identified as "a13 and a23." The FOC and PC images show that it is an almost perfect chance alignment (a12 of Campbell et al. 1992 is also included) of stars of comparable magnitude as discussed in § 2. In Campbell et al. (1992) a13 and a23 are about the same F555W magnitude, and a12 is ~0.5 mag fainter. In the case of perfect alignment, we can predict from the F555W PC data and the discussion in

§ 2 that the three stars together would appear only 0.2 mag fainter than a1. The value from the X-axis solution for "a13 and a23" is 0.36 mag, giving us added confidence in our technique.

Following the discussions of Walborn (1984, 1986), we adopt the values of $V_0 - M_V = 18.6$ (Panagia et al. 1991), $A_V = 1.2$ (Savage et al. 1983), and $V(\mathrm{a}) = 10.77$ for the integrated magnitude of R136a (Schmidt-Kaler & Feitzinger 1981). The relative magnitudes in Table 1, although generally consistent with previous work, do show significant differences. Thus, they provide new material with which to estimate the mass of R136a1. These numbers imply $M_V(\mathrm{a}) = -9$ for R136a. Recently, De Marchi et al. (1993) have used $A_V = 1.39$ and $V \sim 11$. These values yield almost exactly the same number for $M_V(\mathrm{a})$. From the photometry in Table 1 we derive $V(\mathrm{a1}) - V(\mathrm{a}) = 1.75$, implying $M_V(\mathrm{a1}) = -7.25$. Campbell et al. (1992) have established that component a1 is a W-R star. Moffat, Seggewiss, & Shara (1985; see also Walborn 1973) classify the R136a complex as being no later than type WN6. A lower limit for the luminosity of a1 is set by adopting the bolometric correction (BC) for type WN6, BC $= -3.6$ (Schmidt-Kaler 1982). We obtain $M_{\mathrm{bol}}(\mathrm{a1}) = -10.85$ and $\log (L/L_\odot) = 6.24$ ($\log T_e = 4.59$). By assuming spectral type WN3, the upper limit for the luminosity is $M_{\mathrm{bol}}(\mathrm{a1}) = -11.69$ (BC $= -4.4$) and $\log (L/L_\odot) = 6.58$ ($\log T_e = 4.70$).

Using Maeder's models (1990) for solar metallicity, these luminosities imply a present-day mass between 40 and 70 $M_\odot$, main-sequence progenitor mass between 60 and 120 $M_\odot$, and age between 3.6 and 2.6 Myr. Since the metallicity of the LMC is lower than the Galaxy's, we also adopt a metallicity of 0.25 $Z_\odot$ as in De Marchi et al. (1993). In this case, Maeder's models predict a present-day mass between 30 and 80 $M_\odot$, main-sequence progenitor mass between 60 and 120 $M_\odot$, and age between 4.4 and 2.8 Myr. These values are the lowest for the direct mass determination of a1 and are consistent with the limits derived from isochrone fitting of UV color-magnitude diagrams (De Marchi et al. 1993). We note that ground-based spectroscopy favors the WN6 classification for a1 and therefore the lower limit on the mass. Finally, the potential exists that a1 could reveal itself as a multiple star below the FGS limit of 1000 AU at the distance of the LMC.

4. CONCLUSIONS

In this *Letter* we have presented the first FGS interferometric observation of a crowded field embedded in high background. This observation resulted in a new mapping of the R136a cluster with 0".015 resolution per axis and V photometry to 0.1 magnitude. We provide evidence for a third component, a1B, within the a1-a2 system with a separation of 0".08, or a distance of approximately 4000 AU from a1. Finally, our photometry indicates that the range for the present mass of the W-R star R136a1 is between 30 and 80 $M_\odot$, with a main-sequence progenitor between 60 and 120 $M_\odot$. We stress that these are global upper limits, since a1 could still be a multiple system with separations less than 1000 AU.

Based on observations with the NASA/ESA *Hubble Space Telescope* (*HST*), obtained at the Space Telescope Science Institute, which is operated by the Association of Universities for Research in Astronomy, Inc., under NASA contract NAS 5-26555. Supported in part by NASA grants NAGW-2597 and CW-0016-92. R. B. is partially supported by NASA grant NAGW-2509. I. N. E. is supported partially by NASA grant NAG 5-1630. We are grateful to P. Bely, H. Burg, and F. Paresce for very useful discussions and comments all throughout this work. We wish to thank F. Macchetto and P. Stockman for their careful reviews during the preparation of the calibration observations. Finally, we wish to thank the members of the *HST* Astrometry Team (led by W. Jefferys) for stimulating discussions during their regular meetings.

REFERENCES

Abramowicz-Reed, L. (HDOS) 1994, private communication
Bernacca, P. L., et al. 1993, A&A, 278, L47
Bradley, A., Abramowicz-Reed, L., Story, D., Benedict, G., & Jefferys, W. 1991, PASP, 103, 317
Bucciarelli, B., Holfeltz, S. T., Lattanzi, M. G., Taff, L. G., & Vener-Saavedra, P. C. 1994, PASP, in press
Campbell, B., et al. 1992, AJ, 104, 1721
De Marchi, G., Nota, A., Leitherer, C., Ragazzoni, R., & Barbieri, C. 1993, ApJ, 419, 658
Hershey, J. L. 1992, PASP, 104, 592
Lattanzi, M. G., Bucciarelli, B., Holfeltz, S. T., & Taff, L. G. 1992, IAU Colloq. 105, Complementary Approaches to Double and Multiple Star Research, ed. H. A. McAlister & W. I. Hartkopf (ASP Conf. Ser., 32), 377
Maeder, A. 1990, A&AS, 84, 139
Moffat, A. F. J., Seggewiss, W., & Shara, M. M. 1985, ApJ, 295, 109
Panagia, N., Gilmozzi, R., Macchetto, F., Adorf, H.-M., & Kirshner, R. P. 1991, ApJ, 380, L23
Pehlemann, E., Hoffman, K.-H., & Weigelt, G. 1992, A&A, 256, 701
Savage, B. D., Fitzpatrick, E. L., Cassinelli, J. P., & Ebbetts, D. C. 1983, ApJ, 273, 597
Schmidt-Kaler, T. 1982, in Landolt-Börnstein, Numerical Data and Functional Relationships in Science and Technology, Vol. 2B, ed. K. Schaifers & H. H. Voigt (Berlin: Springer), 452
Schmidt-Kaler, T., & Feitzinger, J. V. 1981, ESO Workshop on the Most Massive Stars, ed. S. D'Orico, D. Baade, & K. Kjar (Garching: ESO), 105
Taff, L. G. 1990, ApJ, 365, 407
———. 1991, Adv. Space Res., 11, 97
Walborn, N. R. 1973, ApJ, 179, 517
———. 1984, IAU Symp. 108, Structure and Evolution of the Magellanic Clouds, ed. S. Van der Bergh & K. S. de Boer (Dordrecht: Reidel), 243
———. 1986, IAU Symp. 116, Luminous Stars and Associations in Galaxies, ed. C. W. H. de Loore, A. J. Willis, & P. Laskarides (Dordrecht: Reidel), 185
Weigelt, G., & Baier, G. 1985, A&A, 150, L18
Weigelt, G., et al. 1991, ApJ, 378, L21

THE ASTROPHYSICAL JOURNAL, 418:804–811, 1993 December 1

HUBBLE SPACE TELESCOPE OBSERVATIONS OF PLANETARY NEBULAE IN THE MAGELLANIC CLOUDS. I. THE EXTREME TYPE I SMP 83/WS 35

MICHAEL A. DOPITA,[1] HOLLAND C. FORD,[2] RALPH BOHLIN,[2] IAN N. EVANS,[2] AND STEPHEN J. MEATHERINGHAM[1]

Received 1993 March 15; accepted 1993 May 17

ABSTRACT

We have obtained *Hubble Space Telescope* Planetary Camera images in both the Hα and the [O III] λ5007 emission lines of the planetary nebula SMP 83 alias WS35, alias N66 in the Large Magellanic Cloud. By combining these results with optical and UV spectrophotometry, absolute flux measurements, and dynamical and density information, we have been able to construct a fully self-consistent nebular model. This proves that SMP 83 is an extremely massive type I object having a central star having an effective temperature of 170,000 K and a luminosity of nearly $3 \times 10^4\ L_\odot$. The core mass is estimated in the range 1.0–1.2 $M_\odot$, for which the main-sequence mass was greater than $\sim 6\ M_\odot$. The nebular abundances are higher than the average for the LMC and show evidence for hot-bottom burning.

Subject headings: Magellanic Clouds — planetary nebulae: individual (SMP 83)

1. INTRODUCTION

The mass boundary between stars that evolve to Type I supernovae and those that evolve off the asymptotic giant branch (AGB) through the planetary nebular (PN) stage is still poorly determined. For this reason, the identification of planetary nebular nuclei (PNNs) that have evolved from the most luminous AGB stars is rather important. Such objects are rare, however, because the rate of evolution through the PN stage becomes much higher as the mass of the PNN increases, and the effect of this is to give a rather sharp cutoff in the luminosity function of PN corresponding to a core mass of about 0.7 $M_\odot$ in the Large Magellanic Cloud (LMC) (Dopita & Meatheringham (1991a, b). Indeed, the existence of such a cutoff in the luminosity function is the basis of the use of PN as standard candles (Ciardullo et al. 1989; Jacoby, Walker, & Ciardullo, 1990; Dopita, Jacoby, & Vassiliadis 1992).

In this paper we describe the results of imaging of a particular PN in the LMC, WS 35 in the catalog of Westerlund & Smith (1964), or SMP 83 in the catalog of Sanduleak, MacConnell, & Philip (1978). This PN was selected by the GTO team for observation with Planetary Camera (PC) of the *Hubble Space Telescope* (*HST*) on the basis of its extreme velocity of expansion and other characteristics, in particular its type I (nitrogen-rich; Peimbert 1978) nature strongly suggested that it may be a PN with a rather massive central star (Dopita, Ford, & Webster 1985). We have been able to combine the results of this imaging with the published optical and UV spectrophotometry to generate a self-consistent photoionization model. This allows us, for the first time, to place this object on the Hertzsprung-Russell diagram with reasonable accuracy and we have been able to prove that WS35/SMP 83 is indeed a PN whose central star has a mass close to the Chandrasekar limit.

[1] Mt. Stromlo and Siding Springs Observatories, Institute of Advanced Studies, The Australian National University, Private Bag, Weston Creek P.O., ACT 2611, Australia.

[2] Space Telescope Science Institute, Homewood Campus, Johns Hopkins University, Baltimore, MD 21218.

2. RESULTS OF *HST* IMAGING

2.1. *Observations and Data Processing*

The PN WS35/SMP 83 was observed with the Planetary Camera (PC) of *Hubble Space Telescope* (*HST*) on 1991 May 11 as part of the GTO program. Sequential exposures of 300 s were taken in the Hα line and in the [O III] λ5007 line. The filters employed were the F664N and the F502N, respectively. The wavelengths of the peak transmission and FWHM bandpasses of these filters are 5016, 30 Å and 6634, 132 Å, respectively. The PN was placed on the PC6 chip.

The STSDAS task CALWFPC was used to reprocess both images with the best available bias subtraction and flat-field correction available on 1992 May 5. In order to deconvolve the data, a 256 × 256 pixel subimage centered on WS35 was extracted and cleaned of cosmic-ray hits. A standard Lucy (1974) deconvolution was done using 50 and 100 iterations. Since the point-spread function (PSF) had not been explicitly determined by calibration observations with these filters, the PSF used in the deconvolutions was computed from the *HST* optical model in the code TINYTIM (Krist 1992). We found that, owing to the low signal levels of these observations, 100 iterations tended to amplify noise features and artifacts in the image. Part of this may be the result of the inadequacies of the PSF model.

2.2. *Results*

We show in Figure 1*a* the original F502N and F664N images of WS35 and in Figure 1*b* the images deconvolved using the Lucy algorithm. Inset on the Hα images we show the image of a star which is seen on the original frames at a radial distance of approximately 4″.9 from the nebula. This should therefore be quite a fair approximation to the point-spread function (PSF) at the time of the observation. The improvement in the PSF is quite apparent, and it is clear that the deconvolution procedure has produced no important artefacts in the PSF. All of the features seen in the deconvolved image can be seen in the original image, though at lower contrast because of smearing effects of the spherical aberration. There are two bright filaments, which we have labeled A and B in

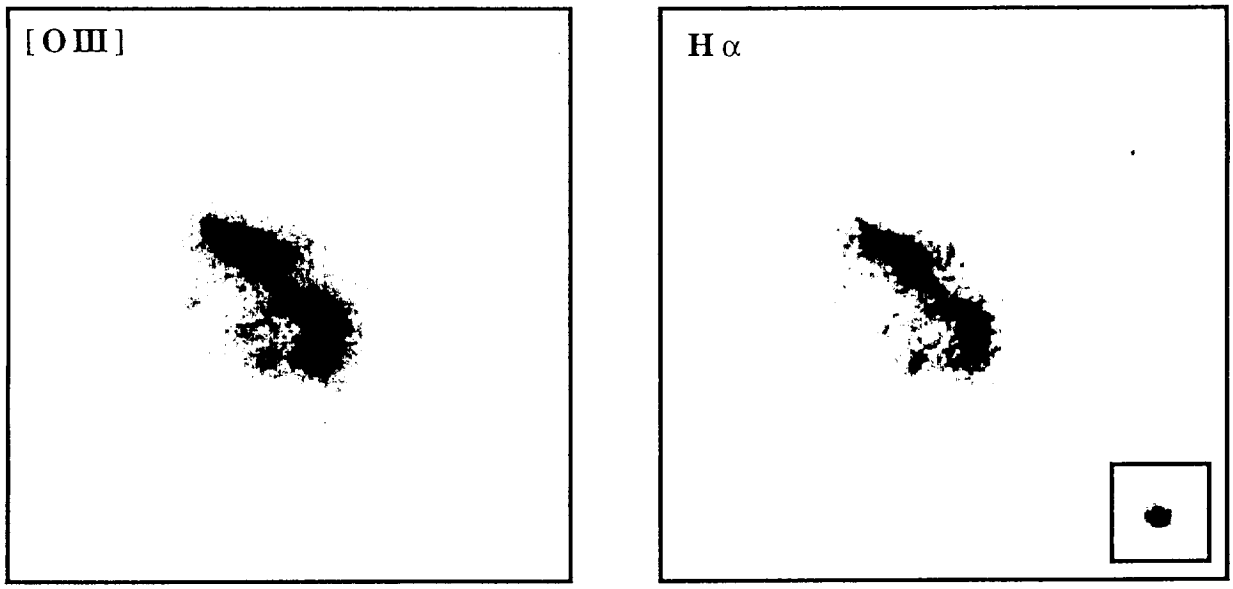

FIG. 1*a*

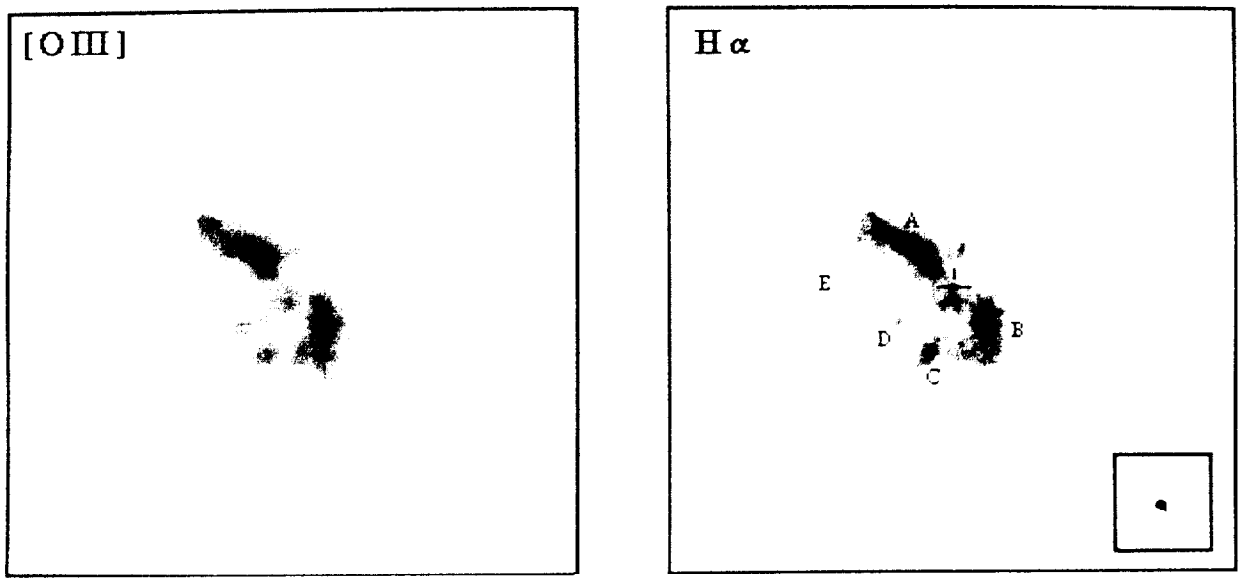

FIG. 1*b*

FIG. 1.—(*a*) The processed [O III] λ5507 and Hα PC images of SMP 83 (alias WS 35, alias N66). Each image is 5.5 arcsec^2. The inset is the Hα image of a star 4".8 away and gives a good idea of the PSF at this wavelength. North is in PA 45°, and east is to the right in this figure. (*b*) As (*a*), but after deconvolution through the Lucy (1974) algorithm. Note the improvement in the PSF. The principal filaments refered to in the text are marked, as is the position of the exciting star.

Figure 1*b*, and three fainter filaments labelled C, D, and E. All of the structures seen in Figure 1 can also be seen in the somewhat deeper [O III] λ5007 Faint Object Camera image of WS35 published by Blades et al. (1992). However, this image emphasises the fainter filamentary extensions to the image which are weakly visible in our [O III] image. These features are relatively stronger in the [O III] image, suggesting that this material is optically thin to the ionising radiation.

The Blades et al. images also allow us to unambiguously identify the exciting star, identified by a cross in Figure 1*b*. The fact that this is also detected in our Hα image allows us to measure the flux of this star by reference with the (known) Hα flux of the nebula. Using the filter transmission curve given in the WF/PC Instrument Handbook, we find that 61.2% of the observed nebular flux is due to Hα, the rest being [N II] emission. From the ratio of observed counts, we measure a stellar flux of $2.07 \pm 0.8 \times 10^{-17}$ ergs cm^{-2} s^{-1} Å^{-1} at Hα. This will be used (below) to determine the luminosity of the star directly.

Approximately 45% of the total observed [O III] λ5007 flux is produced by the two brightest filaments. The overall bipolar "butterfly" appearance of the nebula is similar to galactic PNs such as those illustrated in Balick's (1989) paper as examples of "late-type" "ellipticals" or "butterflies." It is also similar to type I PNs in our own Galaxy such as NGC 6302 or NGC 6537. In particular, the structure of the nebula is very like the short-exposure image of He 2-111 (Webster 1978) and is

remarkably reminiscent of the *HST* image of NGC 2440 (Heap 1992), down to the two bright arcs, and the position of the exciting star with respect to these.

The morphology suggests that the nebula may consist of a partially equatorial ring and a bipolar extension. However, if WS 35/SMP 83 had the large faint lobes observed in He 2-111 or in NGC 2440, then it is highly unlikely that these would be detectable in our images, thanks to their low emissivity relative to the core. The existence of faint, radially directed streamers visible in the images suggests such giant lobes may exist. However, since they would extend over several arcseconds, they should be readily observable in images taken with a ground-based telescope. The [O III] images of Jacoby et al. (1990) show no such extension, and the measured size of the nebula, 1".3, corresponds fairly well to the total extent of the faint filaments seen in the *HST* images. Thus, if giant lobes exist, they must be of very low emissivity, and therefore optically thin.

All of the filaments are resolved with a characteristic full width at half-maximum of approximately 0".2. This corresponds to 1.4×10^{17} cm at the 49 kpc we have assumed as the distance of the LMC (Feast & Walker 1987; Feast 1988). This can be compared with the characteristic dimension of 2.4×10^{17} cm inferred from speckle interferometry (Wood, Bessell, & Dopita, 1986). This quantity was well determined, and what is presumably being determined here is the characteristic width of the bright knots seen in the *HST* images.

If we interpret the image as indicating that the brightest filaments lie on an arc of an equatorial ring, then the dimensions of this ring are as follows: inner radius, $0''.69 \pm 0''.08$ (4.8×10^{17} cm); outer radius, $1''.09 \pm 0''.08$ are (7.6×10^{17} cm); and inclination to the line of sight, $63° \pm 5°$. The fainter filaments can be traced out to a radial distance of 1".86 (1.3×10^{18} cm). These figures are adopted for the photoionization modeling described below.

2.3. *The Geometry of the Nebula and Its Expansion Age*

Three facts bear strongly on any attempt to model the geometry and kinematics of WS 35. First, the [O III] λ5007 line profile in WS35 is bimodal with two peaks separated by approximately 82 km s^{-1} (Dopita et al. 1985; Dopita et al. 1988). Second, the [O II] $\lambda\lambda$3726/3729 line ratio indicates an electron density of 2300 cm^{-3} density in the blue component of the line, which is slightly more than twice the density of 1100 cm^{-3} determined for the red component. Third, the mean velocity of the blue component, 232.5 km s^{-1}, is most likely the systemic velocity of the planetary, since this velocity is only 13.5 km s^{-1} greater than the systemic velocity at this position predicted by the rotation curve solution for the LMC presented by Meatheringham et al. (1988a) when we separate LMC PNs into two age groups according to their estimated core mass, we find that the young PNs like WS35 have a velocity dispersion of 15 km s^{-1} relative to this solution, consistent with that determined using the blue component of WS35. If, on the other hand, we had taken the systemic velocity of WS35 as the mean of the two components (278 km s^{-1}), then its systemic velocity would differ by some 59 km s^{-1} from rotation curve solution. Such a large value is very unlikely for a PNN having a relatively massive and short-lived progenitor. Finally, we note that the line profile shows that there is very little [O III] emission at this systemic velocity of the nebula.

If we make the physically plausible assumption that the high surface brightness filaments A and B are the high-density gas, then the remaining low surface brightness filaments are low-density, redshifted gas. This interpretation would then be fairly consistent with the fraction of the total emission seen in the filaments A and B. From the images, these give 45% of the total [O III] emission, whereas from the low-velocity part of the [O III] line profile accounts for 54% of the total emission. In this model filaments A and B represent optically thick material associated with a reservoir of unionized material near the equatorial plane, and the fainter filaments are part of an optically thin, high-velocity, one-sided polar flow.

A crude expansion age can be derived by dividing a characteristic size of the nebula by its expansion velocity. The filaments in our highly resolved image have a characteristic radial extent of approximately 1".5. If viewed through an angle θ relative to the plane of the sky, the expansion age will then be approximately $\tau = (r/V_{exp}) \tan \theta$. Adopting a radius of 10^{18} cm from the images, an expansion velocity of 82 km s^{-1} from the line profiles and $\tan \theta \sim 0.6$ estimated from the ring parameters given above, we have $\tau \sim 2400$ yr. This age estimate is capable of more subtle interpretation. If the reservoir of unionized material is massive and slow moving, then the velocity of expansion which is measured is the velocity of outflow of ionized gas from the ionization fronts, accelerated by its interaction with the stellar wind. Thus the timescale which is being measured here is the outflow timescale, which may be much less than the timescale for which the nebula has been in existence. However, if this were the case, we would expect to see ionized gas at large radial distance, for which there is no evidence. If, on the other hand, the bipolar flow has undergone acceleration, the above age estimate will be a lower limit to the age of the nebula.

Finally, an age estimate can be derived on the assumption that the velocity dispersion of the denser gas is determined by the expansion velocity of the ringlike structure identified in the images. Adopting 6×10^{17} cm for the ring radius, and an expansion velocity of 57 km s^{-1} given by the velocity dispersion of the [O III] line profile, we obtain an age of $\sim$3400 yr for the nebula. In the absence of a detailed spatiokinematic map, the differences between these various age estimates represents a true measure of our uncertainty in the nebular age.

3. PHOTOIONIZATION MODELING

3.1. *Model Fitting Procedure*

A high-quality global optical spectrum of SMP 83/WS 35 has been presented by Meatheringham & Dopita (1991a). This demonstrates that this object belongs to Peimbert's (1978) type I class, showing both high excitation and strong emission lines of nitrogen. We reproduce the observed spectrum in Table 2 to facilitate comparison with the models. An attempt was made by Dopita & Meatheringham (1991a, b) to model this and other type I PNs using the modeling code MAPPINGS I (Binette, Dopita, & Tuohy 1985) to compute spherically symmetric, isobaric nebulae excited by a central star having a blackbody spectral distribution. In general, the models for type I planetary nebulae show similar problems, as pointed out by Dopita & Meatheringham (1991a, b). In summary, these are as follows. First, the low-excitation lines are predicted to be stronger than observed. Second, the [O III] and [S III] electron temperatures are predicted too low (although electron temperatures defined through the use of species with lower excitation potential such as N II or O II are in good agreement with observation). Third, the models frequently strongly underesti-

mate the line intensities of high-ionization species such as [Ne v]. For the purposes of comparison, the specific parameters of the model given in Dopita & Meatheringham (1991a) are as follows. Central star luminosity and temperature; $L/L_{\odot} = 2880$; $T_{\rm eff} = 170{,}000$ K, nebular density $N(\rm H) = 2880$ cm^{-3} (at 10,000 K, isobaric model), inner nebular radius $r_{\rm in} = 5 \times 10^{16}$ cm and outer nebular radius, $r_{\rm out} = 3.8 \times 10^{17}$ cm. Clearly these sizes are inconsistent with the results of the nebular imaging.

When we consider the UV lines (Meatheringham et al. 1993) the comparison becomes even worse. Virtually all of the UV resonance and intercombination lines are predicted too weak by the simple photoionization model. These lines are mainly produced in the inner part of the nebula where the ionization parameter, Q, is high, requiring either a high stellar luminosity, or else a low nebular density. In the single-zone model, neither of these parameters can be attained, since the nebular luminosity is in this case coupled to the stellar luminosity, and the inner nebular radius is about as small as it can be in the model.

The solution to these problems is evident from the *HST* images. It is clear that a multizone photoionization model must be used to adequately represent the equatorial ring and its bipolar extensions. The simplest model is one of an optically thick ring with optically thin extensions such has been used with success by Clegg et al. (1987) to model NGC 3918. In the case of WS 35/SMP 83, this type of model should be adequate.

For the photoionization modeling presented here, we have used the improved photoionization/shock modeling code MAPPINGS 2 (Sutherland & Dopita 1993). Among the improvements relevant to this exercise, it includes all important ionization stages up to fully stripped Fe and Ni, has a much improved adaptive spatial gridding procedure, explicitly computes all nebular continua, and operates with a much extended and improved set of atomic parameters, particularly with respect to the resonance and intercombination lines.

We adopt a photoionization model (see Fig. 2) in which the global spectrum is the weighted mean of an optically thick component and an optically thin component of arbitrary optical depth; $F_{\rm tot} = \omega F_{\tau(\rm H)\to\infty} + (1-\omega)F_{\tau(\rm H)=\tau_0}$. The optically thick component is assumed to be isobaric and characterized by the pressure which reproduces the observed [O II] 3726/3729 Å line ratio for this component, $P/10^4$ K = 3600 cm^{-3}. This density also agrees well with that given by the observed [S II] $\lambda\lambda$6731/6717 line ratio. The nebula is assumed to have an inner radius of 4.5×10^{17} cm, the measured size. The optically thin component is taken to be isochroric with a density of 1000 cm^{-3}, given by the observed [O II] $\lambda\lambda$3726/3729 line ratio for this component. Since the optically thin gas is presumed to have its origin at the ionisation fronts of the dense material, it is assumed to have the same inner radius, 4.5×10^{17} cm. In a fully self-consistent model, the outer radii of the two components should also agree with what is indicated by the imaging. Apart from the abundances of the elements, the free parameters of the model are the flux-weighting factor ω, the optical depth of the optically thin component, the effective stellar temperature, $T_{\rm eff}$, and the ionization parameter Q(H). Thus, even within the context of such a simple model, the exercise of model fitting is by no means trivial.

Of these parameters, Q(H) and $T_{\rm eff}$ are particularly well constrained. A decrease in Q(H) produces a dramatic decrease in the relative strength of the high-ionization lines arising in the optically thin zone, particularly in the UV. In order to obtain strong enough high-excitation lines, we require $Q \geq 1.2 \times 10^8$ cm s^{-1} for this component. On the other hand, the physical thickness of the optically thick component varies directly as the ionization parameter, since this determines the Strömgren column. Models which produce the correct inner and outer radii in the optically thick component (4.5×10^{17} and 6.3×10^{17} cm, respectively) require a mean ionization parameter of about 10^8 cm s^{-1}.

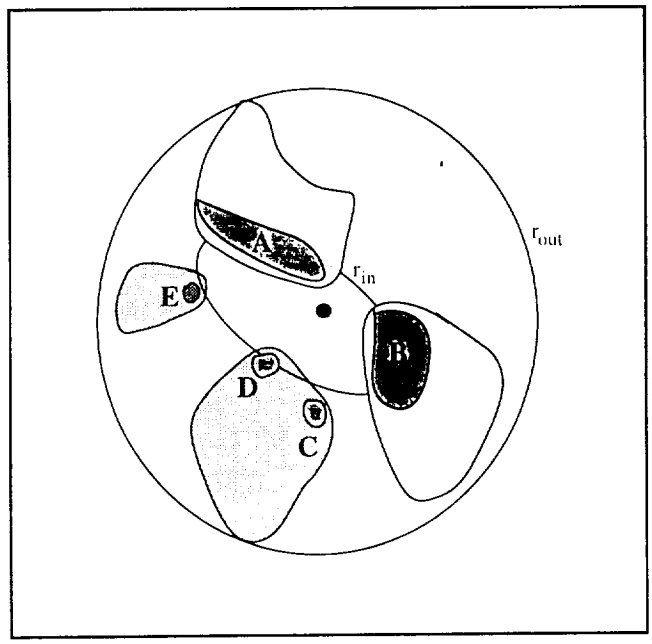

FIG. 2.—The idealized model used in the photoionization modeling. It is assumed that the filaments A to E (*shaded dark*) lie in a dense equatorial ring of radius $r_{\rm in}$ and that these are optically thick to the UV radiation. The ionized flow streaming from the ionization fronts in this ring forms a filamentary, optically thin region of lower density (*shaded light*). The dense component has ~6% covering factor, and the optically thin material a ~30% covering factor with respect to the central star.

The effective stellar temperature $T_{\rm eff}$ is constrained fundamentally by the ionization state of helium, and by the He II lines in particular, since the strength of these lines is effectively independent of the ionization parameter over the region of interest. However, the strength of these lines is dependent on the optical thickness of the nebula, since low optical depth leads to an enhancement of He II lines and a suppression of the He I lines. However, making the extreme assumption that the optically thin zone has negligible optical depth and assuming that the relative contributions of the optically thick and thin zones are equal (so as to be in accord with the imaging and the high-resolution spectrophotometry), we can obtain a lower bound on the temperature. An upper bound can be obtained by the (clearly incorrect) assumption that the nebula is entirely optically thick. These estimates constrain the temperature to lie in the narrow range 150,000 K $< T_{\rm eff} <$ 175,000 K.

Our modeling procedure is therefore to take $T_{\rm eff}$ as a free parameter within the limits given above, and choose the Q which gives the correct outer radius for the optically thick component in an isobaric model having the correct mean [O II] $\lambda\lambda$3726/3729 line ratio. We then construct the (isochoric) optically thin model which corresponds to these parameters, allowing for the lower density in this component. The optical depth is chosen so as to give an outer radius which agrees with total extent of the ionized material in the images (1.3×10^{18} cm). We then seek linear sums of the optically thin and opti-

cally thick models which produce as nearly as possible a constant ratio of observed to predicted line intensities over the full range of ionization states of a given element. If the abundance of an individual element is incorrect, then this will appear as an (approximately constant) offset in the ratio of observed-to-predicted line intensity over the whole range of ionization stages. The abundance can then be altered in a subsequent run so as to bring these ratios for that element to close to unity.

Within the constraints and assumptions of the two-component model itself, this procedure produces a fully self-consistent result, in that it agrees with the observed density and the physical size of the two components, and also gives the correct global line strengths and excitation state of the nebula.

3.2. *Results*

The parameters of our final model are given in Table 1, and the line intensities of this model are compared with the observations in Table 2. Here model M060 is the optically thin component, and M061, the optically thick component. The relative weighting factor ω, defined above, is found to lie between 0.6 and 0.4. This range encompasses the values determined above from the imaging and the [O II] and [O III] line profiles: 0.45 and 0.54, respectively. We adopt $\omega = 0.5$, close to the mean of these other estimates, and which gives the best-fit solution to the line spectrum. The weighted average spectrum which results is shown in the "Sum" column and is to be compared with the observed line fluxes of the final column of Table 2. Figure 3 shows the relative contributions of the optically thin and optically thick components to this best-fit solution for all the lines used in the fitting procedure. For this, we have used neither line blends nor the fainter of two lines with known intensity ratio such as the [O III] λ4959 or the [N II] λ6548 lines. This figure emphasises the need for both optically thin and optically thick components to achieve a satisfactory fit to the observations. In Figure 4 we plot the observed and the theoretical line intensities for each element over all observed ionization stages. As can be seen, the scatter is sufficiently small to give confidence that the elemental abundances have been determined to within $\pm 15\%$. Paradoxically, the worst fit is for the He lines, since we had to take the effective temperature near the upper limit of what is allowed by the

TABLE 1

MODEL PARAMETERS FOR SMP 83

A. INFERRED STELLAR PARAMETERS

Parameter	Value
$L/L_\odot$	27,000 ± 6000 (from nebular model) 32,000 ± 12,000 (from Hα image)
$M/M_\odot$	0.98 ± 0.17 (H-burning); ~1.2 (He-burning)
$T_{\rm eff}$	170,000 ± 10,000 K

B. ABUNDANCES OF THE ELEMENTS BY NUMBER WITH RESPECT TO H [error ~ 10%])

He	C	N	O	Ne	S	Ar
0.13	2.6E−5	1.15E−4	4.17E−4	5.10E−5	2.40E−5	2.80E−6

C. PROPERTIES OF NEBULAR COMPONENTS

Parameter	Value
Optically Thin Component:	
N(H)	1000 cm^{-3} (isochoric)
$r_{\rm in}$	4.5E17 cm
$r_{\rm out}$	7.5E17 cm
τ(H)$_{\rm final}$	1.94
$M_{\rm neb}$	0.4 $M_\odot$
Optically Thick Component:	
N(H)	3600 cm^{-3} (at 10,000 K; isobaric)
$r_{\rm in}$	4.5E17 cm
$r_{\rm out}$	7.0E17 cm
$M_{\rm neb}$	0.19 $M_\odot$

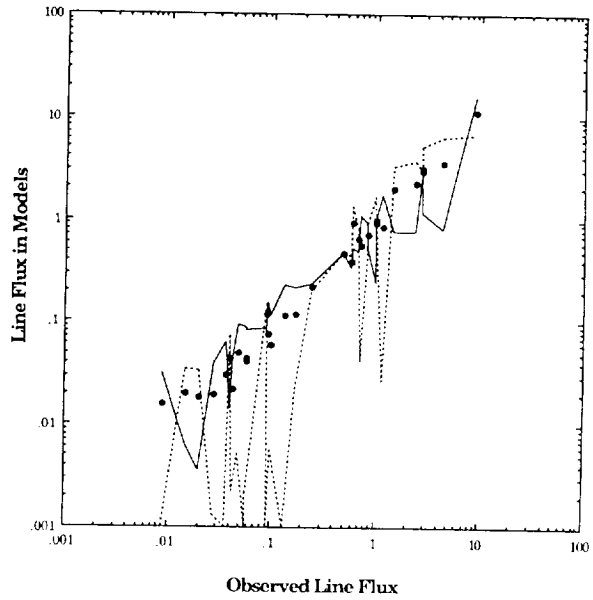

FIG. 3.—The emission-line flux predicted in the models is plotted against the observed line flux with respect to Hβ = 1.0 for all lines that are unblended, or which represent the brighter component of a doublet with known intensity ratio. The contribution of the optically thick component in the models is represented by a solid line, and that of the optically thin component by a dotted line. The weighted sum of these is represented by dots. Note how the two components complement each other in the global fit.

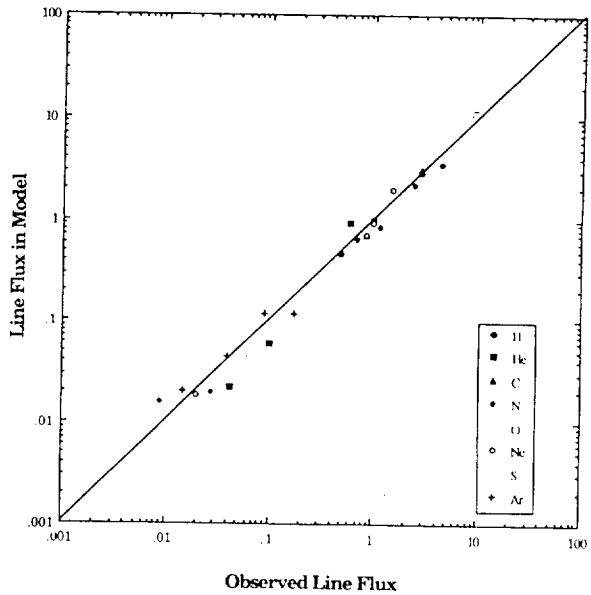

FIG. 4.—As Fig. 3, except that lines of each element are distinguished. It is clear that the accuracy of the fit approaches that of the observations, and that the elemental abundances have been determined to an accuracy of order 15%.

TABLE 2

OBSERVED AND MODELED LINE INTENSITIES WITH RESPECT TO Hβ = 100.0[a]

Ion	Wavelength (Å)	M0060	M0061	Sum	Observed
H I	4100	25.72	25.93	25.82	26.30
	4340	46.81	46.94	46.88	48.60
	4861	100.00	100.00	100.00	100.00
	6563	289.6	285.1	287.3	278.2
He I	4472	0.22	4.19	2.20	4.30
	5876	0.57	11.38	5.97	10.00
	6678	0.16	3.25	1.71	3.20
He II	4686	134.0	52.20	93.10	60.10
C III]	1909	91.44	52.10	71.77	85.00
C IV	1549	502.0	115.02	308.5	280.0
[N I]	5200	0.10	3.12	1.56	0.90
[N II]	5755	0.13	3.82	1.98	2.80
	6584	2.59	168.2	85.39	115.3
N III]	1750	81.34	48.79	65.07	68.00
N IV]	1487	363.2	75.78	219.5	243.0
N V	1245	616.3	80.94	348.6	444.0
[O I]	6300	0.10	8.73	4.37	5.70
[O II]	7325	0.21	8.09	4.15	5.80
	3727	4.08	106.6	55.34	73.20
O III	1666	43.71	33.55	38.63	59.00
[O III]	4363	20.10	23.76	21.93	24.30
	4959	225.1	546.5	385.8	313.3
	5007	648.4	1574.0	1111.2	896.0
[Ne III]	3868	50.14	90.66	70.40	84.90
[Ne IV]	2426	318.50	74.82	196.7	149.7
	4725	3.30	0.35	1.83	2.00
[Ne V]	3346	59.91	8.75	34.33	26.1
	3426	163.00	23.82	93.41	99.20
[S II]	4069.76	0.10	6.19	3.10	3.70
	6717	0.10	15.20	7.60	9.50
	6731	0.10	22.62	11.31	13.30
[S III]	6312	0.53	9.34	4.93	4.90
[Ar III]	7136	2.18	21.36	11.77	17.2
[Ar IV]	4740	14.94	8.55	11.74	9.00
[Ar V]	6435	3.40	0.65	2.03	1.50
[Ar V]	7006	7.30	1.39	4.34	4.00

[a] Arranged by element and ionization stage for unblended lines.

helium excitation in order to correctly reproduce the (high)-excitation state of the other elements. This is presumably the result of our assumption of a blackbody photon distribution for the central star. In reality, blanketing by heavier elements will tend to reduce the number of hard photons at a given effective temperature (Gabler, Kudritski, & Mendez 1991).

The flux of the central star is determined primarily by the density and the observed physical thickness of the optically thick component, since this is a direct measure of the Strömgren column. However, a more indirect estimate can be obtained from the observed Hβ flux. For SMP 83, the observed absolute Hβ flux, corrected for atmospheric absorption and interstellar reddening, is $\log F(\mathrm{H}\beta) = 34.90$ ergs s^{-1} (Meatheringham, Dopita, & Morgan 1988b). From the images, each bright arc is $\sim 0''.2$ wide and $\sim 0''.8$ long (1.4×10^{17} cm $\times$ 5.5×10^{17} cm). Thus the two of them subtend a solid angle not in excess of ~ 0.76 sr, or 6% of the solid angle, as seen from the central star. Thus, from the models, the optically thick component should have a luminosity of $\log F(\mathrm{H}\beta) = 34.18 + \log (L/10^4\ L_\odot)$ ergs s^{-1}. Since we require that this component account for half the total flux to fit the relative line intensities, we have $L \sim 2.6 \times 10^4\ L_\odot$, in good agreement with the value derived from the Strömgren column. For the optically thin material we can then infer an angular covering fraction of ~ 0.33. These figures provide the basis of the nebular mass estimates of Table 1. The sum of the nebular masses of the two components ($0.59\ M_\odot$) is similar to the mass estimate determined from the one-zone model, since both depend on the measured Hβ flux, but of course, our estimated luminosity of the central star is much higher, as a result of leakage of UV photons out of the nebula.

Provided that we can take the temperature of the central star to be given by the photoionization model, the observed flux of the central star, $2.07 \pm 0.8 \times 10^{-17}$ ergs cm^{-2} s^{-1} $Å^{-1}$ at Hα, can be used to directly determine the luminosity of the central star. From this we find $L/L_\odot = 32{,}000 \pm 12{,}000\ L_\odot$, in excellent agreement with that given by the model. We can therefore have considerable confidence that the position of the star on the H-R diagram has been reliably determined.

4. DISCUSSION

From the models presented in Tables 1 and 2, it is clear that the compound photoionization model removes the problems of the simple model as a result of the contribution of the high-

temperature optically thin component. The leakage of the stellar UV radiation from the nebula has a dramatic effect on our estimate of stellar luminosity, which increases by over an order of magnitude, from 2880 $L_\odot$ to somewhere in the range 1.9×10^4 to 3.5×10^4 $L_\odot$. Coincidentally, this estimate is much closer to that given by Dopita et al. (1985), although this was based on a spurious estimate of the Zanstra temperature. Whether the central star is hydrogen- or helium-burning, it is clear that it has a massive central star, which may even be approaching the Chandrasekar limit. The extreme position of this PN on the Hertzsprung-Russell diagram is made clear in Figure 5, in which we have also plotted the positions of all the other PNs placed on the H-R diagram by Dopita & Meatheringham (1991a, b).

The luminosity of the PNN depends upon whether it is on a H-burning or He-burning track, which in turn depends on the phase of the thermal pulse at which the transition to PN occurs. Dopita et al. (1992) argue that the distribution of the LMC PNNs on the Hertzsprung-Russell diagram strongly argues in favor of the hypothesis that the majority of these are helium-burners. For the hydrogen-burning objects, the core mass is well determined, since the evolution to high temperature occurs at an almost constant luminosity, L, which may be expressed in terms of the core mass (Wood & Zarro 1981; Dopita et al. 1992);

$$(L/L_\odot) = 57340[(M_c/M_\odot) - 0.507] \quad (4.1)$$

from which we can derive the core mass given in Table 2,

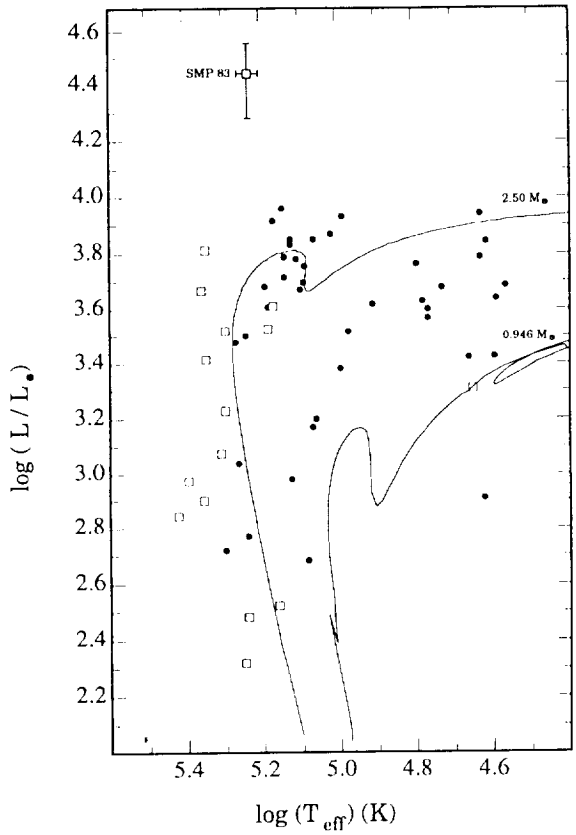

FIG. 5.—The H-R diagram for the PNs in the LMC (from Dopita & Meatheringham 1991b). Here type I PNs are shown as open squares. This clearly demonstrates the extremely luminous nature of SMP 83.

$M_c = 0.98 \pm 0.17$ $M_\odot$. If helium-burning, the core mass is somewhat more uncertain, since the luminosity is much more variable and sometimes multivalued as a function of temperature. However, at the high effective temperature observed, it should be fairly well determined and of order 1.2 $M_\odot$. Dopita et al. (1992) give the relation between the core mass M_c during the PN phase of evolution and the abundance and mass on the main sequence, M:

$$(M_c/M_\odot) = 0.493(Z/Z_\odot)^{-0.035}[1 + 0.147(M/M_\odot)] \quad (4.2)$$

This relation is sensitive to the treatment of mass loss on the asymptotic giant branch. From equation (4.2) we find $M = 6.4$ $M_\odot$ (if hydrogen-burning) and ~ 9 $M_\odot$ (if helium-burning). A lower mass limit for the precursor star can be obtained by simply co-adding the core mass and the mass of the ionized material. This gives $M \geq 1.6$ $M_\odot$ if the PNN is hydrogen-burning or $M \geq 1.8$ $M_\odot$ if helium-burning.

Given the high core mass, the rather long dynamic age (2500–3500 yr) inferred above presents somewhat of a problem. According to PNN evolutionary models (Wood & Faulkner 1986; Vassiliadis 1992), the evolution of hydrogen-burning central stars of this mass is exceedingly rapid. Indeed, such a star will remain luminous for only ~ 100 yr from the time that it becomes hot enough to start to ionize its nebula. The central star has an ionizing photon production rate of 1.4×10^{48} s^{-1}, so that it is capable of driving an ionization front into the cloud material at an initial velocity of ~ 1000 km s^{-2}. Therefore, the *minimum* ionization timescale, the time taken to ionize the dense material at the current stellar luminosity, is 100 yr and may be considerably longer than this, since the flow from the clouds is observed to be optically thick. If we wish to preserve the hypothesis that the central star is hydrogen-burning, we must therefore conclude that the cloud material has been ionized in situ, since it would have had no time to expand in the time available. If this were the case, then the cloud material would have to be identified with envelope material ejected during the last helium shell flash episode, $\sim 20{,}000$ yr ago, based on the observed radius, and an assumed outflow velocity of 10 km s^{-1}. If, on the other hand, the central star is helium burning, these problems are alleviated, since the central star evolves much more slowly and remains luminous for in excess of 1000 yr. Given the very short evolutionary timescales associated with the hydrogen-burning stars, we would expect to be able to see evolution of the central star within the lifetime of the *HST*, or detect such evolution over a few years from evolution in the spectral character of the PN.

The combination of the UV and optical spectra has permitted us for the first time to obtain a reliable set of abundances. The effect of the addition of an optically thin region has been generally to increase our earlier (Dopita & Meatheringham 1991a, b) estimates of the abundances. For the more massive α-process elements, Ne, Ar, and S, which ought not to be influenced by dredge-up processes in the central star, we find a basal metallicity 0.27 dex higher than the mean of the LMC H II regions and SNRs found by Russell & Dopita (1990, 1992). This is exactly consistent with the observed enhancement in the O abundance relative to the corresponding mean LMC value for the H II regions. Although we can draw no firm conclusions from a single object, this is nonetheless an indication that the apparent decrease in the O abundance found by Dopita & Meatheringham (1991b) may be an artifact of the modeling procedure, and not a result of O-N processing, as they suggested.

The elements He and N both show the enhancements expected in a type I object. In particular, the N abundance is much more reliably established, since all the principal stages of ionization are observable. The N/O abundance ratio of 0.28 is at the lower limit of what has been found for the type I PNs in the Magellanic Clouds which may suggest that the degree of N dredge-up may finally decrease for the most massive stars.

The low C abundance, assumed to pertain in type I PNs has been confirmed. However, this cannot be taken as concrete evidence dredge-up in the ejected envelope material. The C + N abundance is very similar to that which would be expected on the basis of the O, Ne, S, and Ar abundances. Thus, the observed C and N abundances are consistent with CN processing in the material that was already there, but little or no dredge-up of CN processed material is allowed. This suggests that "hot-bottom burning" (Kaler 1985) rather than dredge-up has determined the observed abundances of C and N in this planetary.

5. CONCLUSIONS

In this paper, thanks to images made by the *HST*, we have been able to produce the first fully self-consistent model for a Magellanic Cloud planetary nebula. This has proved that WS 35/N66/SMP 83 is the most luminous PN so far identified in the LMC. With a core mass of between 1.0 and 1.2 $M_{\odot}$, it is clearly derived from a main-sequence star which is near the upper mass limit of those which can finally evolve to white dwarfs. Indeed, in both the Magellanic Clouds, it is only surpassed by the nucleus of the type I PN N67 (SMP 22) in the SMC. This has been detected through the thermal emission of the central star at X-ray wavelengths, placing it at log $(L/L_{\odot}) = 4.6 \pm 0.7$; log $(T_{\rm eff}) \sim 5.5$ (Wang 1991).

The dynamical age we derive appears to be inconsistent with the age estimated on the hypothesis that the central star left the AGB as a hydrogen-burning star, suggesting that it may well be a helium burner.

The abundances we derive for the nebula show clear evidence for "hot-bottom burning" of C to N, but little evidence of dredge-up of CN processed material on the asymptotic giant branch and no evidence for ON processing hypothesised by Dopita & Meatheringham (1991b).

The results described in this paper are based on observations with the NASA/ESA *Hubble Space Telescope*, obtained at the Space Telescope Science Institute, which is operated by the Association of Universities for Research in Astronomy, Inc., under NASA contract NAS5-26555. We wish to acknowledge support through NASA grant NAG5-1630, and support through the International Science and Technology Section of the Australian Department of Industry Technology and Commerce. We thank D. J. Lindler who set up the procedure for reprocessing the data and provided the deconvolved images.

The Imaj software used to generate the final images published in this work are part of the "Scientific Data Handling Suite" software developed by (Ralph S. Sutherland) at MSSSO, with the support of a grant from the Australian Apple University Development Fund in 1992.

REFERENCES

Balick, B. 1989, in IAU Symp. 131, Planetary Nebulae, ed. S. Torres-Peimbert (Dordrecht: Kluwer), 83
Binette, L., Dopita, M. A., & Tuohy, I. R. 1985, ApJ, 297, 476
Blades, J. C., et al. 1992, ApJ, 398, L41
Ciardullo, R., Jacoby, G. H., Ford, H. C., & Neill, J. D. 1989, ApJ, 339, 53
Clegg, R. E. S., Harrington, J. B., Barlow, M. J., & Walsh, J. R. 1987, ApJS, 314, 551
Dopita, M. A., Ford, H. C., & Webster, B. L. 1985, ApJ, 297, 593
Dopita, M. A., Jacoby, G. H., & Vassiliadis, E. 1992, ApJ, 389, 27
Dopita, M. A., & Meatheringham, S. J. 1991, ApJ, 367, 115
———. 1991b, ApJ, 377, 480
Dopita, M. A., Meatheringham, S. J., Webster, B. L., & Ford, H. C. 1988, ApJ, 327, 639
Feast, M. W. 1988, in The Extragalactic Distance Scale, ed. S. van den Bergh & C. J. Pritchet (ASP Conf. Ser. 4), 9
Feast, M. W., & Walker, A. R. 1987, ARA&A, 25, 345
Gabler, R., Kudritski, R. P., & Mendez, R. 1991, in Stellar Atmospheres: Beyond Classical Models, ed. L. Crivellari, I. Hubeni, & D. G. Hummer (NATO ASI Series), 143
Heap, S. 1992, HST Photo Release, STSCI-PRC92-12
Jacoby, G. H., Walker, A. R., & Ciardullo, R. 1990, ApJ, 365, 471
Kaler, J. B. 1985, ARA&A, 23, 89
Lucy, L. B. 1974, AJ, 79, 745
Meatheringham, S. J., Aller, L. H., Keyes, C. D., Stecher, T. P., Maran, S. P., Michalitsianos, A. G., & Gull, T. R. 1993, in preparation
Meatheringham, S. J., & Dopita, M. A. 1991a, ApJS, 75, 407
———. 1991b, ApJS, 76, 1085
Meatheringham, S. J., Dopita, M. A., Ford, H. C., & Webster, B. L. 1988a, ApJ, 327, 651
Meatheringham, S. J., Dopita, M. A., & Morgan, D. H. 1988b, ApJ, 329, 166
Peimbert, M. 1978, in IAU Symp. 76, Planetary Nebulae, ed. Y. Terzian (Dordrecht: Reidel), 215
Russell, S. C., & Dopita, M. A. 1990, ApJS, 74, 93
———. 1992, ApJ, 383, 508
Sanduleak, N., MacConnell, D. J., & Philip, A. G. D. 1978, PASP, 90, 621 (SMP)
Sutherland, R. S., & Dopita, M. A. 1993, ApJS, 88, 253
Vassiliadis, E. 1992, PhD thesis, The Australian National University: Canberra
Wang, Qingde. 1991, MNRAS, 252, 47P
Webster, B. L. 1978, MNRAS, 185, 45P
Westerlund, B. E., & Smith, L. F. 1964, MNRAS, 127, 449
Wood, P. R., Bessell, M. S., & Dopita, M. A. 1986, ApJ, 311, 632
Wood, P. R., & Faulkner, D. J. 1986, ApJ, 307, 659
Wood, P. R., & Zarro, D. M. 1981, ApJ, 247, 247

THE ASTROPHYSICAL JOURNAL, 428:292–318, 1994 June 10

GEOMETRY AND PHYSICAL CONDITIONS IN THE STELLAR WIND OF AG CARINAE[1]

CLAUS LEITHERER,[2] RICHARD ALLEN,[3] BRUCE ALTNER,[4] AUGUSTO DAMINELI,[5] LAURENT DRISSEN,[2]
THAIS IDIART,[5] OLIVIA LUPIE,[2] ANTONELLA NOTA,[2,6] CARMELLE ROBERT,[2]
WERNER SCHMUTZ,[7] AND STEVEN N. SHORE[8]
Received 1993 October 6; accepted 1993 December 10

ABSTRACT

AG Carinae is one of the prototypes of the class of Luminous Blue Variables. Since 1990 the star has continuously brightened in its visual continuum. We report on a multi-instrument and -wavelength observing campaign to monitor the current activity phase of AG Car. Ground-based photometry, polarimetry, spectroscopy, and space-ultraviolet spectroscopy and spectropolarimetry have been obtained.

From the variability of the polarization at ultraviolet and optical wavelengths we detect significant intrinsic polarization. $P_{\rm int} \geq 0.5\%$ is a large value for a hot, luminous star, suggesting departures from spherical symmetry in the wind of AG Car. The intrinsic polarization is variable on a timescale of 2 months or less. The measured ultraviolet polarization (intrinsic + interstellar) dropped to 0.5% in 1992 May and returned to 1% in 1992 July. The results are interpreted in terms of a variable outflow with a density enhancement in the equatorial plane. A similar model was suggested for the related object R127 in the Large Magellanic Cloud. This geometry is reminiscent of the large-scale morphology of the gas nebula and dust "jet" surrounding AG Car. It is therefore likely that physical conditions close to the stellar surface are responsible for the geometry of the spatially resolved circumstellar material around AG Car.

The line spectrum in the optical and ultraviolet is dominated by the effects of a massive stellar wind. Two wind components are detected: a slow dense wind, where the bulk of recombination radiation is emitted, and a faster, less dense wind, visible in the absorption components of ultraviolet P Cygni profiles. This wind structure is consistent with the geometry suggested by the spectropolarimetric observations, and it is reminiscent of the wind conditions prevailing in B[e] stars.

An analysis of the photospheric and wind parameters has been performed using an expanding, spherically extended non-LTE model atmosphere. The temperature of AG Car decreased from 21,000 to 14,000 K over $\sim$1 yr, with a corresponding increase of the photospheric radius by a factor of 2. Helium is found to be significantly overabundant, supporting the very evolved state of AG Car. Comparison with evolutionary models leads to an estimate for the zero-age main-sequence mass of $(50 \pm 10)\ M_\odot$. Therefore the possibility cannot entirely be excluded that AG Car is in a post–red supergiant phase.

Despite the drastic change of the photospheric conditions, the mass-loss rate did not increase. We find no evidence for a positive correlation between wind density and stellar radius. This makes models that explain the radius increase by opacity effects in the outflow unlikely. The mechanism responsible for the temperature and radius variations is still unknown but most likely has its origin in subphotospheric regions.

Subject headings: polarization — stars: evolution — stars: individual (AG Carinae) — stars: mass loss — supergiants — ultraviolet: stars

1. INTRODUCTION

AG Carinae (=HD 94910 = CoD −59°3430 = CPD −59°2860) is one of the prototypes of the Luminous Blue Variables (LBVs). The class of LBVs has originally been defined by Conti (1984). For a general discussion of the LBV phenomenon, we refer the reader to the proceedings of IAU Colloquium 113 (Davidson, Moffat, & Lamers 1989). In short, LBVs are early-type, luminous stars displaying dramatic photometric and spectroscopic variations over several distinct timescales, ranging between weeks and decades. LBVs as a class of stars are believed to represent a short-lived (10^4–10^5 yr) phase during the evolution of a massive star when a significant amount of mass is lost (Maeder 1989). It is largely the LBV phase which determines the evolutionary relation between O stars on the hydrogen-burning main-sequence and core-helium-burning Wolf-Rayet stars in the theoretical Hertzsprung-Russell diagram. Therefore understanding the physical processes operating during the LBV phase is crucial for modeling the evolution of massive stars in general.

[1] Based on observations with the NASA/ESA *Hubble Space Telescope*, obtained at the Space Telescope Science Institute, which is operated by AURA for NASA under contract NAS 5-26555; on observations with the *International Ultraviolet Explorer* satellite, which is sponsored and operated by the United States National Aeronautics and Space Administration, by the Science Research Council of the United Kingdom, and by the European Space Agency; on observations obtained at the National Laboratory of Astrophysics (LNA/CNP$_q$); and on observations obtained at the European Southern Observatory, La Silla.

[2] Space Telescope Science Institute, 3700 San Martin Drive, Baltimore, MD 21218; leitherer@stsci.edu, drissen@stsci.edu, lupie@stsci.edu, nota@stsci.edu, crobert@stsci.edu

[3] Steward Observatory, University of Arizona, Tucson, AZ 85721; rallen@as.arizona.edu

[4] Applied Research Corporation, 8201 Corporation Drive, Suite 1120, Landover, MD 20758; altner@fosvax.arclch.com

[5] Instituto 'Astronômico e Geofisico da USP, Caixa Postal 9638, 01065 São Paulo, Brazil; iagusp::damineli, iagusp::thais

[6] Affiliated with the Astrophysics Division, Space Science Department of the European Space Agency.

[7] Institut für Astronomie, ETH-Zentrum, CH-8092 Zürich, Switzerland; schmutz@astro.phys.ethz.ch

[8] Goddard Space Flight Center, Greenbelt, MD 20771; sshore@vines.iusb.indiana.edu

AG Carinae is the cornerstone for the interpretation of the LBV phenomenon. It has a rich history of observations at various wavelengths (see Nota et al. 1992 for the available literature). Viotti et al. (1984) demonstrated that an increase in brightness at optical wavelengths is accompanied by a corresponding decrease in the ultraviolet. Lamers et al. (1989) studied the visual energy distribution at nine epochs and found that the bolometric magnitude of AG Car remains constant. Observations of other LBVs (e.g., R127: Stahl et al. 1983; S Doradus: Leitherer et al. 1985) are consistent with this result. The constancy of the bolometric luminosity during the variability cycle of LBVs led to the suggestion that drastic changes of the physical conditions in the outer stellar atmospheres result in modified opacities and subsequently a redistribution of the stellar radiation field from shorter to longer wavelengths (Leitherer et al. 1989b). In such a scenario, the mass-loss properties of LBVs would be largely determined by the properties of the underlying star, and radiation pressure could be invoked to account for the observed stellar-wind characteristics (Pauldrach & Puls 1990). This situation would be rather similar to massive main-sequence stars where the theory of radiatively driven winds can predict stellar-wind properties from stellar parameters to a high degree of precision (Kudritzki et al. 1992).

Due to its relative proximity ($D \approx 6$ kpc; Humphreys et al. 1989) AG Car and its environment can be studied in much more detail than possible for the majority of LBVs, which are extragalactic. AG Car is surrounded by an extended nebula first described by Thackeray (1950). Spectroscopic studies by Johnson (1976) and Thackeray (1977) led to the suggestion that the circumstellar material had been ejected by AG Car in an outburst $\sim 10^4$ yr ago. High-resolution coronographic imaging of the inner part of the nebulosities (Paresce & Nota 1989) revealed a bipolar, helical structure originating from—or close to—AG Car itself. This discovery spurred detailed imaging and spatially resolved spectroscopy of other LBVs as well. As a result, ejecta which in several cases show evidence for asymmetries have been detected in the LBVs HR Car (Hutsemékers & Van Drom 1991a), WRA 751 (Hutsemékers & Van Drom 1991b), η Car (Hester et al. 1991), P Cyg (Johnson et al. 1992), and R127 (Clampin et al. 1993).

The discovery of highly asymmetric, bipolar ejecta around AG Car bears important consequences for the interpretation of the mass-loss mechanism in LBVs. If asymmetries in the outflows occur in close vicinity of the star (i.e. within a few stellar radii), geometries breaking spherical symmetry of the system may have to be invoked. Gallagher (1989) discussed models for LBVs which include binaries and/or disklike configurations. Such models face difficulties in accounting quantitatively for several LBV parameters, such as the lifetime of the LBV phase. However, the detection of bipolar outflows in some LBVs has revived the interest in such models. Alternatively, the formation of the bipolar outflow could occur far away from the star due to a nozzle mechanism of the interstellar medium (Raga & Cantó 1989). In the latter case, the observed jetlike structures would not necessarily be indicative of large-scale symmetry breaking close to the stellar surface, and stellar-wind models for single, spherical stars could still be applicable.

Ultraviolet spectropolarimetry, optical polarimetry, ultraviolet spectroscopy, and ground-based spectroscopy of AG Car have been obtained in order to probe the geometry and the physical conditions of the outflow within several stellar radii. The goal of this study is twofold. First, the significance of variabilities and asymmetries in the outflow will be assessed. Second, the correlation between mass loss and photospheric parameters will be addressed. An initial study performed by some of us (Leitherer, Damineli, & Schmutz 1992) indicated that the mass loss from AG Car occurs at a rate which is largely independent of photospheric parameters. This result, if confirmed on the basis of a larger data set, differs drastically from the standard scenario thought to apply to all LBVs. The observations are described in § 2. The polarimetric properties are interpreted in § 3. Section 4 contains a discussion of the photometric and spectroscopic evolution of AG Car during our observing campaign. The stellar and wind parameters are derived from a non-LTE analysis of the spectrum in § 5. In § 6 we discuss the astrophysical significance of the wind properties and its geometry. The conclusions are presented in § 7.

2. OBSERVATIONAL DATA

We are monitoring the current activity cycle of AG Car using photometric, polarimetric, and spectroscopic techniques over a wide spectral range. The visual brightness of AG Car had reached a maximum of $m_V \approx 6.0$ around 1981 when Wolf & Stahl (1982) studied the expanding envelope of the object. Subsequently the visual brightness declined to ~ 8.0 around 1985 as described by Stahl (1986). The spectral type changed from A to late O during this time interval. AG Car remained around $m_V \approx 8.0$ until 1990. In 1991 Kilmartin & Bateson (1991) reported an increase in m_V which is still continuing at present. Figure 1 shows the photometric evolution of AG Car for 1980–1993. The data have been compiled from visual measurements of the Variable Star Section of the Royal Astronomical Society of New Zealand (Bateson 1980–1993). The most recent data points are based on photoelectric measurements in the Johnson BV system obtained at the 50 cm telescope of UFRGS Observatory. The data are listed in Table 1. Typical errors are 0.03 in V and 0.02 in $B-V$. Although the measurements obtained at UFRGS Observatory refer to different photometric system than the New Zealand data (photoelectric vs. visual), the two data sets agree rather well. We estimate that the *average* errors of the visual and photoelectric measurements are ~ 0.1 and 0.03 mag, respectively. The individual errors of the visual data, however, can sometimes be much larger. Each New Zealand data point in Figure 1 is the mean of

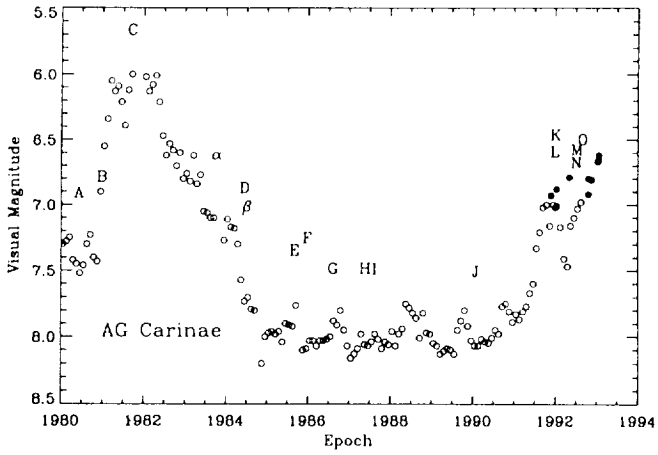

FIG. 1.—Visual light curve of AG Car from 1980 until 1994. Each open circle is the mean of several individual visual estimates. The filled dots denote photoelectric measurements. Letters refer to the *IUE* spectra listed in Table 4.

TABLE 1

PHOTOMETRY OBTAINED AT UFRGS OBSERVATORY

Epoch	V	$B-V$
1991 Dec 2	6.93	0.66
1992 Jan 3	7.02	0.69
1992 Jan 13	6.88	0.66
1992 May 4	6.79	0.66
1992 Oct 21	6.92	0.68
1992 Oct 22	6.80	0.68
1992 Nov 19	6.81	0.71
1993 Jan 12	6.67	0.67
1993 Jan 20	6.65	0.67
1993 Jan 21	6.62	0.67

the visual measurements by several observers. The number of observers contributing to these measurements varies strongly. Especially during the second half of each year, when AG Car is close to the Sun, the mean value is based on very few observers (less than 5), and systematic effects may become important.

Our spectropolarimetric and spectroscopic observations commenced in late 1990, when AG Car showed the first indication of a rise from its minimum of the light curve.

2.1. *Ultraviolet Spectropolarimetry with HST*

The first UV polarization measurements of AG Car were obtained on three separate visits using the *Hubble Space Telescope* (*HST*) Faint Object Spectrograph (FOS) in its spectropolarimetric mode. The observation details are summarized in Table 2. We used the G270H grating (2200–3400 Å) and "B" waveplate, the combination being most sensitive to linear polarization at ultraviolet wavelengths. A detailed description of the instrumentation may be found in the Faint Object Spectrograph Instrument Handbook (Kinney 1992) and in Allen & Angel (1982).

On each of our three visits to AG Car, we acquired four unique polarization sets (each set consisting of eight waveplate positions) over four orbits, in order to assess instrument stability and data repeatability. During the 1991 November data set (where the 0".5 aperture was used) spacecraft jitter was appreciable during orbital day/night transitions (confirmed in the pointing telemetry). We eliminated those specific waveplate positions where jitter significantly reduced the flux. All other common waveplate spectra over the four orbits agreed to within photon statistics. (This implies that at least over a few hours, the polarization appears to remain constant).

Because each orthogonal sense of polarization is not measured simultaneously by the FOS and each falls on a different place on the photocathode, each beam must be reduced independently using the flat field, wavelength and sensitivity calibrations (obtained through the polarizers) supplied in the STScI Calibration Data Base. The polarization processing was done using the code developed by Allen and described in the FOS Science Verification Report. The processing was performed on each beam separately and combined later. The retardation of the waveplates, pass direction of the Wollastons, and offset of the waveplates were calibrated on the ground and verified in-flight (Allen & Smith 1992). Errors in the retardation calibration produce systematic errors in the measured polarization. For grating H27, these errors should be less than 0.02 times the measured linear polarization. A 1% linear polarization could thus be uncertain by $\pm 0.02\%$. A minor oscillation in θ also occurs because of a slight misalignment of the two halves of the waveplate. While some of this oscillation is taken out in the data processing, residual errors of $\pm 1°$ are possible. Allen et al. (1993) found the instrumental polarization to be less than 0.1% overall. Our reported polarization and position angle error estimates are based only on the photon statistics of the observations.

Immediately following each visit to AG Car, we obtained a single short polarization data set on the B1V polarization standard BD +64°106 (Lupie & Stockman 1988; Schmidt, Elston, & Lupie 1992) using the same polarization mode but with the 4".3 aperture (to increase signal and minimize precious *HST* exposure time). Table 3 lists the error-weighted mean polarization, average errors, rms deviation, polarization (inverse) signal-to-noise parameter ϵ_P/P, error-weighted mean position angle, errors, and rms deviation. The data on the three occasions agree to within observational error. The polarization and position angle in the UV (bins of 300 Å to improve S/N) and optical (from Schmidt, Elston, & Lupie 1992) are presented as a function of wavelength in Figure 2.

The solid line is a fit to the optical data and extrapolated to the UV. The fit is based on the Wilking modification to Serkowski's law (Serkowski, Mathewson, & Ford 1975 [hereafter SMF]; Wilking, Lebofsky, & Rieke 1982). The Serkowski relation describes the wavelength dependence of the polarization as a function of P_{max} and λ_{max}.

Data obtained with the Wisconsin Ultraviolet Photo-Polarimeter experiment (WUPPE; Clayton et al. 1992) toward several sight lines revealed that although the polarization decreases, there is "substantial variation" in the wavelength dependence in the UV. Some stars followed the Serkowski extrapolation while others showed excess polarization at the shorter wavelengths. Although the sample was small, those stars showing the excess polarization had shorter values of λ_{max} (≤ 5100 Å). Clayton et al. (1992) did not observe a position angle rotation in any of the polarization standard stars they measured.

For BD +64°106, $P_{max} \approx 5.67\%$ and $\lambda_{max} \approx 5015$ Å. Allen et al. (1993) measured BD +64°106 during the Science Verification Commissioning Phase of *HST*. Our data is consistent with these earlier results, including the mild rise in the position angle toward shorter wavelengths.

TABLE 2

HST OBSERVATIONAL MODE FOR AG CAR

Epoch	Grating, Waveplate	Aperture	Spectral Range (Å)	Dispersion (Å pixel^{-1})
1991 Nov 19	G270H, Wave B	0".5	2230–3400	2.5
1992 May 15	G270H, Wave B	1.0	2230–3400	2.5
1992 Jul 16	G270H, Wave B	1.0	2230–3400	2.5

TABLE 3

HST OBSERVATIONS OF BD +64°106

Wavelength (Å)	$\langle P \rangle$ (%)	$\langle \pm\epsilon_P \rangle$	σ_P	ϵ_P/P	$\langle \theta \rangle$	$\langle \pm\epsilon \rangle$	σ_θ
2357.9	3.95	0.35	0.13	0.09	100°.9	2°.6	1.6
2627.1	4.31	0.20	0.10	0.05	98.5	1.3	1.3
2896.7	4.42	0.16	0.06	0.04	98.9	1.1	0.7
3162.7	4.68	0.17	0.11	0.04	97.9	1.0	1.1

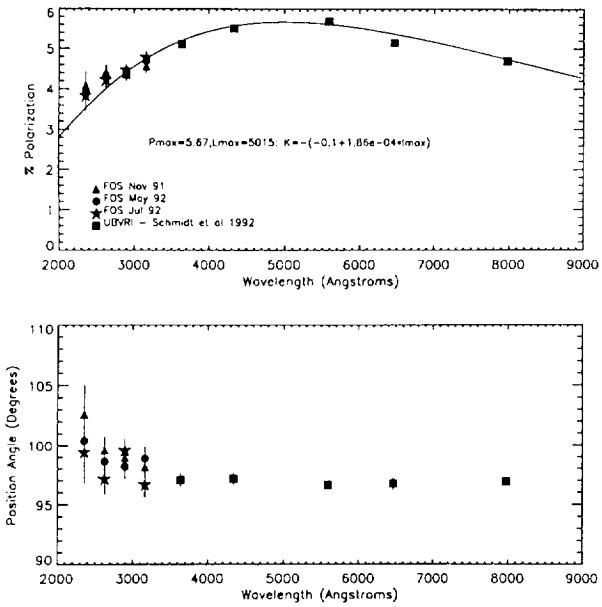

FIG. 2.—Polarization measurements of BD +64°106. Shown are the UV data (averaged into four bins) and the ground-based data (Schmidt, Elston, & Lupie 1992). The UV polarization follows the ISM polarization law. Although the error bars are large, the position angle may be offset by 2°–3° from the optical data. This could represent a real rotation of the ISM plane or a small error in the calibration of the FOS fiducial waveplate position.

2.2. *Ultraviolet Spectroscopy with IUE*

We have used the *International Ultraviolet Explorer* (*IUE*) to obtain both low- and high-dispersion spectra of AG Car, covering the spectral range from 1200 to 2000 Å in the SWP camera and 2000 to 3200 Å in the LWP camera. Low-dispersion spectra achieve a resolution of ~ 6 Å; a velocity resolution of ~ 20 km s^{-1} is normally obtained in the high-dispersion mode. Further details on the satellite and its spectrographs can be found in Boggess et al. (1978).

The data were reduced using the standard spectral image processing scheme currently in place at Goddard. The echelle blaze correction is based on the data of Grady & Garhart (1988) for the SWP camera and Ake (1981, 1982) for the long-wavelength cameras. The spectral orders were merged to form single arrays of wavelengths, fluxes, and data quality flags. The fluxes were subsequently calibrated using the calibration tables of Cassatella et al. (1990).

In addition to the spectra obtained within a few days of the *HST*/FOS observations, the *IUE* archives contain a significant number of previous observations of AG Car, spanning a time period of almost 15 yr (see Table 4). In this paper we shall concentrate on the observed variability of the *IUE* spectra as it relates to the problem of determining the outflow characteristics of the wind. The reader is referred to Johnson (1982) for a discussion of the high-dispersion observations obtained in 1980, which includes an extensive list of lines appearing in the spectra. A discussion of the UV light curve, based on low- and high-dispersion *IUE* spectra, can be found in Shore, Waxin, & Altner (1994).

2.3. *Ground-based Spectroscopy*

Spectroscopic data of AG Car in the visual range have been obtained at the 1.6 m telescope of the Brazilian National Observatory (LNA). The spectrograph at the coudé focus was equipped with a coated GEC CCD detector having useable spectral response from 4000–11000 Å. Gratings of 1800 lines mm^{-1} and 600 lines mm^{-1} yielded a dispersion of 0.13 and 0.39 Å pixel^{-1}, respectively. The effective spectral resolution as measured from the FWHM of the comparison spectrum is slightly less than 2 pixels. The spectra were reduced in the standard way, Doppler corrected into the heliocentric system, and the continuum was normalized to unity. A summary of all spectra obtained in the course of our observing campaign can be found in Table 5.

In addition to the observations collected in Brazil, we secured several high-resolution spectrograms at the 1.4 m CAT of ESO, La Silla. These observations have a spectral resolution of 60,000. The spectral range is ~ 50 Å. The spectra are mostly centered on Hα but data for Hβ and He II λ4686 were also obtained. The observing log is also included in Table 5. Standard reduction techniques were performed.

The relatively narrow spectral range made it difficult to normalize the spectra obtained at ESO to the continuum level. Hα in particular has very broad line wings which extend beyond the limits of the accessible spectral region. This problem did not occur on the spectra obtained at LNA due to the much wider spectral range. Since we always had an LNA spectrum within a few weeks of an ESO spectrum, we used the LNA spectra to determine the level of the continuum at the wavelengths where the ESO spectra cut off. The ESO spectra were corrected and normalized to unity with this information.

Some of the spectra obtained at the two observatories differ in spectral resolution by about a factor of 4. We convolved the ESO data with a Gaussian filter to simulate a degraded resolution appropriate for some of the LNA data. Broad emission lines, such as Hα, are still well resolved even on the lowest resolution spectra in our data set. On the other hand, narrow features, such as blueshifted Hα absorption components are strongly affected by instrumental resolution.

The ground-based spectroscopic data cover the spectral evolution of AG Car at a time resolution of a few months. This corresponds to the flow timescale in the wind, which determines the timescale over which the wind features are expected to exhibit significant variations. Since the main thrust of this study is to learn more about the physics of the stellar wind, we concentrated our spectroscopic efforts on obtaining nearly continuous coverage of Hα, the strongest wind line, at the expense of the blue spectral region.

3. POLARIMETRIC PROPERTIES OF AG CARINAE

Is the mass loss from AG Car spherically symmetric, and if not what is the nature of the asymmetry? Spectropolarimetry is an important diagnostic tool for assessing the symmetry of AG Car's stellar wind. The UV regime is advantageous for the following reasons: (1) The contaminating interstellar (ISM) polarization is smaller in the UV, providing us with a better chance to separate the intrinsic and interstellar components of the polarization. (2) The strongest lines formed in the stellar wind (resonance lines of singly ionized iron and magnesium) are found in the UV. (3) Polarization data over an extended wavelength regime (near-simultaneous observations in the UV, optical, and IR) facilitates the characterization of any intrinsic component. The *HST* UV data allow us to probe for asymmetric ejecta in the innermost unresolved region of the complex, without contamination by nebulosity.

The *HST* polarization data for AG Car are presented in

TABLE 4

JOURNAL OF *IUE* OBSERVATIONS

JD-2,400,000 (1)	Epoch (2)	Symbol (3)	Camera (4)	Image Number (5)	Dispersion (6)	Exposure (s) (7)
44356	1980 Apr 27	A	LWR	7628	H	2400
44551	1980 Nov 8	B	LWR	9259	H	1920
44819	1981 Aug 3	C	LWR	11229	H	1800
44356	1980 Apr 27	A	LWR	7627	L	50
44551	1980 Nov 8	B	LWR	9258	L	40
45818	1984 Apr 28	D	LWP	3236	H	1740
46265	1985 Jul 19	E	LWP	6437	H	2640
46383	1985 Nov 14	F	LWP	7099	H	1800
46604	1986 Jun 23	G	LWP	8469	H	3600
46887	1987 Apr 2	H	LWP	10473	H	2700
47000	1987 Jul 24	I	LWP	11273	H	2700
47883	1989 Dec 23	J	LWP	16985	H	2700
48576	1991 Nov 16	K	LWP	21757	H	1800
48577	1991 Nov 17	L	LWP	21759	H	900
48760	1992 May 18	M	LWP	23126	H	1800
48760	1992 May 18	N	LWP	23130	H	2100
48818	1992 Jul 15	O	LWP	23508	H	1200
46604	1986 Jun 23	G	LWP	8468	L	300
46913	1987 Apr 28	...	LWP	10659	L	30
47001	1987 Jul 25	I	LWP	11275	L	40
48110	1990 Aug 7	...	LWP	18539	L	45
48760	1992 May 18	M	LWP	23127	L	30
44551	1980 Nov 8	B	SWP	10561	H	7440
44829	1981 Aug 13	C	SWP	14750	H	5400
45567	1983 Aug 21	α	SWP	20742	H	10800
45845	1984 May 25	β	SWP	23109	H	12000
46265	1985 Jul 19	E	SWP	26444	H	10800
46604	1986 Jun 23	G	SWP	28536	H	10800
47000	1987 Jul 24	I	SWP	31405	H	8100
47883	1989 Dec 23	J	SWP	37882	H	23400
48576	1991 Nov 16	K	SWP	43124	H	7200
48760	1992 May 18	M	SWP	44713	H	7200
48818	1992 Jul 15	O	SWP	45145	H	7200
43848	1978 Dec 6	...	SWP	3542	L	80
44551	1980 Nov 8	B	SWP	10560	L	240
44819	1981 Aug 3	...	SWP	14639	L	240
45491	1983 Jun 6	...	SWP	20157	L	240
45846	1984 May 26	β	SWP	23110	L	240
46268	1985 Jul 22	E	SWP	26458	L	180
46383	1985 Nov 14	...	SWP	27111	L	180
46604	1986 Jun 23	G	SWP	28537	L	180
46887	1987 Apr 2	H	SWP	30691	L	180
46913	1987 Apr 28	...	SWP	30881	L	90
47151	1987 Dec 22	...	SWP	32588	L	180
47583	1989 Feb 26	...	SWP	35625	L	180
48011	1990 Apr 30	...	SWP	38703	L	240
48576	1991 Nov 16	K	SWP	43123	L	240
48760	1992 May 18	M	SWP	44710	L	240
48818	1992 Jul 15	O	SWP	45144	L	240

NOTES.—The symbols "α" and "β" in col. (3) refer to epochs in which only SWP spectra were obtained.

Figure 3 where we have displayed the relative flux, and the polarization and position angle for all 3 epochs of observations. The error bars in this figure indicate the 1 σ errors. According to our *IUE* monitoring, the dominant spectral features did not vary over the course of our *HST* observations. The prevalent feature in the polarization is the decrease by 0.5% in 1992 May from the 1991 November level, followed by a return in 1992 July to the higher polarization state. The position angle is constant with wavelength and shows a small rotation between 1992 May and 1992 July. The errors are large on the May position angle data because the polarization is so low. We also acquired ground-based polarization data with IAGPOL at the 0.6 m and 1.6 m telescopes of the Brazilian National Observatory on 1991 June 3 and on 1992 May 1. These data are presented in Table 6.

Polarization measurements are very sensitive to asymmetries but quantitative interpretation is made difficult by the presence of interstellar polarization, which is often not known, and possibly by competing intrinsic polarization from different origins (e.g., a variable component superimposed on a constant component). Three methods are used to detect the presence of an intrinsic component: (1) a wavelength dependence that is different from the interstellar law, (2) variability, and (3) polarization structure across absorption/emission lines.

TABLE 5

JOURNAL OF GROUND-BASED SPECTROSCOPIC OBSERVATIONS

Epoch (1)	Telescope (2)	Spectral Range (Å) (3)	Dispersion (Å/pixel^{-1}) (4)
1990 Jun 16	LNA	9950–10190	0.4
1990 Dec 22	LNA	9960–10190	0.4
1990 Dec 27	LNA	8600–8830	0.4
1990 Dec 28	LNA	6490–6714	0.4
1991 Jan 21	ESO	4670–4720	0.05
1991 May 25	LNA	10740–10960	0.4
1991 Jul 31	ESO	6540–6590	0.05
1991 Aug 15	LNA	6500–6730	0.4
	LNA	8580–8800	0.4
	LNA	9950–10170	0.4
1991 Oct 22	LNA	6380–6850	0.4
	LNA	8460–8940	0.4
1991 Nov 18	LNA	6490–6640	0.1
1991 Nov 25	LNA	6600–6750	0.1
1992 Jan 3	ESO	6530–6590	0.05
1992 Mar 17	ESO	6530–6590	0.05
1992 Mar 19	ESO	4840–4880	0.05
1992 Mar 20	LNA	6410–6880	0.4
	LNA	8480–8950	0.4
	LNA	9940–10410	0.4
	LNA	10570–11040	0.4
1992 May 15	ESO	6530–6590	0.05
1992 Jun 3	LNA	4170–5100	0.4
	LNA	5790–6260	0.4
	LNA	6380–6850	0.4
	LNA	8400–8900	0.4

3.1. *Interstellar Polarization of AG Car and Surrounding Field Stars*

The measured polarization is a vector combination of the intrinsic polarization of the star and the interstellar polarization. At this time, we do not know, with sufficient accuracy the interstellar vector toward AG Car. An estimate can be made using polarization measurements of neighboring stars from the catalog of Klare, Neckel, & Schnur (1972) which contains the (effective) B filter polarization of southern stars. The results of the search at distances of (6 ± 3) kpc are given in Table 7 where DM is the distance modulus, δDM is the depth of the region. The rms deviation of P and θ are also given. The projected area on the sky is 1°. From the 6 kpc data, the interstellar position angle is 135° with a $\pm 5°$ uncertainty. From SMF, λ_{max} determined from stars in the *general* area of AG Car is between 5200 and 5700 Å. Using a mean value of $P(B) = 1\%$ at 6 kpc (DM = 13.9) and the Wilking et al. (1982) modification of SMFs formulation, $P_{max} \approx 1.0\%$ and 1.1% using $\lambda_{max} = 5200$ and 5700 Å, respectively.

TABLE 6

RECENT GROUND-BASED PHOTOPOLARIMETRY OF AG CAR

Epoch	Wavelength (Å)	P[a] (%)	θ[b]
1991 Jun 3	3620	0.79 (0.07)	133°.8 (2°.4)
	4506	1.01 (0.05)	134.1 (1.3)
	5445	1.15 (0.06)	133.8 (1.4)
	6519	1.34 (0.05)	134.5 (1.1)
	7975	1.41 (0.06)	132.6 (1.2)
1992 May 2	5445	1.14 (0.11)	148.2 (2.7)
	6519	1.19 (0.09)	151.9 (2.2)
	7975	0.94 (0.17)	145.1 (5.1)

[a] Numbers in parentheses are percentages of errors.
[b] Numbers in parentheses are errors, in degrees.

TABLE 7

POLARIZATION OF NEARBY STARS

DM	δDM	Number	$\%P(B)$	$\theta(B)$
13.9	1	14	1.1 ± 0.2	$141° \pm 4°$
13.9	2	40	0.8 ± 0.3	131 ± 4
12.4	1	40	0.8 ± 0.3	126 ± 3
12.4	2	51	0.8 ± 0.3	127 ± 3
14.8[a]	1	10	1.0 ± 0.3	135 ± 3
14.8	2	15	1.1 ± 0.2	140 ± 3

[a] 2° search area. All others are 1°.

Schulte-Ladbeck, Clayton, & Meade (1993) estimated the interstellar polarization toward AG Car by measuring the polarization across the Hα emission line. If one can assume that the line is unpolarized, a result of seeing less scattering optical depth than the continuum, the polarization at the core represents the interstellar value at 6563 Å. This method is exceedingly more preferable than using neighboring stars. However, the assumption that the line is *totally* unpolarized requires independent confirmation. If the line is unpolarized, then the P_{max} values derived from the Hα data are 1.25% and 1.20% for $\lambda_{max} = 5200$ Å and 5700 Å, respectively, and the position angle is 143°. Both the polarization and position angle slightly exceed the envelope of estimates from neighboring stars.

The polarization and position angle history of AG Car is presented in Figure 4 as a function of wavelength. Here we access measurements obtained by Serkowski (1970) over a 511 day period (1968 February and April, 1969 February–June). The *HST* UV data are displayed in eight bins (150 Å per bin). The Brazil optical data and an optical spectropolarimetric continuum measurement (~6500 Å in 1991 November from Schulte-Ladbeck, Clayton, & Meade 1993) are also shown. The aperture sizes used for ground-based photopolarimetric measurements are 20″ and 30″, significantly larger than our 0″.5 and 1″ apertures used for the UV data. These larger apertures encompass the entire AG Car complex. Schulte-Ladbeck et al.'s data was obtained with a 2″.7 aperture. The data obtained on the same date are connected with a *dashed* line and the data obtained within a month are connected with *dotted* lines. The solid curve is an estimate of the interstellar polarization using the stars from the Klare et al. catalog ($\lambda_{max} = 5500$ Å, $P_{max} = 1\%$). We note that the envelope of uncertainty would outline a swathe many tenths of an arcsecond wide.

A fit using all the AG Car optical data resulted in $\lambda_{max} \approx 6900$ Å. Fitting the interstellar law to a star with variable polarization is only meaningful in that it shows qualitatively that the wavelength dependence is different from the interstellar medium. The position angle is constant with wavelength in the optical whereas the UV shows a rotation of ~10° (cf., 1991 November, UV + optical).

3.2. *Polarization Variability*

Any variation seen in the polarization with time is intrinsic to the star or its immediate surroundings. The variability is a lower limit on the magnitude of the intrinsic component. Table 8 summarizes the polarization variability of AG Car. Columns (1) and (2) list the wavelength and number of visits, columns (3)–(6) and (7)–(10) give the mean, standard deviation, average

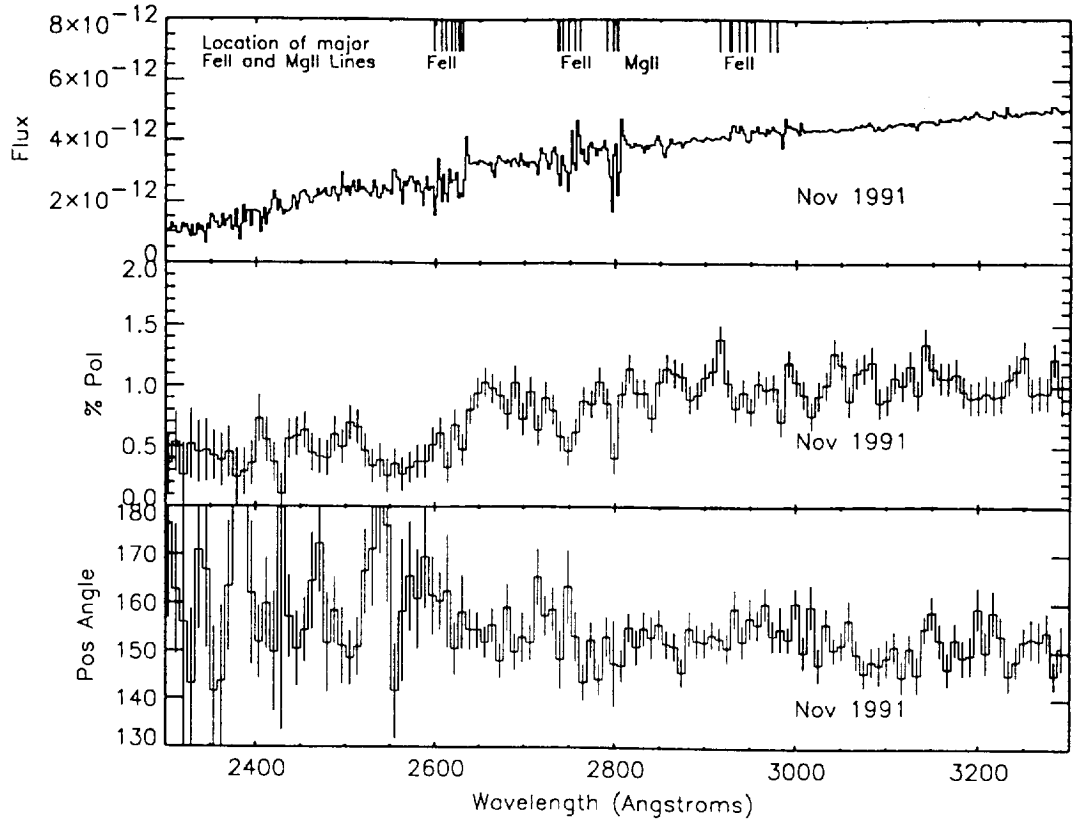

FIG. 3*a*

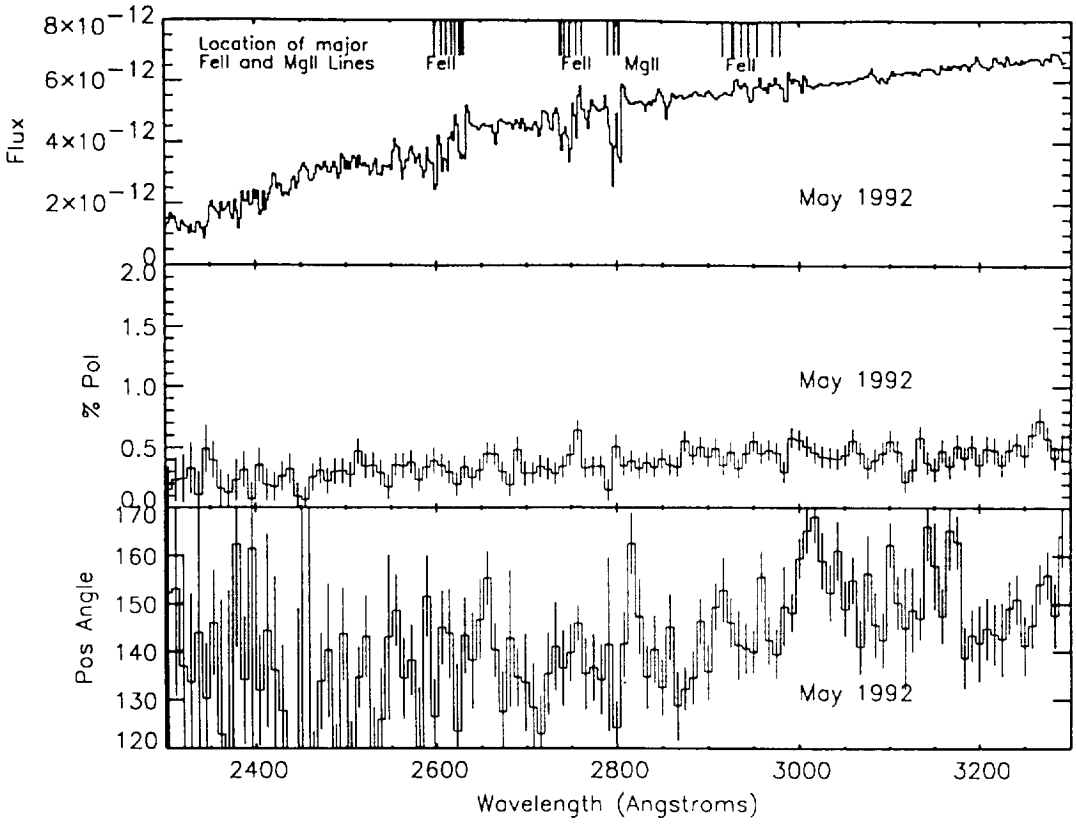

FIG. 3*b*

FIG. 3.—*HST* FOS spectra and polarimetry. Presented here are flux, polarization, and position angle for the (*a*) 1991 November, (*b*) 1992 May, and (*c*) July 1992 FOS spectra. The UV data are displayed in 10 Å bins. The continuum polarization decreases by 0.5% in 1992 May and recovers in 1992 July. Some of the structure seen across the P Cygni lines is a result of saturated absorption and our limited wavelength resolution which causes mixing of the continuum and line fluxes.

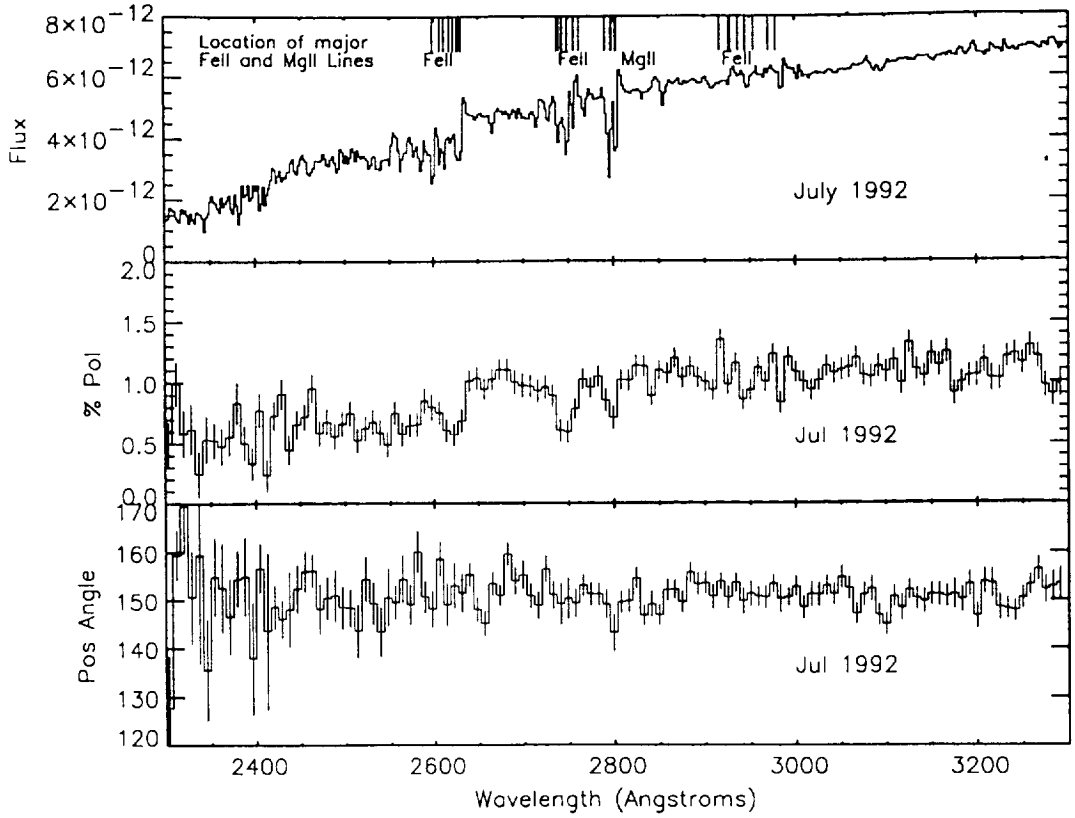

FIG. 3c

TABLE 8

SUMMARY OF AG CARINAE POLARIZATION

Band (1)	Visits (2)	$\langle P \rangle$ (%) (3)	σ_P (%) (4)	$\langle$err$\rangle$ (%) (5)	max δP (%) (6)	$\langle \theta \rangle$ (7)	σ_θ (8)	$\langle$err$\rangle$ (9)	max $\delta\theta$ (10)
Serkowski 1968–1970									
U	4	0.81	0.12	0.06	0.29	141°2	3°5	2°0	9°0
B	8	0.97	0.15	0.06	0.51	138.3	4.0	1.7	13.0
V	3	1.21	0.13	0.06	0.32	137.8	3.2	1.4	7.0
Brazil 1991–1992									
U	1	0.79	...	0.07	...	133.8	...	2.4	...
B	1	1.01	...	0.05	...	134.1	...	1.3	...
V	2	1.15	0.01	0.09	0.01	136.9	8.3	2.0	14.4
R	2	1.31	0.09	0.09	0.16	138.0	10.2	1.7	17.4
I	2	1.36	0.30	0.12	0.47	133.2	8.4	3.2	12.5
HST UV Data (150 Å bins) 1991–1992									
2291	3	0.43	0.16	0.06	0.39	154.2	9.4	4.6	21.8
2425	3	0.41	0.18	0.04	0.45	151.0	15.1	3.1	32.9
2560	3	0.47	0.15	0.03	0.35	150.1	9.7	2.0	23.1
2694	3	0.67	0.24	0.03	0.56	151.5	7.2	1.3	15.3
2829	3	0.75	0.29	0.03	0.66	149.9	6.8	1.1	12.8
2963	3	0.79	0.28	0.03	0.61	152.2	2.0	1.0	4.7
3096	3	0.84	0.32	0.02	0.71	150.8	0.6	1.0	1.1
3229	3	0.83	0.28	0.03	0.62	151.0	1.0	1.1	1.8

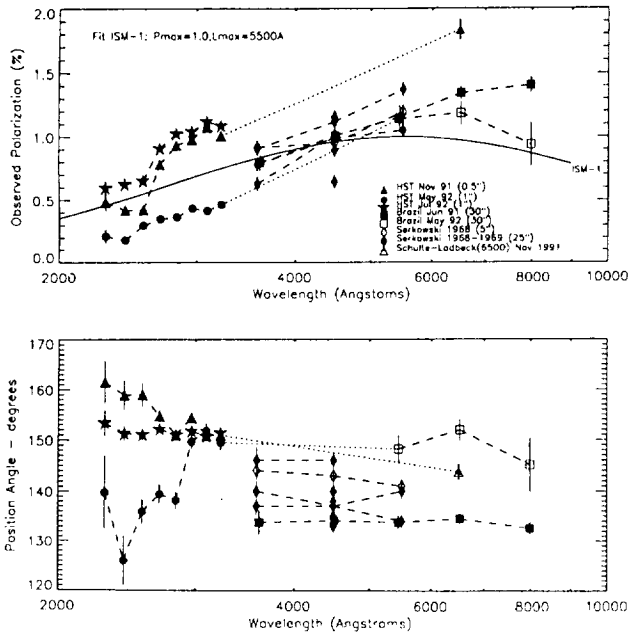

FIG. 4.—Polarization history of AG Car. The UV data is presented in bins of 150 Å. We have included data from Serkowski (1970), Schulte-Ladbeck (1993), and our 1991–1992 optical + UV data as indicated in the key. Data taken on the same date are connected by dashed lines and data taken within a month are connected by dots. The solid line represents a crude estimate of the interstellar polarization derived from nearby stars (see text for discussion).

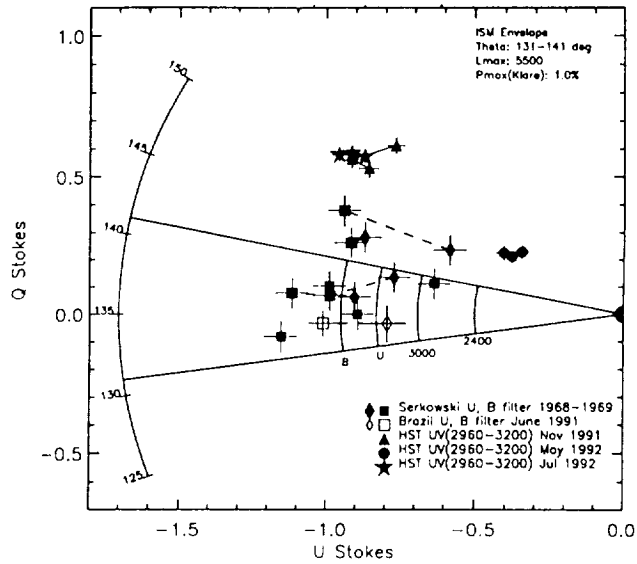

FIG. 5.—Temporal variability of AG Car in the $Q-U$ plane over a limited wavelength range. Displayed are the U and B Serkowski data (1968–1969), the Brazil U and B data (1991 June), and the red end (2900–3200) of the *HST* UV data (binned to 150 Å). *Dashes* connect points on the same date, and *filled circles* connect data obtained within a month. The (0, 0) position on the graph is denoted by a bull's eye. We have also shown the interstellar polarization envelope and our arcs which represent an estimate of the magnitude of the interstellar polarization at four wavelengths (using $P_{max} \approx 1\%$, $\lambda_{max} \approx 5500$ Å, $\theta = 135°$).

(typical) error, and maximum change for the measured polarization and position angle, respectively.

In summary, Serkowski has seen variability of $\sim 0.5\%$ over a few months time, Brazil I data varies by $\sim 0.4\%$ in 11 months, the UV 1991 November and 1992 July data are very similar but the intervening 1992 May data falls to less than 0.5%, resulting in a change in polarization of $\sim 0.6\%$. This small polarization observed in May is *consistent* with the polarization seen by Schulte-Ladbeck (1993, private communication) in the optical continuum a few months earlier, in 1992 March [$P(5500) \approx (0.85 \pm 0.08)\%$, $\theta \approx 145°$]. The timescale of variability is not established but dramatic 0.5% changes in the polarization are seen over a period of 1–2 months.

Presentation of the data on the $Q-U$ plane reveals additional information about the nature of the variable intrinsic component. The polarization data is displayed on the Stokes $Q-U$ plane in Figures 5 and 6. The length of the vector on a $Q-U$ plane is equal to the magnitude of the polarization (intrinsic + interstellar) and a rotation on the $Q-U$ plane is equal to half that value on the plane of the sky. Let us first confine the input to data in *one wavelength regime*. Figure 5 displays the polarization in U, B and the long-wavelength end of the *HST* UV data (2900–3200 Å). The (0, 0) position on the graph is denoted by a bull's eye. We have also shown the interstellar polarization envelope and four arcs which represent the magnitude of the interstellar polarization at four wavelengths (using $P_{max} \approx 1\%$, $\lambda_{max} \approx 5500$ Å, $\theta = 135°$). If the intrinsic polarization is produced by a constant scattering plane, such as an axisymmetric disk (Be stars) or a stable localized region, the measured points (which are a combination of intrinsic and interstellar) would aggregate along a preferred direction, or "time path." If the points aggregated into a circular or elliptical distribution which is repeatable in time, the variability is caused by a periodic phenomenon such as a companion star in a binary system. If the intrinsic position angle varies randomly (such as blobs emitted from many latitudes), one would expect a random pattern clustered around the tip of the interstellar vector. We would expect changes in the polarization also as a result of the outward motion of the blob. Fox & Henrichs (1994) followed the polarization path of a parcel

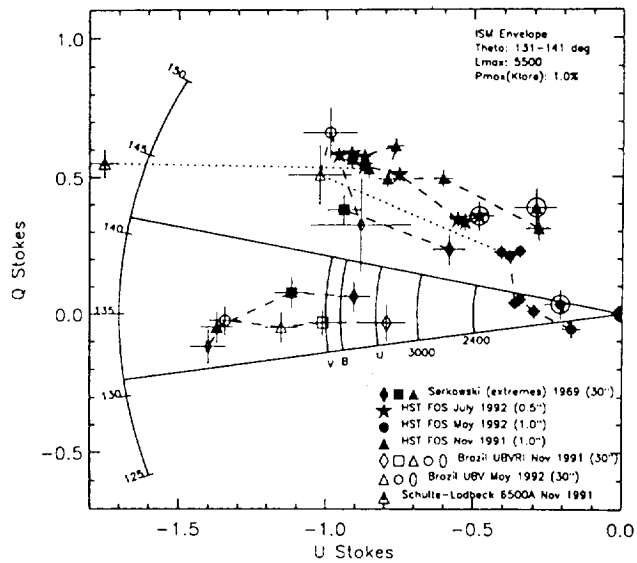

FIG. 6.—AG Car wavelength dependence on the $Q-U$ plane. The observed polarization at several different wavelengths is shown. The two most extreme points from Serkowski (1970) are included. Data obtained on the same date are connected by *dashes* and data obtained within the same month are connected by *filled circles*. It is important to address the multiwavelength data taken at the same time in this diagram. If we adopt the estimate of the interstellar component shown by the arcs, it is clear that there are times when the intrinsic polarization wavelength dependence, and to a lesser extent, the magnitude of the position angle also varies with wavelength.

ejected from a hot star for various combinations of density, inclination angle, and location on the star. As the parcel moves out, the intrinsic component reaches a peak, then decreases. The intrinsic position angle changes as well and flattens out, a result of the aspect angle.

The paucity of points in Figure 5 and the irregular sampling time precludes any assessment of periodicity, or sampling of parcel motion. Even so, a clear-cut "pattern" is not readily revealed. If the interstellar polarization vector falls somewhere within the distribution of points, one might conclude that the intrinsic position angle sometimes has a value of $\sim 5°$ (points falling above the line) and 100° (falling below the line), corresponding to a 90° rotation of the plane of scattering.

Figure 6 is a $Q-U$ diagram which displays the polarization at several different wavelengths but *at approximately the same epoch*. Data obtained on the same date are connected by dashes, and data obtained within the same month are connected by dots. The *HST* UV data are displayed in eight bins (150 Å per bin) as before but the shortest wavelength bin is circled in the figure. Symbols for the other data points are described in the key. It is important to address the multiwavelength data taken at the same time in this diagram. We will assume that the interstellar position angle is wavelength independent. (If multiple interstellar clouds with different properties lie along the sight line, a rotation of θ is possible). If we adopt the estimate of the interstellar component shown by the arcs, it is clear that there are times when the intrinsic position angle has a wavelength dependence, and to a lesser extent, the magnitude of the intrinsic component also varies with wavelength.

3.3. *Polarization Structure across UV P Cygni Lines*

The interstellar polarization is a smoothly varying function with wavelength and has a constant or linear slope across stellar line profiles. Polarization line structure can provide a method to compare the geometry of the line-forming regions with continuum polarization sources.

Polarization and position angle variations across emission lines were first observed in Be stars (e.g., Capps, Coyne, & Dyck 1973; Clarke & McLean 1974) and in the Wolf-Rayet star HD 50896 (McLean et al. 1979). Schulte-Ladbeck, Clayton, & Meade (1993) have measured changes in the polarization across AG Car's Hα line. In the case of the Hα emission line, the region producing the emission sees a smaller electron scattering optical depth than the photospheric light. The addition of the unpolarized emission dilutes the intrinsic polarization at line center and, if the dilution is complete, only the interstellar component will remain at line center. The interstellar and intrinsic contributions add vectorally, hence the position angle may vary across the line as the dominating polarization changes from intrinsic to interstellar. The polarization across P Cygni resonance lines of supernovae is discussed in McCall (1984) and, with, the combined effects of the interstellar polarization is expected to be a complex function.

Our resolution is not sufficient to sample the wings of the strong P Cygni lines without mixing of the local continuum and absorption troughs. An example of a line with an unsaturated core is Fe II (78) at 2985 Å. We see marginal polarization structure across the line if we average together the November and July values. This is reasonable since the polarization in this region has not changed significantly. We are currently in the process of a statistical evaluation of the shapes of all the UV lines (saturated and not) in P and θ and a comparison with the shapes derived from convolving the FOS instrument profile with the *IUE* data. At the least, we hope to qualitatively determine whether the UV resonance lines are polarized differently than the UV continuum light (Lupie 1994).

3.4. *Wavelength Dependence of the Intrinsic Polarization*

The features seen in the UV polarization (1991 November and 1992 July; Fig. 3) include a reduction in the polarization around 2600 Å, structure in the polarization across the strongest Fe II and Mg II resonance lines and a general slope toward longer wavelengths, the latter of which is in part due to the contribution by the interstellar vector. A drop in the polarization has also been seen in the WUPPE UV data for P Cygni (Taylor et al. 1991). In both P Cyg and AG Car, there are many Fe II P Cygni lines in this region. Taylor et al. (1991) speculated that the reduction in the polarization is probably due to line blanketing and that polarization models for these stars should include the absorptive opacity from heavier elements. In our case, our limited wavelength resolution combined with the extensive number of these saturated lines contributes at least in part to the apparent drop in polarization at 2600 Å and similarly across the saturated Fe II and Mg II lines throughout the spectrum.

The intrinsic behavior can be seen in Figures 7 and 8 which display intrinsic polarization and position angle, i.e., the reslting polarization after an assumed interstellar component has been removed. The errors on the points are simply the observational error and do *not* include the uncertainty in the placement of the interstellar vector. In Figure 7, we used the interstellar polarization estimated for nearby stars and adopted the mean value for $\lambda_{max} = 5500$ Å, $P_{max} = 1\%$, and $\theta = 135°$. The results indicate increase in polarization with wavelength by 0.2%–0.4% at least some of the time. The intrinsic position angle for 1991 November and 1992 May shows a 30° rotation from the UV to the optical.

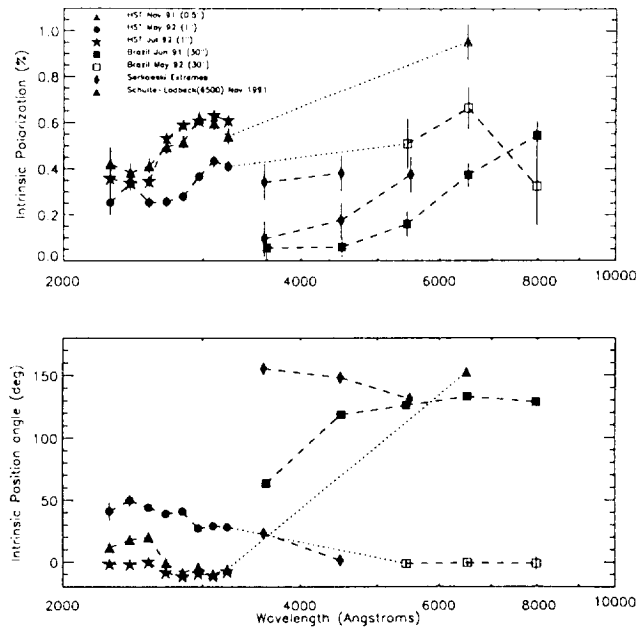

FIG. 7.—AG Car intrinsic polarization using a model for the interstellar component that is based on nearby stars, extracted from the catalog of Klare, Neckel, & Schnur (1972). Note that the nearby stars exhibit a 10° range in position angle and a 0.3%–0.4% range in P_{max}.

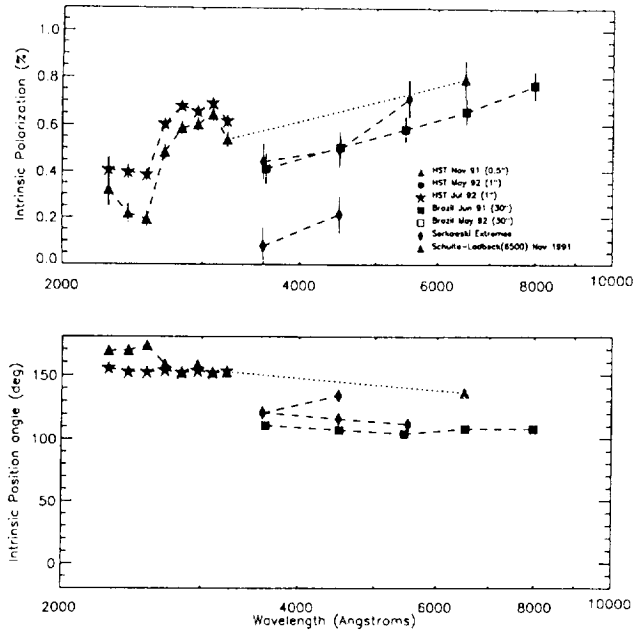

FIG. 8.—AG Car intrinsic polarization using a model for the interstellar component that is based on the 1992 May AG Car data, where the 0.5% drop in polarization suggests that the intrinsic component may have disappeared or have been "cancelled out."

Figure 8 displays the resulting polarization when another model for the interstellar polarization is assumed. Here we adopted a very high value of $\lambda_{max} = 7000$ Å and $P_{max} = 1.1\%$, $\theta = 149°$. These values follow from the assumption that the 1992 May data are not contaminated by any intrinsic polarization, i.e., they are exclusively due to interstellar polarization. The drop in polarization in 1992 May indeed suggests that the component of intrinsic polarization was at a minimum or had disappeared (or was cancelled by changes in the geometrical configuration of asymmetry). Of course, a minimum polarization can be achieved by adding an equal but opposite intrinsic component to the interstellar component. With this model, a 0.2%–0.3% slope is seen in the polarization but the position angle is much flatter.

There are ways to produce a wavelength dependence in the polarization and for this to change as a function of time. Electron scattering polarization is flat with wavelength. McLean (1979) first showed for Be stars that this *flat* polarization could be sculpted by the effects of absorption by hydrogen. In effect the polarization decreases toward the hydrogen series limits. Cassinelli, Nordsieck, & Murison (1987) confirmed that this polarization wavelength dependence can be generated by plumes in hot stars. Taylor & Cassinelli (1992) addressed the polarization wavelength dependence for a two-component (disk + plume) model. In this model, the wavelength dependence for a pole + plume-dominated polarization was shown to have an opposite effect than a disk-dominated polarization, i.e., rather than decreasing as the polarization approaches the series limits, the polarization can show an increase. The contribution from circumstellar dust also results in wavelength-dependent polarization which increases toward the UV. However, this effect should be minimal when observations are made with small apertures which address the innermost region of the star complex. The 30° position angle rotation as a function of wavelength that we see in AG Car is more difficult to explain even with the two-component wind model.

In summary, with the data and wavelength regime we have available, we find (1) AG Car has significant polarization. (2) The polarization is variable on a timescale of 2 months or less. (3) There is evidence that the polarization magnitude varies with wavelength and that the position angle also shows a wavelength dependence. Additional monitoring, i.e., simultaneous measurements over large wavelength regimes is essential for a more quantitative interpretation of these results. We propose an axial-symmetric geometry for the outflow with a variable, equatorial-disk-like density enhancement and a less dense polar wind as being consistent with the polarimetric observations. This geometry is quite similar to the wind structure derived from the spectroscopic observations described in § 4.2.

4. PHOTOMETRIC AND SPECTROSCOPIC EVOLUTION

4.1. *Continuum*

Our spectroscopic and spectropolarimetric campaign began in late 1990 when AG Car was in the steep, ascending part of its light curve (cf. Fig. 1). Observations during this period are particularly well suited to investigate relationships between the wind properties and the rapidly changing photospheric parameters since the spectral types range from late-O to about B2 during this time. In contrast, the only detailed wind analysis of AG Car published so far (Wolf & Stahl 1982) was done when AG Car was at maximum light around 1982. At that time, AG Car had an equivalent spectral type of early-A. If the light curve is extrapolated into the future, we would expect AG Car to reach a state similar to the one observed by Wolf & Stahl (1982) sometime in 1994/1995.

As a word of caution, the apparent periodicity implied by Figure 1 may be misleading. Comparison with light curves from earlier epochs (Mayall 1969) shows that the regular photometric behavior of AG Car over the last 15 yr is exceptional. The light curves obtained at earlier epochs during this century are much more irregular although part of the difference may be due to improved measurement techniques.

Superposed on the broad minimum between 1985 and 1990 are variations on a smaller scale with amplitudes of up to 0.3 mag. (Similar variations may also be present in the ascending and descending parts of the light curve but they would be more difficult to detect.) We performed a period analysis for the epoch 1985.0 until 1991.0, using the phase dispersion minimization algorithm within IRAF (Stellingwerf 1978). The most significant periods are 1.0 yr and multiples of this value. The most likely interpretation is one of observational bias. Observing conditions are strongly dependent on the observing season, in particular if the observations are done visually. This explanation seems even more likely considering that the largest scatter around the mean light curve occurs predominantly in the second half of each year when AG Car is close to the Sun and difficult to observe. We do not challenge the existence of the so-called "microvariations" (van Genderen et al. 1988), which occur on a timescale of days to weeks, with an amplitude smaller than the one discernible in Figure 1: typically 0.1 mag or less.

Viotti et al. (1984) first demonstrated that the brightness variations of AG Car in the visual are anticorrelated with the ultraviolet variability. Subsequently Lamers et al. (1989) refined the analysis of Viotti et al. and showed that the bolometric luminosity remains constant at $\log L/L_{\odot} = 6.2 \pm 0.2$ during an activity cycle, and that $E(B-V) = 0.63 \pm 0.02$. We

used all available low-dispersion ultraviolet observations of AG Car from the *IUE* archive (see Table 4) to determine the bolometric luminosity. The *IUE* data were combined with existing visual and near-infrared (Whitelock et al. 1983) photometry. We found that L = constant if $E(B-V) = 0.63$, in agreement with Lamers et al. (1989). Our somewhat more complete data set resulted in a luminosity which is slightly lower but still consistent with the one found by Lamers et al.: $\log L/L_{\odot} = 6.0 \pm 0.2$. A distance of (6 ± 1) kpc was adopted (Humphreys et al. 1989).

4.2. *Ultraviolet Lines*

A montage of selected *IUE* high-dispersion obtained between 1980 and 1992 is shown in Figure 9. The variations of the line spectrum reflect the very different photospheric and wind conditions at the various epochs. In comparison with the optical lines, the ultraviolet line spectrum shows less dramatic variations. In particular, few variations are apparent between the epochs of our ground-based and *HST* observing campaign. One reason is that many ultraviolet features originate far out in the wind, with correspondingly long response times to variations in the inner regions. However, we will argue below that the ultraviolet properties of AG Car's wind are indeed different from the optical properties.

Many of the UV P Cygni lines in the *IUE* spectra indicate a terminal wind speed close to the -250 km s^{-1} value obtained from the 1990 December Hα observations (see § 5). We measure -290 km s^{-1} at the steep blue edge in both components of the Mg II resonance doublet ($\lambda\lambda$2795, 2802), and the Al II λ1671 line, with little or no variation over the entire span of observation with *IUE*. All velocities refer to the heliocentric system. Somewhat lower terminal velocities can also be identified (-260 km s^{-1} in Fe II λ2585, -250 to -200 km s^{-1} in Si II λ1808 and Ni II λ1455). For the most part, the majority of the P Cygni features mentioned above have well delineated edges. In general, the smaller terminal velocities also tend to be the most variable, although this is likely due to saturation effects in the strong resonance lines such as Mg II. This variability, coupled with the frequent contamination of profiles with overlapping photospheric lines or other wind lines, makes estimation of reliable velocities somewhat difficult in certain cases, even when the blue edge of the profile is steep (i.e., the Fe II λ2599 resonance line appears to have an edge velocity in excess of -400 km s^{-1}, but this is probably an overestimate caused by the neighboring Fe II λ2598 line). Nevertheless, although the observations do not support a simple linear increase in terminal velocity with decreasing excitation, as suggested by Johnson (1982) and Caputo & Vioti (1970), they are qualitatively consistent with the picture of a wind with the excited state transitions forming near the star, where the wind is densest, and gradually accelerating outward, with the maximum velocity showing up in the ground-state lines.

Several rather remarkable spectral signatures complicate this simple picture of a slow, gradually accelerating, dense wind in AG Car. The first of these relates to what may be called "fine structure" in the unsaturated P Cygni line profiles. This phenomenon was first observed among the Fe II lines in P Cygni by Cassatella et al. (1979) and in AG Car by Johnson (1982). Johnson interpreted the variability of the relative strengths of the doubled absorption features (at -175 and -25 km s^{-1}) as evidence of mass ejection "events"; i.e., shells or puffs ejected at different epochs (spectra A and B in Fig. 9, separated by 194 days) with different accelerations.

Johnson (1982) stressed that the variability of the -25 km s^{-1} feature precluded its being interstellar, and the evidence of 10 more years of observation shows him to have been correct on this point, although there is indeed a very strong interstellar component in the spectral line profiles. For example, the λ2585 ground-state transition of Fe II (multiplet 1) shown in Figure 10 with the full line, includes a broad (125 km s^{-1}) absorption in *every* LWR and LWP spectrum. During the phase of optical minimum, when AG Car was at its hottest (here represented by epoch J), the line is largely due to interstellar absorption, since most of the Fe II is ionized to Fe III (note, however, that the centroid of the feature is offset by about -25 km s^{-1}). The dotted line in each plot shows the P Cygni profile due to the 0.08 eV excited state in Fe II (1) at λ2631.32. Although the IS absorption at zero velocity is clearly absent, as to be expected for an excited state, the absorption at ~ 50 km s^{-1} is definitely variable. Thus, the broad absorption of Fe II λ2585 near rest velocity is undoubtedly a superposition of a true IS component and a variable-strength low-velocity wind line.

At epochs before and after optical minimum a deep P Cygni absorption at higher velocity is also present, extending out to -400 km s^{-1} in the λ2585 resonance line, but only to -300 km s^{-1} in the excited state line. Careful examination of these profiles, and of similar profiles in other lines, reveals multiple weak features, some of which are common to both transitions. As Johnson (1982) pointed out, it is at times difficult to identify such features as photospheric or as wind components. In order to shed further light on this question we show in Figure 11 the superposed line profiles of Fe II λ1608.45 (observed with the SWP camera), and Fe II λ2585.88 (observed with the LWP camera) at eight of the 9 epochs common to both cameras. There appears to be a significant degree of agreement between the two lines, even among the weak absorption features (see especially, epoch K). Both of these are reasonance lines and have almost equal oscillator strengths and both include an interstellar component. But because they were measured in two different cameras, and two entirely different wavelength regions, it is highly unlikely that this correspondence is due to detector systematics (i.e., fixed pattern noise) or photospheric lines. Hence, these features must be real. Further, they suggest that several, perhaps many, distinct shells of gas exist in the wind of AG Car, ejected in different events during the course of evolution of this unstable star and now superposed along our line of sight.

The most conspicuous deviation from the behavior described above is seen in the P Cygni profiles of the Si IV resonance doublet at $\lambda\lambda$1393, 1402 (see Fig. 12). During optical minimum the Si IV lines are much stronger than at other phases, as to be expected for a highly ionized species. But what is most interesting about these lines is the gradual climb back toward the continuum, rather than abrupt edge seen in most other lines, and the large velocity of the bluest features identifiable with this flow (-900 to -1000 km s^{-1}). The superposition of the doublets profiles in Figure 12 lends credibility to the claim that the wind really does extend to such a high velocity in Si IV and is not merely attributable to contamination by other lines or by photospheric Si IV. Some contamination by the broad wings of photospheric Si IV may contribute to the broadening of the profile when AG Car was at its hottest. However, it seems unlikely that this could be the case when AG Car was later than spectral type early B. Further, close inspection of Figure 12 suggests that here too fine structure may be present, reminiscent of discrete absorp-

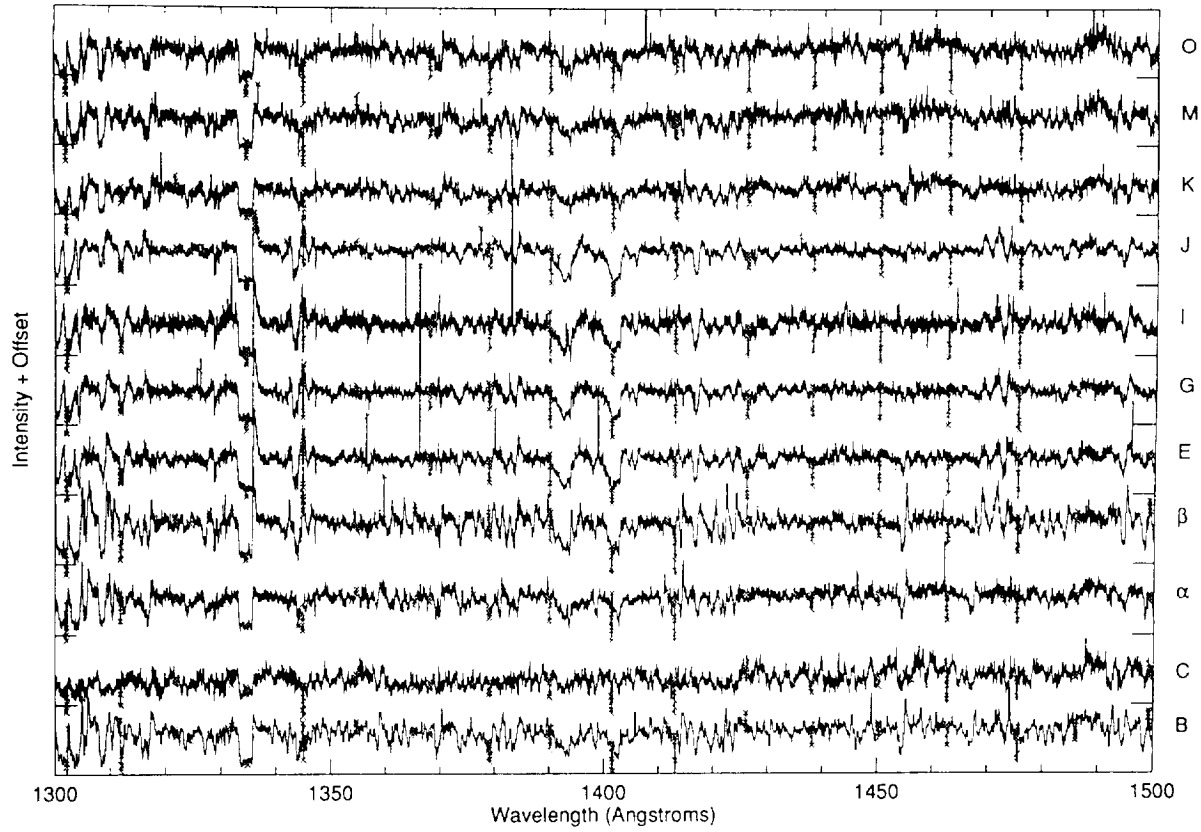

FIG. 9*a*

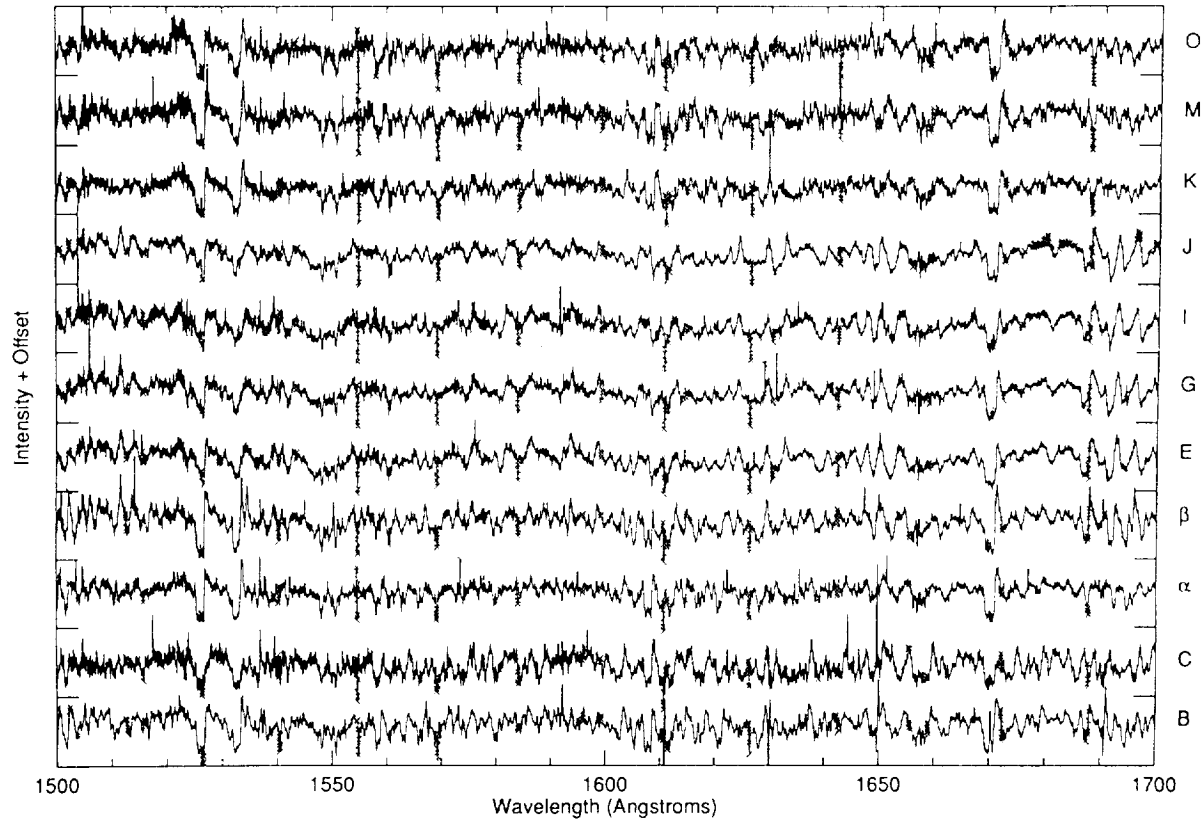

FIG. 9*b*

FIG. 9.—Montage of selected *IUE* high-dispersion spectra covering the period 1980 to 1992. Labels on the right vertical axis correspond to the labels in Fig. 1. (*a*) Wavelength region 1300–1500 Å. (*b*) 1500–1700 Å. (*c*) 2500–2700 Å. (*d*) 2700–2900 Å.

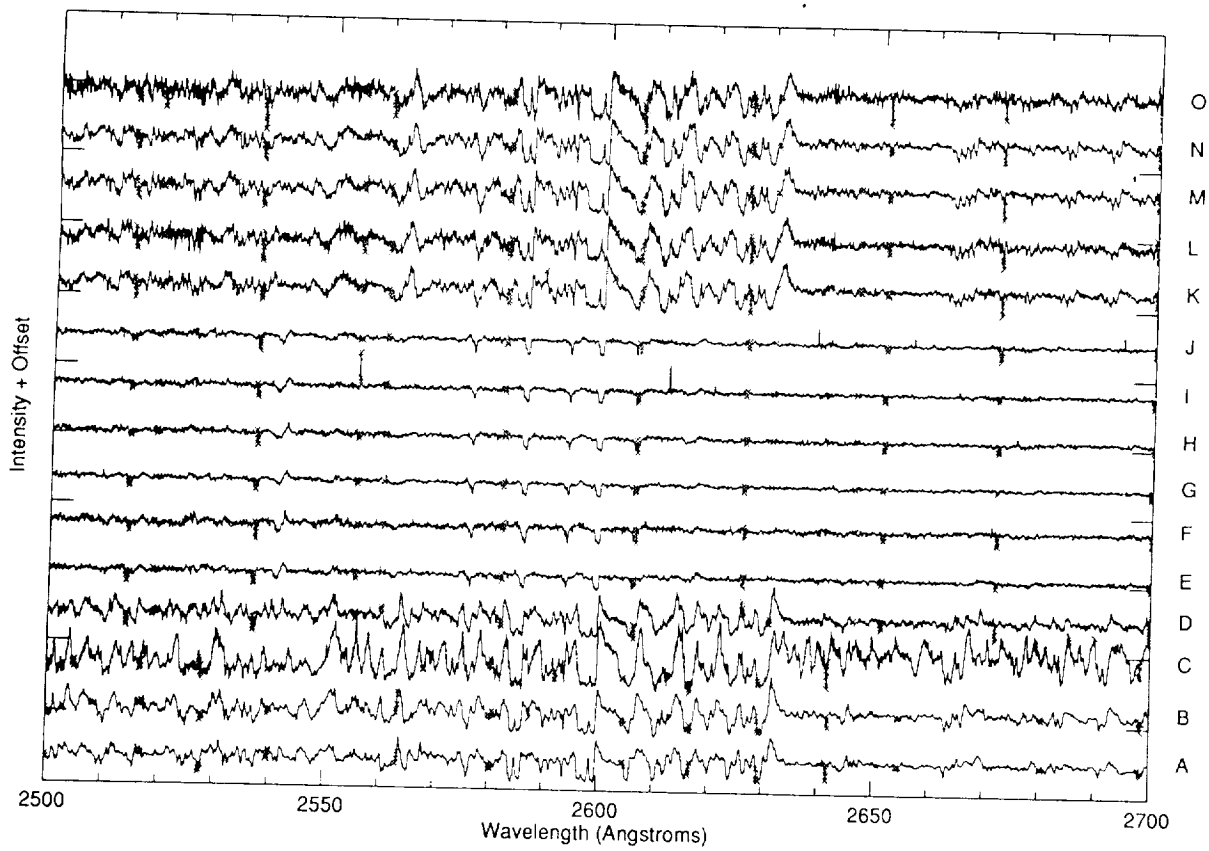
Intensity + Offset
O
N
M
L
K
J
I
H
G
F
E
D
C
B
A
2500
2550
2600
2650
2700
Wavelength (Angstroms)

FIG. 9c

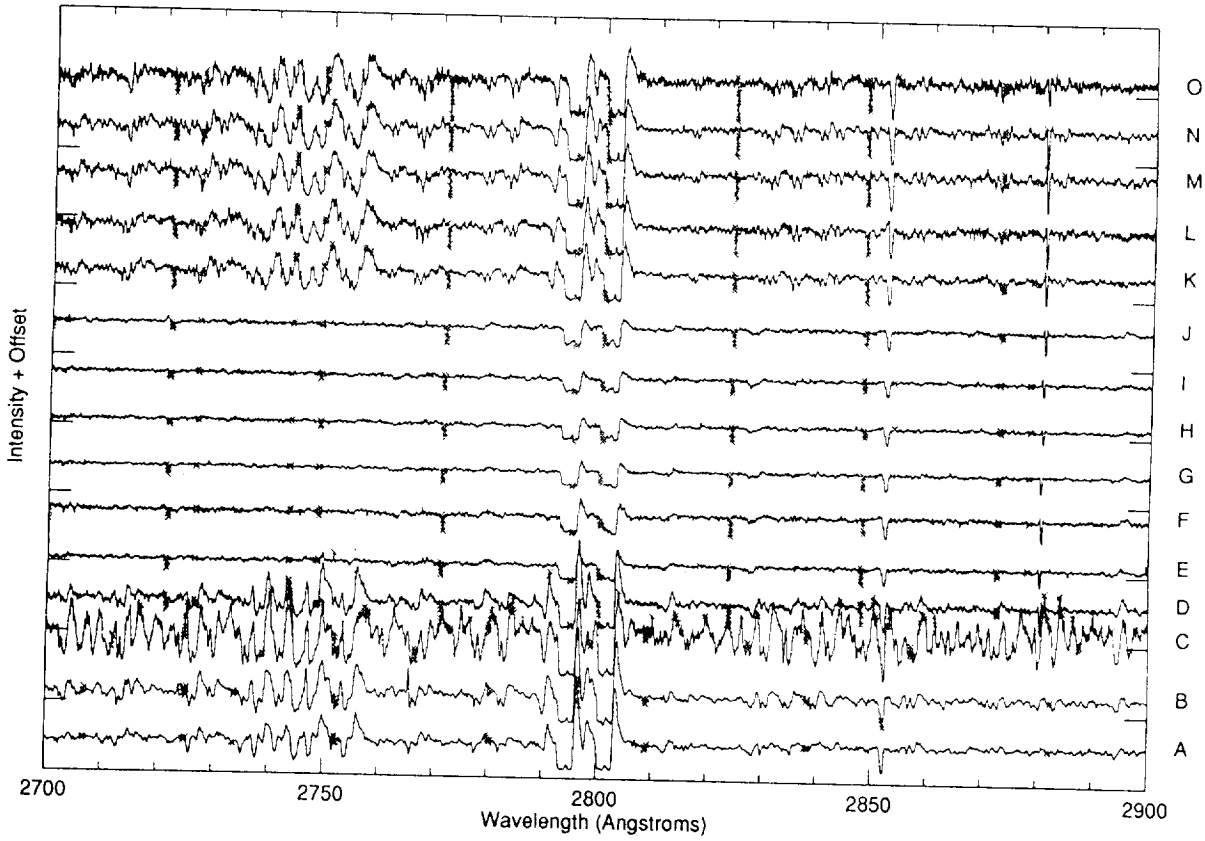
Intensity + Offset
O
N
M
L
K
J
I
H
G
F
E
D
C
B
A
2700
2750
2800
2850
2900
Wavelength (Angstroms)

FIG. 9d

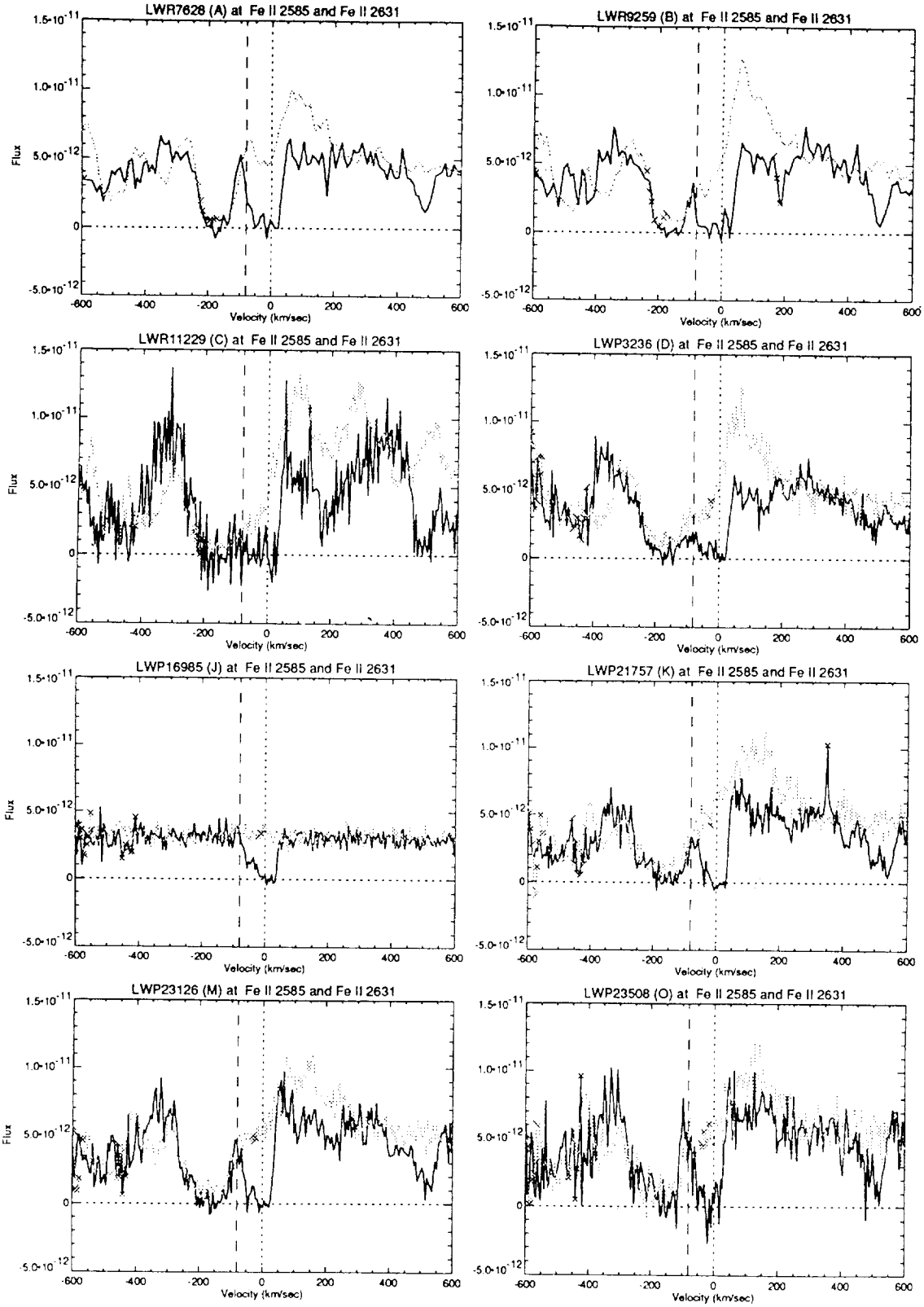

FIG. 10.—Selected profiles of Fe II λ2585 (*solid line*) and Fe II λ2631 (*dotted line*). Letters in parenthesis at the top of each figure refer to the epochs indicated in Fig. 1. Notice the different behavior of Fe II λ2585 (a resonance line) and Fe II λ2631 (an excited line). Vertical lines indicate the zero velocity, as well as the blue-edge velocity of the absorption feature at epoch J.

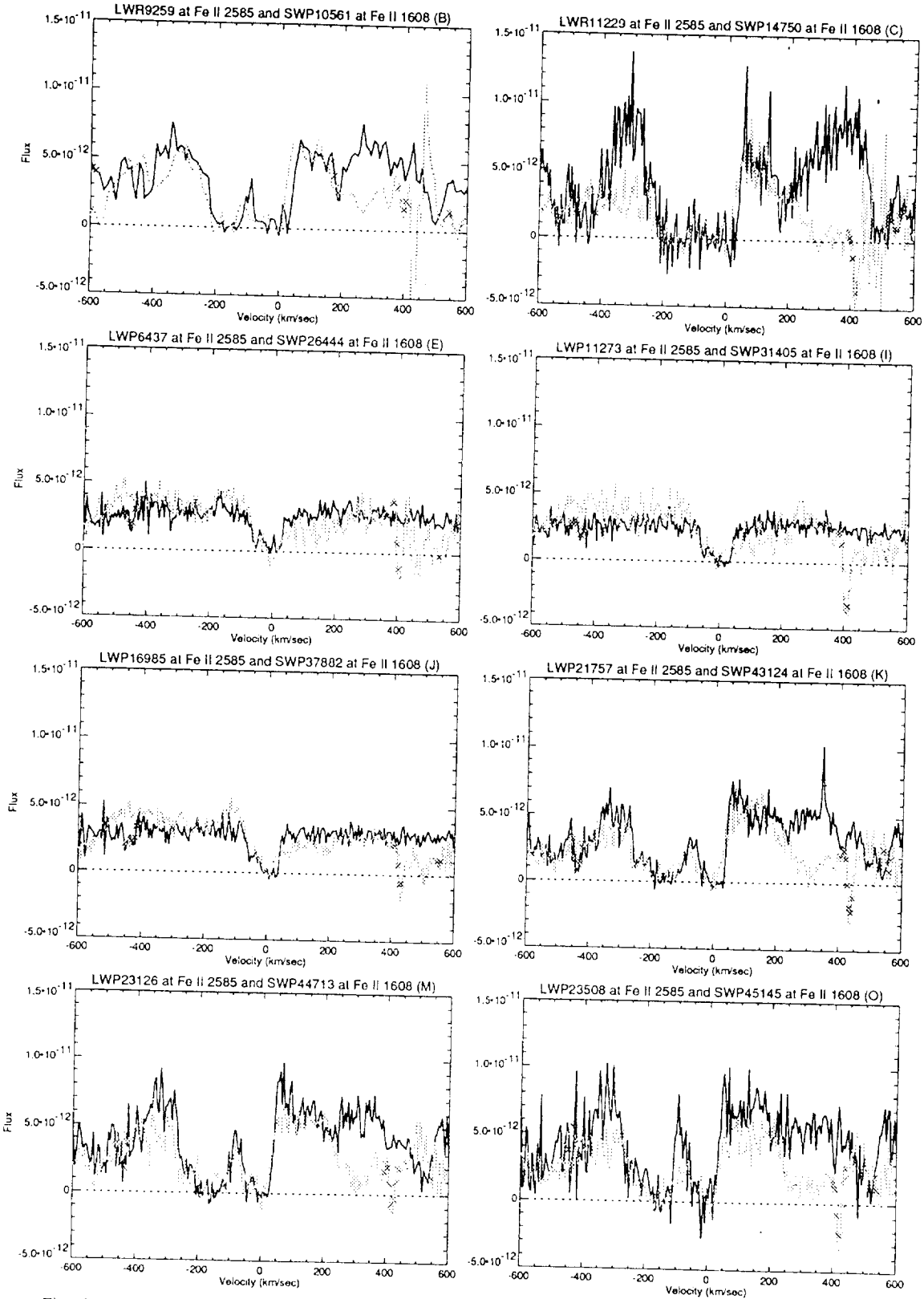

FIG. 11.—Same as Fig. 10, but for Fe II λ2585 (*solid line*) and Fe II λ1608 (*dotted line*). Both lines originate from ground states and have comparable oscillator strengths but were observed with different cameras.

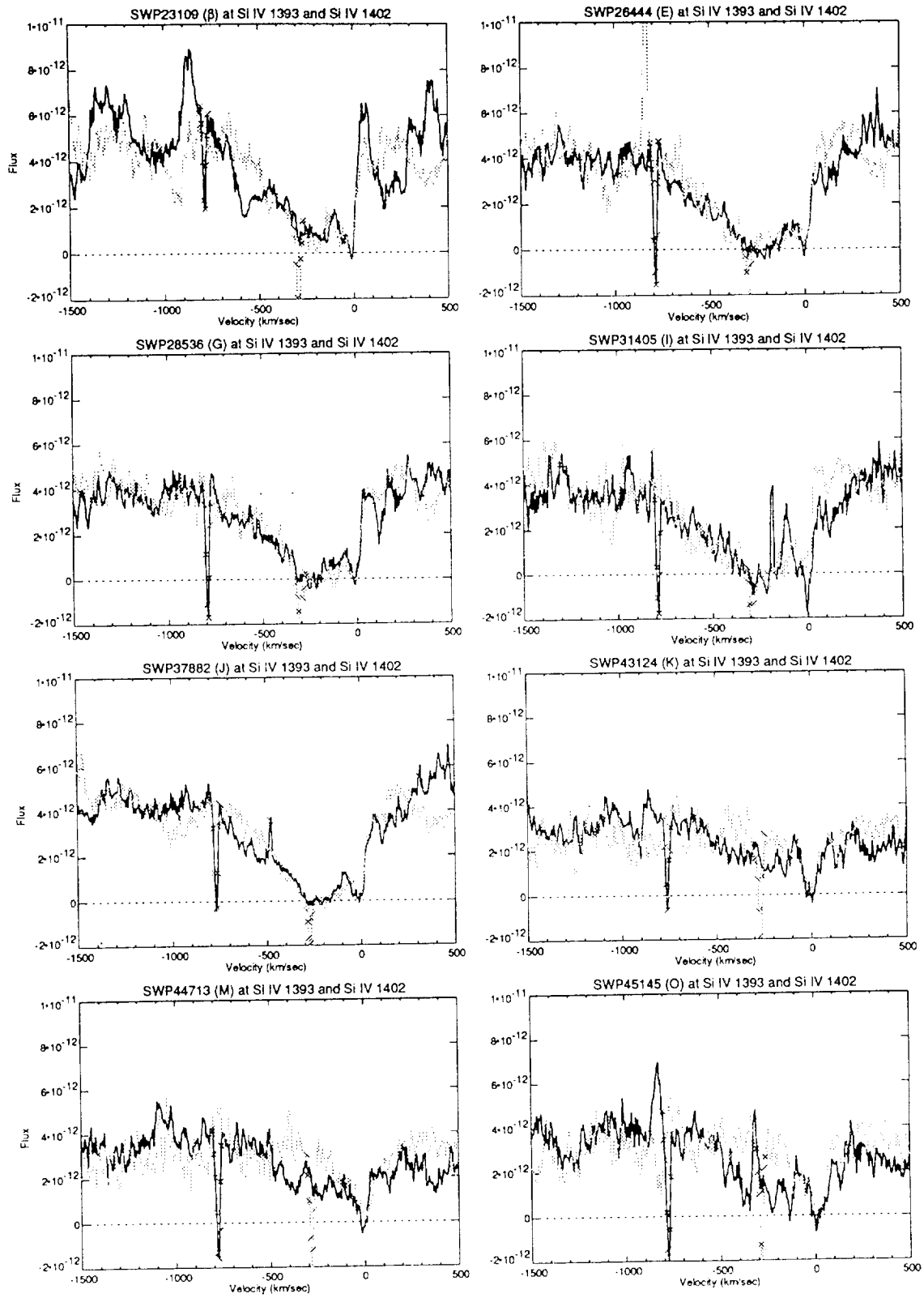

FIG. 12.—Same as Fig. 10, but for the Si IV doublet λλ1393, 1402. *Solid line*: λ1393; *dotted line*: λ1402. The blue wings extend to velocities of up to -1000 km s^{-1}.

tion component in the OB supergiants. This fine structure may to some degree be due to contamination by photospheric Fe lines. Hubeny, Štefl, & Harmanec (1985) demonstrated that an iron blend at ~1400 Å can mimic the Si IV line in the photospheres of late-B stars. Therefore we cannot exclude the possibility that iron lines contribute to the absorption in the Si IV line, especially at epoch O (cf. Fig. 12).

Although wind velocities of up to 1000 km s^{-1} on the basis of Si IV are uncertain, the terminal velocities observed in the ultraviolet are definitely higher than in the optical, and they show hardly any variation. We find $v_\infty \approx 400$ km s^{-1} from the Fe II lines and possibly higher velocities from Si IV. This may be compared to the value seen in Hα, which does not exceed 250 km s^{-1} and may temporarily be as low as 50 km s^{-1} (cf. § 5). The coexistence of both a slow, dense wind and a faster, less dense wind is suggestive of the phenomena observed in Be and B[e] stars. We note that the velocity measured in the ultraviolet lines is high enough to make travel-time effects less important than in, e.g., the Hα line. Therefore the fast wind cannot be a relic of an earlier physical state of AG Car. Zickgraf et al. (1985) proposed a two-component wind for the B[e] star R126 based on its hybrid spectrum. On the one hand, narrow emission lines in R126 indicate the presence of a slow equatorial wind, and on the other, blueshifted ultraviolet absorptions suggest high wind velocities of 400 km s^{-1} or higher. Despite the somewhat lower terminal wind velocity observed in the lines of AG Car, the overall wind geometry of AG Car is very reminiscent of the situation in B[e] stars.

Curiously, in AG Car, the C IV doublet lines (λλ1548, 1550) apparently do not participate in this high-speed flow, being rather narrow and only slightly asymmetric. Most likely this is an ionization effect, since the ionization potential of C III is more than 14 eV above that of Si III—unlike Si IV, the C IV lines show no dramatic change as AG Car varies in spectral type. Both Si IV and C IV, and even N V, provide important evidence of variable superionization in Be stars (see the review by Snow & Stalio 1987) and in B[e] stars (Zickgraf 1992). On the other hand, the C IV profiles in AG Car are consistent with a predominantly photospheric origin, supporting the view that Si IV might as well (at least partially) be contaminated by a photospheric contribution. This was also found to affect the determination of v_∞ in the Ofpe/WNL star R84 (Schmutz et al. 1991).

It is remarkable how constant the outflow velocity remained during the 12 years of *IUE* observations. No significant variation of v_∞ can be claimed on the basis of ultraviolet absorption lines. Most variations are due to changes in the wind- and stellar temperature which cause different ionization conditions. In contrast, the wind density and velocity *as observed in the ultraviolet* is relatively constant.

4.3. *Spectral Lines in the Optical*

In Figure 13 we show a selection of our ground-based spectra. The individual spectra in each figure are normalized to unity and displaced in the y-direction for clarity. The dates in the figure can be used to identify the spectrum in the log of observations in Table 5.

He I λ6678 exhibits a dramatic change from a strong emission and associated blueshifted absorption with a net equivalent width of 6.0 Å in 1990 December, to a very weak line with a net equivalent width of 1.7 Å in 1992 June. The behavior can be understood in terms of changing wind density and decreasing temperature. AG Car had an equivalent spectral type of late-O at the end of 1990 based on the presence of He II λ4686 (see Leitherer et al. 1992). Subsequently the He II feature faded, and we found no evidence for its presence in 1992 June. At that epoch the equivalent spectral type was approximately early- to mid-B. The equivalent width of He I λ6678 clearly correlates with the visual continuum flux, as can be seen in Figure 14. The values for the visual flux in this figure were derived from the data in Figure 1, after dereddening with $E(B-V) = 0.63$ and $A_V/E(B-V) = 3.1$. The value of $E(B-V)$ follows from our ultraviolet analysis under the assumption $L = \text{const}$. He I is strongest when the visual flux is highest. The visual flux rose continuously between 1990 December and 1991 December. During the first few months of 1992 the flux decreased but increased again after epoch 1992.3. Interestingly, He I shows exactly the same behavior. The errors of the equivalent width of He I (and also of Hα) are largely due to the uncertainties of the adopted continuum. Both He I λ6678 and Hα have broad, shallow line wings which contribute significantly to the total equivalent width. These wings are attributed to electron scattering in the outflow (see below). We estimate that the derived equivalent widths have errors of 10% or less. Therefore the rise of the He I equivalent width from 1991.9 to 1992.2 and the subsequent decline at 1992.4 is significant. It is also in accord with the observed profile change (cf. Fig. 13).

The decreasing temperature of AG Car during our observing period favored the appearance of spectral lines of lower ionization. Typical examples are the transitions at λ8629 and λ8680 of N I multiplets (8) and (1), respectively (see Fig. 13). These lines were absent in 1990 December when He II was still recognizable in the spectrum. They increased in strength at later epochs due to ionization conditions in the outflow which favored the formation of N^0. At the same time, the profiles become narrower indicating a lower density and/or lower outflow velocity. The near-IR spectrum of AG Car resembles the one of η Car (Thackeray 1969) with respect to the presence of N I lines. This suggests rather similar temperature and density conditions in these two related objects. On the other hand, AG Car shows significantly stronger N I lines than P Cyg (see Stahl et al. 1993), although P Cyg is supposed to be related to LBVs (Humphreys 1989), and the spectral type of AG Car during 1991 was similar to the one of P Cyg (B1 Ia$^+$). This may suggest that nitrogen is more abundant in AG Car than in P Cyg but stronger observational support is certainly needed for this hypothesis.

Among the most striking characteristics of LBVs is the variability of ionized forbidden and allowed metal lines (e.g., Wolf 1989). The presence or absence of Fe II and [Fe II] lines can be used to describe the physical conditions in the stellar envelope (see Wolf, Appenzeller, & Stahl 1981 for R71). In Figure 13 we show the evolution of Fe II λ9997. This line has also been detected in η Car (Thackeray 1969) and is ascribed to the multiplet $z\,^4F^o_{9/2}$–$b\,^4G_{11/2}$ (Johansson 1977). Fe II λ9997 was first detected in 1991 August but is clearly absent in our spectra of 1990 June and December. Fe II λ9997 and the N I lines discussed before behave very similar in that respect. The similar ionization potential of Fe II (16.2 eV) and N I (14.5 eV) suggests that this is predominantly an ionization effect. Further support for this suggestion comes from the iron spectrum in the ultraviolet. The decrease in the strength of Fe II λλ2585, 2599 during optical minimum, when AG Car was hottest, is most likely due to ionization from Fe$^+$ to Fe^{++} (see § 4.2). As in the case of the N I lines, we note the decreasing line width of Fe II λ9997 with time.

We observe both forbidden and allowed iron lines in the

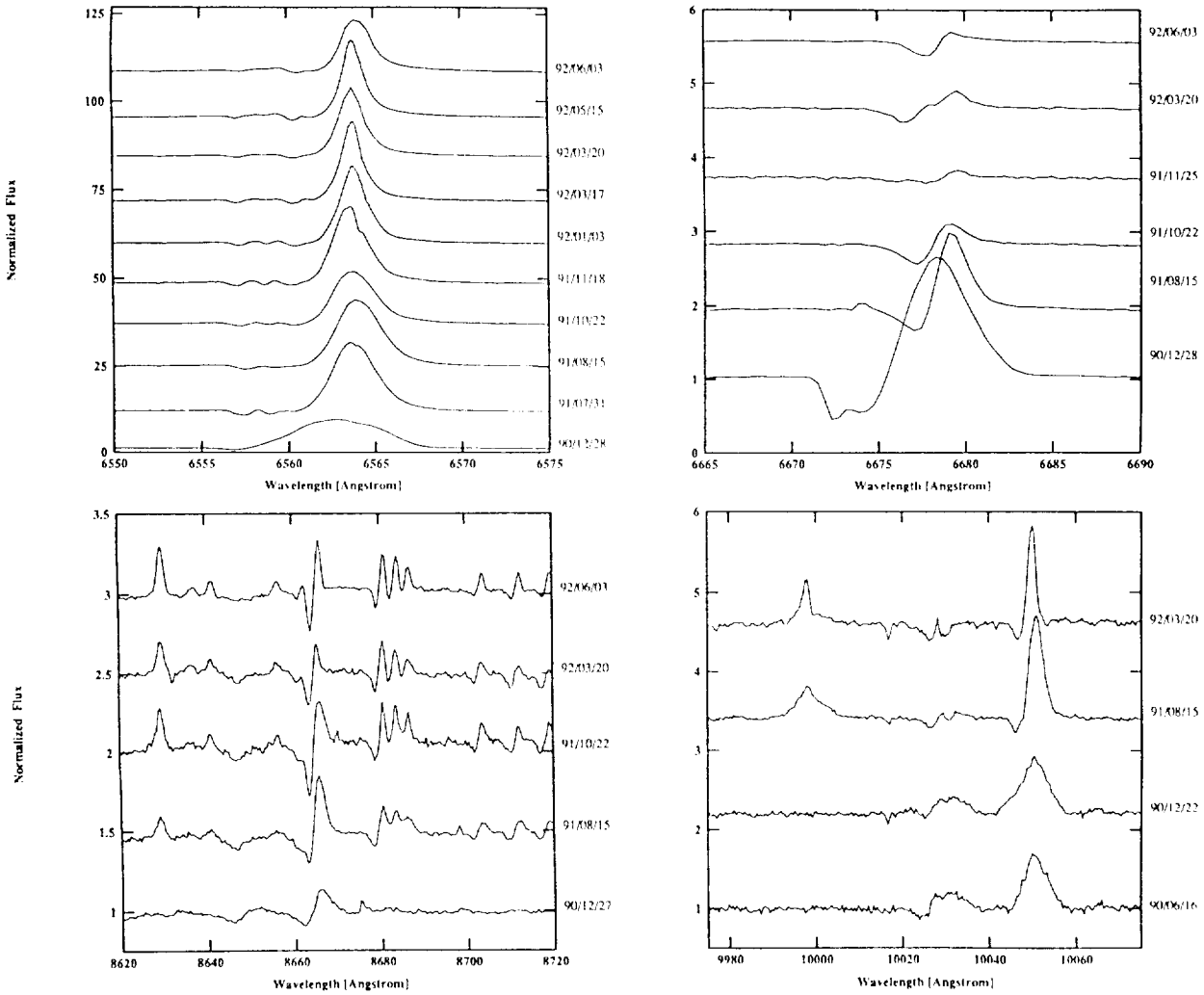

FIG. 13.—Ground-based spectra of AG Car. Four representative spectral regions are shown. The continua are normalized to unity and displaced by a constant δ in all cases. Spectral regions are around Hα (δ = 11.9), He I λ6678 (0.9), Fe II λ9997 (1.2), and N I multiplet (1) $\lambda\lambda$8680 (0.5). The sequence is clockwise, starting from upper left.

spectrum of 1992 June (Fig. 15). Wolf et al. (1981) and Leitherer et al. (1985) observed a correlation between the strength of these lines and the activity state of the LBV in R71 and S Dor, respectively. Forbidden lines dominate when the star is in its photometric minimum, i.e., hottest, and allowed lines take over during maximum state when the surface temperature is lowest. Comparison of Figure 15 with Figure 8 of Leitherer et al. (1985) suggests that the physical conditions in the envelopes of AG Car in 1992 June and of S Dor in 1984 August were somewhat similar. Close inspection of Figure 15 reveals that the profiles of Fe II and [Fe II] are quite different. Allowed lines [such as Fe II (27) λ4233 or Fe II (27) λ4352] are narrow. In contrast, forbidden lines {such as [Fe II] (21) λ4244 or [Fe II] (7) λ4287} are much broader and appear to be *flat topped*. [Fe II] λ4244 is generally formed at lower densities than Fe II λ4233 (Viotti 1976). Since flat-topped profiles are formed in an outflow with a constant velocity (Israelian & de Groot 1992), they could originate further out in the wind at lower densities where the terminal velocity of the outflow has been reached. The half-width of the lines suggest a velocity of $\sim$200 km s^{-1}. However, one should keep in mind that this does not indicate the terminal velocity of the material ejected from the stellar surface in 1992 June. Due to the flow timescale (several months), this value describes wind properties appropriate for an earlier epoch when the velocity was still higher (see below for a discussion).

Hα is the most prominent emission line in the observed spectrum during all epochs (see Fig. 13). Its main characteristics are: a strong emission component reaching up to 25 times the continuum level, broad, shallow electron scattering wings (these wings are not easily visible at the scale of Fig. 13), and several discrete absorption components. Hα is mainly a measure of the wind density, and to a smaller degree, of the stellar temperature. The variation of the equivalent width $W_{\rm H\alpha}$ with time is plotted in Fig. 14. $W_{\rm H\alpha}$ includes the emission part, the absorptions, and the broad wings. No attempt was made to remove the numerous telluric absorption lines in this wavelength region. Their effect on the Hα equivalent width is negligible. $W_{\rm H\alpha}$ increased from the end of 1990 until mid 1991 and decreased again to its original level. The basic trend visible in Figure 14 remains unchanged if we exclude the broad wings from the measurement of $W_{\rm H\alpha}$, although of course $W_{\rm H\alpha}$ is then significantly decreased (by up to a factor of 2 after 1992 January). Figure 13 demonstrates that the variation of $W_{\rm H\alpha}$ is

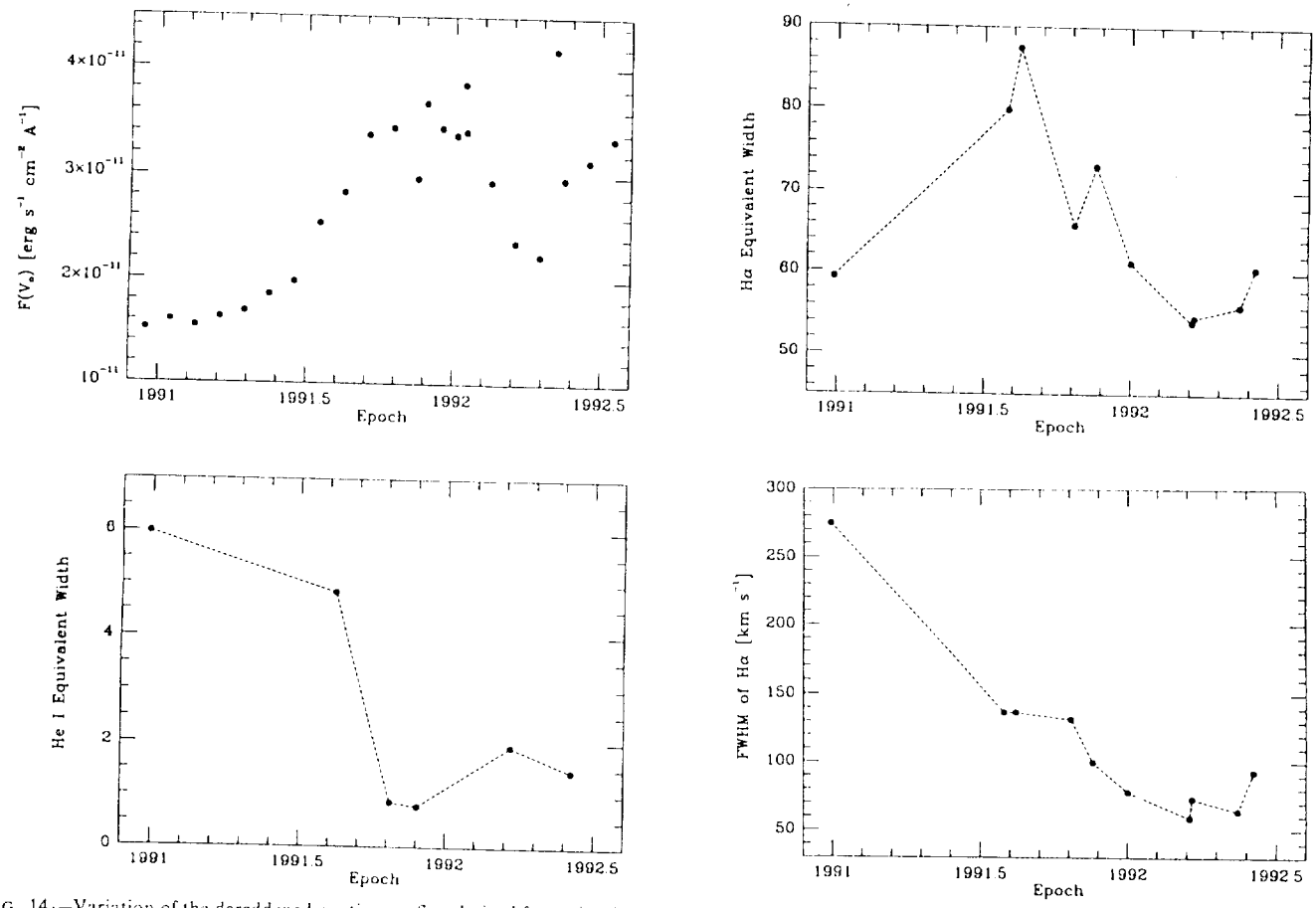

FIG. 14.—Variation of the dereddened continuum flux derived from visual observations, the equivalent widths of Hα and He I λ6678 (in angstroms), and the full width at half-maximum of Hα.

not simply due to a scaling of the line flux but that qualitative changes of the Hα profile occur. Hα is very broad in 1990 December. Subsequently, an increasingly pronounced emission core develops, which is narrowest between 1992 March and May. In 1992 June, the profile becomes broader again, resembling the situation in 1991 August. We measured the full width at half-maximum of Hα. The results are in Figure 14. The line width is determined by the outflow velocity. The decrease of FWHM suggests that the velocity decreased by about a factor of 4 during the observing campaign.

Other lines of hydrogen show the same qualitative behavior as Hα. We present P_7 λ10049 and P_{13} λ8665 as examples in Figure 13. P_{13} forms sufficiently close to the stellar surface that P Cygni absorption is visible during all epochs. The heliocentric velocity of the absorption component is -130 km s^{-1} in 1990 December and decreases to -50 km s^{-1} in 1992 March. This effect is also measured in the other Paschen lines. We do not expect the Paschen lines to indicate the terminal velocity of the outflow. Most likely, they form in the inner, still accelerating part of the wind. Interestingly, the velocity of the P_7 absorption component varied by a similar factor as the FWHM of Hα during the observing campaign. This suggests that the general shape of the velocity law is preserved although the flow velocity changed with time.

The variability of the outflow velocity detected in the hydrogen lines is very different from what is observed in the ultraviolet. Part of the difference may be due to travel-time effects. Hydrogen lines form closer to the star than typical strong ultraviolet resonance lines, and it will take a longer time to observe variations in the ultraviolet. However, the relative lack of variability *over 12 years of IUE* observations rules out this possibility as the only explanation. More likely, the wind conditions observed in the optical and the ultraviolet are really different. The optical wind spectrum is dominated by recombination lines which form in the densest part of the outflow,

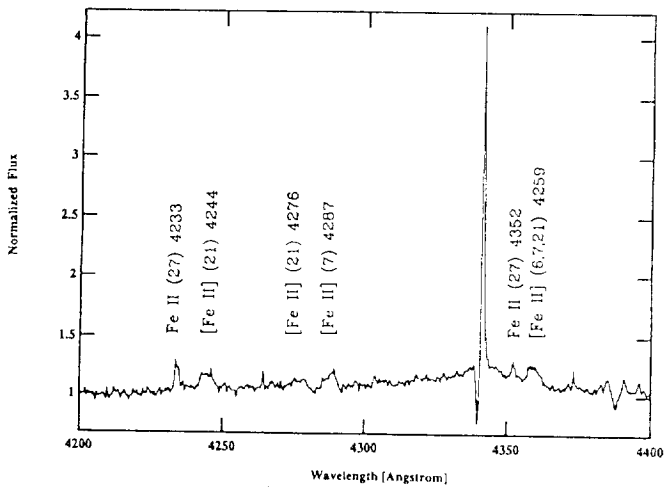

FIG. 15.—Spectrum of AG Car around 4300 Å at epoch 1992 June 3. Broad, flat-topped lines of [Fe II] and narrow lines of Fe II are present.

which in our proposed model is in the disklike equatorial density enhancement. The hydrogen and helium lines indicate that this is the most variable part of AG Car's wind. It is this part of the wind which is responsible for the observed polarization variation. In contrast, the high-speed outflow observed in the ultraviolet lines is rather constant and less affected by varying photospheric conditions.

It is instructive to compare the spectral morphology of the three related objects AG Car, P Cyg, and η Car. In Figure 16 we present the spectral region $\sim$10,000 Å of these three objects. The spectrum of AG Car is the one obtained in 1991 August shown in Figure 13. The spectra of P Cyg and η Car were taken with the same instrumentation at the Brazilian National Observatory in 1991. We discussed before the strength of the nitrogen lines in AG Car, which may suggest that the abundance of nitrogen in AG Car is closer to η Car than to P Cyg. However, Figure 16 demonstrates that the wind characteristics are clearly more pronounced in η Car than in AG Car. P_7 and Fe II λ9997 are by far stronger in emission in η Car than in AG Car. The emission-line spectrum of P Cyg is somewhat less extreme than the one of AG Car. Note the broader, P_7 emission of P Cyg. Also, the absorption component has a more negative blueshift in P Cyg than in AG Car. The maximum outflow of P Cyg is 200 km s^{-1} (Lamers, Korevaar, & Cassatella 1985). Therefore the comparison of the P_7 profiles suggests that the outflow velocity of AG Car in 1991 August was significantly less than 200 km s^{-1}. This is consistent with the result of our wind analysis (see § 5).

Figure 17 is a close-up of Figure 13 showing the absorption components shortward of Hα. We selected only those spectrograms having comparable spectral resolution of $\sim$0.1 Å. Four discrete absorption components are present. We find no significant radial velocity variation with time. The four components are at -250 km s^{-1}, -180 km s^{-1}, -110 km s^{-1}, and -70 km s^{-1} (heliocentric). The four components are highly variable in strength. In general, the faster components are stronger at earlier epochs, and the slower components become stronger during later times. The constant velocity of the absorption components suggests that they are formed in regions expanding at constant velocity, and the decreasing strength is simply a consequence of the decreasing density. An alternative explanation has been suggested by Hillier (1992). He demonstrated that multiple absorption profiles can as well be obtained purely from radiative transfer effects without the need of discrete shells.

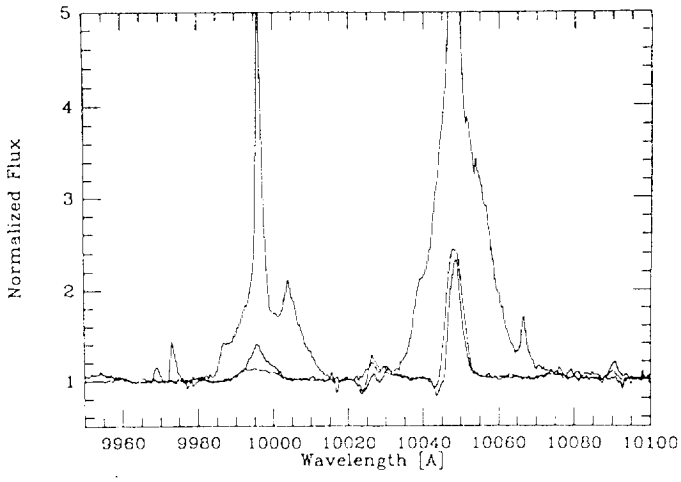

FIG. 16.—Comparison of the spectral region around P_7 in AG Car (*solid curve*), η Car (*dotted curve*), and P Cyg (*dashed curve*). The spectrum of AG Car was taken on 1991 August 15.

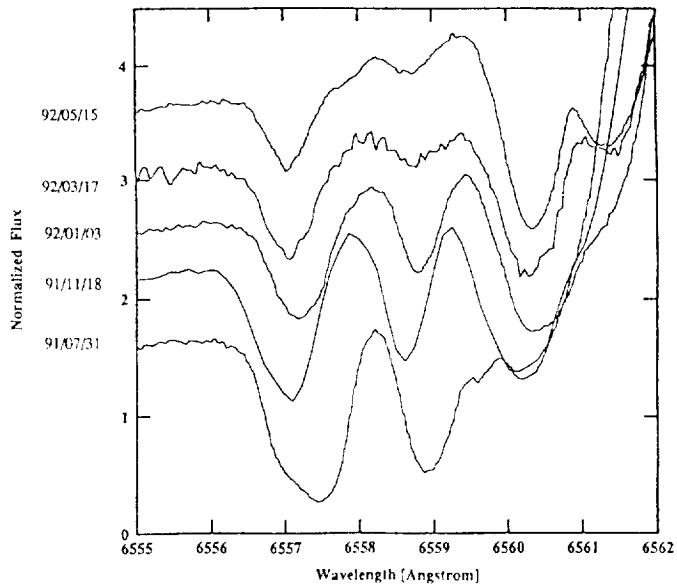

FIG. 17.—Blueshifted absorption components of Hα. All spectra plotted have similar spectral resolution of $\sim$0.1 Å. Spectra are normalized to unity. Offsets of 0.5 have been added.

5. STELLAR-WIND PROPERTIES DERIVED FROM EMISSION-LINE DIAGNOSTICS

5.1. *Method*

Theoretical models for the atmosphere of AG Car were computed with a code described by Hamann & Schmutz (1987). The radiation transfer is solved in the comoving frame, and the coupling between the transfer and the statistical equilibrium equations is treated with the approximate lambda iteration technique (Hamann 1987). The model atmosphere is expanding and spherically extended, as required by the physical conditions in LBVs. The radius of the photosphere is defined as the location where Rosseland optical depth unity is reached. The outflow velocity may be sub- or supersonic at this location. Strong photospheric absorption lines are virtually absent in the spectrum of AG Car so that the velocity of the photosphere is difficult to determine. Moreover, most lines which have their origin close to the photosphere are situated in the blue spectral region. This region is not well represented in our observational material. Wolf & Stahl (1982) studied the radial velocities of various lines in the AG Car spectrum. They found -26 km s^{-1} for Mg II λ4481. This line forms close to the location of the photosphere (cf. S Dor; Leitherer et al. 1985) and provides an upper limit to the velocity of the photosphere. The small expansion velocity of Mg II λ4481 is consistent with our models which predict negligible photospheric velocities. Optical depth unity occurs at a velocity of $\sim$10 km s^{-1} in all our models.

Leitherer et al. (1992) published line profiles obtained with the model atmosphere described above. An important improvement over the models shown in that paper has been made: we are now including electron scattering as an additional mechanism to reproduce the broad wings around strong

emission lines. Such wings are typically found in very luminous hot stars. Bernat & Lambert (1978) attributed these wings to electron scattering of line photons in the ionized stellar wind of P Cyg. In our present study, we do not attempt to perform a detailed profile fit of every hydrogen and helium line for each epoch. Rather, we calculated a grid of representative model atmospheres covering the parameter space occupied by AG Car. The equivalent widths of Hα ($W_{\rm H\alpha}$) and He I λ6678 ($W_{\rm He\,I}$) as well as the continuum flux at 5555 Å (F_{5555}) are predicted by each model. This approach is very similar to the one taken by Schmutz, Hamann, & Wessolowski (1989), who presented diagnostic diagrams for the derivation of mass-loss rates of Wolf-Rayet stars from their emission-line strengths.

The main reason for our simplified approach is that the nature of AG Car precludes a very detailed analysis with our models. We demonstrated in §§ 3 and 4 that significant asymmetries prevail in the circumstellar envelope. In contrast, spherical symmetry is assumed in the model atmosphere. The variability of AG Car introduces a further complication. The typical flow timescale (e.g., for a gas element to travel from the photosphere to 10 stellar radii) is several months. This is comparable to, or even longer, than the timescale over which significant continuum variability occurs. A time-independent model atmosphere cannot predict the line cores (formed at low velocities) and the line wings (formed at high velocities) at the same time. Therefore we expect *absolute* wind properties (such as the mass-loss rate) to be relatively uncertain. Our main goal, however, is to search for relationships between photospheric and wind parameters during the variability cycle, such as the *relative* change of the mass-loss rate. At least to first order, relative quantities are less affected by asymmetries and variability of the outflow.

5.2. *Results*

We assume $\log L/L_\odot = 6.0$ for the analysis. This is consistent with our analysis of the *IUE* data. A model is completely determined by the temperature $T_\star$, the transformed radius R_t, and the abundances of hydrogen and helium. $T_\star$ is the temperature at Rosseland optical depth unity. We used the observed flux at 5555 Å to constrain $T_\star$. F_{5555} is primarily sensitive to $T_\star$ and has only a comparatively weak dependence on the wind density. The parameter R_t has been defined by Schmutz, Hamann, & Wessolowski (1989). Essentially it is a measure of the inverse wind density and scales with the stellar radius $R_\star$ at $T_\star$, the mass-loss rate $\dot{M}$, and the wind velocity $v(r)$.

We adopt a velocity law of the form $v(r) = v_\infty(1 - R_\star/r)$ for the supersonic part of the outflow. This corresponds to the parameterization of the velocity law in hot stars (Groenewegen, Lamers, & Pauldrach 1989), but with a somewhat higher power-law exponent of 1. Support for this particular choice comes from profile fitting of selected emission lines of AG Car (Leitherer et al. 1992), which are well reproduced with this velocity law. The same velocity law was also derived by Schmutz et al. (1991) from a detailed multi-line analysis of the Ofpe/WNL star R84, which is believed to be in an evolutionary state closely related to LBVs (Hillier 1992).

This leaves the terminal velocity v_∞ as the only free parameter for the velocity law. As already discussed, the flow timescale of the wind is several months, whereas significant photospheric variations occur within a few weeks. Therefore emission-line wings (even after correction for electron scattering) or blueshifted absorption components are difficult to use to derive v_∞ at a particular epoch if rapid changes in the wind properties occur. These features respond to changes in the inner part of the outflow only after several months. On the other hand, the line core of Hα forms much closer to the stellar photosphere and has a much shorter response time to changes in the outflow velocity. We compared the FWHM of Hα to v_∞ at epochs when v_∞ could be reliably determined from profile fits. Leitherer et al. (1992) found $v_\infty = 250$ and 120 km s^{-1} at epochs 1990 December and 1991 August, respectively. The decrease of v_∞ by a factor of 2 is also reproduced by FWHM, which also decreases by a factor of 2 (cf. Fig. 14). We assumed that the same scaling holds for subsequent epochs and calculated v_∞ from the full width at half-maximum of Hα after calibration with the derived values of v_∞ at 1990 December and 1991 August. The results are in Table 9.

The decrease of the outflow velocity deduced from the FWHM of Hα is also supported by the variable Hα absorption components (see Fig. 17). The fastest component at -250 km s^{-1} gradually decreased in strength from 1991 July to 1992 May. During this period, slower components increased in strength. The slowest absorption component observed is at -70 km s^{-1}. The presence of discrete components suggests that mass loss does not occur steadily but rather in a discontinuous way. The increase in strength of low-velocity components and the fading of high-velocity components are in agreement with an overall decrease of v_∞ of the wind region where Hα is formed. (Note that travel-time effects must be taken into account when comparing v_∞ derived from the absorption components and from FWHM).

Our arguments relating to the velocity field of AG Car's wind are only applicable if the wind is spherically symmetric. However, the results of the spectropolarimetry and the ultraviolet spectroscopy indicate the presence of an equatorial density enhancement. We expect optical recombination lines of hydrogen and helium to form preferentially in this equatorial region. This is consistent with our approach not to use the ultraviolet lines for a determination of v_∞ but to rely exclusively on Hα. On the other hand, it is likely that the equatorial wind has nonzero angular momentum. Therefore the observed line width of Hα may not only be caused by the outflow velocity but may also be influenced by rotation. However, we estimate the rotational broadening of Hα to be small as compared to the broadening caused by the outflow velocity. A reasonable upper limit to the rotation of the disk material is the rotational velocity of the star itself. In the course of its evolution from the main sequence to the LBV phase, AG Car's radius increased by at least an order of magnitude. The star could not have been gravitationally bound on the main sequence due to the high

TABLE 9

PROPERTIES OF THE STELLAR WIND

Epoch	$T_\star$ (K)	$R_\star$ ($R_\odot$)	FWHM(Hα) (km s^{-1})	v_∞ (km s^{-1})	$\log \dot{M}$(H) ($M_\odot$ yr^{-1})
1990 Dec	21,000	76	275	250	-4.7
1991 Jul	16,000	120	137	120	-4.4
1991 Aug	16,000	130	137	120	-4.6
1991 Oct	14,000	160	132	120	-4.7
1991 Nov	14,000	160	100	90	-4.8
1992 Jan	14,000	160	78	70	-5.0
1992 Mar	17,000	110	59	50	-5.2
1992 May	15,000	140	64	60	5.1
1992 Jun	15,000	150	93	80	-4.9

rotational velocity if a solid rotator model is assumed and if the present rotational velocity exceeded of few tens of km s^{-1}.

The grid of model atmosphere was calculated with equal abundances (*by mass*) for hydrogen and helium, i.e., $X = Y = 0.5$. In principle, the helium abundance of a hot star can be determined from an analysis of the type presented here once the mass-loss rate and the stellar temperature are constrained (see, e.g., Schmutz et al. 1991). In the case of AG Car $\dot{M}$ can be derived almost independently either from the hydrogen or the helium lines. However, the neutral helium lines are sensitive to both the temperature and the helium abundance. Without simultaneous modeling of He II lines, the temperature cannot be constrained (e.g., from F_{5555}) precisely enough to allow a reliable abundance analysis.

The results of our atmospheric analysis of AG Car are summarized in Table 9. $T_\star$ and $R_\star$ were first determined from the visual continuum flux, after normalization to the total bolometric luminosity. Subsequently, we verified that the choice of $T_\star$ reproduces the observed strength of He I λ6678 after the wind density was known from fitting the observed Hα strength. We find that $T_\star$ decreases from 21,000 to 15,000 K between 1990 December and 1992 June. Note that the slightly lower temperatures than in Leitherer et al. (1992) are a consequence of the smaller luminosity adopted here ($10^{6.0}$ vs. $10^{6.2}$). At the same time, the stellar radius increased by a factor of 2. This of course is a consequence of the assumption L = constant. We also derived the $T_{\rm eff}$ and $R_\star$ by fitting a classical Kurucz (1979) model atmosphere to the continuum. The results are not significantly different from those of the non-LTE analysis.

In Table 9 we list the mass fraction lost in hydrogen only. As helium makes a significant contribution to the total mass loss (see below), the values of $\dot{M}(H)$ are a lower limit to the total mass-loss rate. Despite the significant variation of the photospheric parameters, the mass-loss rate did not increase. Leitherer et al. (1992) already found that $\dot{M}$ of AG Car does not vary significantly with phase. We confirm their result and extend it to an even wider range of photospheric parameters. Contrary to previous suggestions (Lamers 1987), $\dot{M}$ does *not* scale inversely with temperature. The mass-loss rate is not higher when AG Car is cooler and visually brighter. In fact, if there is a correlation in the data of Table 9, it is just in the opposite sense: $\dot{M}$ is *lower* at the beginning of 1992 than in 1990 December although the temperature had dropped by 6000 K. However, the decrease in $\dot{M}$ is mostly due to the lower v_∞. Recall that we adopted v_∞ as derived from Hα, which displayed significant variability. On the other hand, the ultraviolet lines do not indicate any significant variation of v_∞ between the epochs of our observations. We argued above that Hα and the ultraviolet lines originate in different wind regions. Our non-LTE analysis refers to those parts of the wind where optical recombination radiation originates, which most likely is in the disklike equatorial density enhancement. The ultraviolet lines are unlikely to indicate the terminal wind velocity in this region. If this is not true, v_∞ used in our non-LTE analysis after 1990 December would be too low, and the derived $\dot{M}$ would be too low, too. Therefore, we do not claim that $\dot{M}$ actually *decreased*. But even under the very conservative assumption of v_∞ = *constant* during all epochs, $\dot{M}$ would at least *not increase* for lower temperatures.

We estimated the He abundance of AG Car from the spectroscopic data of 1990 December. At that epoch AG Car had the highest temperature, and the theoretical models are least sensitive to temperature variations. The mass-loss rate in helium is log $\dot{M}$(He) = -4.1. This suggests that the total mass rate including both hydrogen and helium is $10^{-4.0}\ M_\odot\ {\rm yr}^{-1}$. The helium abundance is $Y \approx 0.8 \pm 0.1$. This value has a relatively large error but taken at face value it suggests that the total mass-loss rate of AG Car can be derived by increasing the entries for $\dot{M}(H)$ in Table 9 by 0.7 dex. The average total (H + He) mass-loss rate during our observational campaign is $\dot{M} = 10^{-4.1}\ M_\odot\ {\rm yr}^{-1}$. We emphasize the uncertainties associated with this value: the uncertain helium abundance, the velocity law, the variability of the outflow, and deviations from spherical symmetry. However, the main new result is the constancy (or probably even decrease) of $\dot{M}$, and this result is much less affected by such uncertainties.

6. AG CARINAE: LBV ROSETTA?

6.1. *Relation between the Photosphere and $\dot{M}$*

The nearly constant (or even decreasing) mass-loss rate of AG Car over a period when the effective temperature decreased significantly is surprising and in disagreement with what was previously thought to be a general property of LBVs (see Lamers 1989). Historically, the first (so far the only) LBV for which an anticorrelation between $\dot{M}$ and $T_{\rm eff}$ could be established was R71. Wolf et al. (1981) found that the mass-loss rate of the S Dor variable R71 varied by one to two orders of magnitude between minimum and maximum state. Leitherer, Abbott, & Schmutz (1989) subsequently demonstrated that such behavior can be understood if radiation pressure drives the optically thin wind and if a subatmospheric mechanism can be identified to increase to stellar radius. The similarity of the spectral morphology suggests that the same arguments apply to the prototype of the S Dor variables, S Dor (=R88) itself (Leitherer et al. 1989). Although it has become customary to extend these results, which were obtained for an LBV subclass, to other LBVs as well, our present study shows that this generalization is invalid. AG Car does not exhibit the $\dot{M}$ versus $T_{\rm eff}$ relation observed in R71 and S Dor (at least not in the temperature range covered in this study).

What can be said about other LBV's? Little observational material exists which would allow us to prove or reject a correlation between mass loss and temperature in other LBVs. Leitherer et al. (1992) suggested that the LBV R127 behaves in a way very similar to AG Car. Comparison of the optical spectrum of R127 when it was hottest (late O; Stahl et al. 1983) and coolest (early-A; Wolf 1992) supports the view that no significant mass-loss variation occurred between these spectral phases. On the other hand, R110 did show temperature-dependent mass-loss variations but in just the opposite sense: $\dot{M}$ was lower at lower temperature (Stahl et al. 1990). Leitherer & Langer (1991) interpreted the lower mass-loss rate as a property of a radiatively driven wind. The stellar radiative momentum flux in the ultraviolet decreases dramatically if $T_{\rm eff} < 8000$ K and the kinematic momentum flux of the outflow is correspondingly low. The lower mass-loss rate is therefore a natural consequence of a radiatively driven wind if the effective temperature becomes lower. The problem still remains which mechanism is capable in modifying the photospheric temperature. Recently Sterken et al. (1991) discovered the galactic star HD 160529 as a new addition to the LBV family. An analysis of the mass loss during several epochs when HD 160529 varied between spectral types early-A and late-B resulted in $\dot{M} \approx$ const.

We conclude that *there is no observational support for a*

unique relation between photospheric temperature (or radius) and *mass-loss rate among LBVs*. Some LBVs have higher mass-loss rates at lower temperature, at least one shows the opposite behavior, and in some LBVs (including AG Car) the temperature variations occur at approximately constant mass-loss rate. Such behavior was also suspected by Wolf (1992). AG Car and HD 160529 have vastly different stellar parameters: AG Car is among the most luminous and hottest LBVs, whereas HD 160529 is one of the least luminous ($L \approx 4 \times 10^5\ L_\odot$; Sterken et al. 1991) and coolest ($T_{\rm eff} = 8000$ K; Sterken et al. 1991). Yet both show the same behavior with respect to the mass-loss rate.

The lack of correlation between photospheric radius and temperature on the one hand, and $\dot{M}$ and the other is incompatible with a model which ascribes the radius variability to optical depth variations in a wind with variable mass-loss rate. This has been suggested by Appenzeller (1986) and Davidson (1987). In principle, such a model could account in a self-consistent way for the observed radius and mass-loss variability in objects like R71 and S Dor. However, Leitherer et al. (1989b) and de Koter (1993) computed radiative wind models to investigate the proposed radius increase with increasing mass-loss rate in a quantitative way. It was found that optical depth effects alone cannot explain the radius variability in R71 and S Dor and that the mechanism responsible for the variable photospheric parameters still needs to be identified. AG Car provides additional observational proof for this theoretical result. $T_{\rm eff}$ and $R_\star$ vary without a significant variation of $\dot{M}$.

6.2. *Geometry of the Stellar Wind*

Traditionally, spherical symmetry has often been assumed for the geometry of the outflows from LBVs. The results from our spectropolarimetry indicate that deviations from spherical symmetry exist in AG Car. Is AG Car unique in this respect, or do related objects show similar evidence for asymmetries in their winds?

The small level of intrinsic, variable polarization found in some O supergiants (Lupie & Nordsieck 1987 and references therein) has been attributed to density perturbations in the wind, also observed as discrete absorption components in the UV spectra of O stars. The high and variable intrinsic polarization observed in Be and B[e] stars ($\sim 1\%$–2%; Poeckert, Bastien, & Landstreet 1979; Zickgraf & Schulte-Ladbeck 1989) is thought to originate from the high-density contrast between the equatorial and polar winds (Cassinelli et al. 1987). Extensive broad-band polarization monitoring of single Wolf-Rayet stars (Drissen et al. 1987; Robert et al. 1989) has shown that the wind structure of most Wolf-Rayet stars is variable ($\Delta P \approx 0.1\%$–0.6%) on timescales of hours to days. As in the case of OB stars, these variations are attributed to condensations of material being randomly ejected from the star. Contrary to Be stars, the random distribution of the data points shows no indication of a global asymmetry in the wind structure for the vast majority of single Wolf-Rayet stars (although a few noticeable exceptions have been found by Schulte-Ladbeck, Meade, & Hillier 1992 based on spectropolarimetric data).

All LBVs observed so far show relatively high levels of intrinsic polarization, indicative of nonspherically symmetric outflows. The brightest and most spectacular Galactic LBV, η Car, is embedded in a very complex gas and dust shell resulting from last century's eruption (Davidson 1989). Hester et al. (1991) detected a jetlike feature pointing away from η Car. High-resolution spectroscopy by Meaburn et al. (1993) confirms that the object has the characteristics of a true interstellar jet. Although there is no observational proof so far that AG Car's resolved bipolar outflow also satisfies the definition of a true jet, a similar physical mechanism for the origin of the "jets" in η Car and AG Car seems plausible.

Imaging polarimetry (Warren-Smith et al. 1979) reveals very high levels of polarization (up to 35%) in the homunculus, in an almost centrosymmetric pattern. Such high levels are produced by scattering of the stellar light by dust particles. The dust is not spherically distributed and strongly attenuates the central object η Car (Hillier & Allen 1992). Because of the dense surrounding shell, very little is known about the polarization properties of the central star itself. The variation in the global polarization observed 20 yr apart (Gnedin et al. 1992) could have been caused by dust redistribution in the shell.

P Cygni shows intrinsic and variable polarization (up to 0.6%; Hayes 1985; Taylor et al. 1991). The absence of a persistent topology in the distribution of the data points in the $Q-U$ diagram of P Cyg argues in favor of ejection of clumps or plumes in random directions rather than in a preferred plane. This agrees rather well with the results of other, independent techniques. White & Becker (1982) resolved P Cyg's stellar wind by radio interferometry and found that the visibility function is consistent with a spherically symmetric wind. Clampin (private communication) obtained coronographic images of the nebulosity detected by Leitherer & Zickgraf (1987) and Johnson et al. (1992). The nebulosity is characterized by a remarkable degree of symmetry.

Large polarization variation across the Hα emission line has been observed in the LMC LBV R127 (Schulte-Ladbeck et al. 1993). The intrinsic polarization of this star (1%–1.5%) is much higher than that of P Cyg, and a global distortion of the wind, similar to that of Be stars, is favored in this case. Clampin et al. (1993) found clear evidence for axial symmetry in the resolved nebula around R127—in contrast to P Cyg which was observed with the same observational technique. Further support for stronger deviations from spherical symmetry in R127's wind (as compared to P Cyg) comes from the detection of inverse P Cygni profiles in R127. Schulte-Ladbeck et al. (1993) suggested a disklike geometry to explain the occasional presence of *redshifted* absorption lines.

How does AG Car compare with these objects? AG Car's intrinsic level of polarization is at least 0.5%. This value is much higher than the vast majority of normal OB and Wolf-Rayet stars. It compares well with that of P Cyg, but on the other hand is not as high as the intrinsic polarization observed in Be stars and the LBV R127.

The most striking observation comes from the fact that the polarization was relatively high in the 1991 November data, went down to an almost negligible value in 1992 May, and *came back up to almost identical values, both in amplitude and position angle* 2 months later, in 1992 July. This behavior suggests that the wind's asymmetry that gave rise to the high polarization had almost identical geometrical configurations in November and July, and vanished in May. Schulte-Ladbeck (private communication) also observed a very low value of optical continuum polarization in 1992 March.

Although the lack of continuous monitoring in the UV prevents us from developing a unique model for AG Car, it is tempting to suggest a model—proposed before for related stars—that is at least consistent with the few observations we have. The "preferred plane" observed in our UV data could be

interpreted as resulting from a rotationally induced density contrast between the equatorial wind of AG Car and its polar counterpart. Our data do not favor the presence of a thick disk around AG Car (since the intrinsic polarization is not extremely high), but Taylor & Cassinelli (1992) have shown that even a relatively low density contrast (factor of 2) between the equatorial and polar winds of massive stars could produce wavelength-dependent polarization of $\sim 1\%$. The presence of a global asymmetry in the wind is also supported by Schulte-Ladbeck (private communication), who observed large variations of both P and θ across the Hα emission line of AG Car.

It is interesting in this context to note that there are indications that the mass-loss rate was lower between March and May (Table 9) and increased again later on. This drop in the mass-loss rate could have resulted in a lower contrast between the equatorial and polar winds, reducing the amount of intrinsic polarization. We carefully note, however, that although this interpretation is consistent with the observations, it is by no means unique, and in particular the possible correlation between the mass-loss rate and polarization needs to be verified.

Although the geometry derived from the polarization data may not be entirely convincing by itself, it receives further support from the *IUE* results. The hybrid spectrum—lower wind velocities in optical emission lines and higher velocities in ultraviolet absorption lines—is naturally explained by a two-component wind with a relatively fast polar outflow and an equatorial density enhancement leading to a slower, dense wind. This is strikingly similar to the geometry found in the outflows from B[e] stars. Therefore the wind properties of LBVs and B[e] stars may be more similar than previously thought. This similarity provokes the suggestion that there may also be an evolutionary relation between LBVs and B[e] stars.

6.3. *Evolutionary Status of AG Carinae*

We compared the observed position of AG Car in the Hertzsprung-Russell diagram to model predictions by Schaller et al. (1992). The high helium abundance found in the non-LTE analysis implies that a large fraction of the original hydrogen-rich surface layer has already been lost. In fact, $Y \approx 0.8$ is predicted only by models with initial masses greater than 40 $M_\odot$ evolving from red to blue toward the Wolf-Rayet phase. A star with an initial mass of $M_i = (50 \pm 10)\ M_\odot$ at the entrance of the Wolf-Rayet phase is consistent with the derived luminosity, effective temperature, and helium abundance. The current mass would then be $(30 \pm 10)\ M_\odot$. The derived value of M_i leaves open the question if AG Car is currently in a post–red supergiant phase. Due to the uncertainties in the evolutionary models and in the value of M_i itself we cannot exclude the possibility that AG Car went through the red supergiant phase.

Schaller et al's models predict a nitrogen overabundance at the stellar surface of a factor of 16 with respect to the zero-age main sequence. Conversely, carbon and oxygen should be strongly deficient. We already noted the strength of neutral nitrogen lines in AG Car compared to P Cyg. In principle, the nebula surrounding AG Car should provide the clue for the presence or absence of a nitrogen overabundance. Mitra & Dufour (1990) measured a very high N/S ratio but rejected a nitrogen overabundance in favor of a sulfur underabundance. Their result—if indicative of the nitrogen surface abundance of AG Car—would be entirely incompatible with the proposed evolutionary state of AG Car. Nota et al. (1992) argued that the nebula could have been ejected during an earlier epoch when AG Car had not yet developed CNO anomalies at the surface. This hypothesis would be consistent with evolutionary calculations and the dynamical timescale of the nebula. De Freitas Pacheco et al. (1992) reanalyzed the chemical composition of the AG Car nebula and favor a nitrogen overabundance by an order of magnitude. Their result would be consistent with the stellar parameters derived here, under the assumption the composition of the nebula reflects the surface composition of AG Car. In view of the importance of the nitrogen abundance in AG Car, more work is urgently needed to settle the question of the chemical composition of the nebula.

We find that AG Car has parameters very close to WNL stars. The close connection between AG Car (and the related object He 3-519) has recently been emphasized by Smith, Crowther, & Prinja (1994) on the basis of similar spectral morphology. These authors suggested to assign a new spectral class of WN 11 to AG Car. According to Smith et al. there may be a deeper astrophysical connection: AG Car could be considered as a Wolf-Rayet star making an excursion into the variability strip of the Hertzsprung-Russell diagram occupied by LBVs, rather than a LBV entering the Wolf-Rayet phase.

7. CONCLUSIONS

Is AG Car the Rosetta Stone for the LBV phenomenon? Due to its brightness, it is the LBV with the highest-quality observational material available. Two key results were found as a consequence of our observing campaign and theoretical modeling of AG Car: (1) *The stellar wind geometry deviates from spherical symmetry and has a two-component structure.* (2) *There is no indication for a positive correlation between stellar radius and mass-loss rate.*

We detected significant, variable intrinsic polarization in AG Car, which is interpreted as due to electron scattering, possibly modified by hydrogen and metal line absorption in a non-spherically symmetric stellar wind. Similar results have already been found for other luminous stars. Since a systematic study of the intrinsic polarization of LBVs has not yet been done, it cannot be excluded—and it appears plausible—that significant deviations from spherical symmetry are a general property of all LBVs. Further support for this generalization comes from the increasing number of detections of aspherical nebulosities around LBVs. η Car (Hester et al. 1991), AG Car (Nota et al. 1992), HR Car (Hutsemékers & Van Drom 1991a), WRA 751 (Hutsemékers & Van Drom 1991b), R127 (Clampin et al. 1993), and S119 (Nota et al. 1994) are now known to be surrounded by resolved nebular ejecta. High-resolution imaging reveals striking similarities in their morphology. In particular, axial symmetry with density enhancements in the equatorial plane is found in AG Car, R127, and S119. The geometry favored by us for inner wind region of AG Car is quite similar to the geometry of the distant, spatially resolved nebula. Therefore it is plausible that the morphology of the AG Car nebula is not a result of the interaction between AG Car's stellar wind and the ambient ISM, but is already determined by the physical conditions close to the stellar photosphere. However, we caution that the AG Car nebula is not a product of a stellar wind similar to the one presently observed. Rather, it was formed in a much more dramatic outburst $\sim 10^4$ yr ago.

Independent support for an equatorial density enhancement of the wind comes from the spectroscopic observations in the ultraviolet. We find evidence for a two-component wind. A

slow, dense wind observed in recombination lines and a less dense, faster wind observed in the absorption components of ultraviolet lines. The density enhancement in the equatorial plane of AG Car's stellar wind is reminiscent of the geometry suggested for the outflows from B[e] stars (Zickgraf 1992). Until now, there has been little evidence for a connection between LBVs and B[e] stars, except for the fact that they occupy roughly the same part of the Hertzsprung-Russell diagram. Shore (1992) noted some striking similarities in the ultraviolet spectra of LBVs and B[e] stars. Our results for AG Car hint at a closer connection than previously thought. Possibly the same mechanism is responsible for axial symmetry in the winds of LBVs and B[e] stars. Lamers & Pauldrach (1991) proposed an explanation for the existence of "disks" in B[e] by means of a bistability mechanism in radiatively driven winds. This mechanism may also have an application in the wind of AG Car.

One of the most striking properties of LBVs is the variability of photospheric and wind parameters. Incidentally, both the flow timescale of the optically thin wind and the dynamical timescale of the optically thick photosphere are comparable in AG Car (weeks to months). Therefore the timescales observed to occur in the outflow bear few clues for the origin of the variations. We find no evidence for an increasing mass-loss rate when AG Car's radius increased by a factor of 2. This result is new and has significant consequences for models attempting to explain the origin of the radius variability in LBVs in general. The radius variability in AG Car cannot be only due to opacity variations in the outflow, a result which has been suggested by us previously for R71 and S Dor (Leitherer et al. 1989b). However, our coverage of AG Car's activity cycle is still incomplete. If the light curve of AG Car can be extrapolated into the future, we expect a decrease of the effective temperature down to below 10,000 K in the next 2–3 years. It will be crucial to determine the wind properties in this temperature regime in order to assess if the relation between $\dot{M}$ and $R_{2/3}$ continues to hold. Intensive monitoring of AG Car in all accessible wavelength bands and observing modes holds the key for deciphering the Rosetta stone AG Car.

We gratefully acknowledge award of Director's Discretionary Time during which part of the *HST* observations were performed. Some spectroscopic observations at ESO were kindly performed by U. Mürset. M. McMaster assisted in the data reduction at STScI. A. Damineli acknowledges financial support by FAPESP. Support for this work was provided by NASA through grant number GO-3663.03-91A from the Space Telescope Science Institute, which is operated by the Association of Universities for Research in Astronomy, Inc., under NASA contract NAS 5-26555.

REFERENCES

Ake, T. B. 1981, NASA *IUE* Newsletter, 15, 60
———. 1982, NASA *IUE* Newsletter, 19, 37
Allen, R. G., & Angel, J. R. P. 1982, in Instrumentation in Astronomy IV, Proc. SPIE 331, 259
Allen, R. G., Smith, P. S., Angel, J. R. P., Miller, B. W., Anderson, S., & Margon, B. 1993, ApJ, 403, 610
Appenzeller, I. 1986, in IAU Symp. 116, Luminous Stars and Associations in Galaxies, ed. C. W. H. de Loore, A. Willis, & P. Laskarides (Dordrecht: Reidel), 139
Bateson, F. M. 1980–1993, Roy. Astron. Soc. New Zealand, Var. Star Sect. Circ.
Bernat, A. P., & Lambert, D. L. 1978, PASP, 90, 520
Boggess, N. W., et al. 1978, Nature, 275, No. 5679, 372
Capps, R. W., Coyne, G. V., & Dyck, H. M. 1973, ApJ, 184, 173
Caputo, F., & Viotti, R. 1970, A&A, 7, 266
Cassatella, A., et al. 1979, A&A, 79, 223
Cassatella, A., Ponz, D., Selvelli, P. L., & Vogel, M. 1990, NASA, *IUE* Newsletter, 41, 155
Cassinelli, J. P., Nordsieck, K. H., & Murison, M. A. 1987, ApJ, 317, 290
Clampin, M., Nota, A., Golimowski, D., Leitherer, C., & Durrance, S. T. 1993, ApJ, 410, L35
Clarke, D., & McLean, I. S. 1974, MNRAS, 167, 27
Clayton, G. C., et al. 1992, ApJ, 385, L53
Conti, P. S. 1984, in IAU Symp. 105, Observational Tests of Stellar Evolution Theory, ed. A. Maeder & A. Renzini (Dordrecht: Reidel), 233
Davidson, K. 1987, ApJ, 317, 760
———. 1989, in IAU Colloq. 113, Physics of Luminous Blue Variables, ed. K. Davidson, A. F. J. Moffat, & H. J. G. L. M. Lamers (Dordrecht: Kluwer), 101
Davidson, K., Moffat, A. F. J., & Lamers, H. J. G. L. M., eds. 1989, IAU Colloq. 113, Physics of Luminous Blue Variables (Dordrecht: Kluwer)
de Freitas Pacheco, J. A., Damineli, A., Costa, R. D. D., & Viotti, R. 1992, A&A, 266, 360
de Koter, A. 1993, Ph.D. thesis, Univ. of Utrecht
Drissen, L., St.-Louis, N., Moffat, A. F. J., & Bastien, P. 1987, ApJ, 322, 888
Fox, G. K., & Henrichs, H. F. 1994, MNRAS, in press
Gallagher, J. S. 1989, in IAU Colloquium 113, Physics of Luminous Blue Variables, ed. K. Davidson, A. F. J. Moffat, & H. J. G. L. M. Lamers (Dordrecht: Kluwer), 185
Gnedin, Y. N., Kiselev, N. N., Pogodin, M. A., Rozenbush, A. E., & Rozenbush, V. K. 1992, Soviet Astron. Lett., 18, 182
Grady, C. A., & Garhart, M. P. 1988, NASA *IUE* Newsletter, 35, 79
Groenewegen, M. A. T., Lamers, H. J. G. L. M., & Pauldrach, A. W. A. 1989, A&A, 221, 78
Hamann, W.-R. 1987, in Numerical Radiative Transfer, ed. W. Kalkofen (Cambridge: Univ. Press), 35
Hamann, W.-R., & Schmutz, W. 1987, A&A, 174, 173
Hayes, D. P. 1985, ApJ, 289, 726
Hester, J. J., Light, R. M., Westphal, J. A., Currie, D. G., Groth, E. J., Holtzman, J. A., Lauer, T. R., & O'Neil, E. J. Jr., AJ, 102, 654
Hillier, D. J. 1992, in The Atmospheres of Early-Type Stars, ed. U. Heber & C. S. Jeffery (Berlin: Springer), 105
Hillier, D. J., & Allen, D. A. 1992, A&A, 262, 153
Hubeny, I., Stefl, S., & Harmanec, P. 1985, Bull. Astron. Inst. Czechoslovakia, 36, 214
Humphreys, R. M. 1989, in IAU Colloq. 113, Physics of Luminous Blue Variables, ed. K. Davidson, A. F. J. Moffat, & H. J. G. L. M. Lamers (Dordrecht: Kluwer), 3
Humphreys, R. M., Lamers, H. J. G. L. M., Hoekzema, N., & Cassatella, A. 1989, A&A, 218, L17
Hutsemékers, D., & Van Drom, E. 1991a, A&A, 248, 141
———. 1991b, A&A, 251, 620
Israelian, G., & de Groot, M. 1992, in Nonisotropic and Variable Outflows from Stars, ed. L. Drissen, C. Leitherer, & A. Nota (Provo: Brigham Young Univ.), 356
Johansson, S. 1977, MNRAS, 178, 17P
Johnson, H. M. 1976, ApJ, 206, 469
———. 1982, APJS, 50, 551
Johnson, R. H., Barlow, M. J., Drew, J. E., & Brinks, E. 1992, MNRAS, 255, 261
Kilmartin, P. M., & Bateson, F. M. 1991, IAU Circ., No. 5307
Kinney, A. L. 1992, Faint Object Spectrograph Instrument Handbook (Baltimore: STScI)
Klare, G., Neckel, Th., & Schnur, G. 1972, A&AS, 5, 239
Kudritzki, R.-P., Hummer, D. G., Pauldrach, A. W. A., Puls, J., Najarro, F., & Imhoff, J. 1992, A&A, 257, 655
Kurucz, R. L. 1979, ApJS, 40, 1
Lamers, H. J. G. L. M. 1987, in Instabilities in Luminous Early-Type Stars, ed. H. J. G. L. M. Lamers & C. W. H. de Loore (Dordrecht: Reidel), 99
———. 1989, in IA Colloq. 113, Physics of Luminous Blue Variables, ed. K. Davidson, A. F. J. Moffat, & H. J. G. L. M. Lamers (Dordrecht: Kluwer), 135
Lamers, H. J. G. L. M., Hoekzema, N., Trams, N. R., Cassatella, A., & Barylak, M. 1989, in IAU Colloq. 113, Physics of Luminous Blue Variables, ed. K. Davidson, A. F. J. Moffat, & H. J. G. L. M. Lamers (Dordrecht: Kluwer), 271
Lamers, H. J. G. L. M., Korevaar, P., & Cassatella, A. 1985, A&A, 149, 29
Lamers, H. J. G. L. M., & Pauldrach, A. W. A. 1991, A&A, 244, L5
Leitherer, C., Abbott, D. C., & Schmutz, W. 1989, in IAU Coll. 113, Physics of Luminous Blue Variables, ed. K. Davidson, A. F. J. Moffat, & H. J. G. L. M. Lamers (Dordrecht: Kluwer), 109
Leitherer, C., Appenzeller, I., Klare, G., Lamers, H. J. G. L. M., Stahl, O., & Waters, L. B. F. M. 1985, A&A, 153, 168
Leitherer, C., Damineli, A., & Schmutz, W. 1992, in Nonisotropic and Variable Outflows from Stars, ed. L. Drissen, C. Leitherer, & A. Nota (Provo: Brigham Young Univ.), 366

Leitherer, C., & Langer, N. 1991, in IAU Symp. 148, The Magellanic Clouds, ed. R. Haynes & D. Milne (Dordrecht: Reidel), 490
Leitherer, C., Schmutz, W., Abbott, D. C., Hamann, W.-R., & Wessolowski, U. 1989b, ApJ, 346, 919
Leitherer, C., & Zickgraf, F. J. 1987, A&A, 174, 103
Lupie, O. L. 1994, in preparation
Lupie, O. L., & Nordsieck, K. H. 1987, AJ, 92, 214
Lupie, O. L., & Stockman, H. S. 1988, in Polarized Radiation of Circumstellar Origin, ed. G. V. Coyne, A. M. Magalhães, A. F. J. Moffat, R. E. Schulte-Ladbeck, S. Tapia, & D. T. Wickramasinghe (Vatican City: Vatican Obs.), 705
Maeder, A. 1989, in IAU Colloq. 113, Physics of Luminous Blue Variables, ed. K. Davidson, A. F. J. Moffat, & H. J. G. L. M. Lamers (Dordrecht: Kluwer), 15
Mayall, M. W. 1969, JRASC, 63, 221
McCall, M., L. 1984, MNRAS, 210, 829
McLean, I. S. 1979, MNRAS, 186, 265
McLean, I. S., Coyne, G. V., Frecher, J. E., & Serkowski, K. 1979, ApJ, 231, L141
Meaburn, J., Gehring, G., Walsh, J. R., Palmer, J. W., Lopez, J. A., Bryce, M., & Raga, A. C. 1993, A&A, 276, L21
Mitra, M. P., & Dufour, R. J. 1990, MNRAS, 242, 98
Nota, A., Drissen, L., Clampin, M., Leitherer, C., Pasquali, A., Robert, C., Paresce, F., & Robberto, M. 1994, in Proc. 34th Herstmonceaux Conf., Circumstellar Media in Late Stages of Stellar Evolution, ed. R. E. S. Clegg (Cambridge: Univ. Press), in press
Nota, A., Leitherer, C., Clampin, M., Greenfield, P., Paresce, F., & Golimowski, D. 1992, ApJ, 398, 469
Paresce, F., & Nota, A. 1989, ApJ, 341, L83
Pauldrach, A. W., & Puls, J. 1990, A&A, 237, 409
Poeckert, R., Bastien, P., & Landstreet, J. D. 1979, AJ, 84, 812
Raga, A. C., & Cantó, J. 1989, ApJ, 344, 404
Robert, C., Moffat, A. F. J., Bastien, P., Drissen, L., & St.-Louis, N. 1989, ApJ, 347, 1034
Schaller, G., Schaerer, D., Meynet, G., & Maeder, A. 1992, A&AS, 96, 269
Schmidt, G. D., Elston, R., & Lupie, O. L. 1992, AJ, 104, 1563
Schmutz, W., Hamann, W.-R., & Wessolowski, U. 1989, A&A, 210, 236
Schmutz, W., Leitherer, C., Hubeny, I., Vogel, M., Hamann, W.-R., & Wessolowski, U. 1991, ApJ, 372, 664
Schulte-Ladbeck, R. E., Clayton, G. C., & Meade, M. R. 1993, in Massive Stars: Their Lives in the Interstellar Medium, ed. J. P. Cassinelli & E. B. Churchwell (Provo: Brigham Young Univ.), 237
Schulte-Ladbeck, R. E., Leitherer, C., Clayton, G. C., Robert, C., Meade, M. R., Drissen, L., Nota, A., & Schmutz, W. 1993, ApJ, 407, 723
Schulte-Ladbeck, R. E., Meade, M. R., & Hillier, D. J. 1992, in Nonisotropic and Variable Outflows from Stars, ed. L. Drissen, C. Leitherer, & A. Nova (Provo: Brigham Young Univ.), 118
Serkowski, K. 1968, ApJ, 154, 115
———. 1970, ApJ, 160, 1083
Serkowski, K., Mathewson, D. S., & Ford, V. L. 1975, ApJ, 196, 261 (SMF)
Shore, S. N. 1992, in Nonisotropic and Variable Outflows from Stars, ed. L. Drissen, C. Leitherer, & A. Nota (Provo: Brigham Young Univ.), 342
Shore, S. N., Waxin, Y., & Altner, B. 1994, in preparation
Smith, L. J., Crowther, P. A., & Prinja, R. K. 1994, A&A, in press
Snow, T. P., & Stalio, R. 1987, in Exploring the Universe with the *IUE* Satellite, ed. Y. Kondo (Dordrecht: Reidel), 183
Stahl, O. 1986, A&A, 164, 321
Stahl, O., Mandel, H., Wolf, B., Gäng, Th., Kaufer, A., Kneer, R. Szeifert, Th., & Zhao, F. 1993, A&AS, 99, 167
Stahl, O., Wolf, B., Klare, G., Cassatella, A., Krautter, J., Persi, P., & Ferrari-Toniolo, M. 1983, A&A, 127, 49
Stahl, O., Wolf, B., Klare, G., Jüttner, A., & Cassatella, A. 1990, A&A, 228, 379
Stellingwerf, R. F. 1978, ApJ, 224, 953
Sterken, C., Gosset, E., Jüttner, A., Stahl, O., Wolf, B., & Axer, M. 1991, A&A, 247, 383
Taylor, M., & Cassinelli, J. P. 1992, ApJ, 401, 311
Taylor, M., Nordsieck, K.-H., Schulte-Ladbeck, R. E., & Bjorkman, K. S. 1991, AJ, 102, 1197
Thackeray, A. D. 1950, MNRAS, 110, 526
———. 1969, M.N.A.S. So. Africa, 28, 37
———. 1977, MNRAS, 180, 85
van Genderen, A. M., et al. 1988, A&AS, 74, 453
Viotti, R. 1976, ApJ, 204, 293
Viotti, R., Altamore, A., Barylak, M., Cassatella, A., Gilmozzi, R., & Rossi, C. 1984, in Future of Ultraviolet Astronomy Based on Six Years of *IUE* Research (NASA CP-2349), 231
Warren-Smith, R. F., Scarrott, S. M., Murdin, P., & Bingham, R. G. 1979, MNRAS, 187, 761
White, R. L., & Becker, R. H. 1982, ApJ, 262, 657
Whitelock, P. A., Carter, P. S., Roberts, G., Whittet, D. C. B., & Baines, D. W. T. 1983, MNRAS, 205, 577
Wilking, B. A., Lebofsky, M. J., & Rieke, G. 1982, AJ, 87, 695
Wolf, B. 1989, in IAU Colloq. 113, Physics of Luminous Blue Variables, ed. K. Davidson, A. F. J. Moffat, & H. J. G. L. M. Lamers (Dordrecht: Kluwer), 91
———. 1992, in Nonisotropic and Variable Outflows from Stars, ed. L. Drissen, C. Leitherer, & A. Nota (Provo: Brigham Young Univ.), 327
Wolf, B., Appenzeller, I., & Stahl, O. 1981, A&A, 103, 94
Wolf, B., & Stahl, O. 1982, A&A, 112, 111
Zickgraf, F.-J. 1992, in Nonisotropic and Variable Outflows from Stars, ed. L. Drissen, C. Leitherer, & A. Nota (Provo: Brigham Young Univ.), 75
Zickgraf, F.-J., & Schulte-Ladbeck, R. E. 1989, A&A, 214, 274
Zickgraf, F.-J., Wolf, B., Stahl, O., Leitherer, C., & Klare, G. 1985, A&A, 143, 421

SPIE, 1994
2198 p. 533

Predicted Scattering Characteristics of the Hubble Space Telescope(HST)/COSTAR/Faint Object Spectrograph(FOS)

Frank Bartko

Bartko Science & Technology

Richard J. Harms

Applied Research Corporation

Holland C. Ford

Johns Hopkins University/Space Telescope Science Institute

George F. Hartig

Space Telescope Science Institute

Geoffrey S. Burks

University of Colorado

ABSTRACT

We describe recent orbital test data acquired with the COSTAR/Faint Object Spectrograph(FOS) on the Hubble Space Telescope(HST). These data exhibit possible internal thruput deficit and scattering features in the FOS . We then describe some data from laboratory measurements of COSTAR optical components carried out at Ball Aerospace Corporation and NASA/Goddard Space Flight Center, which we initially thought might bear on some of the orbital test data.

We next use a theoretical model to simulate some of the HST/COSTAR/FOS imaging and spectral performance. We apply the model to the current data to assist in evaluating COSTAR imaging performance, to attempt to isolate the origin of the thruput deficit and scattering features. The results of these studies will permit a better understanding of the limits of HST performance and permit development of optimal strategies for performing spatially resolved spectroscopy in the FOS scientific observing program.

1.0 INTRODUCTION

We began this study to learn how COSTAR might affect the scientific performance of the FOS. We were not certain at the time of abstract submission, how much orbital data would be available for analysis. In particular we were interested to see if the scattering characteristics that we had determined in an earlier study(4) had changed after COSTAR was installed. During the past several months COSTAR was successfully installed, aligned and focused for all of the axial bay focal plane instruments, and some preliminary scientific data was obtained. As a result, we have modified the emphasis of this paper from dealing with predicted scattering performance to one of describing the actual on orbit test data that we recently acquired, that appears to affect not only the scattering characteristics, but also the overall scientific performance.

COSTAR(Corrective Optics Space Telescope Axial Replacement)(1),(2),(3),(12) is a device built by Ball Aerospace and Communications Group in Boulder, Colorado for NASA Goddard Space Flight Center, which is intended to correct the spherically aberrated images of the Hubble Space Telescope(HST). COSTAR was successfully installed into the HST during the Hubble repair and refurbishment mission in December 1993.and has successfully restored the imaging performance of the HST to its originally

planned performance, providing a Faint Object Camera(FOC) point spread function with approximately 80% of the encircled energy within a 0.20 arcsec diameter. (See the papers by G. F. Hartig et al , J. Crocker et al, and R. Jedrzejewski, et al at this conference). This correction not only enhances the imaging of the HST FOC, but also enables the HST spectrographs to operate far more efficiently by providing greatly improved thruput and reduced integration times for the desired spectral resolution. This correction also provides the capability to perform high spatial resolution spectroscopy of extended objects and point sources in crowded fields.(See the paper by R.J. Harms et al. at this conference). Although the early on-orbit performance of COSTAR has been superb, small amounts of dust contaminants were acquired on the M2 mirrors for both spectrographs during the COSTAR ground-based assembly and test phases at Ball. The GHRS M2 mirror showed that an area of approximately 3.5% was covered by dust while the FOS M2 mirror showed that an area of about 0.5% was affected. Analysis of available test data (13),(14)demonstrated that the impact of the dust contaminants are negligible or very minimal at worst. Hence, cleaning of the mirrors was not attempted.

One objective of this report is to determine if the small amount of dust contaminants on the FOS M2 mirror has any significant effect on the scattering properties of the HST/FOS that were determined in a previously reported study (4). Although the specific on-orbit test that was analyzed in that report has not yet been repeated, analysis of the current test data may give an indication of what changes if any, may be expected. In the following discussions , we describe some of the relevant tests that were performed and summarize our preliminary analysis that was done. We then point out what may be expected from some additional on-orbit testing that is planned for the near term.

2.0 A BRIEF DESCRIPTION OF SOME RELEVANT LABORATORY TEST DATA

The scattering properties of the HST/COSTAR/FOS optical train are primarily affected by diffraction, mirror surface micro roughness, and dust or particulates that may have accumulated on the mirror surfaces(5),(6),(10).
We have to live with the effects of diffraction, but we can minimize the impact of the other contributors by careful handling and controls and imposing tight specs on the mirror surface roughness.

In this section we describe some laboratory test data, which bear on these possible sources of scatter that were measured during assembly and verification testing , prior to delivery of COSTAR to NASA/GSFC. While performing the COSTAR assembly and alignment at Ball, the COSTAR mirrors were inadvertently subjected to contamination by dust particulates during vibration testing. The mirrors were examined with a micro video zoom lens with a CCD camera and frame grabber. Five different areas of the mirror were sampled and particle sizes were measured and counted. The particulates were faceted and specular. The mean particle size was about 7.5 microns. The particle size distribution was estimated by J. Hagopian (NASA/GSFC). The areal coverage on the FOS M2 mirror was less than 0.5%. The particulate contamination on the FOS M2 mirror was identified as graphite fibers, and some moly disulfide lubricant. The fibers originated from vibration testing of the deployable optical bench , during which an FOC light baffle contacted and abraded the surface producing graphite particulates. Witness samples representative of the contamination levels on the FOS M2 mirror were tested for optical reflectivity and scatter. Direct measurement of both FOS channels showed that the transmission was within 2% of the expected value. The reflectivity tests showed no degradation, while the scattered light test, using a TMA Scatterometer at Ball indicated a small degradation in the Bi-Directional Reflectance Function(BRDF) (11)at wavelengths of 3250A and 6328A , at angles greater than 2 arc minutes, but showed no significant change in small angle scatter.

Chris Burrows has kindly provided us with some calculations of the impact of the dust on the GHRS mirrors. We have scaled these calculations to the FOS configuration and areal coverage on the FOS M2 mirror. The results of these calculations are shown in Figure 1, where the scattered intensity in mag/sq arc sec is plotted versus field angle. The calculation uses a zero magnitude star on axis and illustrates the level of the scattered intensity for varying field angle. Contributions from diffraction and mirror micro roughness are also included and compared with the dust contribution. The effect of these contaminants was very

carefully documented and analyzed(13). The resulting light loss is very small for worst case observational scenarios. Based on this analysis, the mirrors were not cleaned since the performance effect was determined to be negligible.

The specification on the COSTAR optics was designed to provide extremely smooth mirror surfaces . Based on preflight measurements of the HST primary and secondary mirror surface roughness and post flight analysis of HST aberrated images, in the absence of spherical aberration , the encircled energy within 0.2" at 1216 ang. would have been 40% (6). The goal of COSTAR was to provide 80% recovery . This translates into a specification of 32% encircled energy within an 0.2" diameter circle at 1216 ang. The product of reflection and scattering losses from the additional M1 and M2 reflections will be no larger than 35% . Measurements of M1 and M2 show that the rms surface roughness of each mirror is about 4ang at all spatial scales shorter than 1 mm, significantly less than the 10ang. spec. The surface quality of the mirrors was measured at NASA/GSFC with both a WYKO TOPO-2D and BAUER profilometers to characterize the surface ripple at scales ranging from less than 1mm to scales of several mm's. Measurements were also made at Tinsley using a Chapman MP2000 instrument. All measurements are in agreement and show an average(over three spots) RMS ripple of 4 ang over the sub-millimeter scales. Thus, the surface micro roughness should not affect the UV imaging or throughput.

Thus we conclude from these laboratory data and analysis that neither the dust on the COSTAR M1 and M2 mirrors for FOS nor their micro roughness contribute in any significant way to the scattering performance and characteristics that we had determined earlier(4).

3.0 ANALYSIS OF ORBITAL DATA AND RESULTS

We have acquired several sets of orbital test data that bear on the scattering properties of the HST/COSTAR/FOS. These data consist largely of target acquisition camera and spectral images from the peak up data on a standard star obtained during the alignment and focus tests for COSTAR after the servicing mission.

The first data set consists of observations of a late A Spectral type star using the FOS camera mirror in conjunction with the target acquisition(4.3"x4.3")aperture. Images were obtained with both the blue and red side detectors. These images are illustrated in Figures 2 and 3. They show a fairly bright halo surrounding the aperture on the blue detector, where approximately 30% of the light appears to be in the halo around the sharp, bright core of the star. On the red side image, a halo is also seen, but it appears to be much fainter than the halo on the blue side. Both linear and logarithmic profile scans are also provided in the figures and show the intensity fall off in the wings. The difference between the two detector channels is evident. We have used the Space Telescope Science Institute developed Telescope Imaging Model(TIM) to calculate the theoretical point spread function at various wavelengths ranging from 1216 ang. to 6363 ang. These profiles are shown in Figure 4. We have taken the theoretical profile at 2000 ang to compare with the intensity distribution seen in the camera image in Figure 2 . The profiles are compared in Figure 5, where it is readily seen that the halo produces broad wings. To see if this halo may have been present earlier, the data archives were searched for blue and red side camera images taken with the same aperture. A set of target acquisition images of the QSO 3C273 were found, which were taken not long after the original HST launch. Scan s through the images on both the blue and red sides are shown in Figure 6. It is apparent that the halo has been present since the original HST launch.

A second set of test data was obtained from the target acquisition sequence of this star. A raster scan is performed starting with the largest aperture(4.3"x4.3"), for coarse acquisition, then moving to the 1" circular aperture for finer angular positioning, and concluding with the 0.3" circular aperture for final image peak up and centering. The low resolution(G160L:1250-2450 ang.) grating is used during this sequence to avoid saturating the detector. These data are illustrated in Figures 7, 8 , and 9. A surface and a contour plot illustrate and reveal a very sharp core in the image as it passes over the edges of the aperture. Figure 7 uses a coarse angular step of 0.172 arc sec. Figure 8 uses an angular step size of 0.062 arc sec. Figures 7 and 8 are both blue side peak ups. Figure 9 illustrates the peak up for the red side using the fine step size(0.062 arc sec). These data may be compared with a simulated peak up sequence which uses a theoretical point spread function calculated for the HST/COSTAR/FOS with the TIM. Figure 10 illustrates this simulated peak up sequence for the blue side with the same aperture and step size used in Figure 8. It

is clear from comparing these data with the simulation, that the COSTAR provides the FOS with a sharp image. Furthermore, we compare the theoretical profile with the target acquisition image profile determined above and see that the target acquisition profile is very sharp and consistent with the theoretical profile. Hence we conclude that the source of the halo seen in Figure 2 is not due to the COSTAR but must arise within the FOS itself. We don't know the location of the optical element within the FOS which produces the halo as yet , but further analysis with additional data to be acquired will help isolate the source, and allow us to look for possible temporal changes.

A third set of data consists of the spectrum of an O spectral type star(G191B2B) that was obtained after COSTAR fine alignment and focusing. This spectrum was compared with the spectrum of the same star taken with the same FOS setup before COSTAR was installed. The ratio of these spectra was taken for both the blue and red side detectors. These ratios are shown in Figures 10 and 11. For the blue side detector, a fairly broad thruput deficit occurs at about 2000 ang., while the response at shorter wavelengths seems to be enhanced. The red side detector shows a fairly flat ratio indicating no significant change. The diamond marks are expected values based on pre flight witness samples and TIM calculations. It is not clear at this point if the thruput deficit in the blue side detector is related to the appearance of the halo seen in the blue side images. It is difficult to postulate a reasonable source that can simultaneously provide the broad deficit seen at 2000ang. , while explaining the apparent increase in response at the shorter wavelengths. It is conceivable that the large point spread function of the pre COSTAR aberrated images could have provided underestimates of the light loss at the shorter wavelengths. If this were the case, the COSTAR corrected point spread function could reduce the light loss such that the short wavelength sensitivity would appear to be enhanced.

We have performed one additional analysis based on the target acquisition peak up data described earlier, in an attempt to isolate the source of the thruput deficit seen in Figure 10. We normalized the spectra obtained at each target acquisition location by the spectrum of the peak image to look for possible wavelength dependence. The ratioed spectra appear to show an increase or a decrease toward shorter wavelengths, depending on how the aperture is sampling the PSF at various wavelengths(we are using a relatively large aperture(0.26 arc sec diam.) to sample a narrow PSF). When the core of the PSF is outside the aperture area, we are sampling the near wings of the point spread function where the shorter wavelengths dominate, and hence the ratioed spectra appear to show an increase at shorter wavelengths. When the core of the PSF is largely inside the aperture, the longer wavelengths dominate and the ratioed spectra show a decrease toward shorter wavelengths. This effect may be understood by examining the point spread function behavior as a function of wavelength seen in Figure 4. The longer wavelengths dominate the core of the PSF, while the wings are dominated by the shorter wavelengths. There is simply not enough angular range to sample the far wings of the PSF with the limited angular range provided by the target acquisition sequence. We will have to wait for further tests to sample the far wings for any potential real wavelength dependence that we could use to evaluate mirror ripple.

While the source of the halo and thruput deficit feature are not presently known, their effect on the FOS scientific performance does not appear to be very significant, unless additional changes occur. We plan to monitor the FOS closely and analyze further tests which are planned in the near term.

4.0 SUMMARY AND CONCLUSIONS

As a result of the data presented above, we draw the following conclusions from this brief analysis: 1). COSTAR provides a very sharp image to the FOS ; 2). Based on our analysis of the target acquisition peak up data, the halo seen in the camera images appears to originate within the FOS and seems to have been present from the time of the original HST launch. We don't presently know the source of this halo within the FOS. ; 3). The FOS blue side detector used with the low resolution grating(G160L) shows a broad thruput deficit around 2000 ang. We also don't know or understand the source of this feature at the present time, or if the two phenomena are related. However, we are pursuing additional tests to isolate these features, and to understand the temporal behavior, if any, and quantify their impact on the scientific observations. We will report on the results of those additional tests at a later date.

Some of the tests planned include an FOS throughput and sensitivity test using all gratings, both detectors and all relevant apertures. Also an aperture location test to determine precise positions and effective sizes of the apertures will be conducted. Additional fine peak up scans using a smaller aperture on stellar sources can be used to probe finer details of the PSF with the FOS camera mode. Flat field testing may help in locating the source of the thruput deficit feature seen at 2000 ang.. The high resolution grating H19 will be used to verify the characteristics of this feature.

The Science Verification test that had been previously done(SV1319) and which was analyzed to determine the scattering properties of the HST/FOS , will also be repeated at some future time. When the results of this test become available , we expect that the sharpened PSF will allow us to characterize the mid spatial frequency structure of the HST mirror surfaces. These results are needed to provide us with the achievable performance levels that may be realistically expected from a coronagraphic mode of any proposed advanced camera designs for the HST.

5.0 ACKNOWLEDGMENTS

We acknowledge help from Chris Burrows at STSCI for providing some of the calculations, and from the Ball Aerospace and NASA/GSFC engineers who performed the difficult tests during the COSTAR test and verification phase. This work was supported by NASA Grant ~~NAS 5-29293~~ NAS 5-1630.

6.0 REFERENCES

1). Crocker, J. H., "Fixing the Hubble Space Telescope", *SPIE Proceedings*, Vol. 1494, 1991.
2). Lightsey, P.A., Gerber, J.D., Kaplan, M.L., and Teusch, D.A., "System Performance Analysis for COSTAR Design", *SPIE Proceedings*, Vol. 1945, 1993.
3). Hartig, G. F., Crocker, J. H., and Ford, H. C.,"Status and Optical Performance of the Corrective Optics Space Telescope Axial Replacement(COSTAR)", *SPIE Proceedings*, Vol. 1945, 1993.
4.) Bartko, F., et al., "Scattered Light Characteristics of the Hubble Space Telescope Faint Object Spectrograph, *SPIE Proceedings* , Vol. 1945, pp 318-327, 1993.
5.) Brown, R. A. and Burrows, C. J. , "On the Feasibility of Detecting Extra Solar Planets by Reflected Star Light using the Hubble Space Telescope", *Icarus*, Vol.87, pp 484-497,1990.
6.) Burrows, C. J. ,"Hubble Space Telescope Optical Assembly Handbook",Version 1.0, STSCI, 1990.
7.) Ford, H. C. ," Faint Object Spectrograph Handbook," STSCI, Oct. 1985.
8.) Harms, R. J., et al., "The Faint Object Spectrograph", *SPIE Proceedings*, Vol. 183,p.74.
9.) Harms, R. J., et al., "Astronomical Capabilities of the Faint Object Spectrograph on Space Telescope", IAU Commission 44, *The Space Telescope Observatory*, Aug. 1982.
10.) Hasan, H. "Point Spread Function Scattering Test", Instrument Science Report-OTA, STSCI, Feb. 1992.
11.) Stover, J. C., *Optical Scattering*, McGraw Hill, New York, 1990.
12.) Bottema, M., BASD Internal Memo-Sept. 9, 1991.
13.) Ford, H. C. , STSCI Memo-Aug. 10, 1993.
14.) Williams, R., STSCI Memo-Nov. 8, 1993.

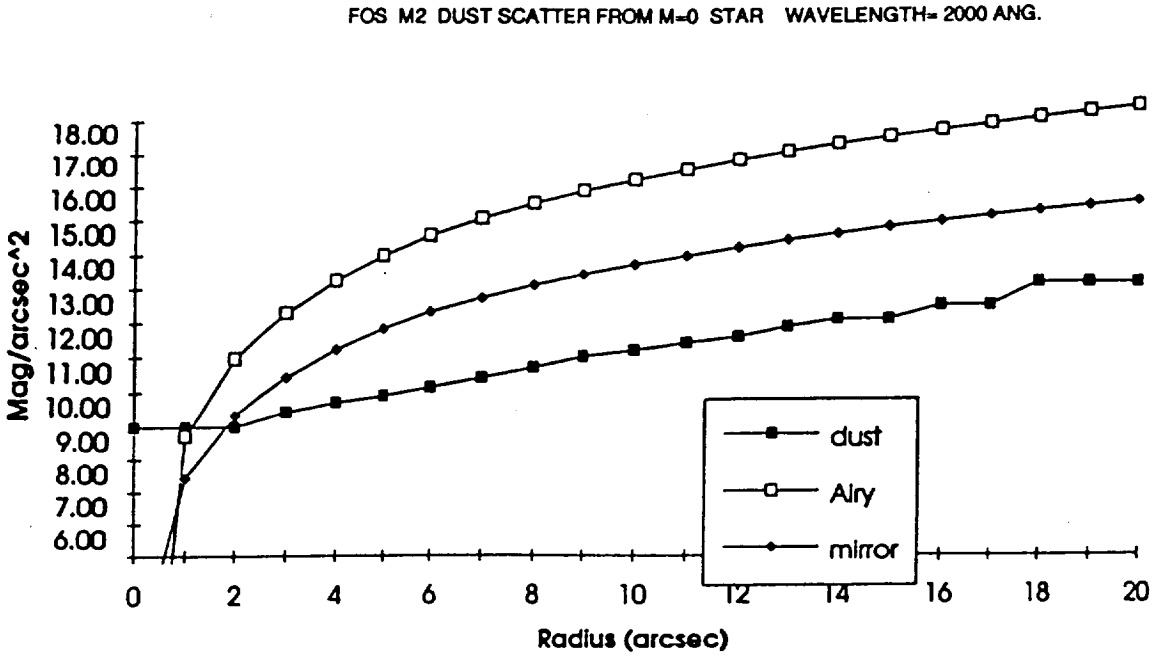

Figure 1. Theoretical calculations , scaled for the FOS , of the scattered intensity produced by residual dust contaminants on the COSTAR FOS M2 mirror. The calculations illustrate the intensity(at 2000 ang.) at the FOS aperture resulting from a zero magnitude star situated on axis. The contributions include diffraction, mirror micro roughness and dust particles(based on the particle size distribution which peaks at about 7.5 microns). The calculations show that the intensity due to scattered light from the dust (which covers about 0.5% of the M2 mirror surface) is less than the required specification and hence will be negligible.

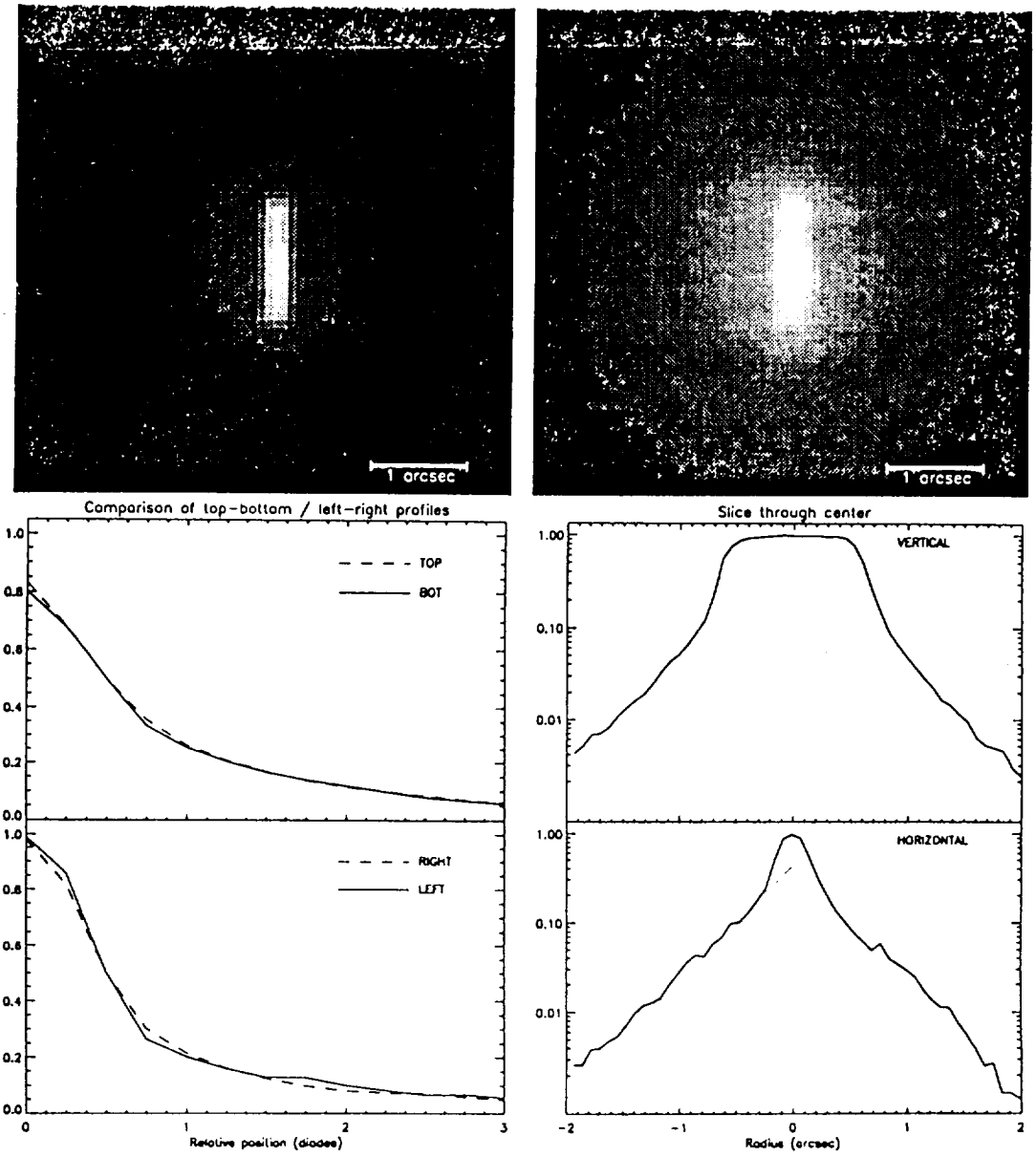

Figure 2. Images of a standard star illuminating the FOS target acquisition(4.3"x4.3") aperture using the blue detector. Note the fairly bright halo surrounding the diode. The origin of this halo is not presently known or understood. Note the intensity in the wings of the profile, where both linear and logarithmic scales are shown

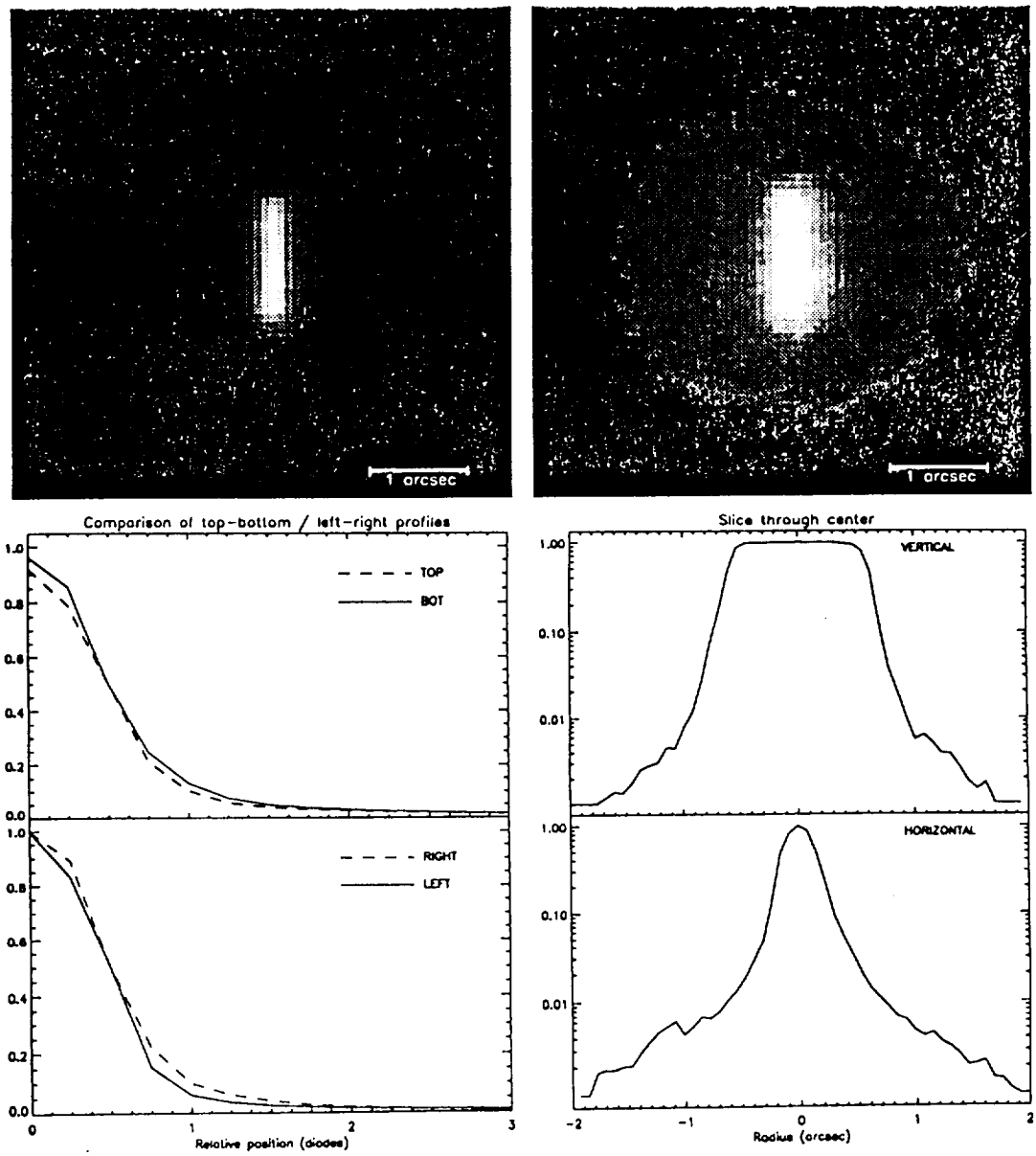

Figure 3. Images of the same standard star illuminating the target acquisition aperture using the red detector. In th case a halo is still seen but it is much fainter than that for the blue side. Compare the intensity drop off in the wing in the logarithmic plots with those seen in Figure 2.

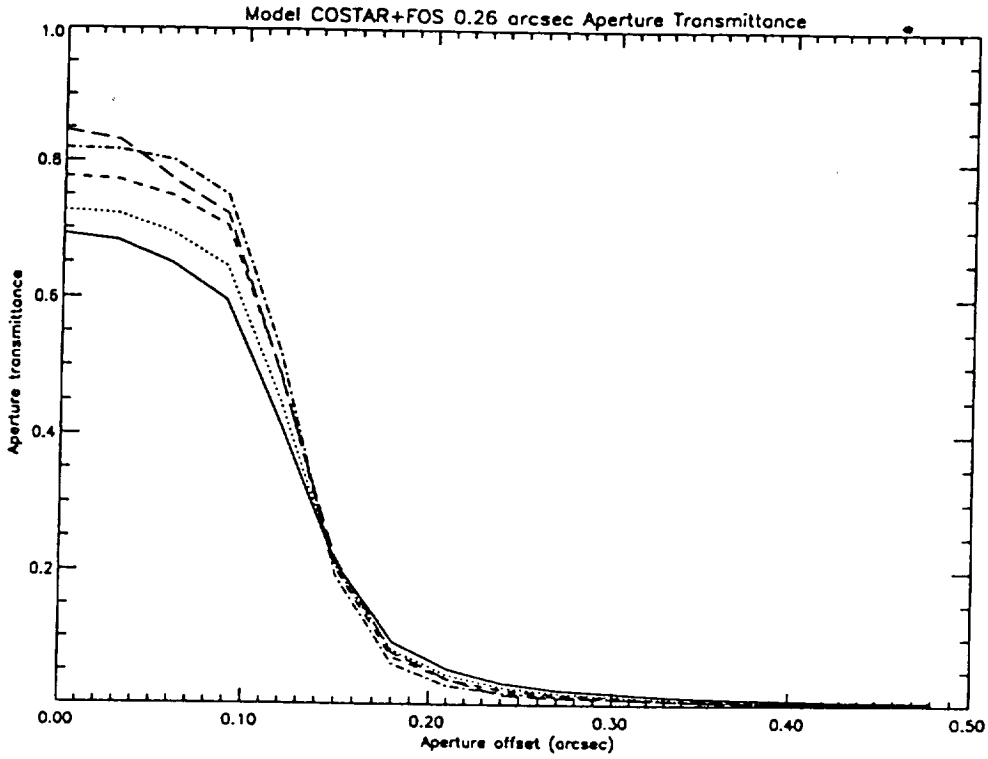

Figure 4. Theoretical Point Spread Function profiles for various wavelengths. Solid is 1216 ang., dotted is 1500 ang., short dash is 2000 ang., long dash is 4000 ang., and dot-dash is 6300 ang. These were calculated using the Space Telescope Science Institute developed Telescope Imaging Model(TIM).

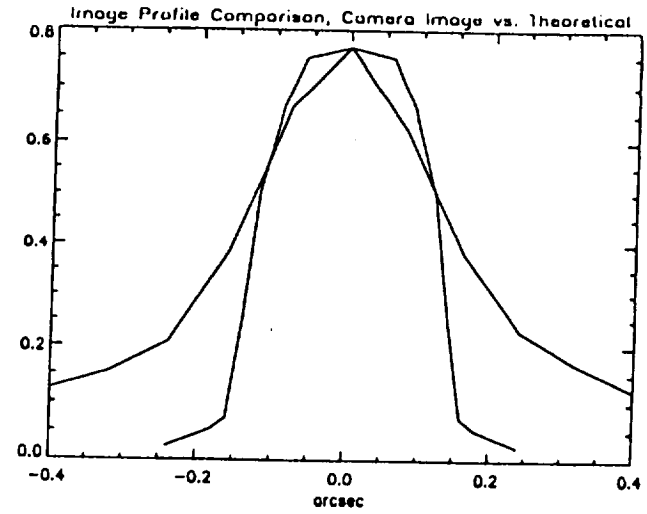

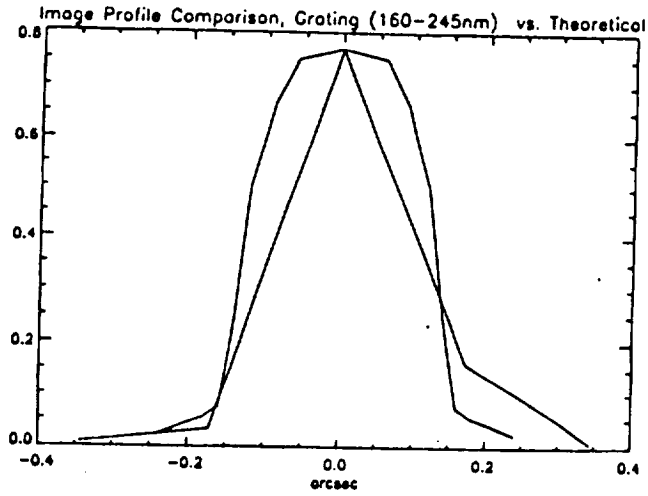

Figure 5. A comparison is shown of profiles of point spread functions determined from the target acquisition sequence in Figure 8 and from the direct camera image on the blue side detector shown in Figure 2. It is readily seen that the observed image profile from the target acquisition sequence is sharp and consistent with the theoretical profile ,while the image profile from the direct camera image on the FOS blue side shows much broader wings, indicative of the halo seen in Figure 2.

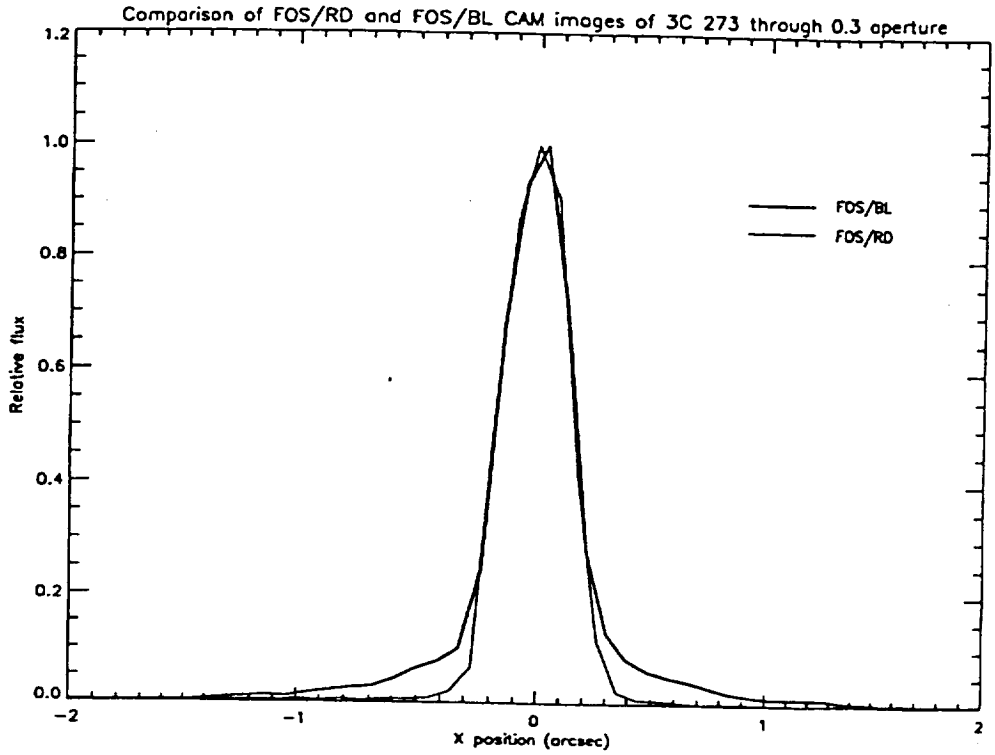

Figure 6. A pre-COSTAR comparison of the FOS blue and red side images acquired during target acquisition on the QSO 3C273 in the camera mode is shown. These data are taken from the archive at the STSCI and represent data taken with the HST/FOS shortly after launch. The halo surrounding the blue image is present at that time. Thus, the halo seen in Figure 2 has been present from the beginning and is not necessarily associated with the COSTAR replacement mission. This halo was probably masked by the large PSF of the aberrated HST.

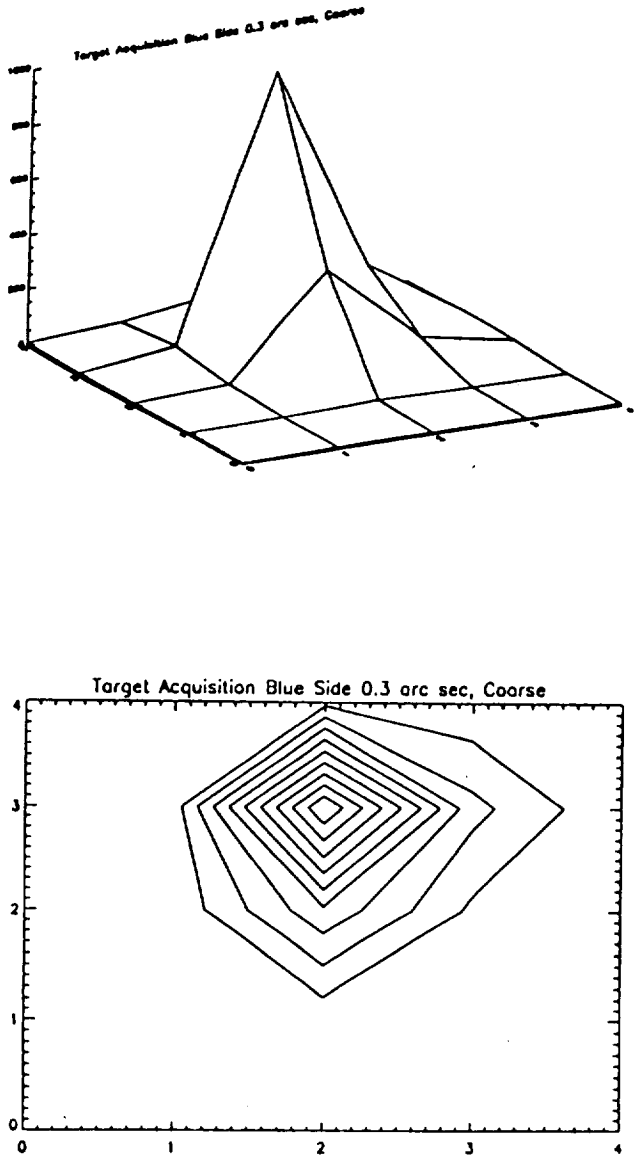

Figure 7. Target acquisition sequence on a standard star in the 0.26 arc sec aperture using the blue side detector with the low resolution(R=200) grating(G160L:1200-2450 ang.). The step size is 0.172 arc sec in both directions. A surface plot is shown above and a contour plot below.

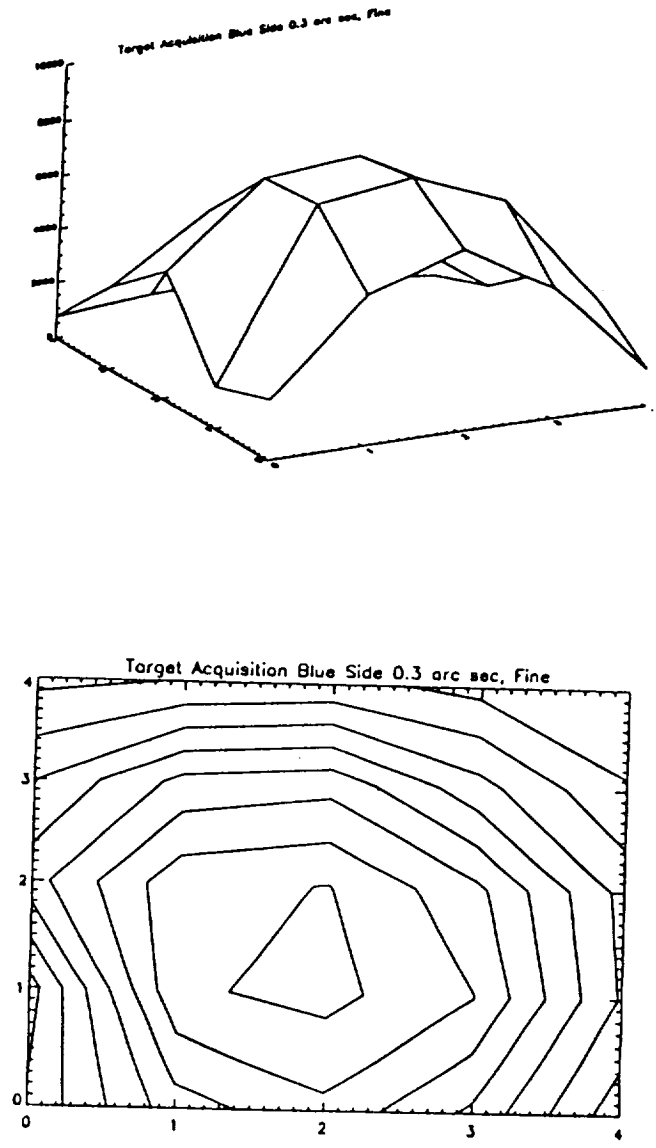

Figure 8. Target acquisition sequence on the A type star in the 0.26 arc sec aperture using the blue side detector with the low resolution(R=200) grating(G160L:1200-2450 ang.). The step size is 0.062 arc sec in both directions. A surface plot is shown above and a contour plot below. The image is not perfectly centered.

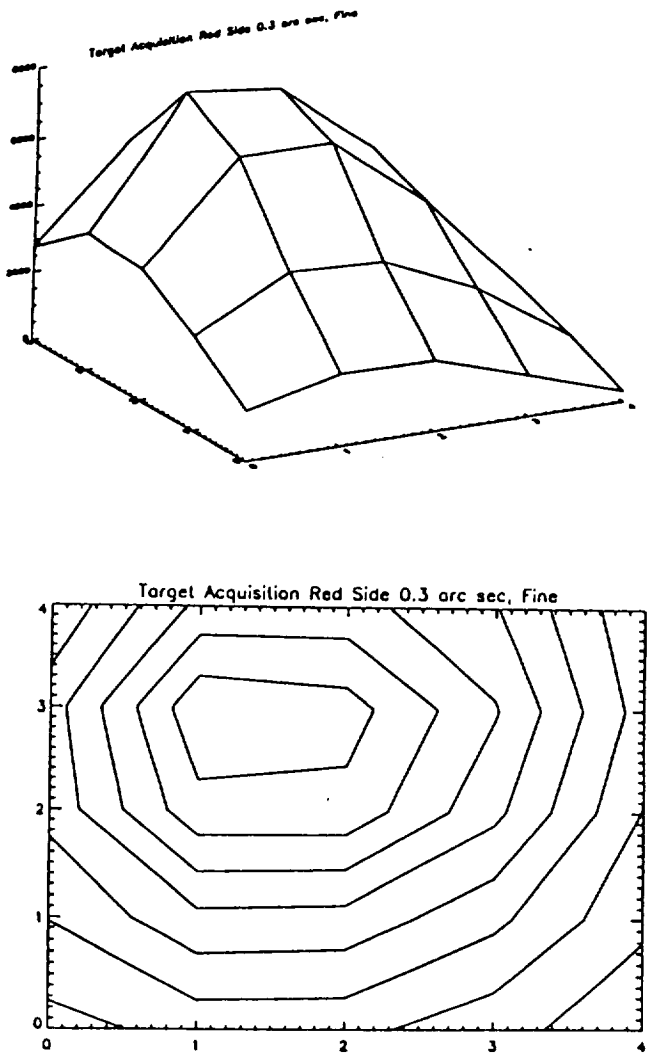

Figure 9. Target acquisition sequence on the A type star in the 0.26 arc sec aperture using the red side detector with the low resolution(R=200) grating(G160L: 1600-2450 ang.) The step size is 0.062 arc sec in both directions. .A surface plot is shown above and a contour plot below. The image is not exactly centered.

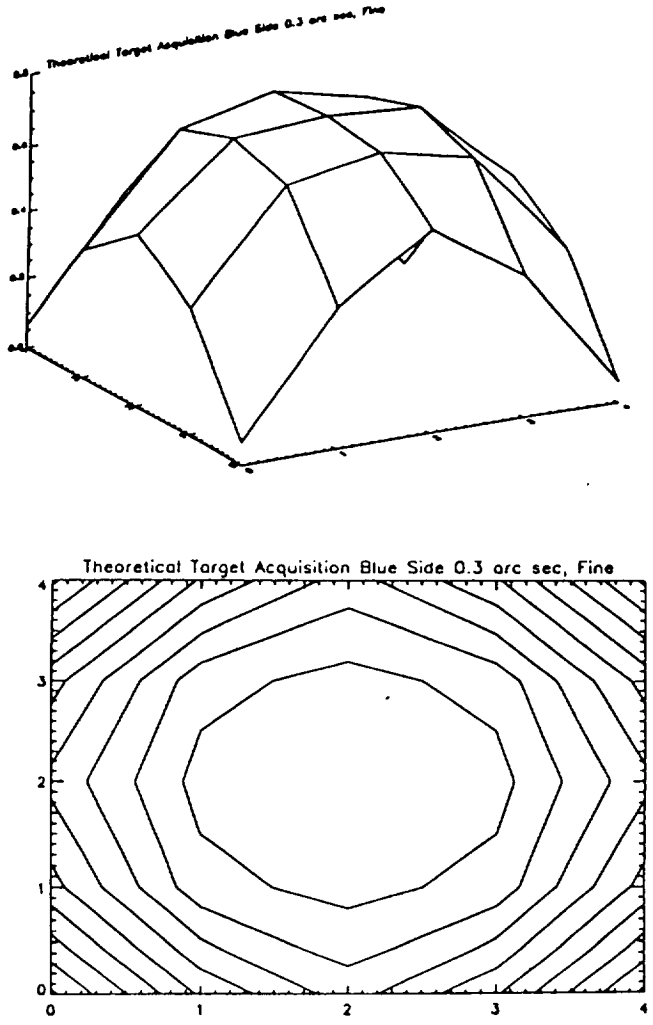

Figure 10. Simulated target acquisition sequence on a theoretical point spread function, again using the blue side detector with the low resolution(R=200) grating(G160L:1200-2450 ang.). The step size is 0.062 arc sec in both directions. A surface plot is shown above and a contour plot below. Compare these plots with those shown in Figure 8 and note their similarity.

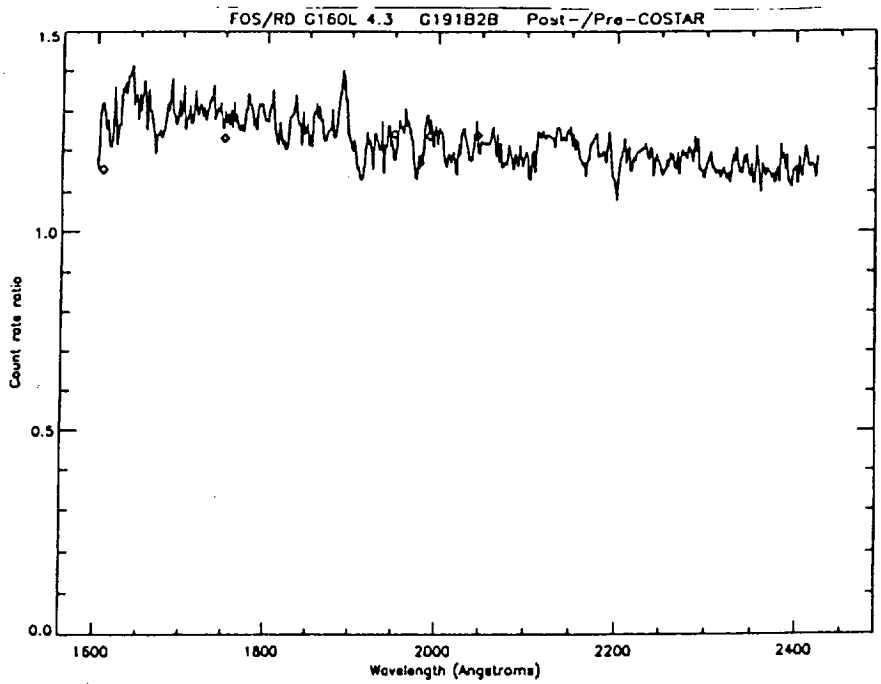

Figure 11. Spectra of an O type standard star(G191B2B) were taken with the FOS Red detector and low resolution grating(G160L:1600-2450 ang.) through the large acquisition aperture, both before and after COSTAR installation. The ratio (post COSTAR/ pre COSTAR) is illustrated. The ratio is fairly flat indicating no significant change in spectral sensitivity resulting from the COSTAR installation process. The diamonds indicate expected values based on witness samples and TIM calculations.

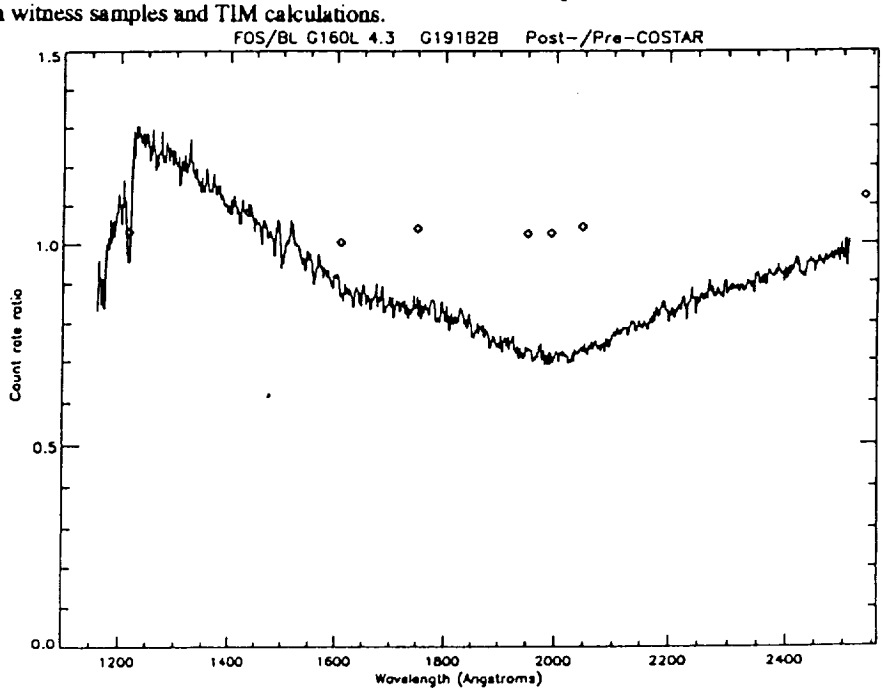

Figure 12. Spectra of the same O type star were also taken with the FOS Blue detector and low resolution grating(G160L:1200-2450 ang.) through the large acquisition aperture, before and after COSTAR installation. The ratio (post COSTAR/ pre COSTAR)is again illustrated. In this case however, the ratio shows marked departures from expectations. A large thruput deficit appears at 2000 ang. while an increased sensitivity is seen at shorter wavelengths near 1300 ang. We currently have no viable explanation for this apparent change in FOS spectral response at these wavelengths, but are pursuing additional tests that will hopefully provide some insight on the source of this anomaly. Again the diamonds indicate expected values based on witness samples and TIM calculations.